

**NON-DESTRUCTIVE TESTING AND SURFACE EVALUATION
OF
ELECTRICAL STEELS**

by

Sam Nyamekye Konadu B. Eng, MSc.

**A thesis submitted to Cardiff University in candidature for the degree of
Doctor of Philosophy**

Cardiff School of Engineering, Cardiff University

May, 2006

UMI Number: U584862

All rights reserved

INFORMATION TO ALL USERS

The quality of this reproduction is dependent upon the quality of the copy submitted.

In the unlikely event that the author did not send a complete manuscript and there are missing pages, these will be noted. Also, if material had to be removed, a note will indicate the deletion.



UMI U584862

Published by ProQuest LLC 2013. Copyright in the Dissertation held by the Author.
Microform Edition © ProQuest LLC.

All rights reserved. This work is protected against
unauthorized copying under Title 17, United States Code.



ProQuest LLC
789 East Eisenhower Parkway
P.O. Box 1346
Ann Arbor, MI 48106-1346

DECLARATION

This book has not previously been accepted in substance for any degree and is not being concurrently submitted in candidature for any degree.

Signed.....*K. Rajanthy*.....(candidate)

Date.....*31/5/06*.....

STATEMENT 1

This thesis is the result of my own investigations, except where otherwise stated.

Other sources are acknowledged by footnotes giving explicit references. A bibliography is appended.

Signed.....*K. Rajanthy*.....(candidate)

Date.....*31/5/06*.....

STATEMENT 2

I hereby give consent for my thesis, if accepted, to be available for photocopying and for inter-library loan, and for the title and summary to be made available to outside organisations.

Signed.....*K. Rajanthy*.....(candidate)

Date.....*31/5/06*.....

NB: Candidates on whose behalf a bar on access has been approved by the University (see Appendix 2), Should use the following version of statement 2:

I hereby give consent for my thesis, if accepted, to be available for photocopying and for inter-library loans after **expiry of a bar on access approved by the University of Wales on the special recommendation of the Constituent Institution/University College concerned.**

Signed.....*K. Rajanthy*.....(candidate)

Date.....*31/5/06*.....

ACKNOWLEDGEMENT

This work was carried out at the Wolfson Centre for Magnetic Technology, Cardiff School of Engineering, Cardiff University.

I would like to express my profound gratitude to Professor A. J. Moses for supervising my project and for his support, the useful suggestions, encouragements and the ready assistance he offered whenever there was the need. I must thank him for his patience too.

Secondly, I wish to thank Pamela Cummings of Cogent Power Ltd. for granting me the permission to use her office and measuring system, and also for her advice. Finally I wish to express my heartfelt thanks to my friend, Stan Zurek for his help, advice and encouragement.

Dedicated

to:

**Cecilia, my dear wife, Samuel Agyemang Konadu
(son) and Grace Yeboaa Konadu (daughter), for your
deep love, prayer and moral support, without which I
would not have come this far.**

Blessed be the name of the LORD GOD ALMIGHTY.

**He has become my salvation, my strength
and my song.**

**He is clothed in majesty and strength,
and for ever His word is settled in heaven.**

His hand has accomplished this.

ABSTRACT

The ultimate objective of this project has been to develop a non destructive and surface evaluation on-line system for the determination of localised power loss in electrical steels

Three different approaches were made by employing three different methods or measuring systems on steel samples to study sequentially:

(1) the position of a grain boundary from both the front and the exact opposite side at the back of the grain-oriented electrical steel sample,

(2) the position of grain boundaries at the surface of grain-oriented electrical steels through the measurement of the field distribution at the surface of the magnetised steel samples, and

(3) the localised power loss in 3.25% grain-oriented electrical steels.

In the first case, a computer based optical microscope and a 3-Chip colour video camera system was used to establish positions of grain boundaries in order to explain differences in field profiles outside the systematic accuracy of measurements

In the second case a Magnetic (Atomic) Force Microscopy (MFM) system was used to raster scan the top surface of samples such as high permeability Grain oriented 3.25% Silicon Steel, Cobalt based nanocrystalline material and Nickel Iron alloy W597 Vacoperm 100, producing images for the establishment of grain boundaries. Grain boundaries of width between 50nm and 150nm were established.

Thirdly, a three dimensional integrated Hall effect sensor has been used together with two pairs of needle probes to measure localised power loss in two

dimensions $P(x)$ and $P(y)$ in a 3.25% silicon iron material, with the total localised power loss, $P(t)$ being equal to the sum of the power loss in x-direction, $P(x)$ and the power loss in y-direction $P(y)$.

The 3-D i.c. Hall effect sensor and the needles together in a single package were moved on an arm of Perspex material attached to an X-Y-Z precision position control system. A LabView software package was used for the purpose of controlling the movement of the precision position control system as well as the data acquisition and processing.

Colour images and contours, and also other graph representations showing variations in the intensity of power loss, strayed vertical magnetic field and flux density have been obtained.

The overall mapped results showed a good correlation with predictions made from observed static domains. The correlation not only showed that loss varies from grain to grain, but it is non-uniform in the individual grains.

CONTENTS

ABSTRACT

CHAPTER ONE: INTRODUCTION

- | | | |
|-----|--------------|-------|
| 1.1 | Introduction | (1-1) |
| 1.2 | References | (1-3) |

CHAPTER TWO: BACKGROUND

- | | | |
|------|--|--------|
| 2.1 | Concept of Ferromagnetism, Ferromagnetic materials and domain formation in Silicon Iron. | (2-4) |
| 2.2 | Energy minimisation in a single crystal of silicon iron. | (2-7) |
| 2.3 | Supplementary domain structures related to silicon iron. | (2-12) |
| 2.4 | Magnetic materials and the hysteresis loop | (2-15) |
| 2.5 | Silicon iron | (2.20) |
| 2.6. | The grain - oriented silicon iron | (2-24) |
| 2.7 | Highly oriented grain-oriented material | (2-26) |
| 2.8. | References | (2-28) |

CHAPTER THREE: CONCEPTS OF POWER LOSS

- 3.1. Introduction: Components of power loss (3-31)
- 3.2. Parameters that affect power loss (3-35)
 - 3.2.1. Domain walls not perpendicular to the surface of the sheet (3-35)
 - 3.2.2 Non-planar domain walls (wall bowing) (3-35)
 - 3.2.3 Non-uniform domain wall motion (wall pinning) (3-36)
- 3.3 Interaction between grains, the effect of grain orientation, grain size and lamination thickness (3-41)
- 3.4 Sheet coating and effect of stress in grain oriented silicon steel (3-42)
- 3.5 References. (3-45)

CHAPTER FOUR: METHODS FOR THE DETECTION OF SURFACE FIELDS ON ELECTRICAL STEELS.

- 4.1. Magnetic field detecting sensors (4-48)
- 4.2. Minimum specifications of magnetic fields, H, sensor required for this project (4-49).
- 4.3. Vibrating pick up loop magnetometer, (VPLM) (4-49)
- 4.4 Magnetotransistor (4-50)
- 4.5. Permalloy probe (4-51)

4.6	Magnetoresistive head	(4-52)
4.7	The Hall Probe	(4-55)
4.8	Choice of sensor	(4-56)
4.9	Grain and static domain observation techniques in silicon steels	(4-58)
4.10	References.	(4-61)

**CHAPTER FIVE: INVESTIGATION INTO GRAIN BOUNDARIES OF
GRAIN ORIENTED SILICON IRON.**

5.1.	Background.	(5-63)
5.2	The preparation of Electrical Steel sample	(5-64)
5.3	Investigation of grain boundary positions with a linear Hall effect i.c. sensor	(5-66)
5.4	Measurements of positions of grain boundaries	(5-67)
5.5	Summary of results	(5-72)
5.6	References	(5-73)

**CHAPTER SIX: OBSERVATION OF DOMAIN / GRAIN BOUNDARIES
USING MAGNETIC FORCE MICROSCOPY.**

6.1.	Introduction.	(6-74)
------	---------------	--------

6.2.	Brief description of the MFM system.	(6-77)
6.2.1.	Magnetic Force Imaging overview	(6-82)
6.2.2.	Scanning resolution	(6-84)
6.2.3.	Scanning sensitivity	(6-84)
6.3	Experimental procedure	(6-85)
6.4	Results and discussion.	(6-86)
6.4.1	Magnetic film (metal evaporated tape)	(6-86)
6.4.2	Nickel iron	(6-88)
6.4.3	3.25% grain-oriented silicon iron sample	(6-91)
6.4.4	Further investigation into the silicon iron image	(6-94)
6.4.5	Investigation into a nano crystalline material	(6-98)
6.5	Conclusion	(6-101)
6.6	Reference	(6-102)

CHAPTER SEVEN: DESIGN AND DEVELOPMENT OF POWER LOSS SYSTEM.

7.1.	Introduction (the overview of the system)	(7-103)
------	---	---------

7.2.	The magnetising system	(7-108)
7.3.	The static characteristics of the Integrated Hall Effect sensor and the field detection.	(7-109)
7.4.	Needle probes	(7-112)
7.5.	The LabView programme.	(7-116)
7.6.	The scanning / precision positioning system.	(7-122)
7.7.	Signal circuit and conditioning	(7-124)
7.8.	Power loss representation.	(7-128)
7.9.	Uncertainty of the measurement	(7-130)
7.9.1	Random uncertainties	(7-130)
7.9.2	Systematic uncertainties	(7-131)
7.9.3	Total uncertainty	(7-133)
7.10	References.	(7-135)

CHAPTER EIGHT: RESULTS AND DISCUSSION

8.1.	Introduction.	(8-138)
8.2.	Grain-oriented electrical steel sheet	(8-139)
8.3	The sensor system	(8-144)

8.4.	Investigation into the images obtained	(8-146)
8.5	Investigation of region E (across grain boundaries)	(8-158)
8.6	Variation of power loss within individual regions and the use of a "Soken tester"	(8-162)
8.7	Variation of alternating power loss with induction in 3.25% grain oriented silicon iron	(-164)
8.8	Conclusion	(8-168)
8.9	References	(8-169)
CHAPTER NINE: CONCLUSION AND FUTURE WORK		(9-170)

CHAPTER ONE**INTRODUCTION****1.1 Introduction**

Electrical steels play an important role in the generation and transformation of electrical energy. They are used in many transformer and motor core applications where a.c. magnetic permeability or losses are important. They are used in sheet form typically 0.23mm to 0.65mm thick. Grain oriented 3.25% Silicon Steel has a strong [001](110) texture with grains of up to 10mm in diameter. Its surfaces are usually coated with non-magnetic layers to impose beneficial tensile stress in the steel as well as providing the necessary interlaminar or interturn insulation when built into cores [1.1].

In grain oriented electrical steel the bulk of the material in the demagnetised state comprises anti-parallel bar domains with 180° walls. The domain structure, which depends on the grain size and orientation, is changed by the application of an external field, and during the process magnetic losses occur. The energy loss under a.c. magnetisation is very important and is proportional to the time integral of the product of the instantaneous tangential component of surface field and the instantaneous spatial averaged rate of change of flux density. The energy lost during these processes, is in the form of heat. A large percentage of this loss which is associated with magnetic core material costs the electrical generating companies millions of pounds annually [1.2]. The surface magnetic field in the magnetised or demagnetised state can give an indication of material structure, which in turn has a large influence on the losses and permeability.

Domain or grain detection techniques on grain oriented silicon iron (Si-Fe), used by electrical steel manufacturers, can form a useful quality control technique, and

also help research into producing better materials. With a growing demand for electrical energy, and also the global warming in mind, loss reduction is still considered to be very important.

However, to observe the grain structure, the coating must be removed. This can be achieved by means of a time consuming chemical etching process. This process can be destructive because it can have effect on the magnetic properties of the material. Moreover, the removal of coating reveals only the grain size, and does not provide any indication of the orientation of individual grains.

A physical discontinuity on the surface of a magnetic material can cause a distinguished stray magnetic field pattern. Magnetic stray field detection techniques have been employed in the magnetic data handling industry where data strips can be tested for physical and magnetic damage [1.3].

A system employing an integrated 3 dimensional Hall effect sensor to detect the components of stray surface magnetic field, and needle probes to detect flux density, has been used in this project to determine localised power loss from the field distribution at the surface of grain oriented electrical steel sample. A 3 axes (*X-Y-Z*) precision position control system run by the labview software package has been employed to scan the sensor over the sample surface with spatial resolution of 0.1 mm.

The Vertical (*Z*) component of the field has been used to develop images revealing surface features related to the position of grain boundaries.

A Magnetic Field Microscopy (*MFM*) has also been used in this project to obtain images of magnetic field activities on the surface of the material, which in turn might give an insight to the internal structure of the sample

1.2 Reference

- [1.1] S. D. Washko and E. G. Choby (1979), "Evidence of the effectiveness of stress coating in improving the magnetic properties of high permeability 3%Si-Fe", IEEE Trans. Magn MAG-15, no. 6, pp. 1585-1591.
- [1.2] A. J. Moses (1990), "Electrical steels: past, present and future developments", IEE proc. vol. 137, no. 5, pp. 233-245.
- [1.3] M. Sibley (1996), "Introduction to electromagnetism", Essential electronics, Arnold, p. 166.

CHAPTER TWO**BACKGROUND****2.1. Concept of ferromagnetism, ferromagnetic materials and domain formation in silicon iron.**

All material may fall into one of the categories of magnetism as illustrated in table 2. 1. depending on their bulk magnetic susceptibility. Diamagnetism, paramagnetism, ferromagnetism and ferrimagnetism are the most common groups of magnetism, and among these, ferromagnetic materials are used in electromagnetic machinery because they have large relative permeability. Ferrimagnetic materials exhibit a substantial spontaneous magnetisation at room temperature just like ferromagnetic material but have a lower saturation value [2.1].

The existence of magnetism which led to magnetization in magnetic material is attributed to orbital and spin motion of electrons around the nucleus and along their own axes respectively. Each of these motions constitutes an electric current and therefore, has a magnetic moment associated with it.

Ferromagnetic materials exhibit a large magnetisation which in turn produces large internal and external magnetic fields. In ferromagnetic materials, each atom has a relatively large magnetic dipole moment, caused primarily by uncompensated electron spin moments. Inter-atomic forces cause these moments to line up in a parallel fashion over regions containing a large number of atoms. Ferromagnetic materials such as cobalt, nickel or iron are composed of many small domains, their linear dimensions ranging from a few nanometers to about one millimetre. These domains, each containing about 10^{15} or 10^{16} atoms are fully magnetised in

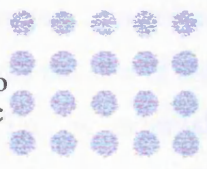

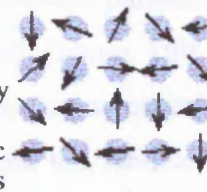
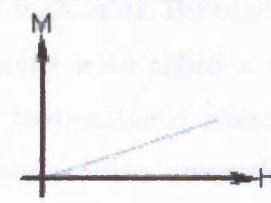
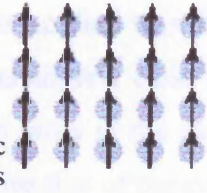
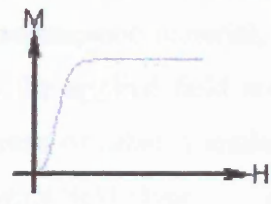
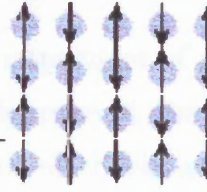
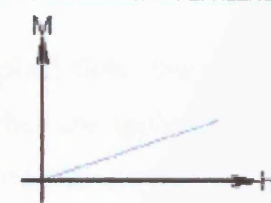
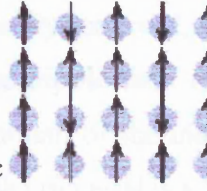
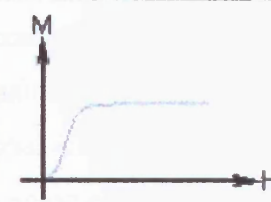
Type of Magnetism	Susceptibility	Atomic / Magnetic Behaviour	Example Susceptibility
Diamagnetism	Small & negative.	Atoms have no magnetic moment  	Au -2.74×10^{-6} Cu 0.77×10^{-6}
Paramagnetism	Small & positive.	Atoms have randomly oriented magnetic moments  	β -Sn 0.19×10^{-6} Pt 21.04×10^{-6} Mn 66.10×10^{-6}
Ferromagnetism	Large & positive, function of applied field, microstructure dependent.	Atoms have parallel aligned magnetic moments  	Fe $\sim 100,000$
Antiferromagnetism	Small & positive.	Atoms have mixed parallel and anti-parallel aligned magnetic moments  	Cr 3.6×10^{-6}
Ferrimagnetism	Large & positive, function of applied field, microstructure dependent	Atoms have anti-parallel aligned magnetic moments  	Ba ferrite ~ 3

Table 2.1: Summary of different types of magnetic dipole behaviour [2.1].

the sense that they contain aligned magnetic dipoles resulting from spinning electrons even in the absence of applied magnetic field.

Weiss, in 1907, postulated the existence of a powerful internal molecular field, which aligns the individual electron spins of atoms parallel to each other in small domains. This alignment within the domain is spontaneous i.e., no external field is required [2.2]. Quantum theory states that, strong coupling forces exist between the magnetic dipole moments of the atoms in a domain, holding the dipole moments parallel to each other. Between adjacent domains there is a transition region typically about 100 atoms wide called a domain wall. The magnetic moments of the adjacent domains in a ferromagnetic material have different directions. In the unmagnetised state the random nature of the orientations in the various domains results in no net magnetization because the overall effect is one of cancellation. When an external magnetic field is applied to a ferromagnetic material, the walls of those domains having magnetic moments aligned close to the applied field move in such a way that the volumes of those domains grow at the expense of other domains, and the internal magnetic field increases greatly above that of the external field alone.

At the initial stages, i.e., at small magnitudes of applied field, the domain movements are reversible when the external field is removed. But when the applied field becomes stronger domain-wall movements are no more reversible, and domain rotation toward the direction of the applied field occurs.

When the external field is subsequently removed, a completely random domain alignment is not usually attained, and a residual dipole field remains in the microscopic structure. The phenomenon that the magnetic moment of the material is different after the field has been removed, or the magnetic state of the material is a function of its magnetic history, is known as magnetic hysteresis.

2.2 Energy minimisation in a single crystal of silicon iron

Domains exist within crystals primarily due to the fact that their formation reduces the magnetic energy of the system. When an external field is applied, the internal energy increases, causing the domains with their magnetisation in the same orientation as the field to grow at the expense of others (figure 2.2). In the simplest case for a single crystal, the energy, E , is the combination of several free energy terms as follows: magnetostatic energy (E_m), magnetoelastic energy (E_λ), energy of the domains when an external field is applied (E_h), exchange energy (E_{ex}) and magnetocrystalline anisotropy energy (E_k). Thus, the energy, (E), is given by:

$$E = E_m + E_\lambda + E_h + E_{ex} + E_k \quad (Jm^{-3}) \dots\dots\dots(2.1)$$

Magnetocrystalline energy, E_k is defined as the energy required to magnetise a crystal along a certain direction; and it is minimum if the magnetisation is along a so-called easy axis.

The width of a domain wall is controlled by the balance between E_k and E_{ex} within the wall and we can write:

$$E_w = E_{ex} + E_k \quad (Jm^{-3}) \dots\dots\dots(2.2)$$

where E_w is wall energy.

The magnetisation versus the applied field curves shown in Figure 2.1 depends on the crystal orientation relative to the magnetic field. This curve shows the amount of external field required to magnetise a single crystal to saturation along the three principal axes.

For a silicon-iron crystal, the direction of easy and hard magnetisation are $[100]$ and $[111]$ respectively. The magnetization process for $[110]$ and $[111]$ directions involve domain rotation and require a large magnetic field to attain the saturation magnetization. The energy is minimum if the various domain magnetizations all lie along the easy magnetization directions.

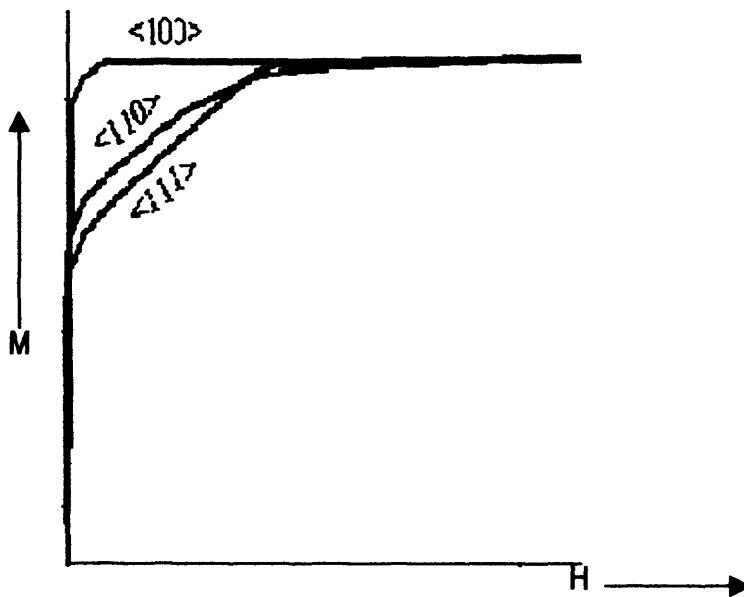


Fig. (2.1): Typical magnetisation curves for a single cubic crystal of iron along a cube edge $[100]$, a cube face diagonal $[110]$ and a cube body diagonal $[111]$.

Magnetostriction is a phenomenon which, like magnetic anisotropy, originates from the interactions between atomic magnetic moments. It can be considered as the change in dimensions of a ferromagnetic material as a result of the magnetisation. Magnetisation parallel to the easy axis of a material with uniaxial anisotropy results in no magnetostriction. However, as is illustrated in figure 2.2, magnetostriction does occur when the magnetic field is applied perpendicular to the easy axis due to magnetization rotation [2.3].

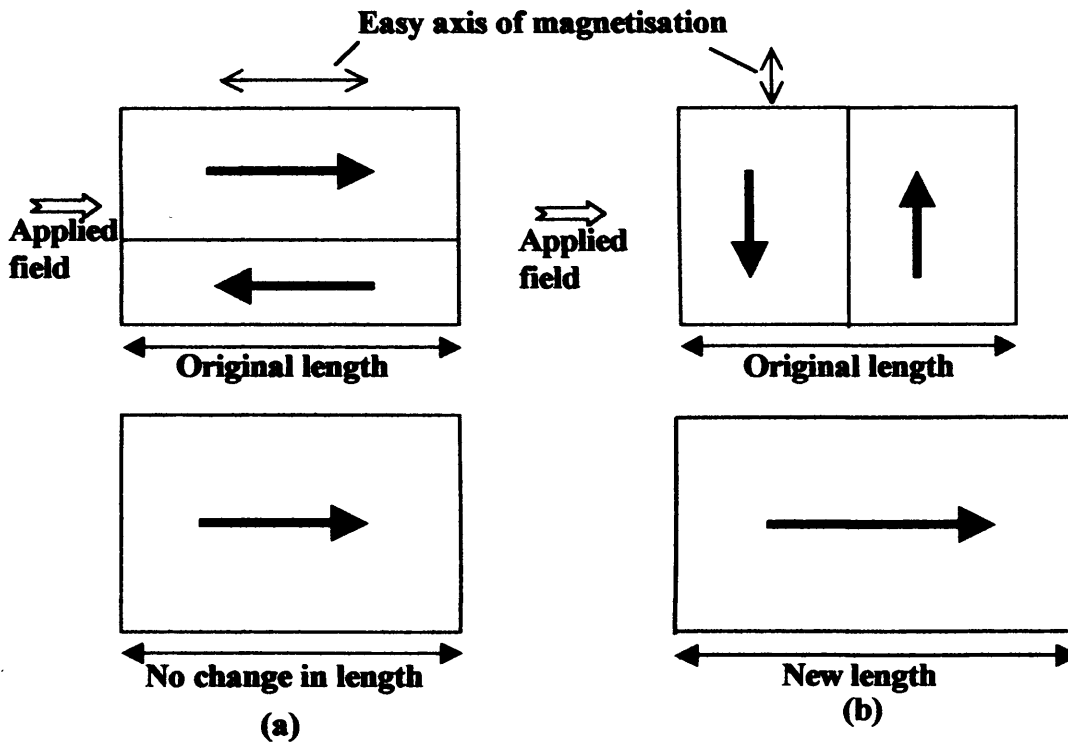


Fig. (2.2) Domain structures and magnetostriction:
 (a) Domain growth when external field applied parallel to easy axis.
 (b) Domain rotation and resulting magnetostriction when field is applied perpendicular to the easy axis.

The magnetisation of cubic anisotropic materials changes from one easy axis to another by domain wall motion on application of external field. The rotation of the atomic magnetic moments into a new alignment causes the length of the bonds between them to change. Consequently, the dimensions of the material change. A state of strain may be created in a ferromagnetic crystal if not allowed to expand freely. This constitutes a further free energy of the crystal called magnetoelastic energy (E_λ).

Exchange energy, E_{ex} , is due to the exchange interactions between magnetic moments and is the result of strong forces which exist in neighbouring atoms causing parallel spin alignment. Figure 2.3 illustrates that dipole moments of the atoms within the wall are in a higher energy state because they are not lying along the easy direction of magnetisation. Secondly, it can clearly be observed that the atomic dipoles within the wall are not anti parallel to each

Figure 2.4a illustrates a uniformly magnetized specimen with a large magnetostatic energy associated with it as a result of the presence of magnetic flux poles at the surface of the

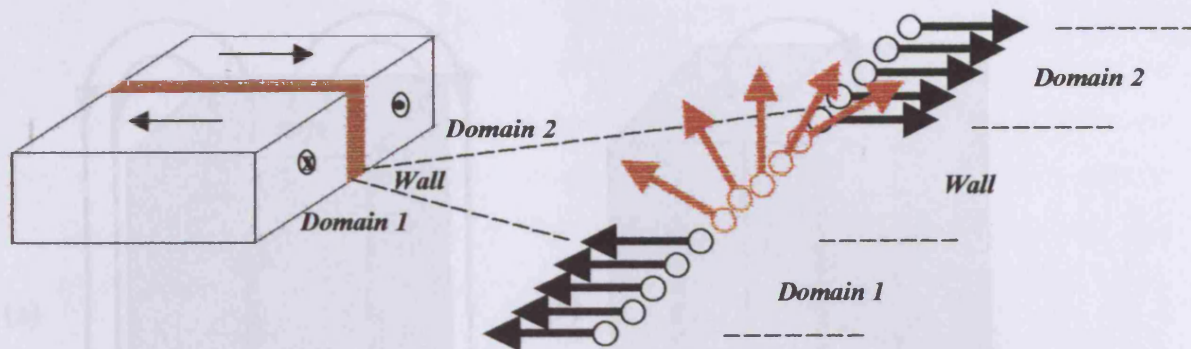


Fig. (2.3): Illustration of 180° Bloch wall showing rotation of spins.

other and so the exchange energy is also raised within the wall. It could therefore be concluded that the domain wall energy is an intrinsic property of a material depending on the degree of magnetocrystalline anisotropy and the strength of the exchange interaction between neighbouring atoms, the parameters which largely determine the thickness of the wall. During the change in magnetisation, magnetic anisotropy energy is induced and this energy contribution will increase with increasing wall thickness.

Magnetostatic energy (E_m), is associated with the existence of the demagnetising field on the surface of the material by free magnetic dipoles, and can be considered as the energy required to assemble all constituent dipoles. Magnetostatic energy has the effect of eliminating the emergence of flux from the surface of the material by encouraging the formation of domain structures which would produce an internal field opposite in direction to the magnetization field. This is achieved when the direction of domain magnetization adjacent to the surfaces lies in a plane parallel to the surface. This is called a closure domain. Formation of such domains provides a closed path for magnetization in the underlying domains. Thus the emergence of the magnetic field from the surface is thus avoided.

(2.4): (a) Single domain (b) Domains and domain walls
(c) Four domains (d) Closure domains

Figure 2.4a illustrates a uniformly magnetized specimen with a large magneto-static energy associated with it as a result of the presence of magnetic free poles at the surface of the

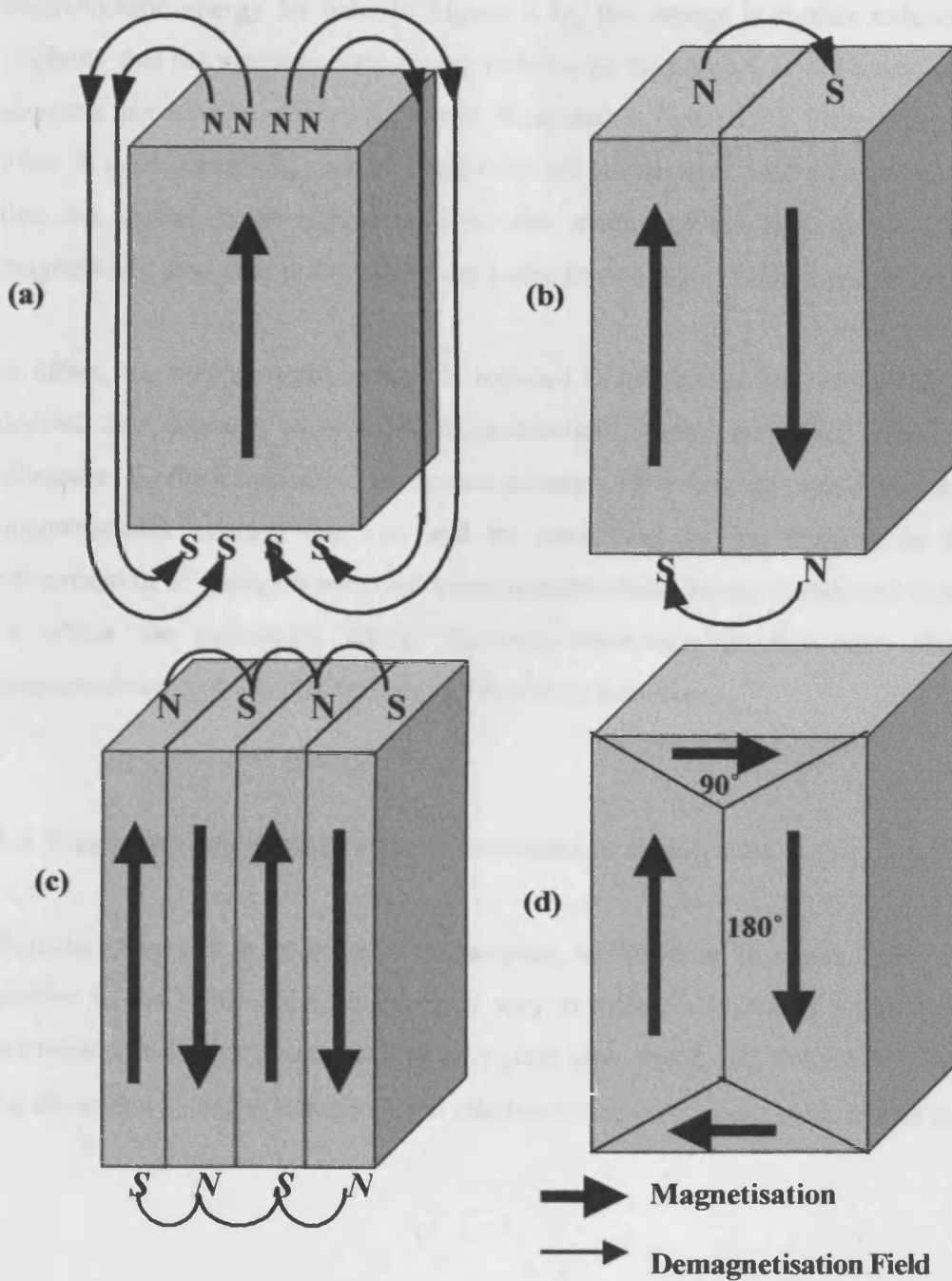


Fig. 2.4: Energy minimisation and domain patterns (after [2.4]): (a) Single domain (b) Domain split into two. (c) four domains (d) Closure domains.

specimen generating a demagnetising field which is opposed to the magnetization in the specimen. Figure 2.4b illustrates the split of the domain into two, thereby reducing the magnetostatic energy by half. In Figure 2.4c, the energy is further reduced to a quarter implying that the magnetostatic energy reduces as the number of the break up or split of the domains increases. A closure domain is illustrated in figure 2.4d. This structure occurs more often in cubic materials, such as grain-oriented silicon iron, where cubic anisotropy ensures that the directions at right angles to the magnetization in a given domain are also magnetically easy axes providing return paths for the magnetic flux within the solid [2.4].

In effect, the magnetostatic energy is reduced in relation to how many times the crystal is divided into domains of opposite magnetization. Again, the effect of this can totally be eliminated by the introduction of closure domains. Of course, closure domains also introduce magnetoelastic energy, that can still be minimized by the increase in their numbers. Minimisation of energy is achieved when magnetostatic energy is reduced to zero, as a result of which the anisotropy energy becomes minimum. In this case, the sum of the magnetoelastic and domain wall energy becomes minimum.

2.3 Supplementary domain structures related to silicon iron

Domain structures in polycrystalline samples, unlike those in single crystals with surfaces parallel to the (110) sheet planes, may vary at different locations depending on the grain orientation and other parameters such as grain size, stress, etc. Silicon iron lattice with both the tilt angle (β) and yaw angle (α) in relation to the sheet plane is illustrated in figure (2.5).

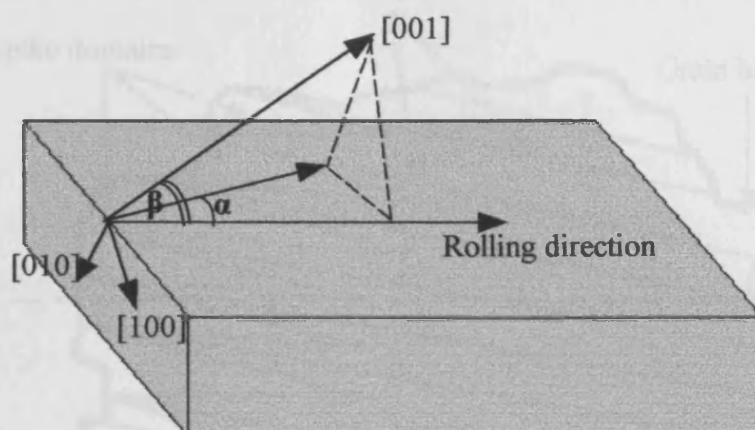


Fig. (2.5). Schematic representation of a silicon iron lattice showing tilt angle β and the yaw angle α relative to the sheet plane.

By the use of the colloid technique and a computerised field scanning technique [2.5], the Bitter technique etc. [2.6], different domain patterns have been observed. These variations were related to the angle of deviation of the [001] direction of the grain from the rolling plane of the sheet (the tilt angle).

More domain magnetisation is directed out of the surface plane with the increase in the tilt angle (β), However, in this case, more free magnetic poles are induced on the sheet surface and this consequently increases the magnetostatic energy.

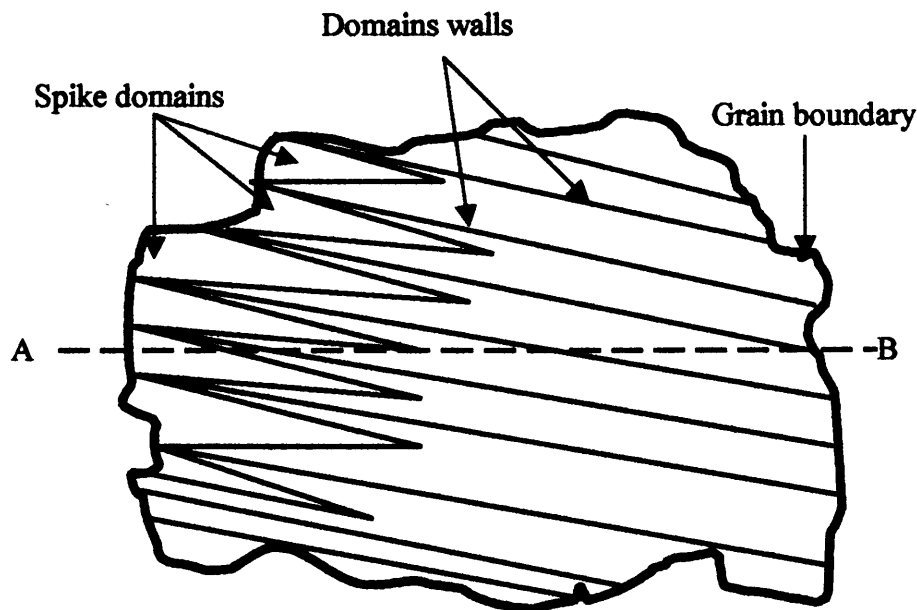


Fig. (2.6) Illustration of static spike domain structure (after [2.7])

Spike domains of reverse magnetisation are formed spontaneously at such places, and also other places where domains of opposite magnetisation directions would meet, in order to reduce the high stray fields that otherwise would arise. The spike domains become large and point to the [001] direction when (β) is between 1° and 2° , but when it increases from 2° to 6° the spike domains become reduced in size and increased in number. The volume of the transverse domains also increases below the surface of the material forming lozenges domains. Lace pattern domains are formed when (β) is higher than 7° and the transverse domain volume increases even more. [2.5]

Spike domains and the other domain structures can apparently fulfil two missions:

- a) reduce surface stray fields resulting from a misorientation [2.6]
- b) reduce the stray field energy at the grain boundaries [2.7].

2.4 Magnetic materials and the hysteresis loop.

A great deal of information on the magnetic properties of a material is obtainable by the study of its hysteresis loop. It also provides the means by which the various essential parameters can be determined [2.8]. The relationship between the induced magnetic induction (B) and the magnetic field (H) is illustrated by the B-H loop.

The SI system of units is employed, in which the magnetic field, H, is measured in amperes per meter (Am^{-1}), and the magnetic induction, B, measured in Teslas (T). A hysteresis loop can be represented in terms of B-H or M-H, where M represents magnetisation. The relation between magnetisation, (M) and induction, (B) is:

$$B = \mu_0 (H + M) \quad (\text{T}) \quad (2.3)$$

μ_0 , ($4\pi \times 10^{-7} \text{ Hm}^{-1}$), is the permeability of free space.

By measuring the magnetic induction, B of a ferromagnetic material while changing the magnetic field, H, the loop is generated. Ferromagnetic as well as ferrimagnetic materials have non-linear initial magnetization, illustrated by the curve from the initial point (0) through (1) to (2) in figure. 2.7. The curves in figure 2.7 are for a material that has never been previously magnetized or has been thoroughly demagnetised. At point (3) the material is said to have reached its point of magnetic saturation. At this point, the material is effectively a single domain as illustrated in figure 2.8, and further increase in magnetic field, H, will produce very little increase in magnetic induction, B. From the saturation point (3), the curve moves to point (4) when the magnetic field, H, is reduced to zero. It can be seen that, though the magnetic field is zero, some magnetic induction still remains in the material. This point (4) is normally referred to as the remanence (B_r). The reason for this condition is that, some of the magnetic domains remain aligned but some have lost their alignment. As the magnetic field is reversed, the magnetic induction is finally reduced to zero at the point (5), which is referred to as the coercivity. At this point, the net magnetic induction within the

material is zero. The field required to remove the residual magnetism in the material from the remanence to zero is termed the coercive field.

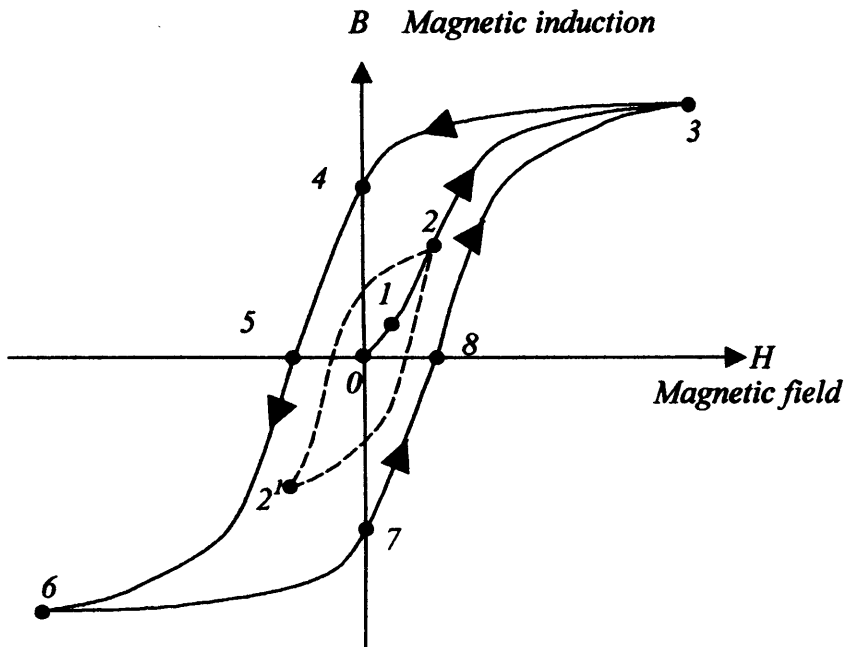


Fig. 2.7 Magnetic characteristics of silicon iron.

By increasing the magnetic field in the negative direction, the material again reaches its point of magnetic saturation at point (6). Then reducing H to zero brings the curve to point (7). Another point of remanence equal to the previous one but in the opposite direction is achieved here. Further increase in the magnetic field, H , returns the magnetic induction to zero. However, the curve does not return to the origin but to point (8). The reason is that, some magnetic field, H , is required to remove the residual magnetism. The curve follows a different path through (8) back to the saturation point where it will have completed the loop. As the applied magnetic field varies periodically between $\pm H_{\text{max}}$, the hysteresis loop is traced once per cycle.

The absolute permeability, μ , which is the ratio of the magnetic induction to the magnetic field, is given by:

$$\mu = \frac{B}{H} \dots(Hm^{-1})\dots\dots\dots(2.4)$$

This is the property of the magnetic material that indicates how easily magnetic flux is established within it.

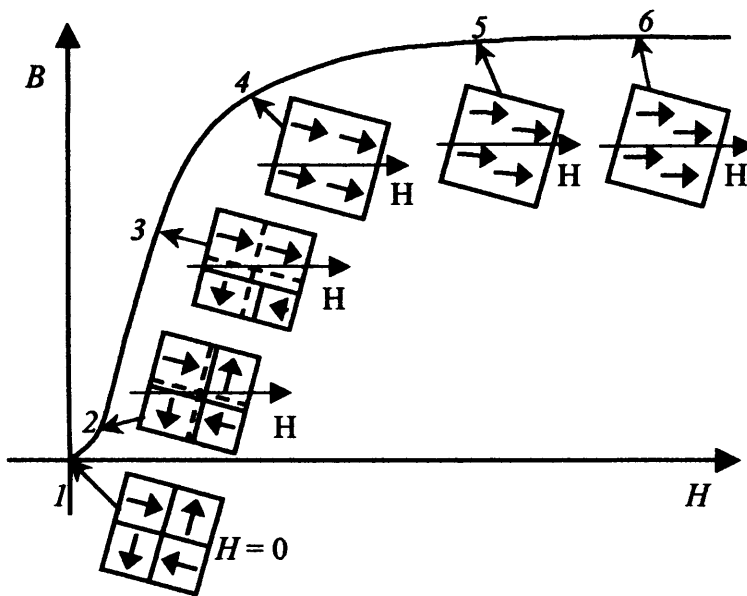


Fig. 2.8. Magnetisation of a material and the subsequent changes in the domain structure: 1 - demagnetised state with no external field, 2 - domain wall movement, 3 - rapid change of domain direction, 4 - single domain state, 5 - rotation of the domain, 6 - saturation; (adapted from[2.9])

The maximum permeability is the point where the slope of the B-H curve for the material is highest, and this point is often taken as where a straight line from the origin is tangent to the B-H curve (figure 2.9). Usually, the maximum permeability or the maximum relative permeability is quoted for a given material. The relative permeability, μ_r is given by:

$$\mu_r = \frac{\mu}{\mu_0} \text{ (Dimensionless)}\dots\dots\dots(2.5)$$

Then in a magnetic medium, the magnetic field is given by

$$H = \frac{B}{\mu_0 \mu_r} \text{ Am}^{-1} \dots\dots\dots(2.6)$$

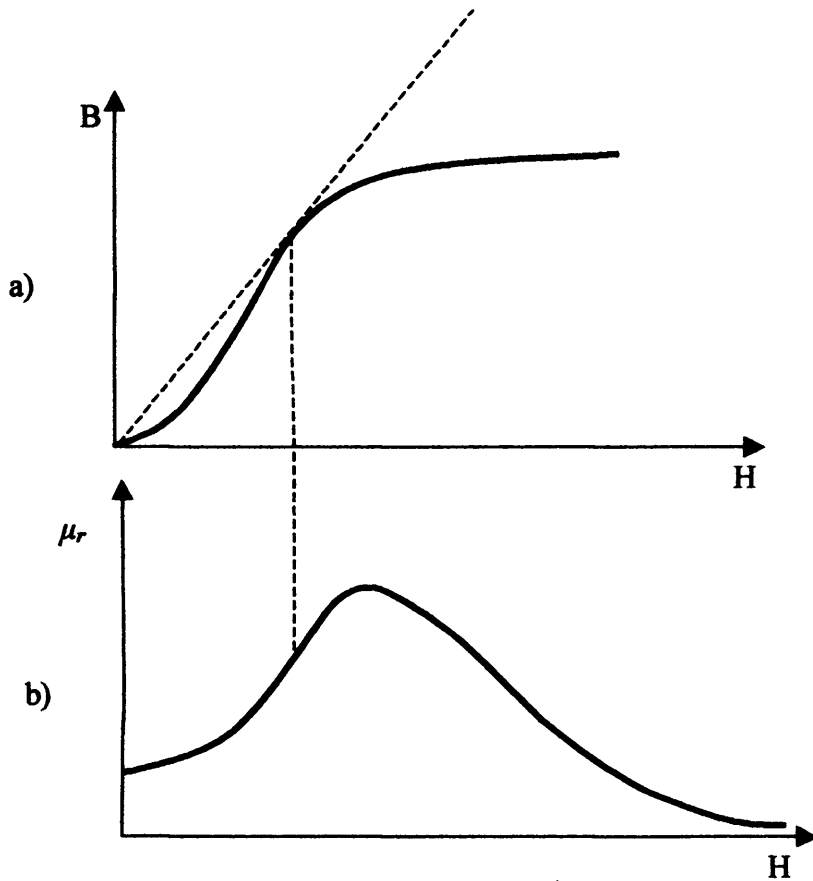


Fig. 2.9. Typical characteristics of a ferromagnet material showing part of maximum permeability: a) B(H) curve. b) corresponding curve of relative permeability μ_r (adapted from [2.10])

Much information about the performance of a magnetic material can be inferred from the shape of its B-H loop. For example, a material with a wide hysteresis loop has low permeability, high remanence (high residual magnetism) and high coercivity.

In a soft material, the fields involved in the hysteresis loop are much smaller than the corresponding magnetization values, so that to a very good approximation, $B \approx \mu_0 M$, and plotting B-H or M-H makes a very little difference and can be safely neglected. On the other hand, in hard materials, H and M are orders of different magnitude and the B-H loop is significantly different from the M-H loop.

Ferromagnetic materials for use in electric generators, motors, and transformers should have a large magnetisation for a very small applied magnetic field; they should have tall, narrow hysteresis loops. Permeability depends on carbon content which in turn effects the coercivity and remanence.

Ferromagnetic materials are not normally isotropic in single crystals, and one of their characteristics as anisotropic magnetic materials is magnetostriction. The magnetic moments of a magnetic material are tied to the mechanical structure. Therefore when the magnetisation is changed by a magnetic field the mechanical structure is strained.

This is magnetostrictive strain or magnetostriction, λ , is given by:

$$\lambda = dl/L \quad (\text{Dimensionless}) \dots\dots\dots (2.7)$$

where, dl is the change in length (m) and
 L is the original length (m).

A ferromagnetic material loses its ferromagnetic properties and becomes paramagnetic at a temperature referred to as Curie point. In silicon iron the curie point, at which the thermal agitation is sufficient to destroy the spontaneous magnetisation, is about 770°C (1043K)

Ferromagnetic materials which have tall narrow hysteresis loop with small loop areas, are referred to as “soft “ materials. They are usually well-annealed materials with few impurities so that the domain walls can move easily [2.11]

Under a.c. magnetisation, all ferromagnetic materials exhibit energy loss which can be separated into hysteresis, eddy current and anomalous components. Loss per cycle is proportional to area enclosed by the B-H loop, and is discussed in more detail in chapter 3.

2.5 Silicon iron

Silicon-iron alloys are of prime importance to the electrical engineering industry. This industry consumes hundreds of thousands of tons of the alloy annually. Alloys with silicon content 0.5% to 6% feature prominently in the manufacture of power transformers and rotating electrical machines [2.12]

Silicon-iron alloys, also known as electrical steels, which can be defined generically as “magnetically soft, thin steel sheets” and whose function is to carry magnetic flux efficiently in electromagnetic equipment, has been estimated to present approximately 97% of the whole market of soft magnetic materials and approximately 84% of their sales value [2.13].

The most important magnetic parameters in rotating machines and transformer cores are high permeability, low apparent power and low core loss. As electrical machines have developed and efficiency has become a more major factor the magnetic properties have become more important.

Earliest designs of transformers and generators employed cast or wrought iron as magnetic cores. Plain carbon steels were also used. However, significant developments were realised

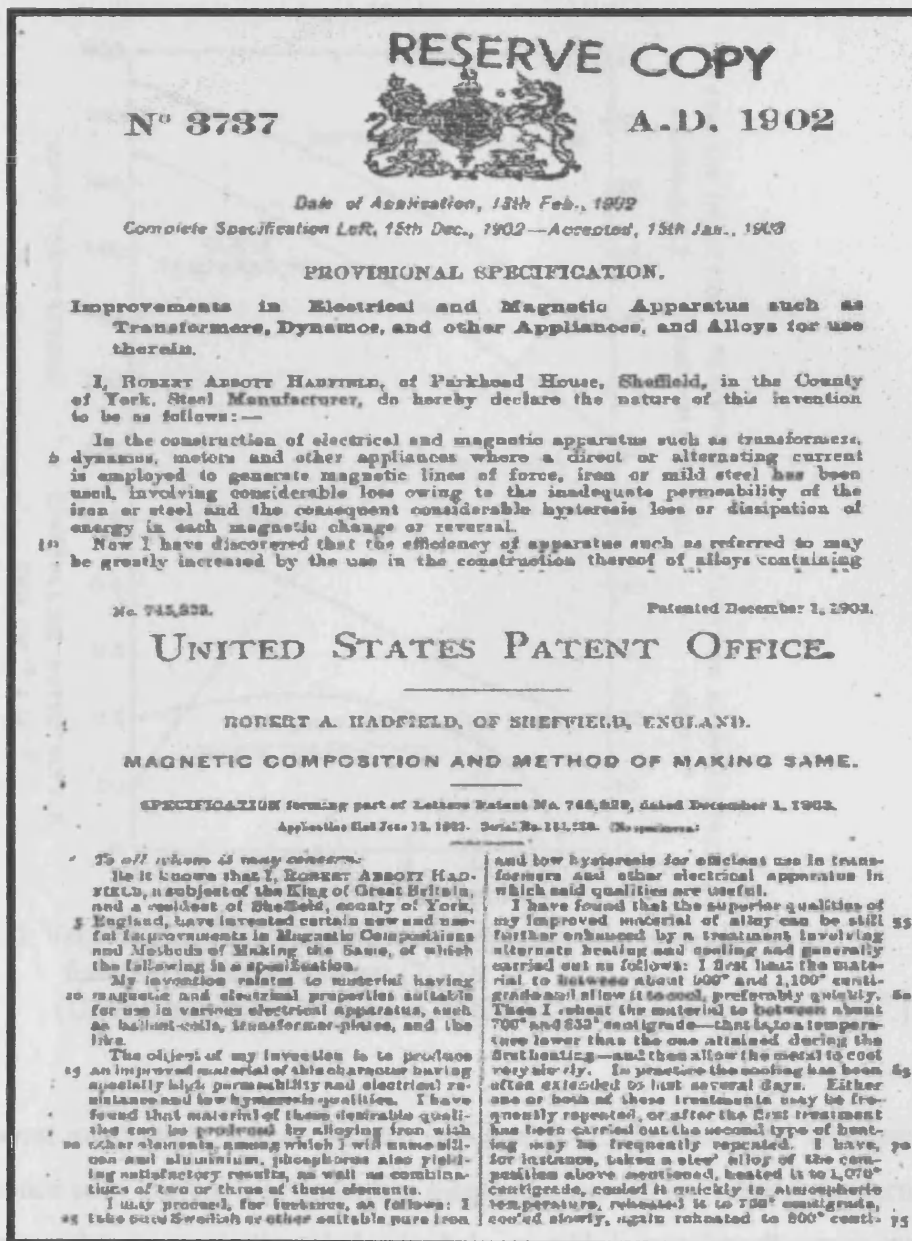


Fig. 2.10: Copy of first page of Hadfield's patent on Silicon steel.

only as the scientific and technical pursuit in this area began to yield fruit at the turn of the 20th century when Hadfield et al discovered that the magnetic properties of low carbon steel could be improved by the introduction of silicon. Figure 2.10 shows the front page of Hadfield's original patent [2.14]

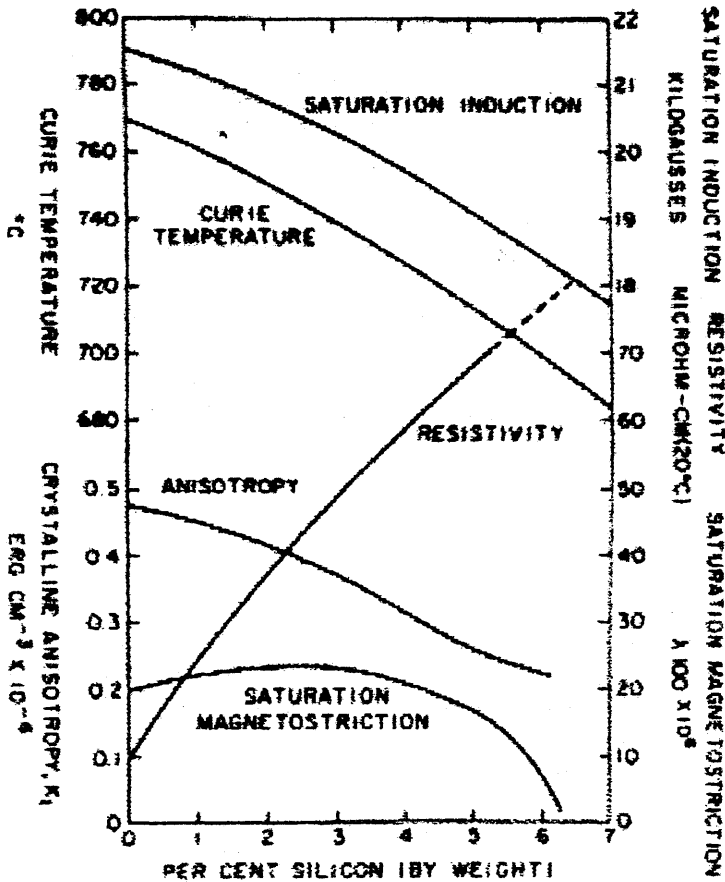


Fig. 2.11: Various magnetic and electrical properties of silicon-iron as a function of silicon content [2.15].
 (Units conversion: 1 Gauss = 79.58Am⁻¹ and 1 Ergcm⁻³ = 0.1 Jm⁻³.)

Most importantly, as can be seen in figure 2.11, the resistivity increases with silicon content hence eddy current loss under a.c. magnetisation will be reduced. Unfortunately the saturation magnetisation (induction) drops with increasing silicon content which will lead to a fall in permeability.

This was a significant break through since addition of silicon reduces the magnetocrystalline anisotropy and the magnetostriction. It also modifies phase changes in the steel such that the low silicon alloys have body-centre-cube (B.C.C) structure [2.15] at all temperatures up to

the melting point, a property which enables the development of the steel texture by the use of high temperature heat treatments which are impossible for pure iron.

By adding 3% silicon to iron the resistivity is increased four times. Furthermore, addition of silicon to iron leads to increases in the average grain size [2.16]. This in general is harmful because, as it is illustrated in figure 2.12, though the eddy current loss decreases with decreasing grain size, conversely hysteresis loss increases sharply.

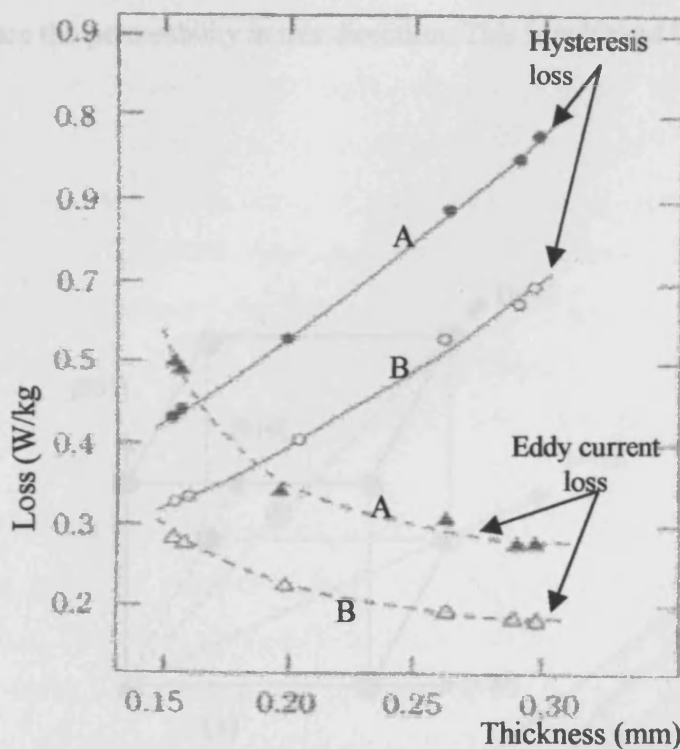


Fig. 2.12 :Influence of grain size on eddy current loss and hysteresis loss (After [2.17])

However, in spite of the benefits that silicon has on magnetic properties of electrical steels, it also has disadvantages. The higher the percentage of silicon in the silicon iron alloy, the more brittle the alloy becomes. The brittleness normally restricts the percentage of silicon to less than 3.5% but special processing enables this to be increased to 6.5% which is desirable because the magnetostriction is close to zero.

2.6 The grain oriented silicon iron

In 1918, Beck [2.18] discovered that silicon iron has a B.C.C lattice structure with the easy direction of magnetization lying along the cube edge direction of the crystal (Fig. 2.13).

Goss in 1935 produced the first polycrystalline silicon iron sheet which had a high degree of anisotropic properties comparable with a single crystal [2.19]. For transformer applications the flux lies predominantly along the length of the laminations and therefore it is desirable to enhance the permeability in this direction. This is achieved by various hot and cold rolling

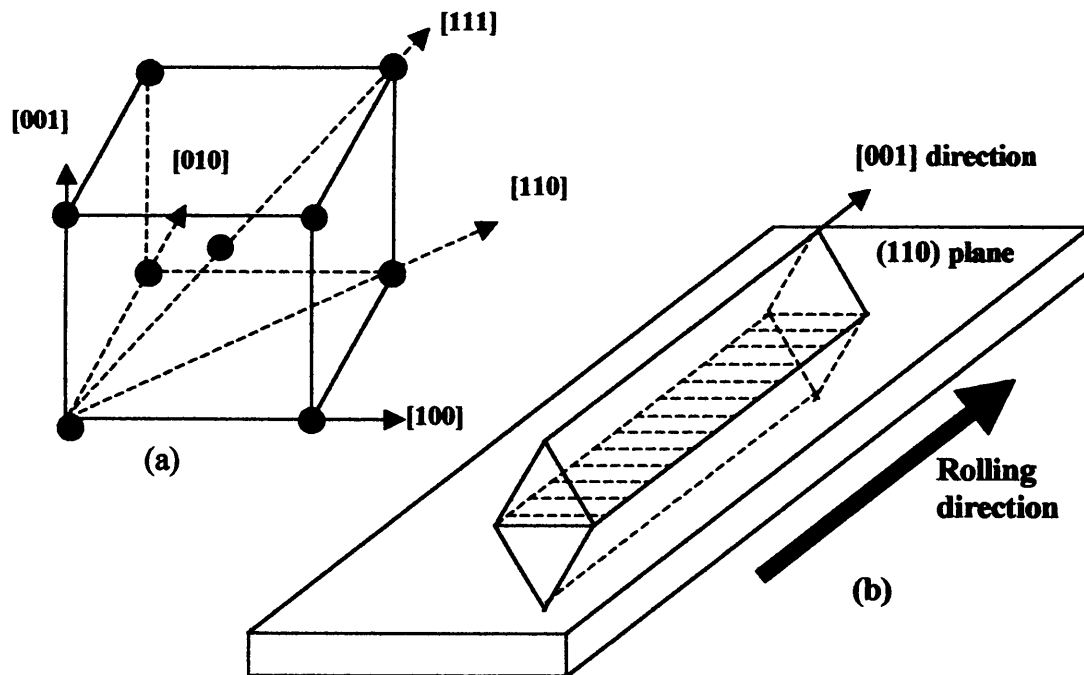


Fig.2.13: Schematic diagram illustrating: (a). Silicon Iron Body Centred Cube (BCC), and (b). GOSS Texture.

stages to produce textured sheets, known as the grain oriented silicon steel with the [001] direction of each grain close to the rolling direction of the lamination. The first polycrystalline silicon iron sheet was produced by Goss in 1935. The crystals in the grain oriented silicon iron tend to arrange themselves with the [001] direction parallel to the rolling direction and the (110) plane parallel to the surface of the sheet. This is the easy direction of magnetisation and hence the permeability is greater when the material is magnetised along this direction.

The foundations of the creation of the Goss structure are laid at the steel making stage. And this steel produced has a typical composition that could be 3.25% silicon, 0.06% manganese, 0.025% sulphur and 0.035% carbon. The essence of the silicon component is primarily to raise the resistivity level of the material [2.20]. A good control of the chemical composition as well as the minimisation of impurities such as nitrogen, oxygen and a number of undesired elements have been attained due to the improvements in steel making. The carbon component influences the sharpness of crystallographic orientation, however, due to its detrimental effect on the final product (brittleness), the decarburisation process is carried out in a wet hydrogen/nitrogen atmosphere to reduce the carbon level to less than 0.003% [2.21].

Electrical equipments such as transformers or motors have two types of electrical power losses, iron loss, originating from the core material used, and copper loss in the machine windings. To reduce the core loss, Armco in the U.S.A, in 1939, modified and improved the Goss method to produce and commercialise a 0.32mm thick grain oriented material which had a loss of around 1.5W/kg at 1.5T, 50Hz. From then the strong ambition to attain a significant improvement in the manufacturing technique continued until the 1960's when the loss was brought down to 0.9W/kg. Since then, further attempts have achieved incremental improvements partly due to the reduction in the thickness of the grain-oriented material.

The increase in silicon content and purer steel to achieve lower loss and higher permeability has been thought to have practically reached its limit. As a result, efforts were concentrated

on the production of higher oriented and thinner material [2.22]. In the United States, 9-mil (1mil = 2.54×10^{-4} mm.) sheets were manufactured for some time with the view to producing higher grade sheets. However, because of high cost and failure to obtain the desired low core loss, the industrial production of 9-mil sheets came to an end [2.23]. However, some later work [2.24] has shown that higher permeability material with a thickness of 0.1 mm and loss as low as 0.22 W/kg at 1.5T, 50Hz can be produced. An ultra thin material (with thickness from 80 μ m to 20 μ m) which is reported to have achieved a higher permeability (1.9T at 800 A/m) and a loss of 0.17W/kg at 1.3T, 50 Hz was shown to be feasible many years earlier [2.25].

2.7 Highly oriented grain oriented material.

Although the basic method of manufacturing grain oriented electrical steel was developed in the middle of the 1930s, the revolutionary improvement in the quality and establishment of mass production technology in the recent years was achieved in Japan [2.26]

Grain oriented silicon steel is mainly used as a core for high efficiency transformers, confronted with the requirements for low iron loss, high grade as well as low magnetostriction materials to cope with transformer noise and also the problem of increasing design flux density as a way to reduce the ever increasing size of power and distribution transformers [2.23].

As an example of the importance of core loss, in Japan, power statistics for 1995 revealed that, the total loss attributable to transformers during power transmission was approximately 17 billion kWh annually, corresponding to 1.7% of the total generated power. Iron loss was estimated at 10 billion kWh, or approximately 60% of total loss. Furthermore, the demand for electrical power in Japan, and in the developing nations will increase in the future, heightening the need for energy efficiency as part of the solution to the global environmental

problem. Thus, the use of core materials with small loss is a matter of extremely great significance, even when considered on the global scale [2.25].

The turning point in higher quality Goss texture was in 1968 when Nippon Steel commercially manufactured highly oriented silicon iron known as Hi-B. This material has a higher degree of orientation which was achieved by the addition of a new grain growth inhibitor which constrains the growth of Goss nuclei to only 1-2° of rolling direction orientation so that grains grow to wider. The better orientation of a crystalline texture result in higher permeability and lower losses; a typical value of induction B is about 1.92T at a field strength of 1000A/m, whereas B for conventional grain oriented material is 1.8T for the same applied field strength. Typical grain sizes in Hi-B and conventional grain oriented material are 10-15mm and 3-5mm in length respectively [2.23]. Large grain size causes wider domain wall spacing, which increases the eddy current loss as shown in figure 2.12. This is counteracted to some extent by the application of a tensile stress coating.

The attainment of improved magnetic properties in finished grain oriented material is dependent upon the combination of a high degree of crystal orientation and appropriate grain size. These two characteristics distinguish grain oriented electrical steels into two sub-groups: a) conventional grain-oriented and b) high permeability grain oriented steels. The difference in the production process of the high permeability material lies in the elimination of one of the cold-rolling stages due to the introduction of 0.025% aluminium that formed aluminium nitride (AlN) that supplements and strengthens the MnS inhibitor. High permeability grain oriented materials are also produced around the world using other inhibitors such as manganese selenide (MnSe), antimony (Sb) and boron (B) [2.27]

In general high permeability grain oriented material is characterised by wider grain. Though walls of wider grains may be prone to bowing and nucleation [2.28], the wider the grains the better for steel magnetic performance.

2.8 References

- [2.1] NDT Educational Resources (2005), (www.ndt-ed.org/educationresources).
- [2.2] P Weiss (1907), cited in R. Carey and E. D (1966), "Magnetic domains and techniques for their observation", London, The English University Press Ltd.
- [2.3] A. Hubert and R. Schafer (1998), "Magnetic domains – The analysis of magnetic microstructures" 1Springer, Germany, 1st Edition, p.102.].
- [2.4] R. M Bozorth.(1951), Ferromagnetism, D. Van Nostrand Company, Inc., Princeton, New Jersey, USA.
- [2.5] H. Pfutzner (1985) "Domain investigation on coated unpolished Si-Fe sheets", IEEE Trans. Mag., MAG-21, 6, p.260.
- [2.6] W.S. Paxton and T.G. Nilan (1955), "Domain configurations and crystallographic orientation in grain-oriented silicon steel", J. Appl. Phys., 26, p994.
- [2.7] A. J. Moghaddam and A. J. Moses (1993), "Localised power loss measurement using remote sensors", IEEE Trans. Mag., 29, 6, p.2998.
- [2.8] R. Harris et al (2005), "Magnetic materials", Applied Alloy Chemistry group, Birmingham University,(www.aacg.bham.ac.uk/magnetic_material).
- [2.9] F. Braisford (1954), "Magnetic materials", Methuen & Co. Ltd., London, UK.
- [2.10] Soinski M (2001), "Magnetic materials in engineering (Materiały magnetyczne w technice - in Polish)", Biblioteka COSiW SEP, Warsaw, Poland.

- [2.11] D. K. Cheng (1994), "Fundamentals of Engineering Electromagnetics," Addison-Wesley, 1st Edition, p197.
- [2.12] Tony Moses (2002), "Opportunities for exploitation of magnetic materials in an energy conscious world", Interdisciplinary science reviews, vol. 27, no. 2, p. 100
- [2.13] J. Schneider, A. Schoppa and K. Peters (1998), "Magnetic application choice among different non-oriented electrical steels", J. Phys. 1V, vol. 8.
- [2.14] R. A. Hadfield (1902), "Magnetic composition and the method for making same", United States patent office, No. 3737.
- [2.15] D. Jiles (1998),"Introduction to magnetism and magnetic materials", Chapman & Hall, 2nd Edition, p. 333.
- [2.16] D. Jiles (1991),"Introduction to magnetism and magnetic materials", Chapman & Hall, 1st Edition, p. 275.
- [2.17] N. Morito, M. Komatsubara and Y. Shimizu (1998) "History and recent development of grain oriented electrical steel at Kawasaki steel", Kawasaki technical report, No. 39, p. 1.
- [2.18] K. Beck (1918), cited in Khanlou (1994), "A non-enwrapping on-line power loss testing system for the steel industry", Thesis (Ph.D), . University of Wales, Cardiff.
- [2.19] N.P Goss (1935), New development in electrical strip steels characterized by fine grain structure approaching properties of a single crystal", Trans. Am. Soc. Metal, 23, p515 cited in R.M. Bozorth. (1978), "Ferromagnetism", IEEE press, Lucent

Technologies, Inc. New York.

- [2.20] P. Beckley (2000), "Electrical Steels - A Handbook for Producers and Users", EES, Newport, p. 106.
- [2.21] A. J. Moses (1990), "Electrical steels: past, present and future developments", IEEE Proceedings, vol. 137.Pt.A, No. 5.
- [2.22] S. Taguchi, T. Yamamoto and A. Sakakura (1974), "New grain oriented silicon steel with high permeability – Orientcore HI-B," IEEE Trans. Mag., MAG-10, p.123.
- [2.23] S. Taguchi, T. Wada, T. Yamamoto, F. Matsumoto, A. Sakakura and K. Ueno (1973), "New grain oriented silicon steel - Orientcore HI-B", Nippon Steel Technical report overseas, No. 4.
- [2.24] K.I Arai, H. Satoh, S. Agatsum, and K. Ishiyama (1990), "Tertiary recrystallization and iron loss of ultra thin silicon steels", IEEE Trans. Mag., Mag-26, p. 1969.
- [2.25] W.S. Paxton and T.G. Nilan (1955), "Domain configurations and crystallographic orientation in grain-oriented silicon steel", J. Appl. Phys., 26, p. 994.
- [2.26] N. Morito, M. Komatsubara and Y. Shimizu (1998), History and recent development of grain oriented electrical steel at Kawasaki steel", Kawasaki steel technical report, No. 39.
- [2.27] A. J. Moses (1990), "Electrical steels: past, present and future developments", IEE proceedings, vol. 137, no. 5, p. 233.
- [2.28] P. Beckley (2000), "Electrical Steels - A Handbook for Producers and Users", EES, Newport, p. 135.

CHAPTER THREE

POWER LOSS IN ELECTRICAL STEELS

3.1 Components of power loss

One of the most important parameters in a magnetic material for a.c. application is its electrical power loss, which is dissipated in the form of heat. Power loss depends on frequency (f), maximum flux density (B_m), the thickness (w) and the resistivity (ρ) of the material. It has been split into the hysteresis and the eddy current loss components. The eddy current component is further split into the classical loss and the anomalous loss (i.e., excess current loss). Hence the total power loss (P_T) can be expressed as:

$$P_T = P_H + P_E + P_A \quad (W \text{ kg}^{-1}) \dots\dots\dots (3.1)$$

Where P_H is the hysteresis loss,

P_E is the eddy current dissipation and

P_A the anomalous (or excess) loss

(All measured in $W \text{ kg}^{-1}$).

The hysteresis loss per cycle is defined as the area within a d.c. (static) B-H loop which represents the energy expended when the material is magnetised in a slowly changing cyclic field, as illustrated in figure 3.1, and is assumed to be a measure of wall pinning effects. It is therefore customarily estimated by slowly traversing a B-H loop where the eddy current losses are assumed to be negligible.

It has been said, though, that the hysteresis loss arises mostly from the micro eddy currents which occur when domain walls 'flick' free of inclusions or are suddenly nucleated [3.1]. It is, in fact, the result of energy dissipated in moving the domain walls through the material.

This loss is closely related to stress, impurities, dislocations, surface roughness, etc., factors which negatively affect the magnitude of the permeability of the material.

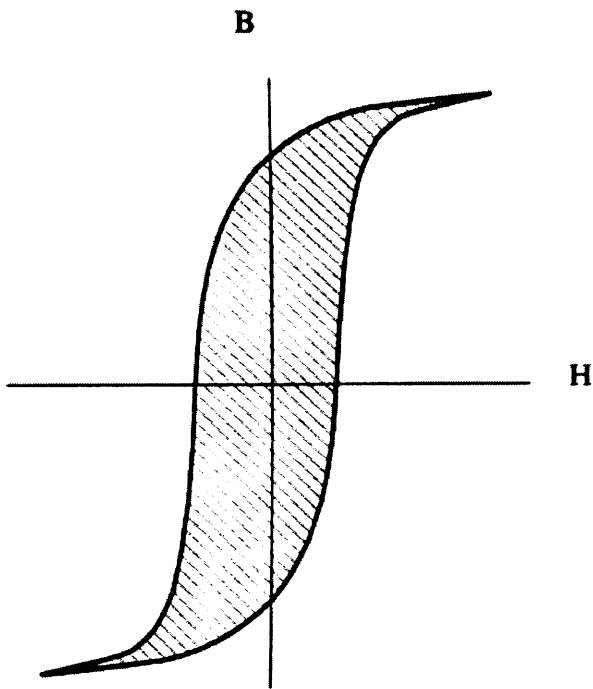


Fig. 3.1: Area of loop indicative of energy loss

The hysteresis loss (P_H), is known to depend on maximum flux density (B_m) and frequency (f) in the relation as follows:[3.2]

$$P_H = kf(B_m)^x (W kg^{-1}) \dots \dots \dots (3.2)$$

Where, k is a constant for a given material and a given flux density, and x is the Steinmetz index which lies in the range 1.6-2.0 for electrical steel.

Electrical steel laminations used as transformer cores work under alternating conditions. The ideal operating condition is when the total magnetic flux in the lamination is sinusoidal. However, eddy currents are induced in the material by the changing magnetic field, causing eddy current energy loss. Eddy currents in steel causes a phase lag between applied field and magnetisation. The energy is dissipated as heat due to ohmic resistance of the laminations. The eddy currents increase with the thickness, the magnetising frequency and the conductivity of the steel sample. They generate their own magnetic field in opposition to the magnetising field. This, according to Lenz’s law, have a demagnetising effect tending to reduce flux density from its surface value to a minimum value at the centre of the material.

The eddy current loss (P_E) for thin steel laminations or specimen can be obtained according to their geometry and the frequency of the penetrating flux, and can be written as follows:

$$P_E = \frac{(\pi \cdot B_m \cdot f \cdot w)^2}{6 \rho d} \quad (W \text{ kg}^{-1}) \dots\dots\dots (3.3)$$

- Where, B_m is the maximum flux density (T),
- w is the thickness of the specimen (m),
- ρ is the resistivity (ohm-m),
- d is the density (kg/m^3) and
- f is the excitation frequency (Hz).

The eddy current losses have been estimated using both the classical theory and domain theories assuming uniform wall motion. However, when the estimated hysteresis and eddy current losses are added, their sum is significantly less than measured losses. The difference between the measured losses and the sum of the estimated hysteresis and eddy current losses (as illustrated in figure 3.2) has been termed anomalous or excess loss (P_A). The anomalous losses have been linked to continuous rearrangements of domain configurations [3.3]. The ratio of the total eddy current loss ($P_A + P_E$) to the value of classical eddy current loss P_E is known as the anomaly factor, η .

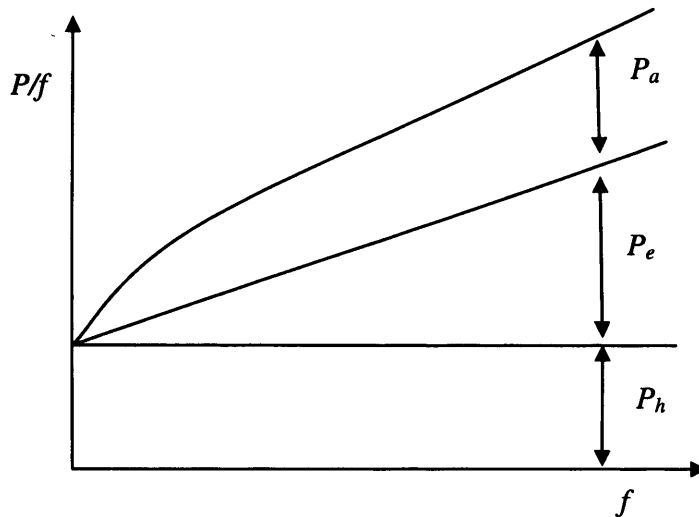


Fig. 3.2: The concept of separating the power loss into hysteresis and eddy currents components, P_h - hysteresis loss, P_e - eddy current loss, P_a - anomalous loss (excess loss)

William et al defined clearly the occurrence of the loss in the ferromagnetic material by the behaviour of domains, and were the first to calculate the power loss using a single moving wall in an infinite medium [3.4]. The occurrence of anomalous loss that accounts for about 50% of the total loss in modern grain oriented 3% silicon iron prompted further investigations in an attempt to deduce the cause of this difference [3.5]. All attempts to deal with loss have taken domain wall motion into account ever since. Bertotti [3.6] also joined in the attempt to close the gap between the measured and the calculated eddy current losses.

In an earlier contribution of Bertotti et al [3.7] assumed that: (a) all the elementary magnetisation changes occur along the longitudinal axis of the sample, (b) the random character of magnetisation changes with respect to position and time and (c) the progressive increase of applied field reduces the irregularities of domain wall motions, assuming also that the field in excess of local coercive field is proportional to wall velocity, which in turn is proportional to the increase of active wall areas.

3.2 Parameters that affect power loss.

Parameters which may affect the motion of domain walls during magnetisation cannot be overlooked since there is obviously a difficulty in correlating power loss calculation with the movement of domain wall theories based on rigid or flexible walls. These parameters may be considered as follows: (a) domain walls not being perpendicular to the surface of the sheet, (b) the domain walls not remaining planar, since wall bowing occurs, (c) the motion of domain walls not being uniform; that is the occurrence of wall pinning and (d) interaction between grains, the effect of grain orientation, grain size, and lamination thickness.

3.2.1 Domain walls not perpendicular to the surface of the sheet.

Basically, the assumption made in the early power loss calculations was that the domain wall, in harmony with neighbouring walls, moves sinusoidally and is or remains perpendicular to the surface. This was the observation made in well oriented (110) [001] Goss textured silicon iron by the magneto-optic techniques [3.8]. However, the idea that walls tilting at angles to the surface, which was contrary to the initial assumption, emerged later. It was even revealed from an eddy current loss analysis that the tilted domain wall increases the wall area. The current concentration is thereby reduced, and consequently, the loss which depends on the mean square of the eddy current is also reduced [3.9]

3.2.2 Non-planar domain walls (wall bowing).

During magnetisation, the domain wall does not remain planar as assumed in the simplest model. A 180° wall develops curvature about an axis parallel to the easy direction without an increase in magnetostatic energy. The skin effect shielding of eddy currents can cause the field at the surface to exceed that at the centre of the sample and consequently cause the domain wall at the surface to move ahead of the central portion of the wall. This

phenomenon is known as domain wall bowing. The velocity of the wall on the surface is greater than the velocity at the centre of the sample, as shown in figure 3.3. The greater the degree of bowing the greater the difference in the velocities, causing the surface of the sample to saturate prematurely. Shilling et al indicated that wall bowing may occur during 60Hz magnetization of commercial (110) [001] grain oriented 3% Si-Fe [3.5]

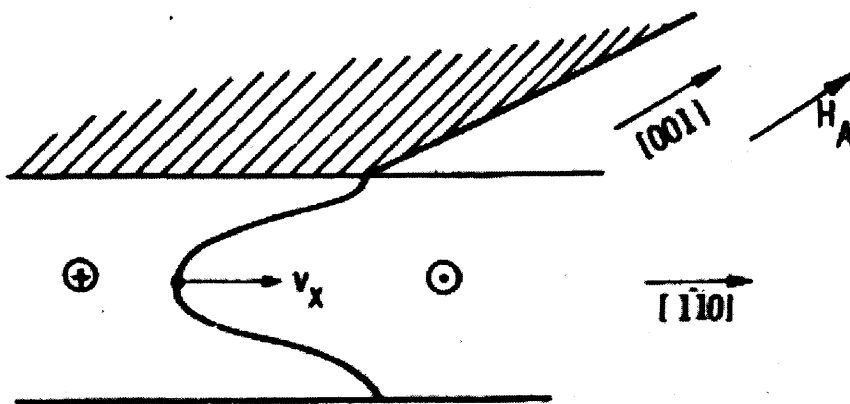


Fig. 3.3: Wall bowing during magnetization of (110) [001] 3% Si-Fe. Centre of wall lags behind wall segments near sheet surface. H_A is the applied field. (After [3.4])

It has also been indicated that, the domain wall bowing phenomenon does affect the measured losses to a large extent [3.10]. Comparatively, the simple wall bowing causes lower losses than those calculated for a planar wall, since its mean velocity per cycle will be less. However, the direction of the bowing reverses when the direction of wall motion reverses; this means that the magnetisation reversal is to some extent concentrated in the surface layer which increases the eddy current loss.

3.2.3 Non-uniform domain wall motion (wall pinning).

The domain walls in a crystal are expected to exhibit a smooth movement when a magnetic

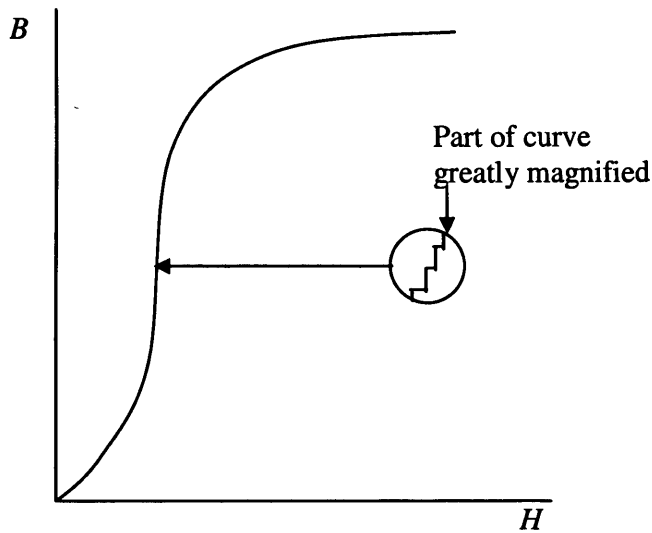


Fig.3.4: Illustration of the Barkhausen effect

field is applied. However, in reality this is not the case, since crystal imperfections produce obstacles to free movement of the walls, and thus cause a discontinuous, non-uniform, jerky movement. This phenomenon, illustrated in figure 3.4 was first realised by Barkhausen [3.11] who discovered that the magnetisation of ferromagnetic materials increase in minute steps due to discontinuous changes in the magnetisation [3.12]

Evidently real materials contain crystal imperfections, which hinder the easy motion of walls. Inclusions, a type of crystal imperfection, may take many forms. They may be oxides or carbides, cementite (Fe_3C) in iron and steel, pores, voids, cracks or other mechanical inhomogeneities.

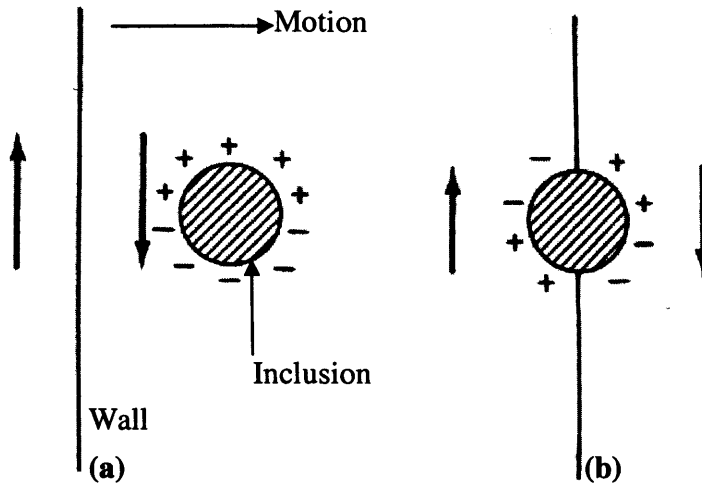


Fig. 3.5: Wall motion and inclusions

Figure 3.5 illustrates the interaction of a domain wall with an inclusion. When a moving wall encounters an inclusion and moves to the position bisecting it, the wall tends to cling to the inclusion which results in the wall area being decreased leading to the wall energy being reduced. However, it was pointed out by Néel [3.13] that the magnetostatic energy associated with free poles of inclusion is much greater than the change in the wall energy at the inclusion, so much so that the latter can be neglected. The magnetostatic energy of an inclusion isolated within a domain could be reduced if suitable spike domains are formed on the inclusion or even reduced to zero by formation of closure domain when the inclusion is bisected by the wall as shown in Figure 3.6.

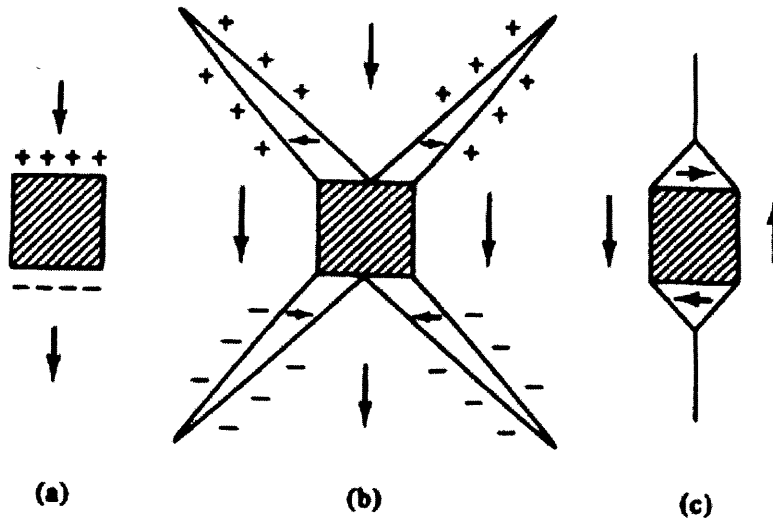


Fig. 3.6: Spike and closure domains on inclusions

- (a) Inclusion within a domain.
- (b) Inclusion bisected by domain wall.
- (c) Inclusion with two closure domains.

Thus for example, a cube shaped inclusion, wholly within a domain, such as shown in figure 3.6, might have spike domains attached to it (b). The total free pole strength in (a) is spread over a larger surface in (b) and that consequently reduces the magnetostatic energy.

This localised domain wall pinning at imperfections together with the magnetostatic field arising from the misalignment of the grains from the ideal orientation form the retarding force on the moving domain wall termed frictional hysteresis whose existence was suggested by Boon and Robey [3.14].

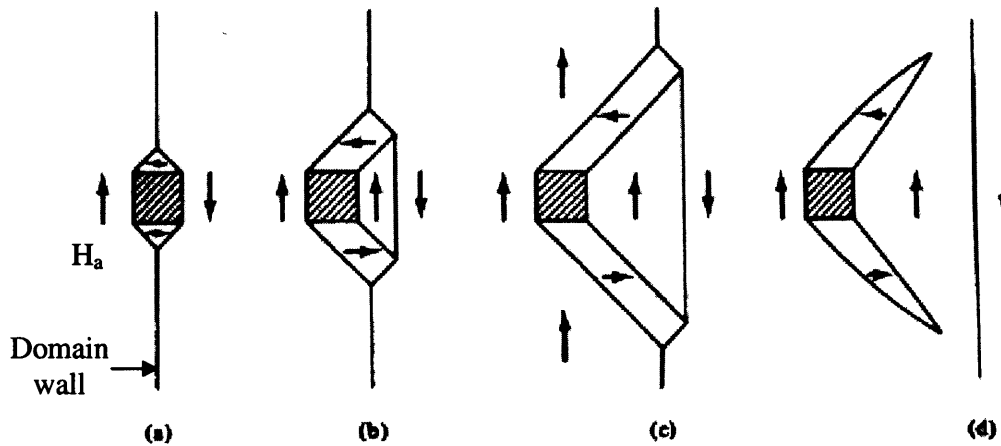


Fig. 3.7 :Passage of a domain wall through an inclusion.
 H_a is the direction of the applied magnetic field.

Considering figure 3.7, the wall in (a) moves to the right as shown in (b) in response to an upward applied magnetic field. Pinned to the inclusion, it drags out the closure domains into “tubes” creating a new domain just to the right of the inclusion. The “tubular” domains increase in width as the motion continues (c). Up to this point, the domain arrangement as in (a) can be regained if the field is reduced since the change that has taken place is still reversible. A point is reached as motion continues with the increment in the field when the wall energy also increases because their increasing surface area adds to it. The main wall eventually snaps off the “tubular” domains and jumps a distance to the right. This is an irreversible situation. Now two spike domains attached to the inclusion (d) has been created. This is the Barkhausen jump mentioned earlier. Reports indicated also that the walls could be pinned several times during the reversal cycle, and instantaneous wall velocities depend on the magnitude of the unpinning field and the local rate of change of the field. When the wall is dislodged from the inclusion, it results in high instantaneous wall velocities, and in a material such as the grain oriented silicon steel, where there is an appreciable number of such imperfections, this may account for the discrepancies between the calculated and measured value of the eddy current losses [3.15].

Scratching a specimen surface perpendicular to the 180° wall [3.16], is found to decrease the total loss as the scratch tends to cause a decrease in 180° main domain wall spacing and the occurrence of reverse sub-domains in its vicinity. Better results have been attained by the employment of a more efficient technique, (spark ablation) which works basically on the same principle [3.17].

3.3 Interaction between grains, the effect of grain orientation, grain size, and lamination thickness.

Grain orientation and the demagnetisation effect of the grains are the two main factors that control domain wall spacing. Furthermore, the domain structure of any one grain in a group is dependent to some degree on the energies associated with the surrounding grains. The interaction between the grains was explained and illustrated for the surface field distribution over Hi-B, 3.25% silicon iron by Bengtsson et al [3.18] Theoretical expectation is for a uniform surface field distribution, at least, over a grain, but findings have shown that the surface field is different in neighbouring grains, and also non uniform even within the same grain. This phenomenon was explained with a model, and showed that the surface field generated by sections of a grain is taken over by sections of neighbouring grains [3.19].

Grain size plays a vital role in controlling magnetic properties, in that, increasing the grain size in electrical steels leads to increase in losses [3.20]. The reason is that, magnetic domains get wider and walls have to move further during magnetisation processes. Reducing grain size, on the other hand, causes high stray field at grain boundaries, which in turn causes an increase in hysteresis loss because of the formation of domain closures.

The effect of grain size on the power loss of grain oriented silicon is the result of two conflicting mechanisms. On one hand, the domain wall spacings decrease with decreasing grain size due to the increase in magnetostatic energy at the grain boundaries with the

beneficial reduction of eddy current loss. On the other hand, as the grain size decreases, the grain to grain misorientation tends to increase, consequently increasing the loss associated with misoriented grains as described in the previous section, and a smaller grain size introduces more boundaries acting as pinning points for domain wall motion. This increases the hysteresis loss.

3.4 Sheet coating and effect of stress in grain-oriented silicon steel.

Insulation coatings are applied to electrical steel laminations used for magnetic cores of a wide range of electrical machines primarily to reduce eddy current formation in the core. It may help to accommodate burr, which might otherwise cause short circuits and, also improve punching characteristics. Hence its reduction effect on total power loss.

The insulation is usually provided by a double coating. In the first case, the surface is coated with a layer of silicon dioxide (SiO_2) during annealing, and then a second coating of magnesium oxide (MgO) is applied primarily to serve as an annealing separator to prevent sticking of adjacent coil wraps. The MgO reacts with the surface SiO_2 and form forsterite (MgSiO_4). The forsterite coating produced is commonly called the mill glass and is followed by phosphate coating which produces stress [21]. Thus, the coating not only provides good

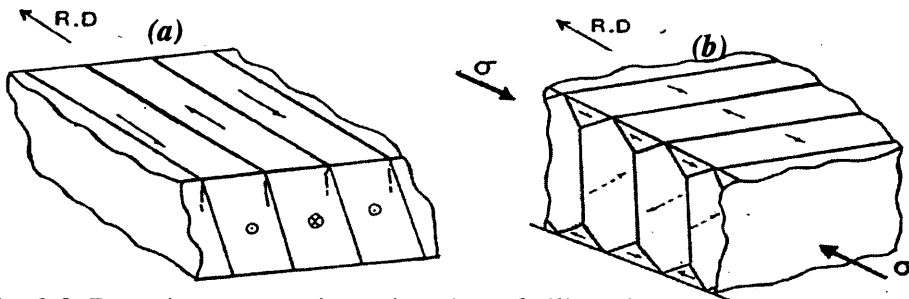


Fig. 3.8: Domain structure in grain oriented silicon iron.
 Stress free bar domains
 Closure domains caused after being subjected to compressive stress.
 (R.D.- Rolling direction; σ - Compressive stress).

dielectric properties but also imparts an equivalent uniaxial tensile stress in the rolling direction. Then the inducement of the uniaxial tensile stress parallel to the rolling direction, causes a substantial reduction in the density of the lancet supplementary domain structures.

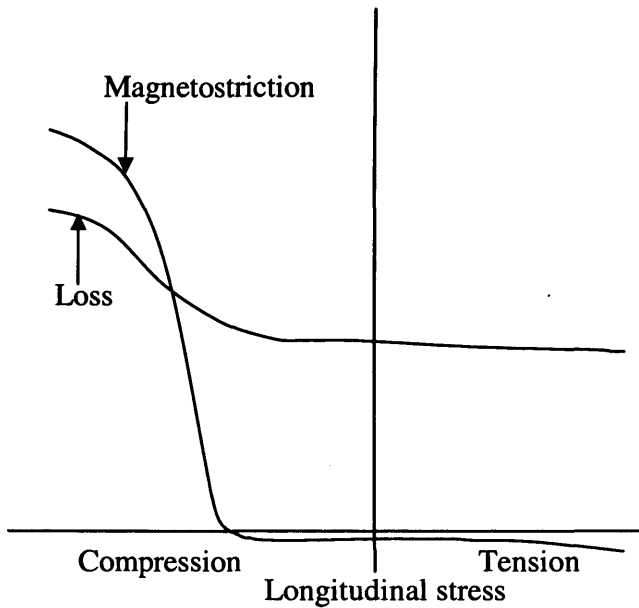


Fig. 3.9: Variation of loss and magnetostriction with stress in typical high permeability electrical steel.

Additionally, tensile stress results in a refinement of 180° domain wall spacing [3.5] and reduces eddy current losses and magnetostriction.

Magnetoelastic energy is introduced into a silicon iron material when compressive stress is applied to it. The resulting domain structure in grain oriented material is as seen in figure 3.8(b) where the domains align themselves in the [010] and [100] direction. In this condition, the power loss increases if the material is magnetised in the rolling direction because, the magnetisation vectors will have to rotate through 90° . This increase is illustrated of power loss and magnetostriction in figure 3.9.

Reference.

- [3.1] P. Beckley (1999), "Modern steels for transformers and machines", IEE Power Engineering Journal, Vol. 13, No. 4, p. 190-200.
- [3.2] D. Jiles (1998) "Introduction to magnetism and magnetic materials", 2nd Edition, Chapman and Hall, London, p. 328.
- [3.3] G. Bertotti (1988), "General properties of power losses in soft ferromagnetic materials", IEEE Trans. Magn. MAG-24, no. 1, pp. 621-630.
- [3.4] H. J. Williams, W. Shockly and C. Kittel (1950), "Studies of the propagation velocity of a ferromagnetic domain boundary", Phys. Rev., 80, pp. 1090-1094
- [3.5] J. W. Shilling and G. L. Houze, Jr. (1974) "Magnetic properties and domain structure in grain-oriented 3% Si-Fe", IEEE Trans. Magn. MAG-10, no. 2, pp. 195-222.
- [3.6] G. Bertotti (1985), "Physical interpretation of eddy current losses in ferromagnetic materials", J. Appl. Phys., vol. 57, pp. 2110-2126.
- [3.7] G. Bertotti and F. Fiorillo (1984), "Power losses and domain structure dynamics in 3% Si-Fe single crystals", IEEE Trans Magn. MAG-20 ,no. 5, pp. 1475-1477.
- [3.8] R. H. Pry and C. P. Bean (1958), "Calculation of energy loss in magnetic sheet materials using a domain model", J. Appl. Phys., 29, pp. 532-533.
- [3.9] P. Beckley (2000). "Electrical steels", EES, Newport, p. 132.

- [3.10] B.N. Filippov, and S.V. Zhakov, (1975), *Phys. Met. Metal.*, 39, p24.
- [3.11] H. Barkhausen (1919), “Two phenomena uncovered with help of the new amplifiers” *Phys.Z*, 20, pp. 401-403 [as cited in Cullity, see 3.13]
- [3.12] B. D. Cullity (1972), “Introduction to magnetic materials”, Addison-Wesley, 1st Edition, p. 313.
- [3.13] L. Néel (1944), “Effects des cavité et des inclusions sur le champ coercitif”, *Cahiers de Physique*, 25, pp. 21-44 [as cited in Cullity, see 3.13].
- [3.14] C. R. Boon, and J. A. Robey (1968), “Effect of domain wall motion on power loss in grain-oriented silicon-iron sheet”, *Proc. IEE*. 115, p1535-1540.
- [3.15] P. Beckley and J. E. Thompson (1970), “Influence of inclusions on domain-wall motion and power loss in oriented electrical steel”, *Proc. IEE*, Vol. 117, No. 11, pp. 2194-2200.
- [3.16] Nozawa, T., Yamamoto, T., Matsuo, and Y. Ohya (1983), “Relationship between total losses under tensile stress in 3 percent Si-Fe single crystals and their orientations near (110)[001]”, *IEEE Trans. Magn. MAG-14*, no. 4, pp. 252-257.
- [3.17] P. Beckley, D. Snell and C. Lockhart (1985); “Domain control by spark ablation”, *J. Appl. Phys.* 57 (1), pp. 4212-4213.
- [3.18] C. Bengtsson and H. Pfutzner (1984), “Stray fields at grain boundaries in demagnetised stress coated HI-B sheets”, *IEEE Trans. Mag.*, MAG-20, no. 5, pp. 1478-1480.

- [3.19] H. Pfutzner, G. Schwarz, and J. Fielder (1983), "Computer-controlled domain detector", Jap. J. Appl. Phys., 22, no. 2, pp. 361-364.
- [3.20] A. J. Moses (2002), "Opportunities for exploitation of magnetic materials in an energy conscious world", Interdisciplinary Science Review, vol 27, no. 2, pp.100-113.
- [3.21] D. Snell and A. Coombs (1999), "Novel coating technology for non-oriented electrical steels", SMM14, Hungary, pp. 1-3.

CHAPTER FOUR

METHODS FOR THE DETECTION OF SURFACE FIELDS ON ELECTRICAL STEELS.

4.1 Magnetic field detecting sensors.

The detection of grains and grain boundaries through the study of the normal component of the stray magnetic field (H_z) at the surface of a specimen, and the determination of localised power loss are the main driving force behind the consideration of the choice of the sensors for this work.

Sensors capable of detecting the vertical and also the tangential components (i.e., H_x , H_y and H_z , with respect to the rolling direction) of the magnetic field which is continuous across the surface of the specimen are vital for this investigation. It is assumed that the tangential component of the field above a sample but very close to its surface is identical to the effective field just inside the sample itself. Therefore, a suitable magnetic field sensor placed on the surface of the specimen is expected to measure the effective tangential field just inside the sample. The additional factor is the choice of sensor(s) for the detection of the flux density components, B_x and B_y , required to calculate the localised power loss. This is fully discussed in section 7.4.

Many types of magnetic field sensors are available, each with its own merits and demerits, depending on the requirements of the specific applications. Sensors such as the H-coils detect magnetic fields over a large area, whereas others such as the vibrating pick-up loop magnetometer (VPLM), magnetotransistor, magnetoresistive recording head (MRH), the permalloy probe and the Hall sensors are capable of

Chapter Four: Methods for detection of surface fields on electrical steels

detecting localised fields in small regions. In theory all are capable of measuring local surface fields on electrical steels so they are briefly compared in this chapter.

4.2 Minimum specification of magnetic field, H, sensor required for this project.

The minimum specification required for the magnetic field, H sensor are as follows:

- a. It should be a three dimensional,
- b. It should be able to operate in both a.c. and d.c. excitation,
- c. In a.c. excitation, it should be able to operate at frequency of 50 Hz,
- d. It should be small in dimensions (each side being about 5mm or less)
- e. It should have a field range of about $\pm 500 \text{ Am}^{-1}$ and
- f. It should be purchased, if possible, rather than developed.

4.3 Vibrating pick-up loop magnetometer, (VPLM)

The principle of operation of the VPLM is based upon induction produced by vibrating a pick up loop with respect to a d.c. field [4.1] [4.2]. The construction of the device is as illustrated in figure 4.1. The pick up loop section of the device is constructed from a rectangular conducting material with its length much greater than its width. A voltage is induced across the terminals of the pick up loop when made to vibrate along its length, in the vicinity of a perpendicular field.

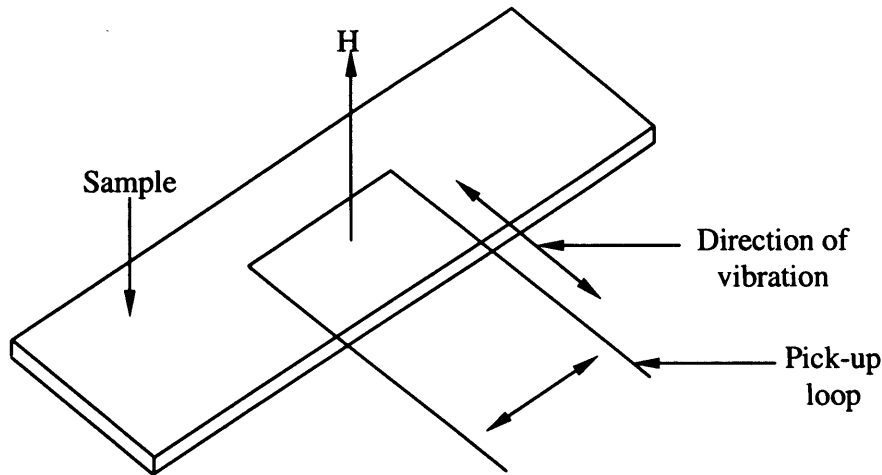


Fig. 4.1: Vibration pick-up loop used for the detection of normal magnetic field (H_z).

The size of a VPLM developed by Wurmbach et al was about 25mm long, 55 μ m wide. It was etched from a 0.3 μ m thick Cr-Au-Cr layer on a thin glass substrate. The sensitivity of the device, when operated at a frequency of 1824.1Hz and amplitude of 9.4 μ m was 5.3×10^{-12} V/A/m with a field resolution of 79.6A/m. Although, it has a low sensitivity, the sensor can be employed where high spatial resolution is required, and it has been used effectively to detect grain boundaries of grain oriented material.[4.2]

4.4 The Magnetotransistor

The magnetotransistor (figure 4.2) is based on the conventional semiconductor bipolar transistor, having two collectors. The device is operated in common base mode with equal voltages applied to both collectors. When there is no external field, there is no output voltage, because the charge carriers from the emitter are divided equally

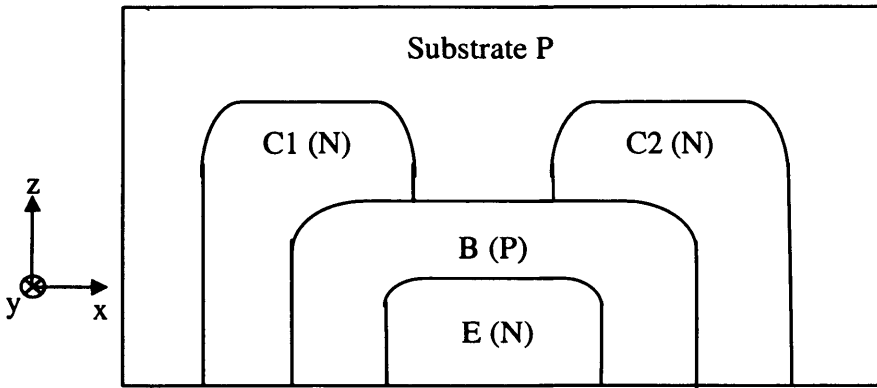


Fig. 4.2: Cross-section of a magnetotransistor.
E, - Emitter; B - Base and C1 and C2 – Collectors.
N and P are the material type [4.3]

between the collectors. Application of an external magnetic field in the vertical, Z direction causes the charge carriers in the base region to deflect, causing a different flow of carriers to the two collectors. The difference in the charge carrier flow (i.e electric current) between the collectors can be calibrated to measure the magnetic field [4.3]. A sensor with a sensitivity, up 1.2V/T has been reported by R.S. Popovic et al [4.4].

4.5 Permalloy probe

This micro-size device is able to detect low fields on the surface of a magnetic material. The sensor works, when the tip of permalloy film, a few microns thick, is made to vibrate inside a multi-turn pick up coil, close to the surface of the sample (figure 4.3). During this process, if the sample is magnetised under a.c. condition a voltage(V_0), proportional to the rate of change of the flux ($d\phi/dt$) in the coil is

Chapter Four: Methods for detection of surface fields on electrical steels

induced. The induced voltage in a pick up coil is in the order of $100\mu\text{V}$. The surface field can then be calculated from the induced voltage.

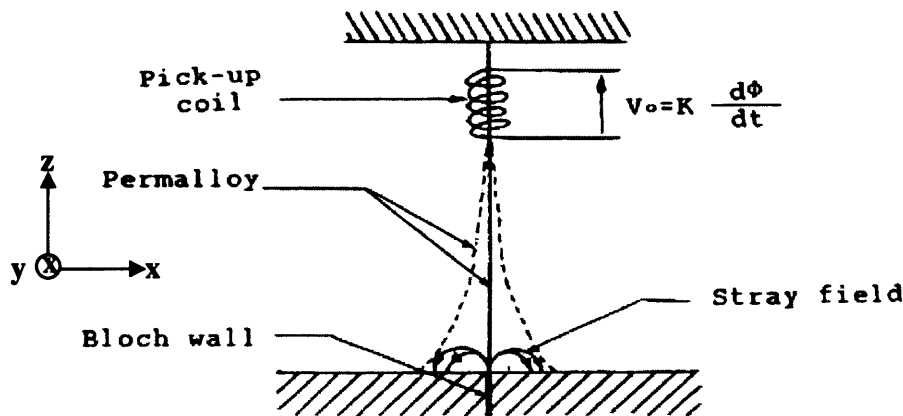


Fig. 4.3: Permalloy probe for the stray field detection over a Bloch wall. (After [4.5])

The signal produced by the probe is proportional both to the $\left(\frac{dH_z}{dy}\right)$ and to the velocity of the probe tip [4.5].

The sensitivity of the device depends upon sensor factors such as the number of turns, the amplitude of the vibration of the permalloy tip and its angular frequency.

4.6 Magnetoresistive head

The magnetoresistance effect has been known for more than a century, but only recently has it been developed and exploited in thin ferromagnetic films. These developments have led to the wider applications of magnetoresistance sensors. Applications include: Magnetic card readers, coin validation mechanisms, Non-destructive testing, Linear and rotary encoder, Speed and position sensing, etc, [4.6]

Chapter Four: Methods for detection of surface fields on electrical steels

Magnetoresistive thin film detectors are two terminal device which experience a change in resistance when acted upon by a suitably oriented magnetic field. The change in resistance is usually detected as a change in voltage across the detector when it carries a constant current, I . It can be shown that the resistivity, ρ of the material, when subjected to a transverse magnetic field is;

$$\rho = \rho_0 + \Delta\rho_{\max} \cos^2 \theta \quad (4.1)$$

Where ρ_0 is the resistivity of the material perpendicular to the current density J , θ is the angle between the current density, J and magnetisation vector, M_s and $\Delta\rho_{\max}$ is the magnetoresistance coefficient. as illustrated in figure 4.4(a).

Equation (4.1) can be expressed in terms of the applied field H_y and H_0 the effective anisotropy field which acts to restrain the magnetisation along the element of the sensor. H_0 represents the combined effect of the demagnetising field H_D across the sensor width, and the anisotropy field H_k arising from the uniaxial anisotropy induced along the element length during the deposition of the film.

Figure 4.4(b) shows the static characteristics of magnetoresistive sensor.

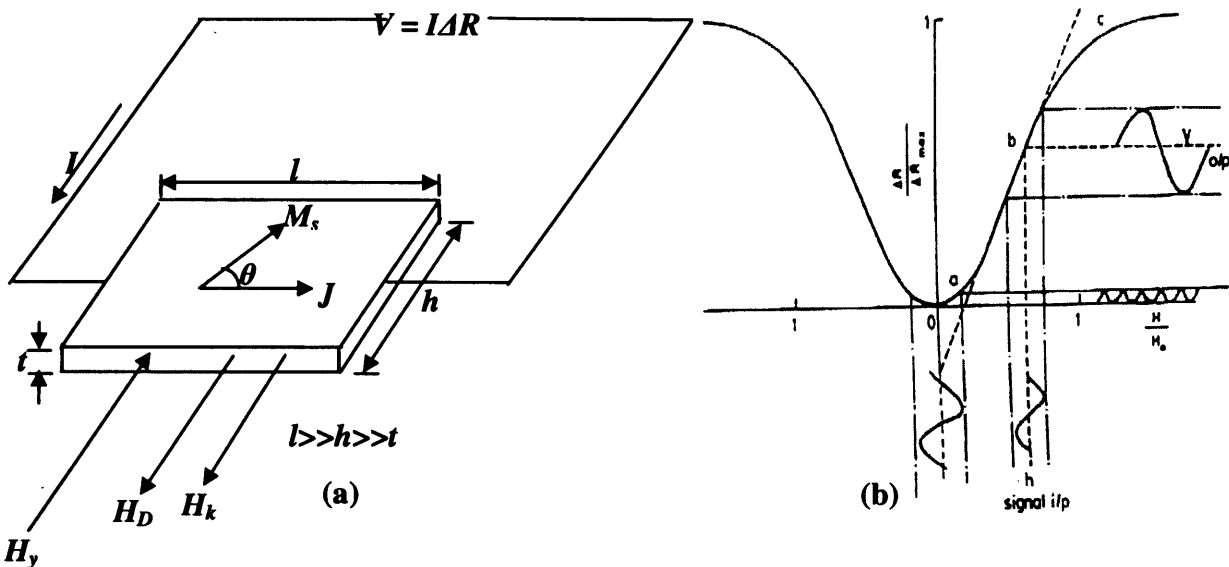


Fig. 4.4: (a) Magnetostrictive thin film sensor: H_y : Total field acting across the width of element, H_D demagnetizing field, and H_k the anisotropic field.
 (b) The static characteristics of magnetostrictive sensor (After 4.6]

When the magnetostrictive sensor is placed in a small field its characteristic is essentially non-linear (quadratic). If the sensor is operated around this point the output produced is unipolarly distorted, double the frequency of the applied field.

As the field is further increased the magnetisation M_s in the element rotates towards an angle of approximately 45° to the element length, and this corresponds to point (b) in Fig. 4.5 and further increase in field will cause the magnetostrictance effect to approach a saturation level, (point c).

Therefore, in order to operate the sensor in the linear portion of its characteristic (b) to obtain maximum linearity and sensitivity and minimum distortion, it is necessary to rotate the magnetisation vector M_s to lie at 45° to the current vector J (figure 4.4(a)). This is achieved by biasing the sensor. Various techniques have been developed for biasing the sensor. (a) Permanent magnet, (b) Hard/soft adjacent layer

Chapter Four: Methods for detection of surface fields on electrical steels

technique [4.7], (c) Current conductor technique (d) Anisotropy field technique [4.8] and (e) Barber-pole technique [4.9]. All these techniques help to enhance the performance of the sensor, however, they have their individual shortcomings.

4.7 The Hall probe

Hall probes are widely used in commercial instruments for measurement of d.c. or a.c. magnetic fields. The effect arises from the interaction of current carrying

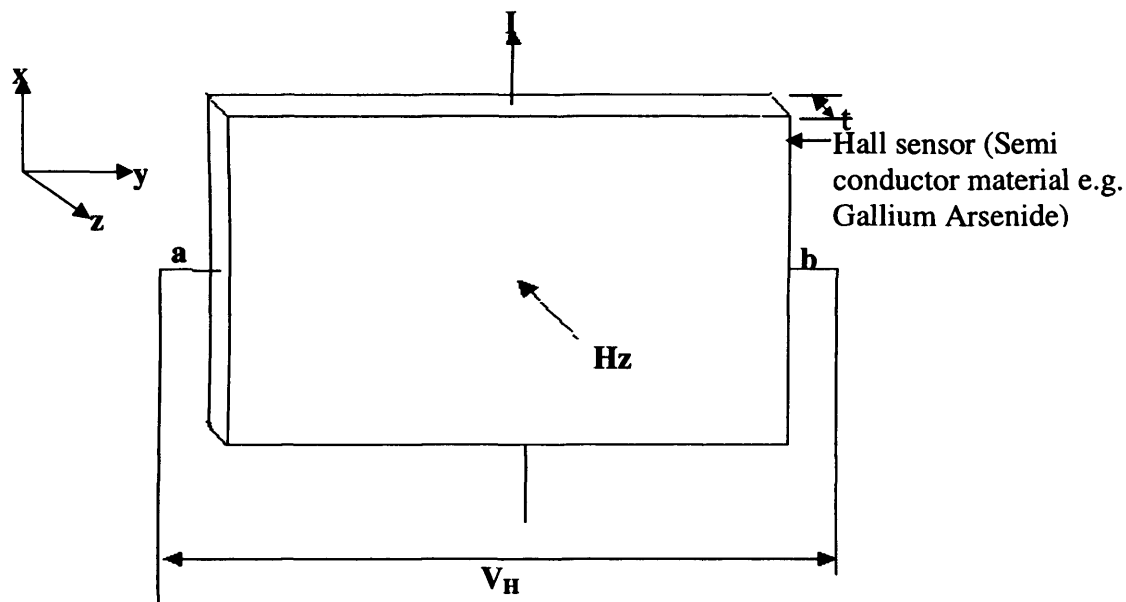


Fig. 4.7: The Hall effect configuration

conductors with the external magnetic field. A voltage is produced across a conductor carrying a current at a right angle to both the external magnetic field and the current.

Figure 4.8 illustrates the Hall effect. The two opposite points (a) and (b) will be at the same potential with no external field present. When the plate (e.g. Indium Antimony) is subjected to a magnetic field (H_z) perpendicular to it, the current crossing the

Chapter Four: Methods for detection of surface fields on electrical steels

conductor is distorted, causing the development of an e.m.f (V_H) between points (a) and (b). The classic expression for the Hall voltage can be written as:

$$V_H = -\frac{R_H I_x H_z}{t} \quad (4.1)$$

where t is the thickness of the plate, R_H is the Hall constant, which is a property of which material. If the current, I_x is kept constant, then V_H is proportional to the magnetic field H_z . Calibration in a known field is necessary.

Hall probes can be manufactured with a very small active area, down to $1.0 \times 10^{-2} \text{ cm}^2$. They can therefore be used to measure a magnetic field with high spatial resolution [4.10]. A micro-size Hall probe, with an active area of $20 \times 20 \mu\text{m}^2$ has been used to detect the domain configuration in cobalt films, and also the domain structures in grain oriented silicon iron [4.11]. The device suffers from deviations from linearity at higher field and from the dependence of the response.

4.8 Choice of sensor

Taking into account the size of the grains within which scanning was to be performed, micro size magnetic sensors capable of detecting both normal and tangential components of the magnetic field at one spot (a 3-dimensional sensor) on the surface of the specimen was desirable.

Table 4.1 shows the comparison between the probes considered for the this project. Among the micro-size sensors described VPLM and the permalloy are not suitable, since they are only able to detect the vertical component of the surface field.

Chapter Four: Methods for detection of surface fields on electrical steels

The magnetotransistor is claimed to be capable of detecting both vertical and horizontal components of the field. It also has an exceptionally high sensitivity and can measure field directly. It is not widely used for field detection or measurement

Table 4.1: Comparative table of the probes considered for this project.

Techniques / Typical sensor specifications	VPLM	Permalloy probe	MR Probe	Magnetotransistor	Hall probe
Material application	Silicon iron sheet	Silicon iron sheet	Silicon iron sheet	Silicon iron sheet	Silicon iron sheet.
Effective distance from sample surface	?	1 μm	35 μm	?	35 μm
Average detectable field range	Greater than 10^{-4}T	$\sim 6.3 \times 10^{-2}\text{T}$	0 – 2.5 T	0 – 1 T	0 – 10T
Typical frequency range	$\sim 2\text{kHz}$	25 Hz – 20 kHz	d.c.	0 – 210kHz	0 – 1kHz
Resolution	?	$\sim 100 \mu\text{V}$	$\sim 100 \mu\text{T}$	$\sim 1.0 \mu\text{T}$	$\sim 10 \mu\text{T}$
Ease of use (with respect to dimensions of the physical quantity sensed: x,y z)	Difficult	Difficult	Easy	Difficult	Easy
Ease of use (in combination with the needle probes)	Difficult	Difficult	Easy	Medium	Easy

? – Information not available

except by those who produce them for research purposes. Moreover the sensor, like any transistor, has to be protected by a casing, with the disadvantages of separation of the sensor from the simple surface resulting in the introduction of field measurement errors.

Chapter Four: Methods for detection of surface fields on electrical steels

Micro size 3-Dimensional integrated Hall effect sensors, with high sensitivity, are available. Therefore it was more convenient to employ one of them in a special design with two pairs of needle probes for this work.

4.9 Grain and static domain observation techniques in silicon steels

The obvious and, perhaps, a simple means by which grain observation in grain oriented silicon iron could be made is by etching the surface to remove the coating. However, this method is destructive. In this project it is desirable to see the grain structure through the coating without etching and produce domain imaging without coating removal.

Many techniques such as Kerr effect, the Scanning Electron Microscope (SEM), the ferromagnetic colloid techniques, etc., have been developed and employed for the observation of the size and orientation of domains and grain structures in electrical steels [4.12] [4.13] [4.14]. However, special sample preparation may be involved when some of these techniques, e.g., Kerr effect and SEM are employed. In some cases, the coating on the electrical steel sample has to be removed, a process known to affect the magnetic domains and hence the properties of the sample. The sample has to be annealed later for the restoration of its properties before it is used. This makes the technique more costly and time consuming.

In the ferromagnetic colloid technique, for example, where iron filings of between 10-100nm diameter are suspended in a colloid and used to detect the magnetic field, there is no need for any sample treatment to remove the stress coating. This therefore makes it quicker and easier to employ.

Chapter Four: Methods for detection of surface fields on electrical steels

When the colloid suspension is applied to or spread on the surface of the magnetic material, due to the interaction between the magnetisation and the magnetic particles, the particles freely move to positions determined by distribution of the inhomogeneous stray surface magnetic field. Figure. 4.8a illustrates this interaction, showing how these fields attract the colloid particles to outline the domain structure.

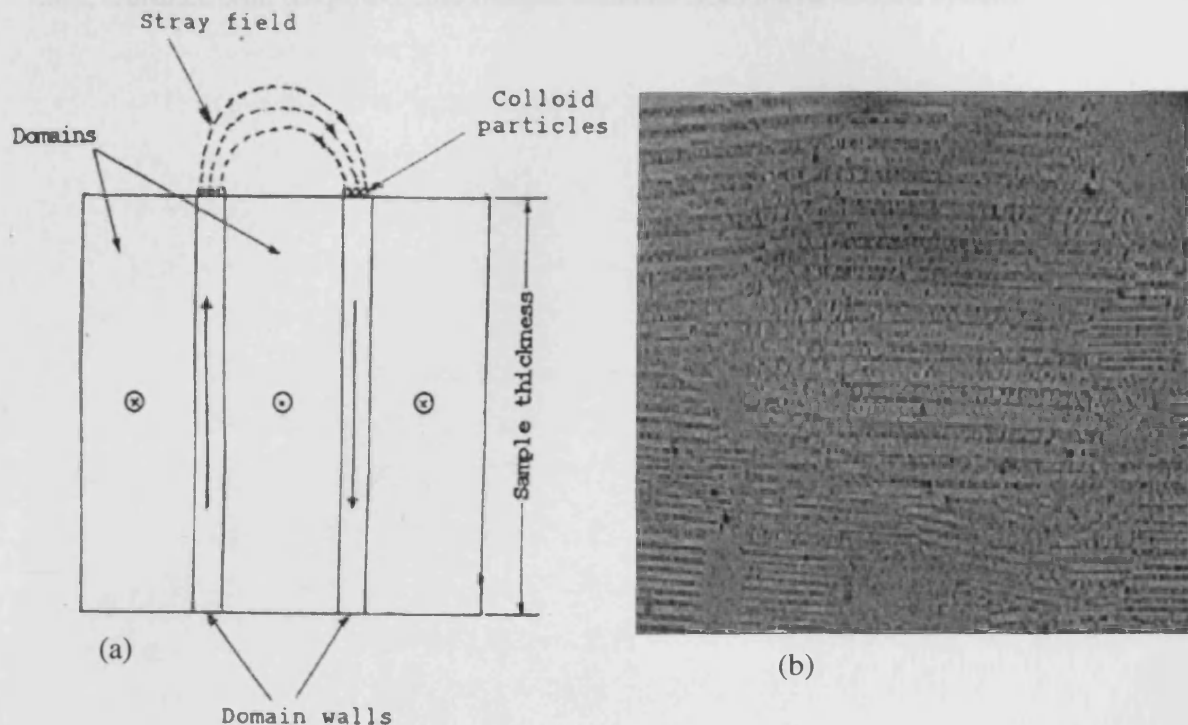


Fig. 4.8:(a.) Interaction between stray fields and colloid particles.
(b) an image from the surface of SiFe taken using this technique.

More research have been carried out on this technique [4.15] since it is obviously a tool for easy observation of the grain size and orientation without coating removal, and therefore a useful tool or technique for quality control and improvement of the silicon iron.

Chapter Four: Methods for detection of surface fields on electrical steels

Further research led to the manufacture of the magnetic domain viewer, a commercial instrument whose principle of work is based on the colloid technique [4.16]. This instrument has high resolution and is easy to use. It was used in this investigation to observe and compare the static domains and also the grains as seen on the coated specimen to what was obtained from the instrument, and finally see how these will, in turn, correlate with the power loss images obtained from the developed system.

Chapter Four: Methods for detection of surface fields on electrical steels

4.10 References

- [4.1] J. Grosz-Kowski (1937), "The vibration magnetometer", *J. Sci. Instrum.* 14. pp. 335-339.
- [4.2] G Wurmbach, N. Normann and H. H.. Mende (1978), "Measuring equipment to register the local dependence of magnetic fields with high geometrical resolution", *J. Mag. Magn. Matl.*, vol. 9, Issue 1-3, pp. 242 - 244.
- [4.3] E. C. Hudson Jr. (1968), US Patent no. 3.389.230.
- [4.4] R. S. Popovic, H.P. Baltes (1983)"A CMOS magnetic field sensor", *IEEE J. solid -state circuits* SC-18, p.426-428.
- [4.5] J. Kaczer and R. Gemperle (1956), "Vibrating permalloy probe for mapping magnetic fields", *Czech. J. Phys.*, 6, pp. 173-175.
- [4.6] D.J. Mapps, N. Fry and D. Smith(1995), "Non linear magnetoresistance, Proc. of international ISEM symposium on nonlinear electromagnetic systems, Cardiff, Wales, U.K., 1996, Editors A.J. Moses, A. Basak, IOS Press, p.628-633.
- [4.7] C. H. Bajorek, S. Kromgelb, L. T. Ramankiw and D. A. Thompson (1974), "An integrated magnetoresistive read, inductive write high density recording head", 20th AIP Conf. on Mag. Magn. Matl, San Francisco, paper 3D-2.
- [4.8] R.P. Hunt, German Patent application, 21-214-43.
- [4.9] K.E. Kuijk, W. J. Van Gestel and F. W. Gorter (1975), "The Barber pole, a linear magnetoresistive head", *IEE Trans. Magn.*, MAG-11, no. 5, pp.1215-1217.

Chapter Four: Methods for detection of surface fields on electrical steels

- [4.10] D. Jiles (1991), "Introduction to magnetism and magnetic materials", Chapman and Hall, 1st Edition, p. 55.
- [4.11] P. Schonhuber and H. Pfutzner (1989), "A hall sensor for automatic detection of domains in coated silicon iron", Phys. Scr. 40, pp. 558-568.
- [4.12] J.W. Shilling and G.L. Houze (1974),"Magnetic properties and domain structure in grain-oriented 3% Si-Fe", IEEE Trans Magn, MAG-10, no. 2, pp. 195-222.
- [4.13] P. Beckley, E. Mivechi, D.H. Horrocks and C.H.Porter (1990),"Strboscopic observation of domain coated Si-Fe sheet using scanning electron microscope", IEEE Trans. Mag. vol. 26, no. 5, pp.1975-1977.
- [4.14] R. Carey and E.D. Isaac (1966),"Magnetic domains and the techniques for their observation", London, The English University Press Ltd., p 66.
- [4.15] H. Pfutzner, C. Bengtsson and A. Leeb (1985), "Domain investigation on coated unpolished Si-Fe sheets", IEEE Trans Mag. MAG-21, no. 6, pp. 2620-2625.
- [4.16] P. Beckley (2000), "Electrical steels", Ees, Newport, pp. 124-128.

CHAPTER FIVE

INVESTIGATION INTO GRAIN BOUNDARIES IN GRAIN-ORIENTED
SILICON IRON.

5.1 Background:

In this work some effects of the grain structure on the distribution of the vertical (normal) component of magnetic field are measured. The vertical component of field is made up of three parts: H_b , stray field generated at grain boundaries, H_w , stray field generated at 180° domain walls and H_s , stray field generated on the surface of the

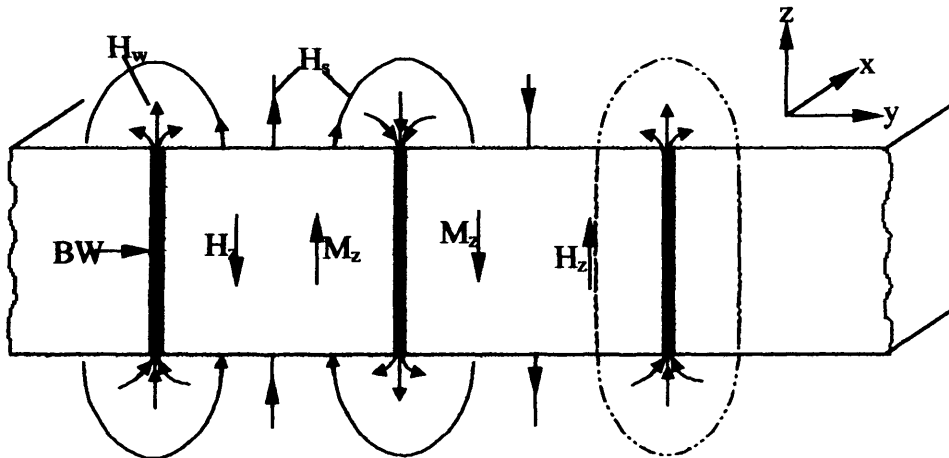


Fig. 5.1: Schematic model for stray field generation of Demagnetised sheet: H_z , M_z – z components of magnetic field, H and magnetisation, M respectively. BW – Bloch wall (After [5.1])

grains with misorientation angle not equal to zero. Generally $H_s > H_w$, and if a high d.c. external, in-plane field is applied then the domain walls will mostly be annihilated leaving two possible vertical field components originating at grain boundaries and on the saturated grain surfaces where $s > 0$ [5.1][5.2][5.3].

Three techniques described later in this chapter have been employed in investigating into grain boundaries. In the first technique a linear Hall effect i.c. sensor was used to scan, in a straight line, the stray surface vertical magnetic field on the surface of a magnetised grain oriented electrical steel. Using a personal computer, quantitative analysis was performed on the data obtained from this surface field distribution.

In the second technique, a system comprising of an travelling microscope, a vernier and ancillary equipment was used to measure the distances between grain boundaries following the same line mentioned above. The result was compared with the profiles obtained from the first technique. Observation of the edge of a grain oriented silicon steel was made, in the third technique using an optical microscope, to study the grain boundary through the thickness of the material.

5.2 The Preparation of the Electrical Steel sample

A rectangular sheet of grain oriented electrical steel 116 mm (rolling direction) by 78 mm by 0.23 mm which had been chemically decoated by Cogent Power Ltd to reveal the grain structures, is as shown in figure 5.2.

The sample was designated as shown in figure 5.3 before the scan was commenced. The line DE (20 mm) was marked on the bisector of the sheet along the rolling direction (RD) on the top surface. A corresponding line D1E1 was designated opposite to DE on the reversed surface of the sample. The sheet was magnetised along its rolling direction by a d.c. external field of 1 kA/m using a C-core magnetising yoke.

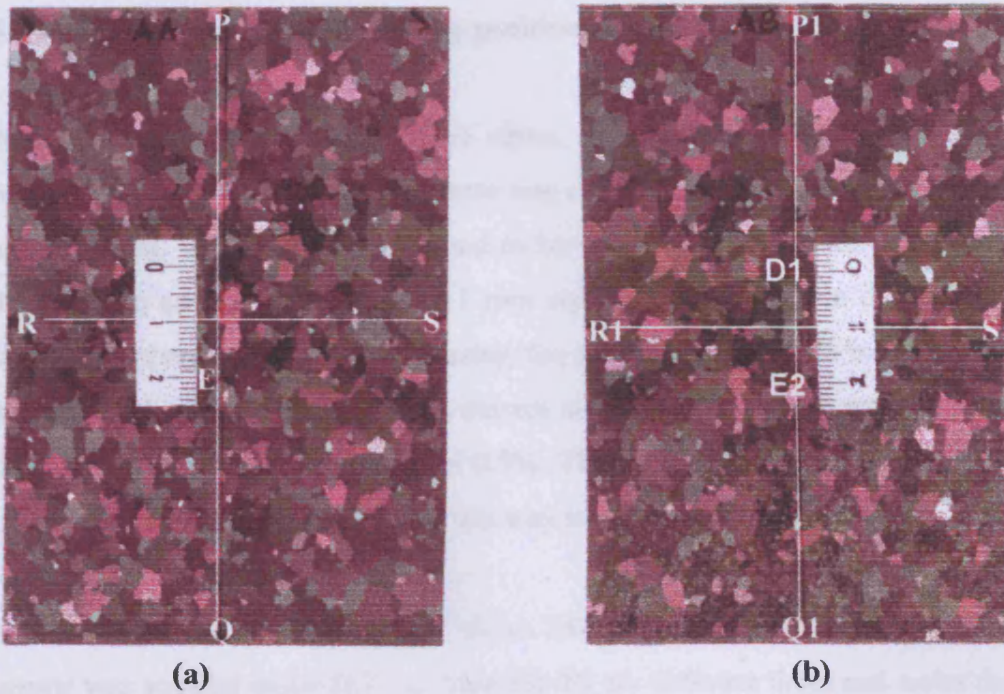


Fig. 5.2. The electrical steel sample investigated: (a) and (b) show the top and the bottom surfaces respectively (dimensions shown in cm).

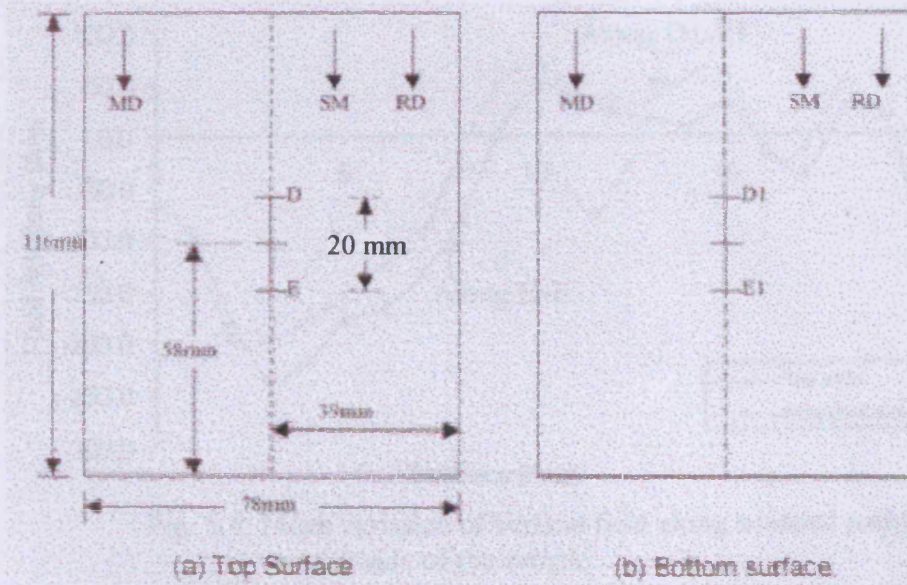


Fig .5.3 Diagram illustrating the sections on both surfaces of the sample scanned.

5.3 Investigation of grain boundary positions with a linear Hall effect i. c. sensor.

A linear integrated circuit (IC) Hall effect. Sensor in a moulded 4-pin dil plastic package, with an active length of 1 mm was calibrated in a uniform solenoid carrying a d.c. current. Its sensitivity was found to be 0.03mV/A/m when the bias current was 3.5mA . The sensor was moved in 1 mm steps along the surface of the sheet at a height of approximately 0.25 mm using the scanning unit shown in figure 5.6. The sensor was energised by the 3.5 mA current and its output voltage was measured on a digital voltmeter with an accuracy of 0.5%. The peak value of the vertical component of the surface field was measured in this way to the accuracy of $\pm 0.76\text{ A/m}$

Direct current, (d.c.) excitation of about 580mA was applied at about 1.8 T. The sensor was scanned along D-E and then D1-E1 six different times and under the same magnetising conditions. The vertical components of field was plotted along the paths as shown in figure 5.4.

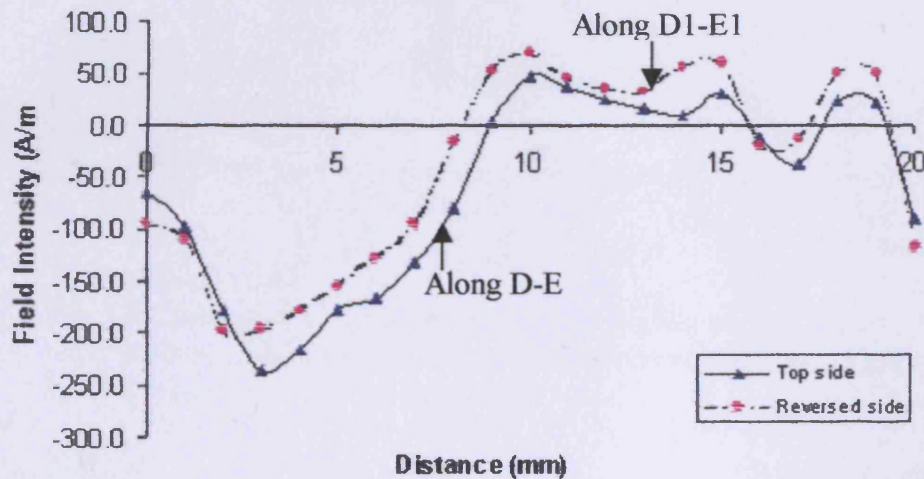


Fig. 5.4: Mean variation of vertical field along scanned paths on each side of the sample.

The positive and negative values indicate field directed out of or into the surface respectively. There is a difference between the distributions on either surface although they broadly follow the same pattern, the maximum field of about 250 A/m occurs at around 2 - 3 mm from D and D1.

5.4 Measurement of position of grain boundaries.

In order to attempt to explain the difference of the field patterns shown in figures 5.4 and 5.5, the positions of the grain boundaries were measured on either surfaces of the sample using a traveling microscope with a resolution of ± 0.01 mm. The position of boundaries were measured along D-E and D1-E1 with respect to points D and D1. The pattern of the results matched with figure 5.4. is as shown in figure 5.5.

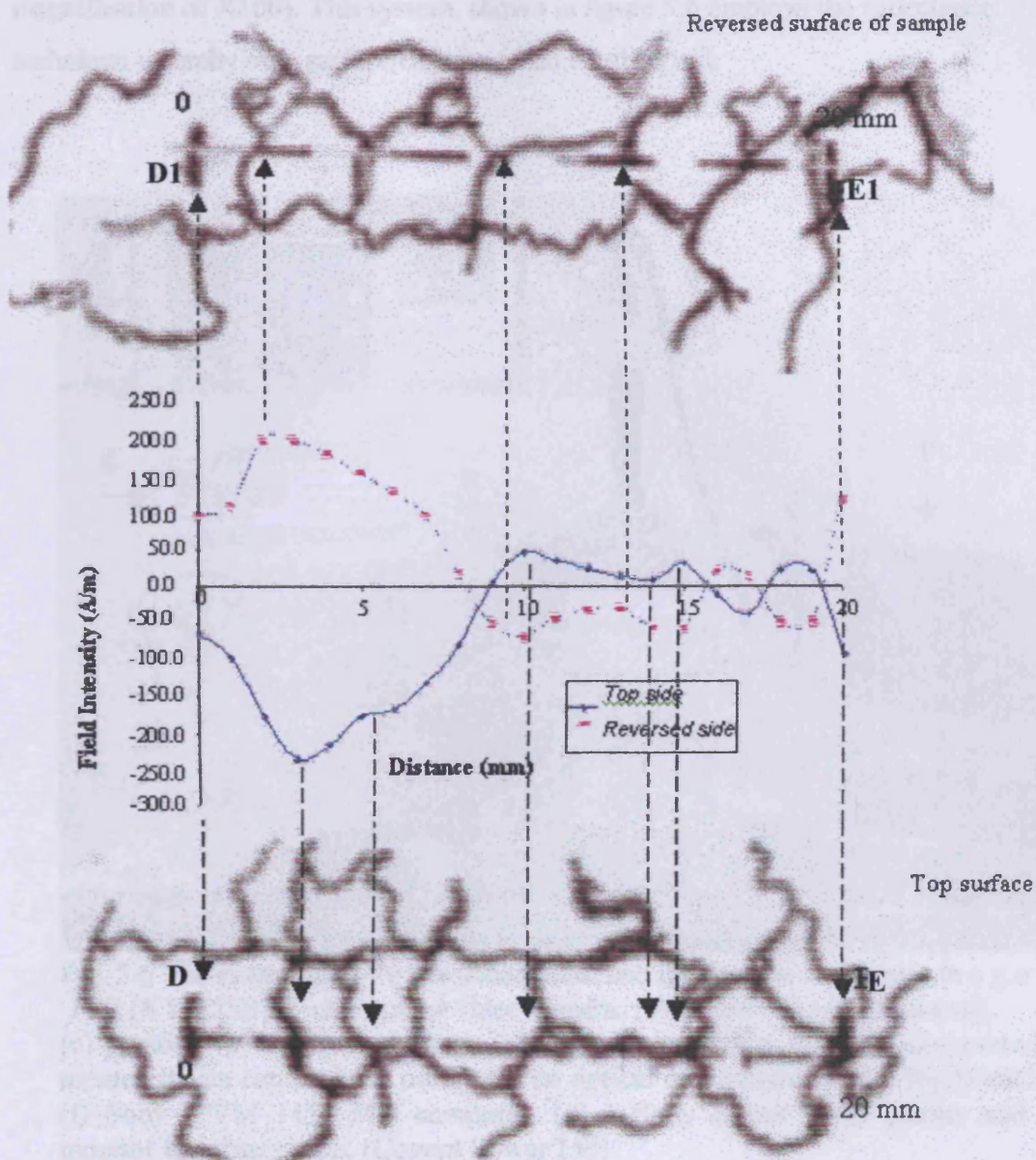


Fig. 5.4. Illustration of the mean results of the scans carried out on either surface of the sample relative to the observed positions of grain boundaries on either side of the sample.

It is normally assumed that the grain boundaries lie at 90° to the sheet surfaces and are therefore in identical relative positions on either surface. The positions of grain boundaries on either surface were measured with an optical microscope (set to the

magnification of X100). This system, shown in figure 5.6 employs the reflectance technique whereby only surface objects could be observed.

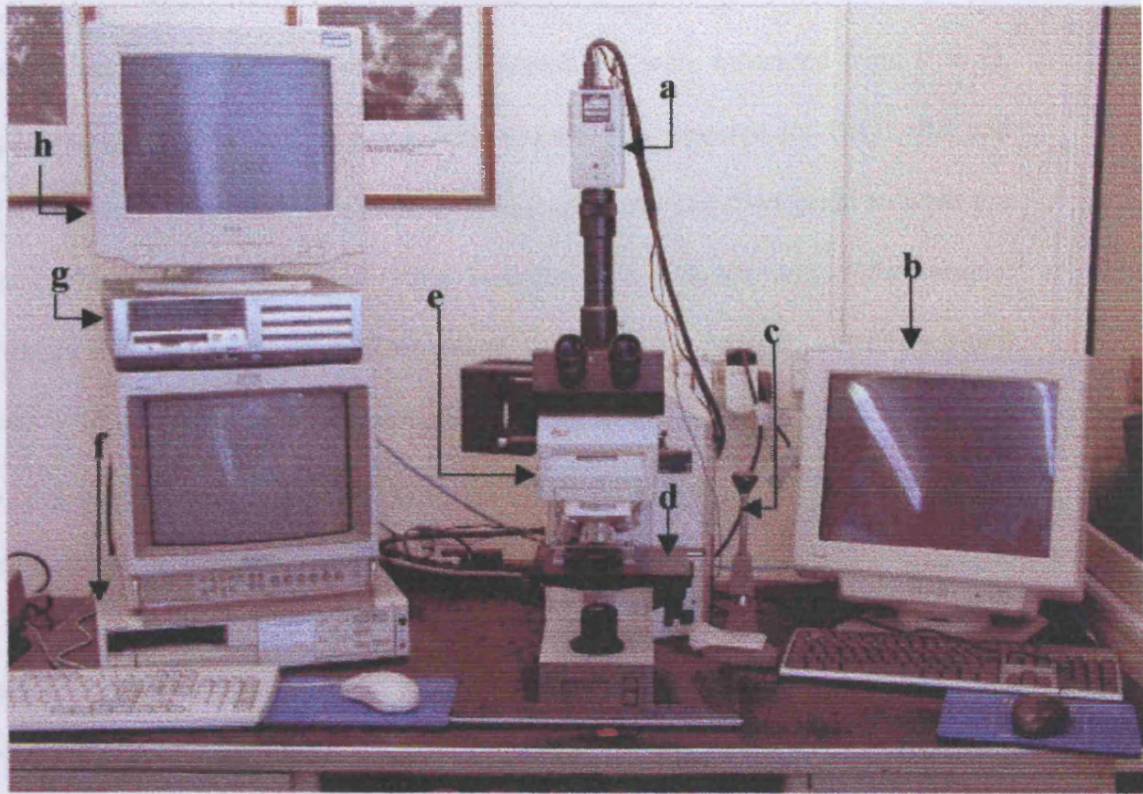


Fig. 5.6 The system used for the observation and measurement of grains in a g.o sample: JVC (KY-F55B), 3-chip colour video camera, (b) 15-inch monitor (control), (c) joystick (d) an X-Y platform (sliding system with a vernier incorporated for micrometre measurements can be fixed on it), (e) an optical microscope system (by DMRXE LEICA) (f) Sony (PVM 1453 MD computer, (g) a Sony colour video printer and (h) 15-inch monitor for observation. (Cogent Power Ltd)

The grain oriented silicon iron specimen shown in figure 5.2 was mounted on a sliding (XY) system so as to facilitate its movement under the microscope. Grain boundary positions were observed and measured with the help of a vernier. Lines P-Q and P1-Q1 similar to D-E and D1-E1 were drawn on the specimen, along the rolling direction. Line P1-Q1 was drawn directly opposite to P-Q on the reverse side. Lines

Chapter Five: Investigation into grain boundaries in g.o. Silicon Iron

RS and R1S1 were also drawn in the same manner but along the transverse direction of the specimen.

Distances (in millimetres) of visible grain boundaries were measured from P to Q, with P considered as reference point. This process was repeated for P1Q1, RS and R1S1. The results are shown in table 1. The double arrowed lines point to what are probably the positions of the individual boundaries on opposite side of the sample. Obviously if large angles of inclination are present, a given grain boundary could emerge at the opposite surfaces displaced by 1mm or more so the links in table 1 are only postulations. It is interesting however that along the lines RS/R1S1 the inclination angles appear to be all close to 90° to the sheet plane.

Table 1: Positions of grain boundaries along arbitrary paths parallel (PQ and P1Q1) and perpendicular (RS and R1S1) to the rolling direction.

<i>Boundary</i>	<i>Line PQ (mm)</i>	<i>Line P₁Q₁ (mm)</i>	<i>Line RS (mm)</i> <i>(Ref. Point – R)</i>	<i>Line R₁S₁ (mm)</i> <i>(Ref. Point – R₁)</i>
1	3.8	7.0*	0.1	2.1*
2	4.9	8.5	1.7*	10.7*
3	7.3*	8.9	10.6*	18.6*
4	9.4*	9.1*	11.0	25.6*
5	10.0*	10.5*	18.8*	28.5
6	16.3*	11.0	25.7*	32.5*
7	23.7*	12.2	28.3	
8	27.7*	14.5	32.8*	
9	30.5	17.3*		
10	32.8	21.3*		
11	34.0	28.7*		
12	34.5	35.0		
13	35.9*	35.6*		
14	36.1	37.7		
15	36.5	40.1		
16	38.0	41.2		

A 10mm x 10mm x 0.23mm square was cut from the sample shown in figure 5.2 by guillotine and polished using standard metallurgical preparation method. It was set on edge, supported with cold setting mount material to harden. It was etched in 3% nitric acid in alcohol (nitol) to reveal the boundaries along the edge of the sample.

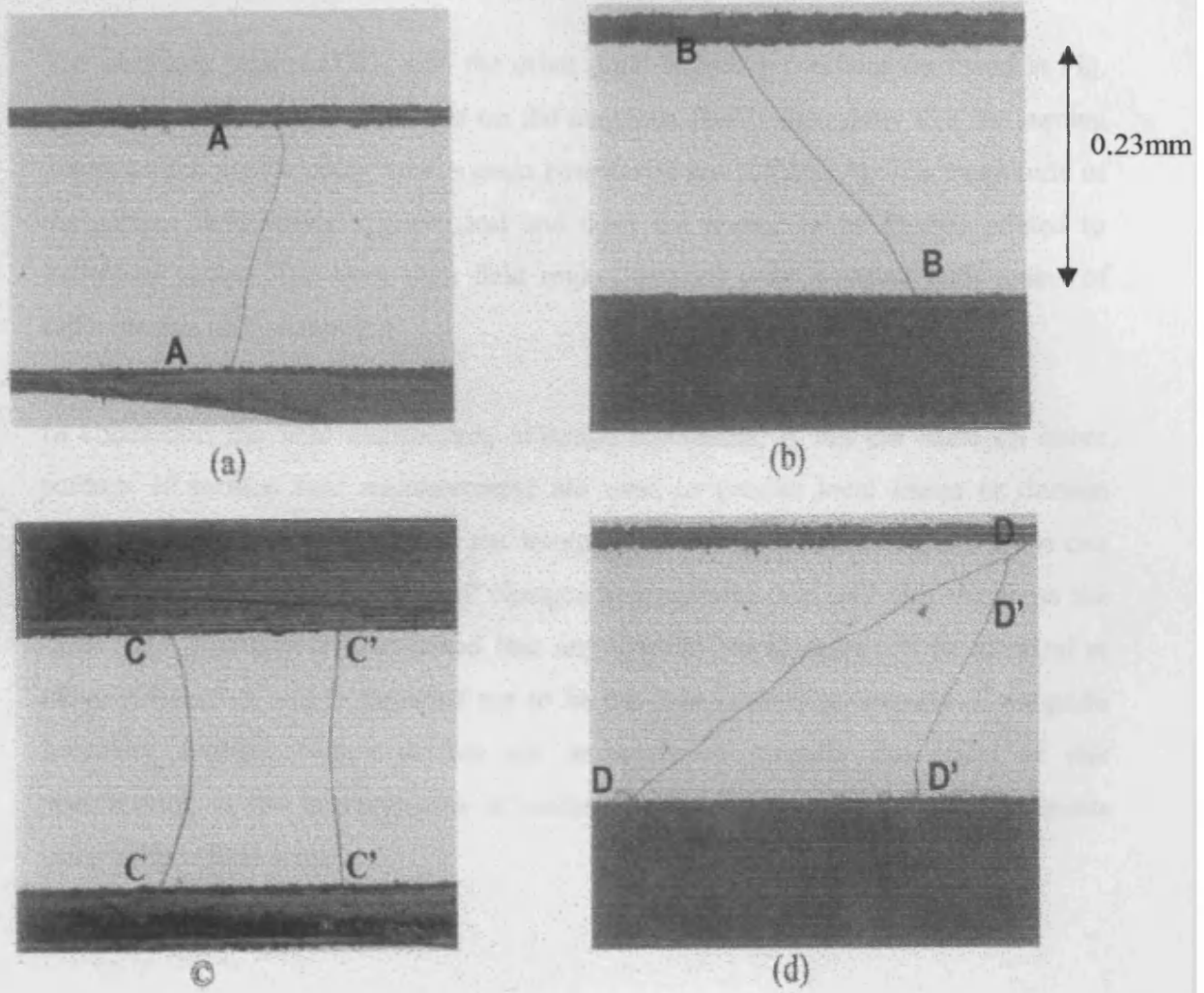


Fig.5.7 Micrographs showing typical grain boundary profiles through the thickness of a sheet of grain oriented steel [5.5].

Images obtained are shown in figure 5.7. Typical walls are inclined at angles from 89° to 26° degrees to the sheet surface. Figure 5.7(d) shows the case of a grain visible from only one surface.

5.5 Summary of results.

The distances between DD1 and the other grain boundary positions (arrowed in Fig. 5.5), compared with the distances on the magnetic field profile show that the turning points on the profile occur where grain boundaries are visible[5.4]. The magnitude of the surface field varies a great deal and does not appear to be directly related to individual grains. The very high field region extends over a region with grains of different size and orientation.

In conclusion the field distribution, although repeatable, is not the same on either surface. If surface field measurements are used to predict local losses or domain structures then care is needed in the interpretation of the results obtained from one side of a sheet only because small changes in tangential field will also occur on the other side. Normally it is assumed that any specific bar domain will be identical at either surface but this is expected not to be the case in practice because of the grain boundary profiles. Future studies are necessary to quantify the effect of this phenomenon in the interpretation of surface or bulk properties of electrical steels using surface field sensors.

5.6 References

- [5.1] H. Pfutzner (1980), "Computer mapping of grain structure in coated silicon iron", *J. Magn. Mag. Mat.* (1980), 19, p. 27.
- [5.2] H. Pfutzner, G. Schwarz and J. Fidler (1983), "Computer control domain detector", *Jpn. J. Appl. Phys.*, 22, p. 361.
- [5.3] K. Mohri and T. Fujimoto (1977), "New grain detection methods for grain oriented SiFe with coating", *Mem. Kyushu Inst. Technology*, 7, p. 33.
- [5.4] M. H. So, P. I. Nicholson, T. Meydan and A. J. Moses (1995), "Magnetic domain imaging in coating SiFe using magnetoresistive sensors", *IEEE Trans Mag.* 31, (6), p. 3370.
- [5.5] A. J. Moses and S. N. Konadu (2000), "Some effects of grain boundaries on the field distribution on the surface of grain oriented electrical steels" *IJAEM*, vol.13, 1-4, p. 339.

CHAPTER SIX

OBSERVATION OF DOMAIN / GRAIN BOUNDARIES USING MAGNETIC FORCE MICROSCOPY.

6.1 Introduction

Scanning probe microscopy (SPM) has been found to be among the most powerful tools for surface metrology of our time; measuring surface features whose dimensions are in the range from inter-atomic spacings (10^{-10} m) to tenths of a millimetre (10^{-4} m), and they have been used to map the properties of surfaces of various materials.

Although, initially scanning probe microscopes (SPMs) were used to study surface topography, they are now employed to measure other surface properties such as magnetic quantities. With the advent of magnetic force microscopy (MFM), otherwise called magnetic force imaging, which can operate in air whilst maintaining atomic resolution, there now exists the possibility of quick, simple, accurate and precise measurements of magnetic quantities even in complex structures.

The measurements in all SPMs are based on a sharp probe (or “tip”) of silicon nitride, which is raster scanned over the surface of a sample. The interaction between the tip and the sample is used to build up the image and may take the form of forces as the two come into close contact, or of electrical currents passing between them. By oscillating the tip, magnetising it or even attaching different chemical species to it, many different types of interaction can be examined and all with extremely high spatial resolution.

Chapter Six: Observation of domain/grain boundaries using the MFM

MFM, being a non-destructive technique of measurement, does not require any special sample preparation, and this makes it an attractive choice. All that is essential is a flat surface to enable the probe to be in very close proximity to the sample.

Terms frequently used in magnetic force microscopy includes atomic force microscopy (AFM), magnetic force microscopy (MFM), tapping mode (TM), scanning tunnel microscopy (STM), electric force microscopy (EFM), lateral force microscopy (LFM) and scanning capacitance microscopy (SCM).

It has been shown in previous work that the MFM system is capable of detecting the presence of a domain wall or grain boundary [6.1]. The system was used to scan the surface of a magnetic film along the direction of x , over the interval between 0 and 1600 Å as shown in Figure (6.1). The vertical distance between the tip (needle) and the sample was 100 Å.

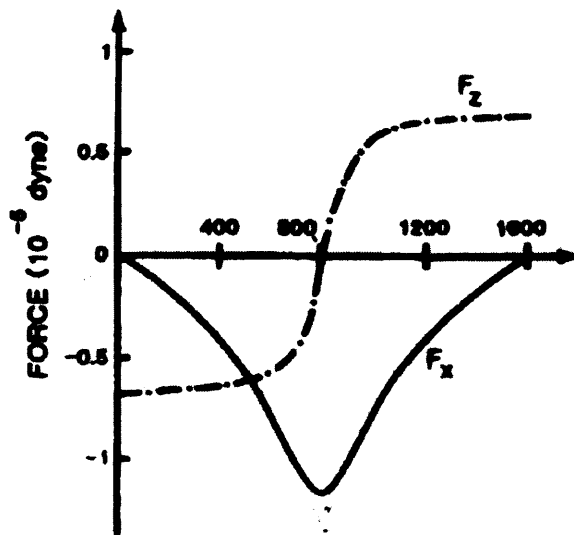


Fig. 6.1 Horizontal and vertical components of force versus tip position along x . The sample has perpendicular magnetization with the straight Bloch wall at $x = 800\text{Å}$. [6.1]

Chapter Six: Observation of domain/grain boundaries using the MFM

The forces F_x and F_z are calculated or obtained as the needle moved. It was noted that the peak of F_x and the zero-crossing of F_z occur at the wall centre.

Similarly, Takekuma et al concluded that there are magnetization fluctuations not detectable by the conventional analysis, and proposed a new evaluation parameter based on the variance profile which can quantitatively analyse the magnetisation fluctuation as shown in figure (6.2).

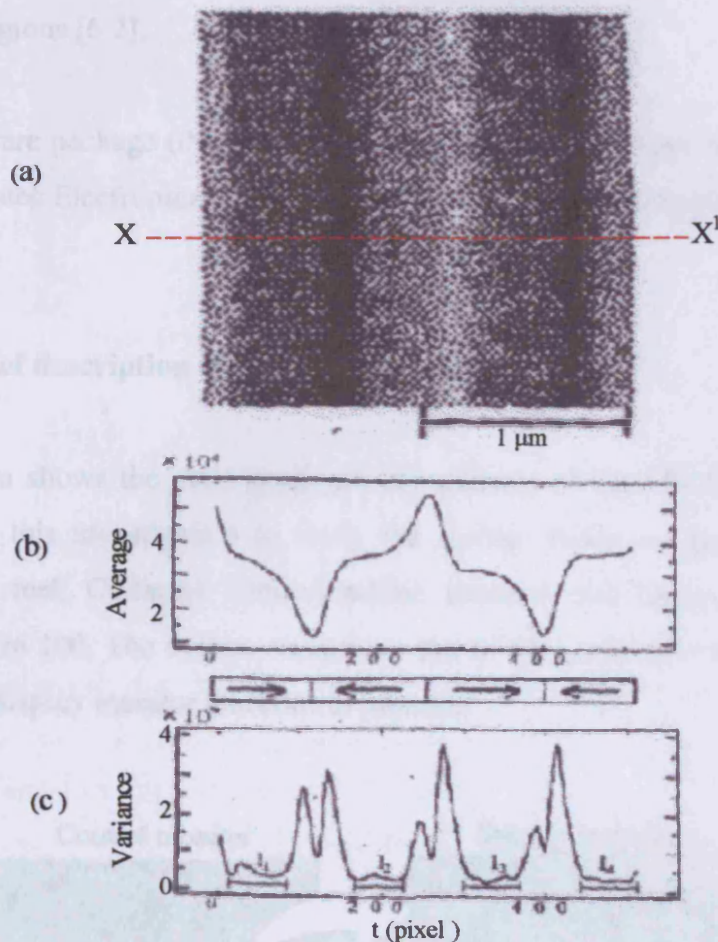


Fig.6.2: (a) An MFM image of a recorded medium (Co-13Cr-6Ta-4Pt)
(b) Average profile and
(c) Variance profile determined from (a), where $t = 1, \dots, 512$,
and $512 \text{ pixels} = 2 \mu\text{m}$. After [6.2]

Chapter Six: Observation of domain/grain boundaries using the MFM

Figure 6.2 shows the average and the variance of the MFM image of a recorded medium (recorded at 1.97 Mfm^{-1} , (Mega flux changes per metre)). The average profile shown in figure 6.2(b) is the same as the profile produced by the conventional MFM analysis. However, from the variance profile of the MFM signals across the track direction, figure (6.2b), it can be observed that the minimum values; I_1, I_2, \dots , are sandwiched by two peaks which occur at each transition region. Since the peaks appear only at the transition regions, it can be predicted that the variance profile has relation to the magnetization fluctuations in these regions [6.2].

A software package (the WSxM scanning probe microscopy software), developed by Nanotec Electronica [6.3] was used for a similar investigation in this work.

6.2: Brief description of the MFM system.

Fig. 6.3a shows the main hardware components of the MultiMode SPM system used in this investigation to study the surface fields on grain oriented 3.25% silicon steel, Cu-based nanocrystalline material and nickel iron alloy W597 Vacoperm 100. The system comprises: the SPM, controller, computer, keyboard, mouse, display monitor and control monitor.

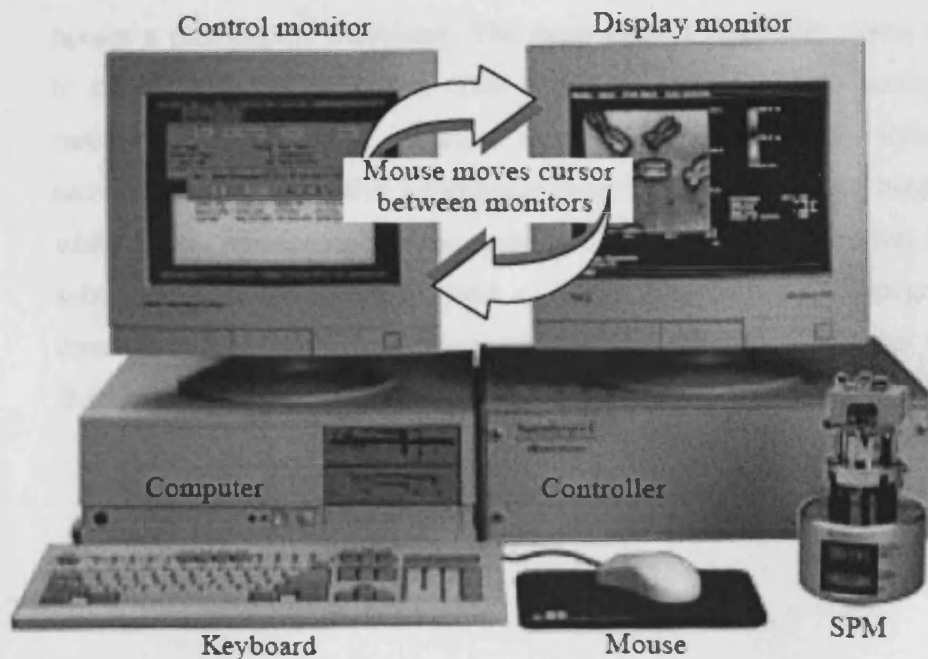


Fig. 6.3a. Multimode Scanning Probe Microscopy system.
Hardware showing the major components (After [6.4]).

Chapter Six: Observation of domain/grain boundaries using the MFM

By the movements of the mouse, the cursor is automatically transferred from one monitor to the other. This makes it easy for the operator to handle the scanning programme, seamlessly switching between the control functions on one monitor and the display functions on the other. Fig. 6.3b shows the system in the Physics and Astronomy department of Cardiff university where this work was carried out.

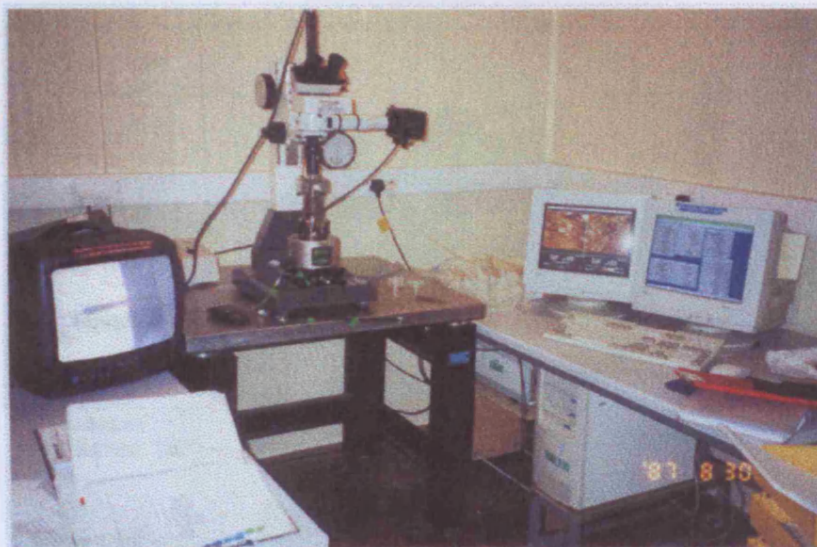


Fig. 6.3b. Multimode Scanning Probe Microscopy system used for this work.

The Scanning Probe Microscope (SPM), in which the scanning and the other measurements were carried out is as shown in Fig. 6.4. There are two main components of the system; the scanner and the detection system. The scanner houses a piezoelectric transducer. The piezo element physically moves the sample in the X, Y and Z directions. This is a two-part, proprietary surface imaging method which consists of a surface scan to obtain height data, followed by a second scan to extract other information about the surface (such as magnetic field) while the tip profiles the previous path at a constant height. The two images are subtracted from each other to yield an image uninfluenced by topography. The detection system consists of a laser which generates a spot of light that is reflected from a micro-fabricated cantilever onto a mirror and finally into a photodetector.

Chapter Six: Observation of domain/grain boundaries using the MFM

This instrument uses a semiconductor diode laser emitting a maximum 1.0 mW beam at 670 nm. The light is emitted downward and normally reflects back into the system's optics from the back of the cantilever probe. The position of the spot is determined by circuitry which generates a voltage from the difference between the photodiode segments. The circuit outputs a voltage ranging from +10V to -10V depending on the position of the spot on the two photodiodes.

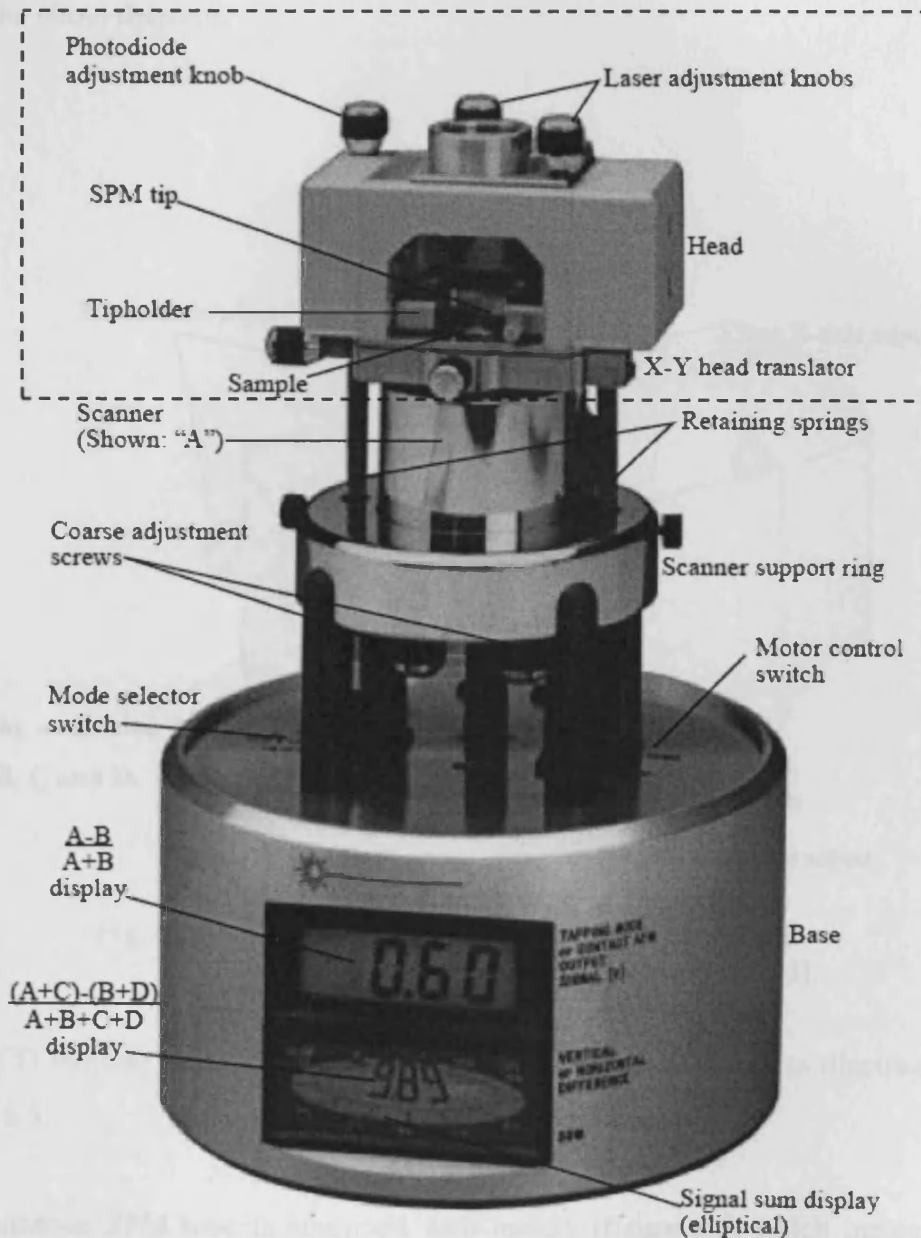


Fig. 6.4 The Multi-mode Scanning Probe Microscopy (SPM) (After [6.4])

Chapter Six: Observation of domain/grain boundaries using the MFM

The head, also shown in figure 6.5(a), houses the tip holder, the mirror, the cantilever, the laser, the tilt mirror, etc. The middle section which links the head to the base, accommodates the scanner tube and also supports the head.

Figure 6.5(a) shows a Multimode scanning probe microscopy (MM-SPM) head with various adjustment knobs. The major components in the head are as numbered: (1) laser, (2) the mirror, (3) the cantilever (probe), (4) the tilt mirror and (5) the photo detector.

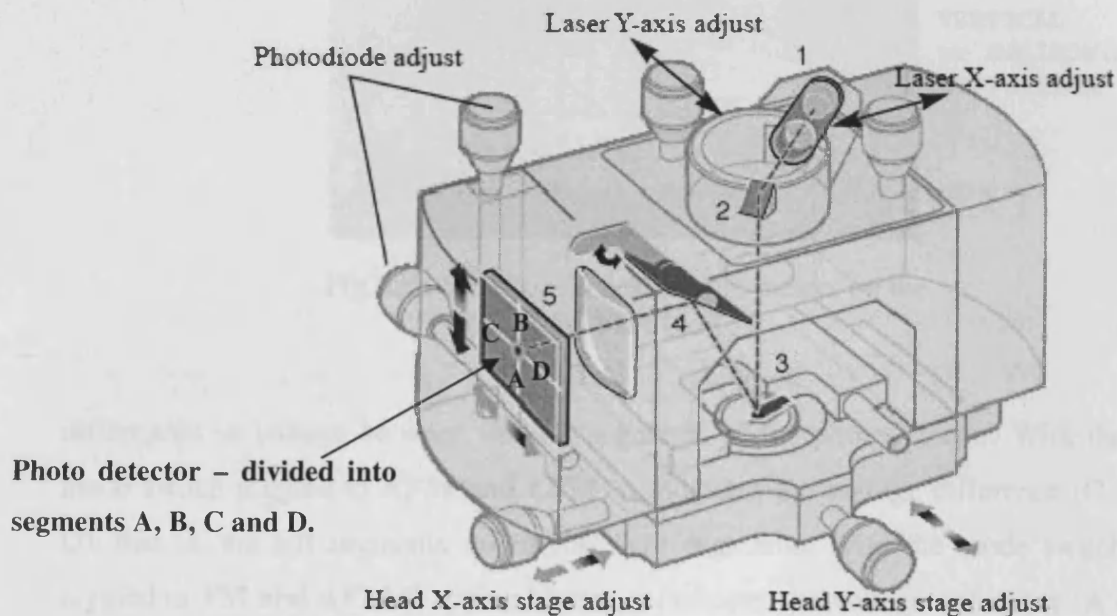


Fig. 6.5: Multimode Scanning Probe Microscopy head Hardware showing the major components [6.4].

AB and CD indicate the vertical and lateral deflections respectively as illustrated in figure 6.5.

The MultiMode SPM base is equipped with meters (figure 6.6) which indicate voltage coming from the four-segment photodetector.

Chapter Six: Observation of domain/grain boundaries using the MFM

The elliptical (SUM) meter 1 indicates the total voltage generated by the photodetector. That is, the combined voltage of photodetector segments. This is displayed during all modes (except STM when all meters are off). The bottom digital meter 2 reads

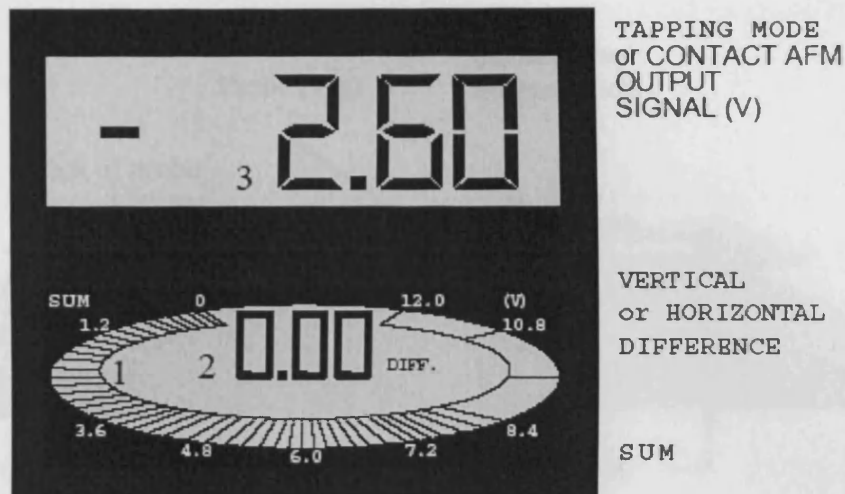


Fig. 6.6: SPM's voltages and the meters on the front of the base [6.4]

differences in voltage between various segments of the photodetector. With the mode switch toggled to **AFM and LFM**, it indicates the voltage difference (C - D), that is, the left segments minus the right segments. With the mode switch toggled to **TM and AFM** (Tapping Mode), it indicates the voltage difference (A - B), that is, the bottom segments minus the top segments. The topmost digital meter 3 indicates the output signal of the SPM depending upon the mode selected. When the mode switch is toggled to **AFM and LFM**, the topmost meter reads the (A - B) voltage difference. On the other hand when the mode switch is toggled to **TM AFM** the topmost meter reads the rms voltage [6.4]

The head and attached X-Y stage are kinematically mated to the scanner via three contact points. A pair of retaining springs hold down the head, allowing it to be raised and lowered using adjustment screws threaded through the scanner body.

6.2.1. Magnetic Force Imaging Overview

There are two main modes of scanning: the LiftMode and the TappingMode. MFM imaging utilizes the Interleave and LiftMode procedures as illustrated in figure 6.7.

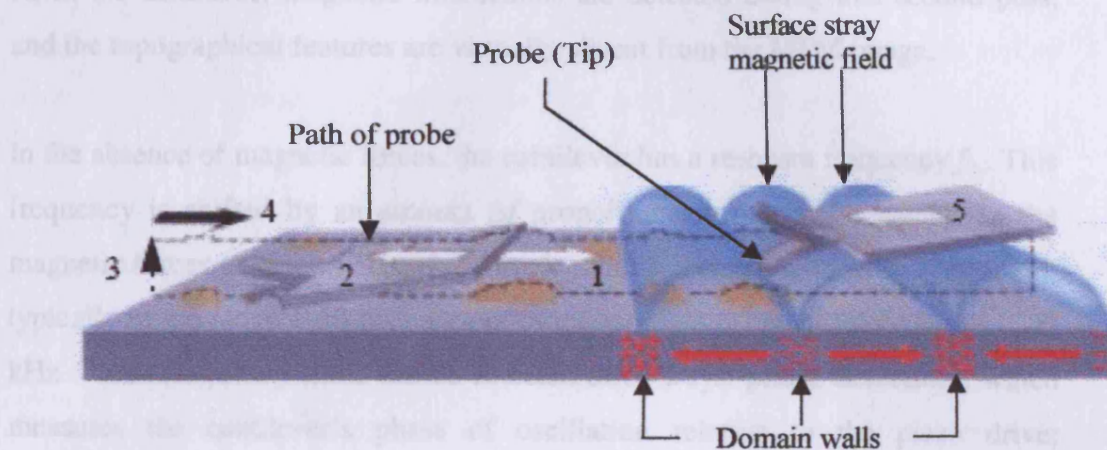


Fig. 6.7 The MFM LiftMode principles. [6.4]

A tapping cantilever equipped with a magnetic coated tip is first scanned over the surface of the sample to obtain topographic information. The **LiftMode** allows the imaging of relatively weak but long-range magnetic interactions while minimizing the influence of topography (figure 6.7). Measurements are taken in two passes across each scanline; each pass consists of one trace and one retrace. In the first pass, topographical data is taken in TappingMode on one trace and retrace. The tip is then raised to the lift scan height and a second trace and retrace performed while maintaining a constant separation between the tip and local surface topography. Magnetic interactions are detected during this second pass.

After the topographical data is taken in TappingMode on one trace and retrace in the first pass, the tip is raised just above the sample surface (between 10-200nm). It is advisable to raise it to 50nm and then lower it down to about 25nm. The

Chapter Six: Observation of domain/grain boundaries using the MFM

surface topography is scanned while being monitored for the influence of magnetic forces. These influences are measured using the principle of force gradient detection. Thus, on the first trace (1) and retrace (2), as shown in figure 6.7, the cantilever traces surface topography. The cantilever then ascends to a height called the Lift Scan Height (3) maintaining a constant separation between the tip and local surface. Then on the second trace (4) and retrace (5), the lifted cantilever profiles the topography while responding to magnetic influences. That is, in the LiftMode, magnetic interactions are detected during this second pass, and the topographical features are virtually absent from the MFM image.

In the absence of magnetic forces, the cantilever has a resonant frequency f_0 . This frequency is shifted by an amount Δf proportional to vertical gradients in the magnetic forces on the tip. The shifts in resonant frequency tend to be very small, typically in the range 1-50 Hz for cantilevers having a resonant frequency $f_0 \sim 100$ kHz. These frequency shifts can be detected three ways: **phase detection**, which measures the cantilever's phase of oscillation relative to the piezo drive; **amplitude detection**, which tracks variations in oscillation amplitude; and **frequency modulation**, which directly tracks shifts in resonant frequency. **Phase detection** and **frequency modulation** produce results that are generally superior to **amplitude detection**.

Best results are normally obtained with Digital Instruments' Extender™ Electronics Module. This hardware unit allows phase detection and frequency modulation for optimal MFM imaging.

The sample and mode of SPM to be performed dictate the choice of tip and tipholder. The Probes which are made from tungsten or platinum indium alloy wires are cut or etched to produce sharp tips at one end. Other technologies have been developed recently by which tips with high resolutions are manufactured[6.5].

Chapter Six: Observation of domain/grain boundaries using the MFM

Most SPM work is done using cantilevered probes. These consist of a flexible cantilever extending from a rigid substrate, to which a tip has been attached. The MFM probe is crystal of silicon having a magnetic coating on the tip. As the magnetized tip oscillates through magnetic fields on the sample surface, it modulates the cantilever's phase and frequency. These are monitored, providing a measure of magnetic field strength and providing images of magnetic domains.

The circuit outputs a voltage ranging from +10V to -10V depending on the position of the spot on the two photodiodes. The feedback loop moves the sample in the vertical direction (Z) to restore the spot to its original position.

6.2.2. Scanning Resolution

The most important parameter affecting imaging resolution is the Lift scan height. The range of 10–200 nm is most useful. In general, MFM resolution is roughly equal to the lift height: smaller Lift Scan heights give better resolution; conversely, magnetic features smaller than the Lift Scan height may not be resolved. The tip also experiences stronger fields close to the surface, giving improved signal-to-noise ratios. The resolution of my work was 50nm.

6.2.3. Scanning sensitivity

The relationship between setpoint voltage and oscillation amplitude is known as the sensitivity. Its value can be determined by Force Calibration. For 225 μm MFM cantilevers, the sensitivity is typically in the range 15-20 nm/V. A 1V Setpoint typically corresponds to the mean tip - sample distance (h_T) ~15-20 nm.

6.3. Experimental procedure

The Multi-mode Scanning Probe Microscopy (SPM), shown in figure 6.4, is the instrument or component of the system which houses the sample under investigation as well as the tip (probe), and all the scanning processes take place in it.

The sample and mode of SPM to be performed dictate the choice of tip and tipholder. For example, if contact AFM is to be used for imaging, a silicon nitride cantilever mounted in a standard tipholder is the better choice. In this investigation, silicon tips coated with CoCr thin films were used.

Each sample used should not measure more than 10 mm by 10 mm to fit the top of the scanner tube and should be less than 8 mm in thickness. The top of the sample should protrude not more than a few millimeters above the top of the head's X-Y translation stage. All the specimen used in this investigation were cut to 10 mm by 10 mm and all the measurements were carried out under room temperature.

To load the sample, the head of the SPM (figure 6.5) was gently removed. This exposed the top of the scanner tube. The sample puck was mounted with the calibration standard on top of the scanner tube. An internal magnet held the puck down. After securing the sample in this chamber, the head was carefully fitted back. On average, each scanning process took about twenty minutes to complete. The scanning process was repeated three times for each sample and the results were averaged. A feedback system used to control tip-sample interactions and render images was optimized for each new sample. This was accomplished by adjusting various gains in the SPM's feedback circuit.

6.4 Results and discussion.

6.4.1 Magnetic film (metal evaporated tape)

Figure 6.8 shows an output of an MFM scan of a magnetic film. The surface topography of the material is as shown in figure 6.8(a), while figure 6.8(b) illustrates the magnetic force gradient “phase” image obtained. The scanned area was $5 \mu\text{m} \times 5 \mu\text{m}$, and it was performed at a resolution of 100nm (lift scan height).

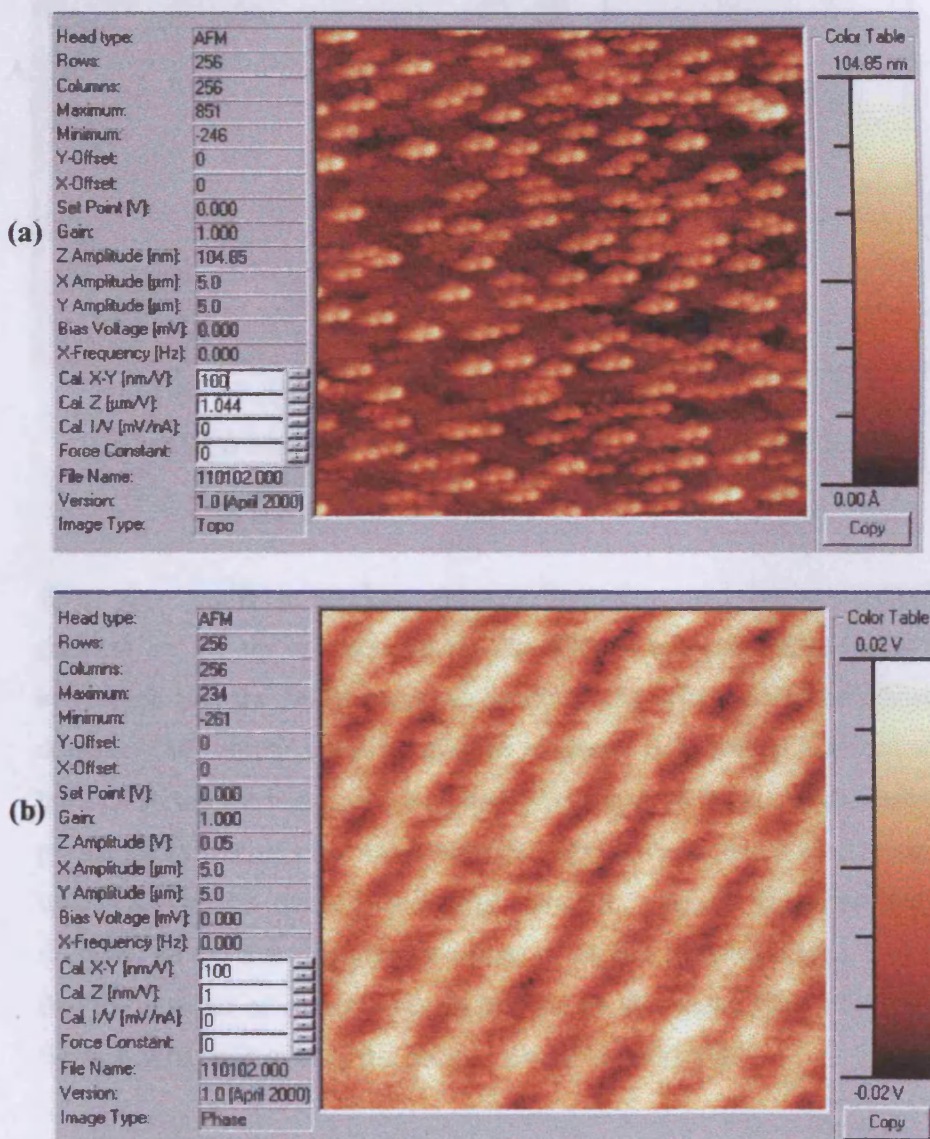


Fig. 6.8: The output of an MFM scan of a metal evaporated NiCo tape showing:
 (a) The surface topography of the sample and,
 (b) The “Phase” magnetic field activities at the surface of the material –

It can be observed that greater magnetic field activity occur in some regions (lighter areas) than others (darker regions) but no correlation has been found with bulk domain structures. The alternating dark and light shades or “stripe domains” in figures 6.8(b) and 6.9(a) represent the recorded magnetic information.

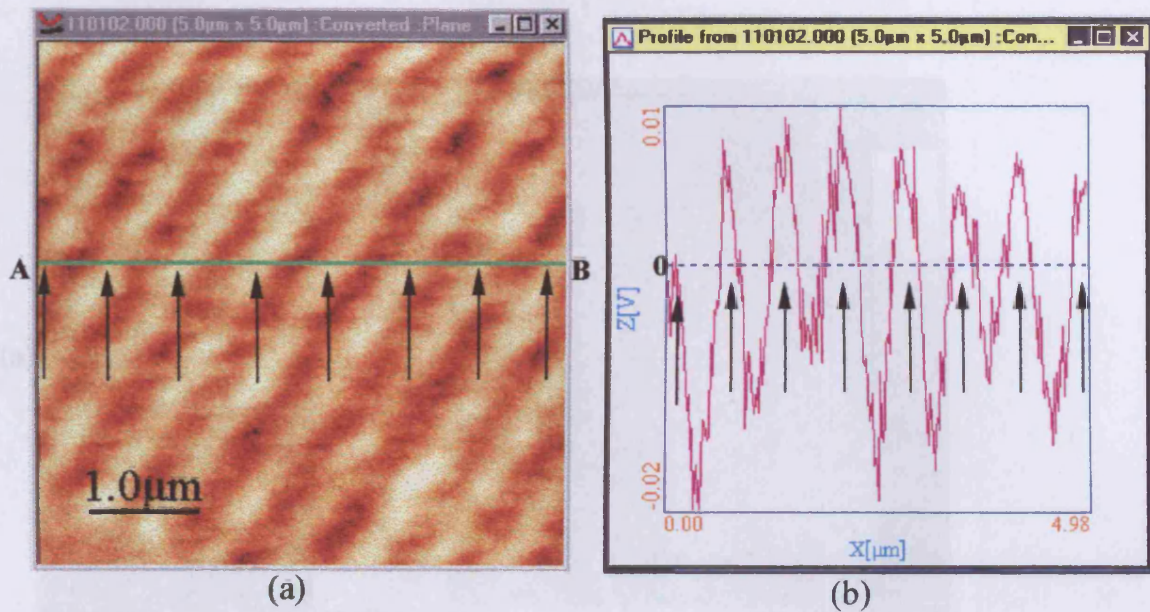


Fig. 6.9:(a) Magnetic force gradient image of metal evaporated tape Scanned at 100nm Lift scan height (resolution). (b) and the magnetic field profile along the line AB.

They also signify a varying resonant frequency, and hence magnetic force gradient on the tip or probe [6.6]. The SWxM analysis software was used to investigate into the MFM image in figure 6.9(a), which could be related to the domain (180° Bloch) walls. Firstly, the magnetic field profile obtained along the line AB across the image was then observed (figure 6.9(b)). An alternating signal profile about the zero line was observed. Arrows were then placed in the regions where the line AB crossed the lighter coloured “stripes”. The same process was followed for the corresponding positions or regions in figure 6.9(b). It can be seen that the number of arrows in both images are the same. Also all the arrows in figure 6.9(b) point to only the positive peaks of the profile.

6.4.2 Nickel Iron

The MFM images of a Nickel Iron (W597 Vacoperm 100) specimen are as shown in figure 6.10. The scanned area was $5\mu\text{m} \times 5\mu\text{m}$. Figure 6.10a shows the topographical image, while 6.10b. shows the “phase” image.

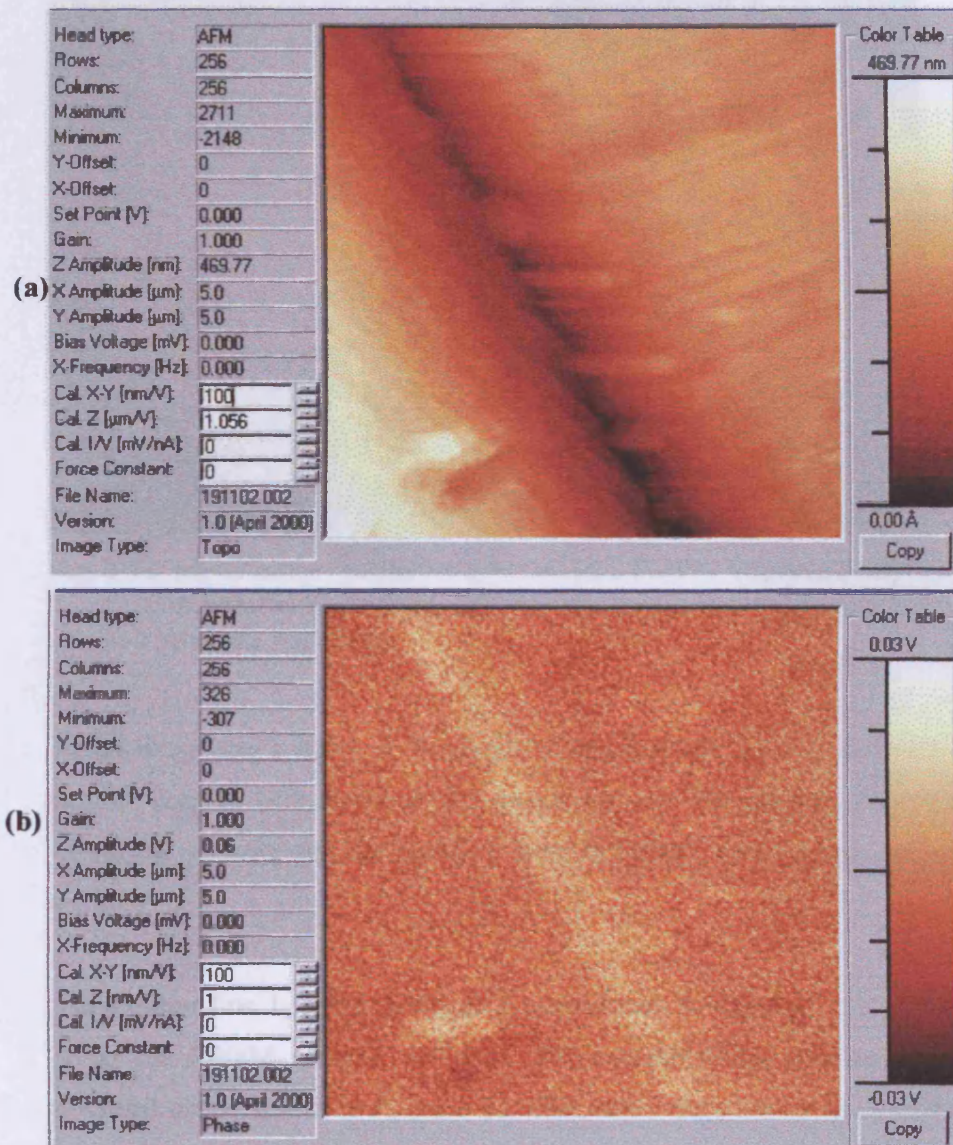


Fig.6.10: MFM image of a Nickel Iron (W597 Vacoperm 100) material.
 (a) Surface topography.
 (b) Magnetic field “Phase” image.

Chapter Six: Observation of domain/grain boundaries using the MFM

Figure 6.11 illustrates a 3-dimensional view of the “phase” image. The base is added just to enhance the image.

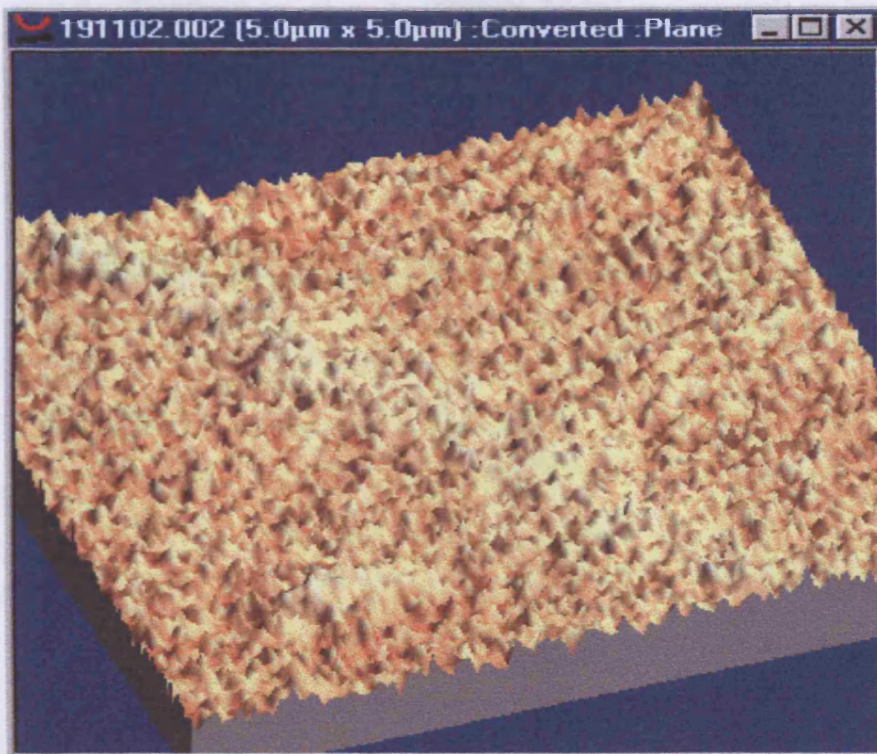


Fig. 6.11: MFM image “phase” of a Nickel Iron (W597 Vacoperm 100) material in 3-dimensional view. The base was provided just to enhance the image.

In this image too, a region is observed running from the top left corner to the right bottom corner. This region in the image was also investigated into by looking closely at variance profiles across it from different points as indicated in figure 6.12.

Three lines; line 1, line 2 and line 3 were drawn horizontally across the region using the SWxM analysis software. The corresponding profiles 1, 2, and 3 obtained are as shown in figure 6.12. There was a sharp rise in each of the signal profiles at any point the lines crossed the region.

Chapter Six: Observation of domain/grain boundaries using the MFM

The observation made from the analysis of the MFM image of the magnetic tape in figure 6.9. was that, positive peaks of the profile appeared at certain identical sections. In this investigation too (figure 6.12), similar positive peaks weresignificantly observed on the structure. Nickel iron materials are known to have small grains sizes (averagely between $10\mu\text{m}$ to $30\mu\text{m}$) [6.8]. Considering the the area scanned ($5\mu\text{m} \times 5\mu\text{m}$), one would have expected to see, at least, two or

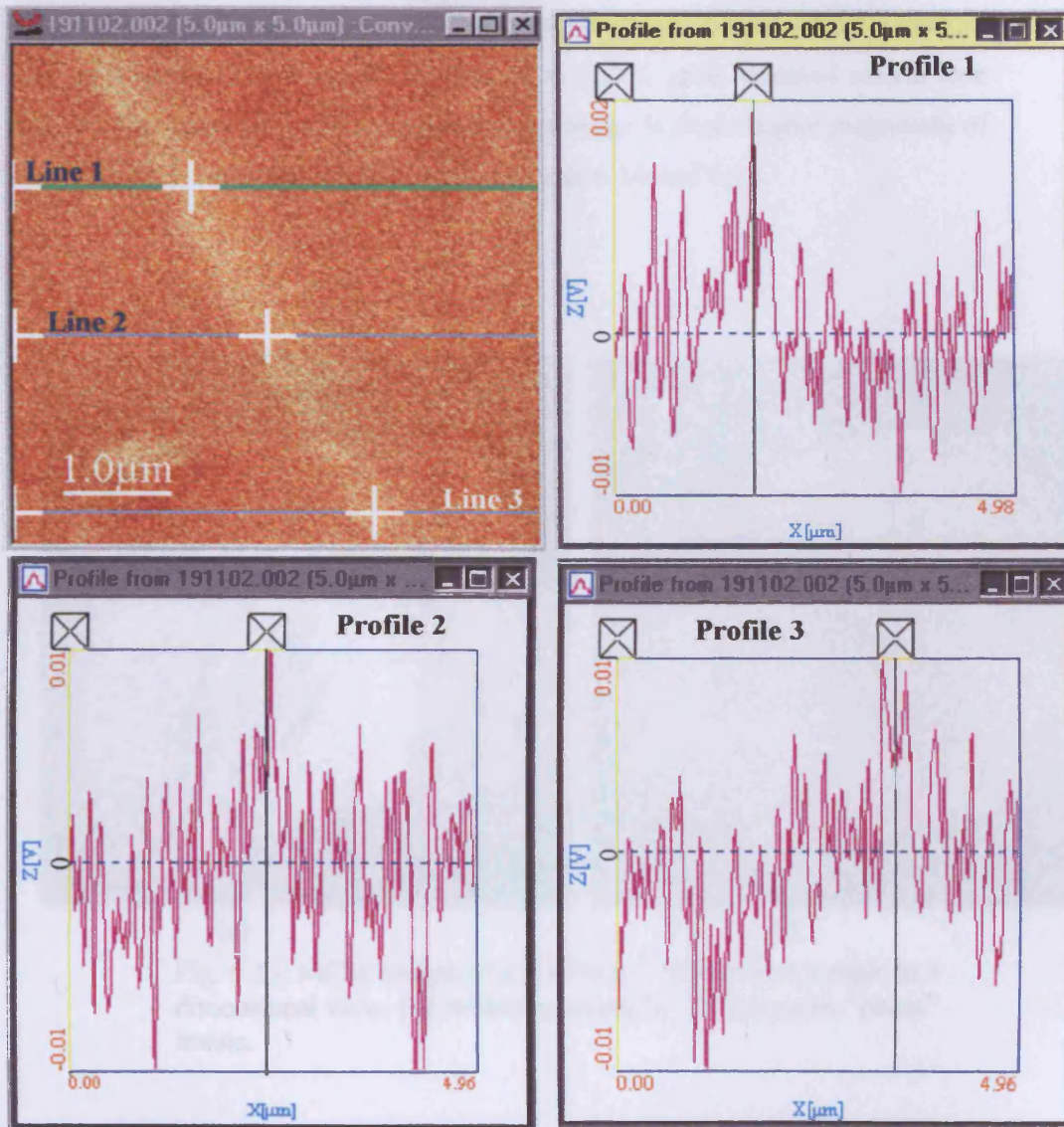


Fig. 6.12: Magnetic field profiles along lines drawn across a structure on a magnetic field image of the surface of a Nickel Iron material (W597 Vacoperm 100) material.

more domains and domain (Bloch) walls. However, only one such structure can be observed from the image. Therefore it is more likely that the structure under investigation is rather a grain boundary.

6.4.3 3.25% grain – oriented silicon iron sample

Figure 6.13: shows the topography and the phase images obtained from a random area of $15\mu\text{m} \times 15\mu\text{m}$ on the surface of a 3.25% grain oriented silicon iron sample. The lighter or whitish colours in the image indicate higher magnitude of magnetic field, and these are indicated in figures 6.14 and 6.15.

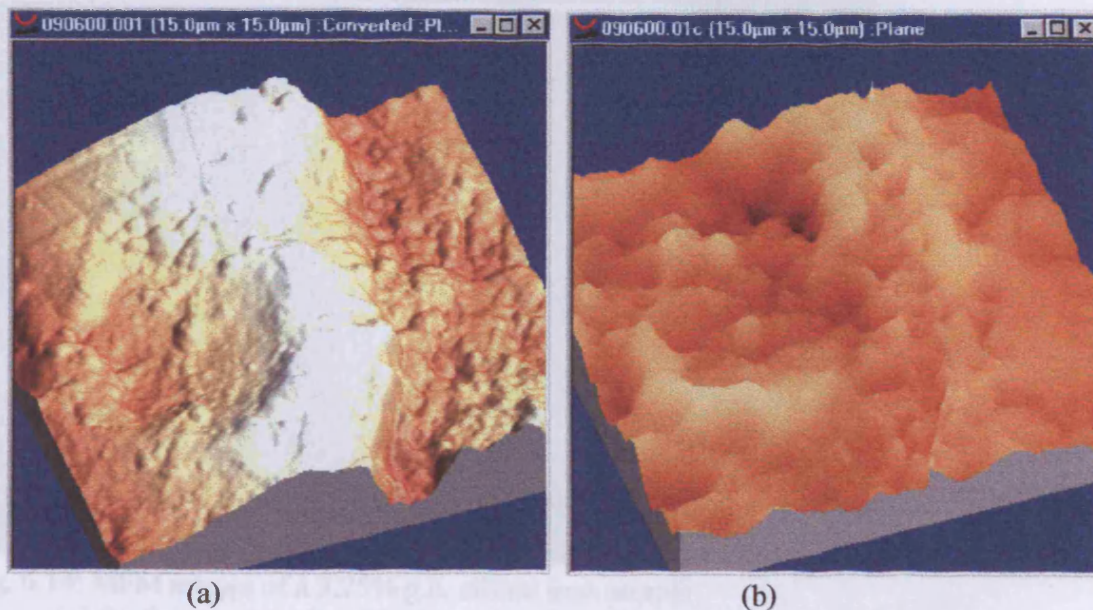


Fig. 6.13: MFM images of a 3.25% g.o. silicon iron sample in 3 dimensional view. (a) surface topography, (b) magnetic “phase” image.

Another region was observed that appears to run from top to bottom of the image.

Chapter Six: Observation of domain/grain boundaries using the MFM

Figure 6.15 shows the region, labelled AB, more clearly from both a single and 3 dimensional views.

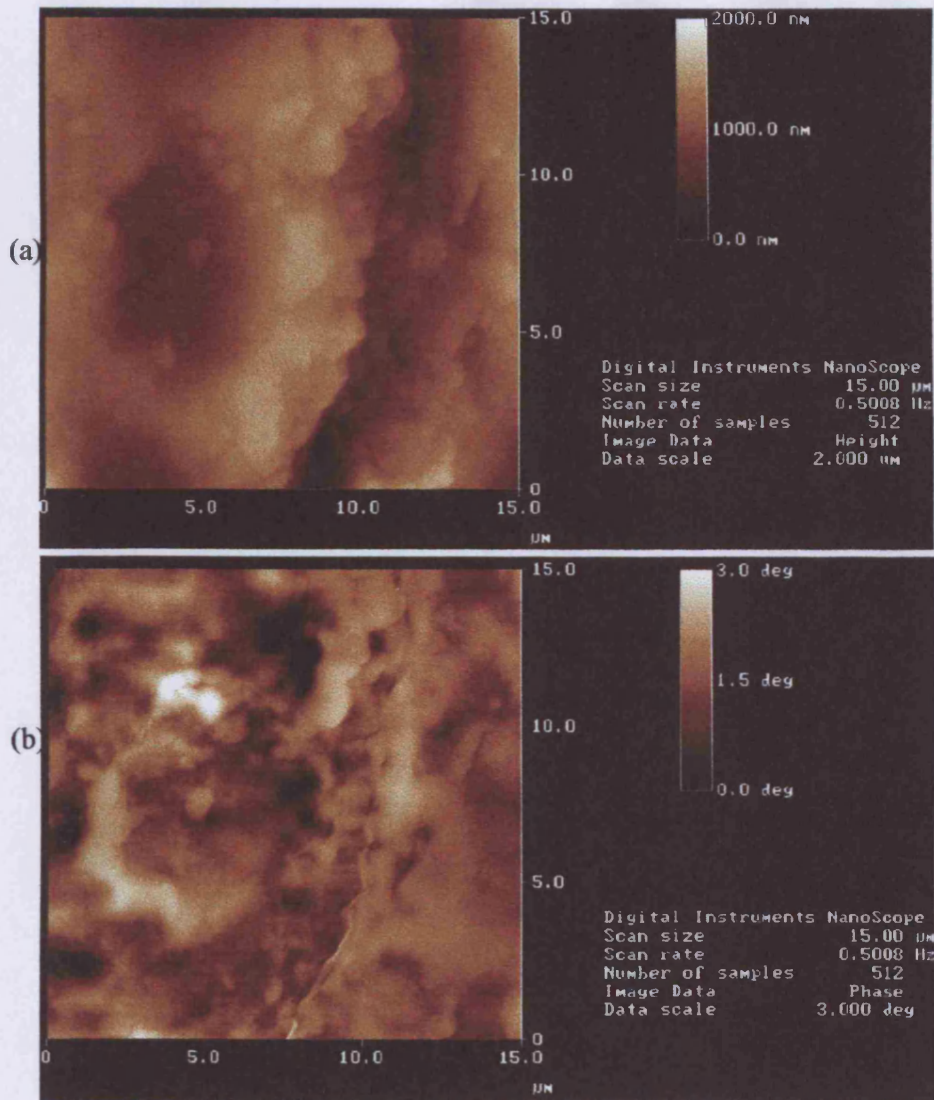


Fig. 6.14: MFM images of a 3.25% g.o. silicon iron sample
(a) Surface topography, (b) Magnetic "phase" image.

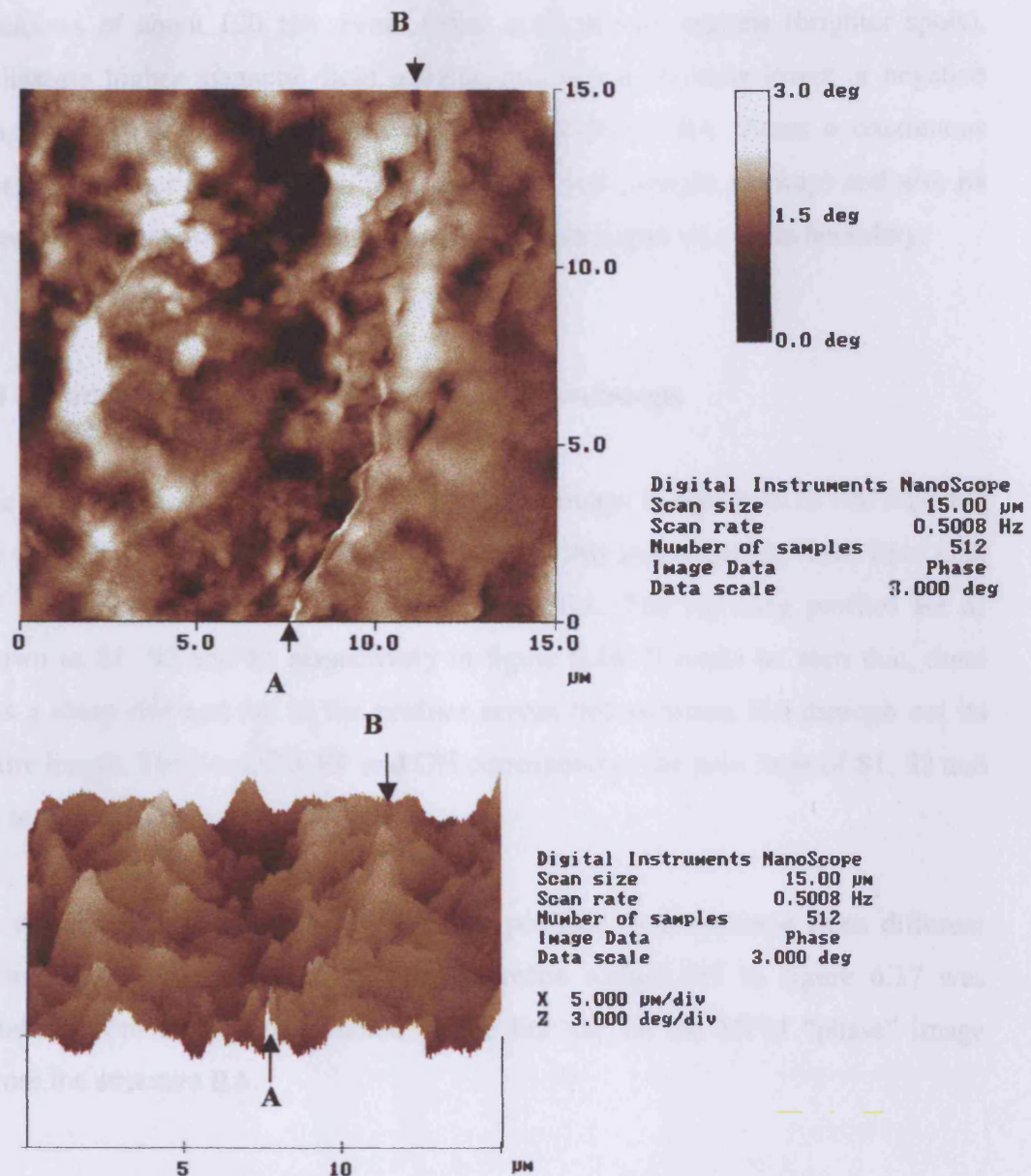


Fig. 6.15: Image of the magnetic surface activities over a 15 mx 15 m area of the grain oriented 3.25% silicon steel. Sample. (a) 2-D image and (b) 3-D image.

The region was measured using the SWxM analysis software. It has an average thickness of about 120 nm. From figure 6.15, certain regions (brighter spots), indicating higher magnetic field activity, and others showing lower or negative magnetic activity could be observed [6.5]. However, BA shows a continuous stretch of higher field activity. Its long stretch (not straight anyway) and also its average thickness of about 120 nm suggests the presence of a grain boundary.

6.4 4. Further investigation into the silicon iron image.

The investigation which was carried out on the image in figures 6.12 was repeated for the MFM “phase” image in figure 6.16. In this investigation, three lines CD, EF and GH were drawn across the structure BA. The resulting profiles are as shown as S1, S2 and S3 respectively in figure 6.16. It could be seen that, there was a sharp rise and fall in the profiles across this structure BA through out its entire length. The lines CD, EF and GH correspond to the zero lines of S1, S2 and S3 respectively

To continue with the investigation, more profiles were obtained from different sections as shown in figure 6.17. The profile named Pf1 in figure 6.17 was obtained from the section denoted by the line OP on the MFM “phase” image across the structure BA.

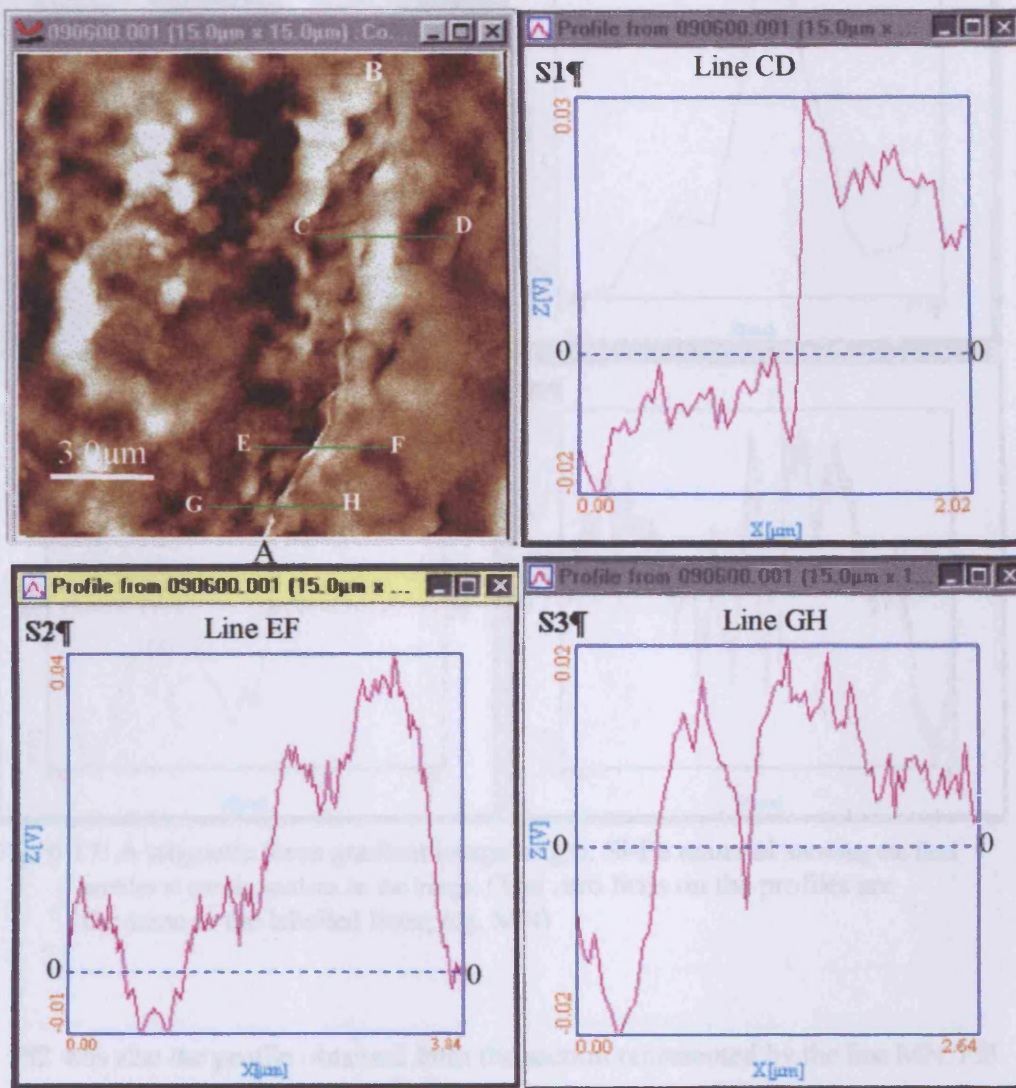


Fig. 6.16: 3.25% G.0. SiFe sample showing magnetic field profiles along lines drawn across a “strip” expected to be a grain boundary.

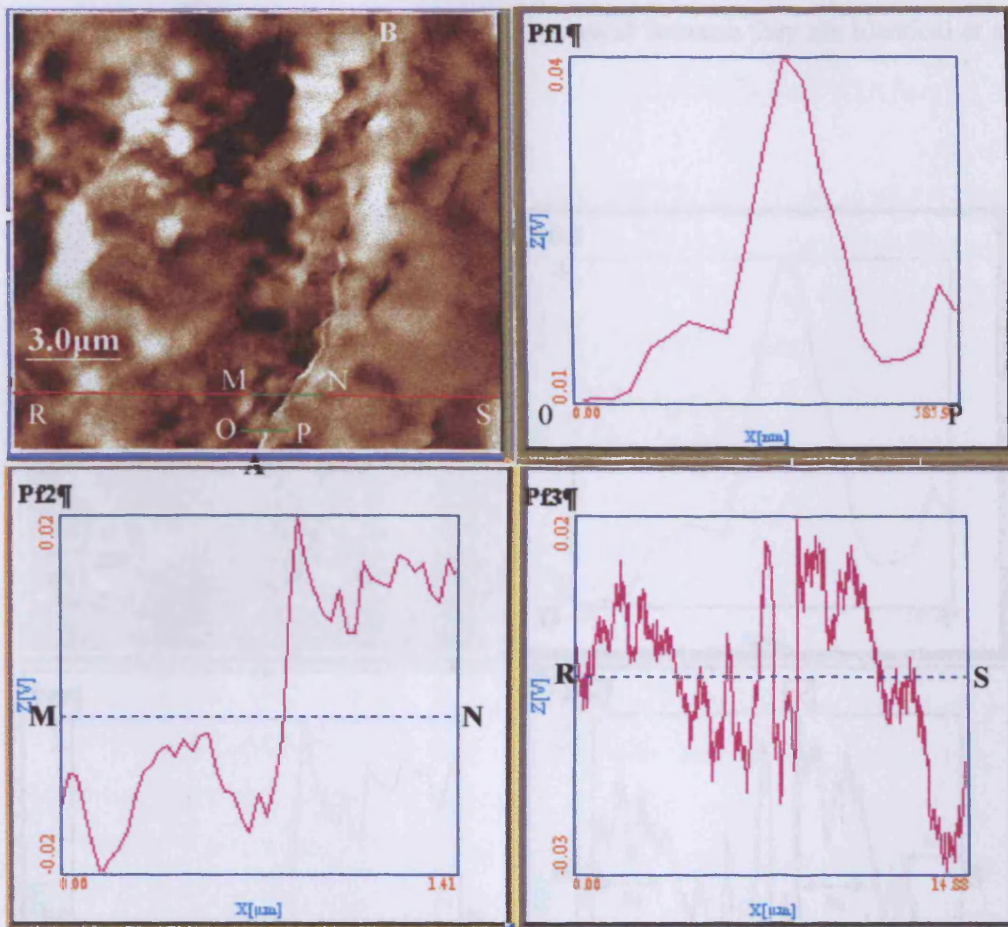


Fig. 6.17: A magnetic force gradient image of g.o. Si-Fe material showing the field profiles at certain sections on the image. (The zero lines on the profiles are the same as the labelled lines; e.g. MN)

Pf2 was also the profile obtained from the section represented by the line MN. Pf3 was the profile obtained from the section represented by the line RS across the image. It could be observed that RS was superimposed on MN. This was to ascertain the validity of the signals; and the idea was to find out if the profile of MN (i.e., Pf2) could be traced in the profile of RS (i.e., Pf3).

Before drawing any conclusion, a further step was taken which is shown in figure 6.18. Using the analysis software, a mark (+) was placed exactly at the point where both MN and RS crossed the structure BA. That point is as indicated by a

Chapter Six: Observation of domain/grain boundaries using the MFM

vertical line (about $9\mu\text{m}$ from the left edge) of the profile Pf3 (figure 6.18). It could be concluded then that the profiles are valid because they are identical at a single point.

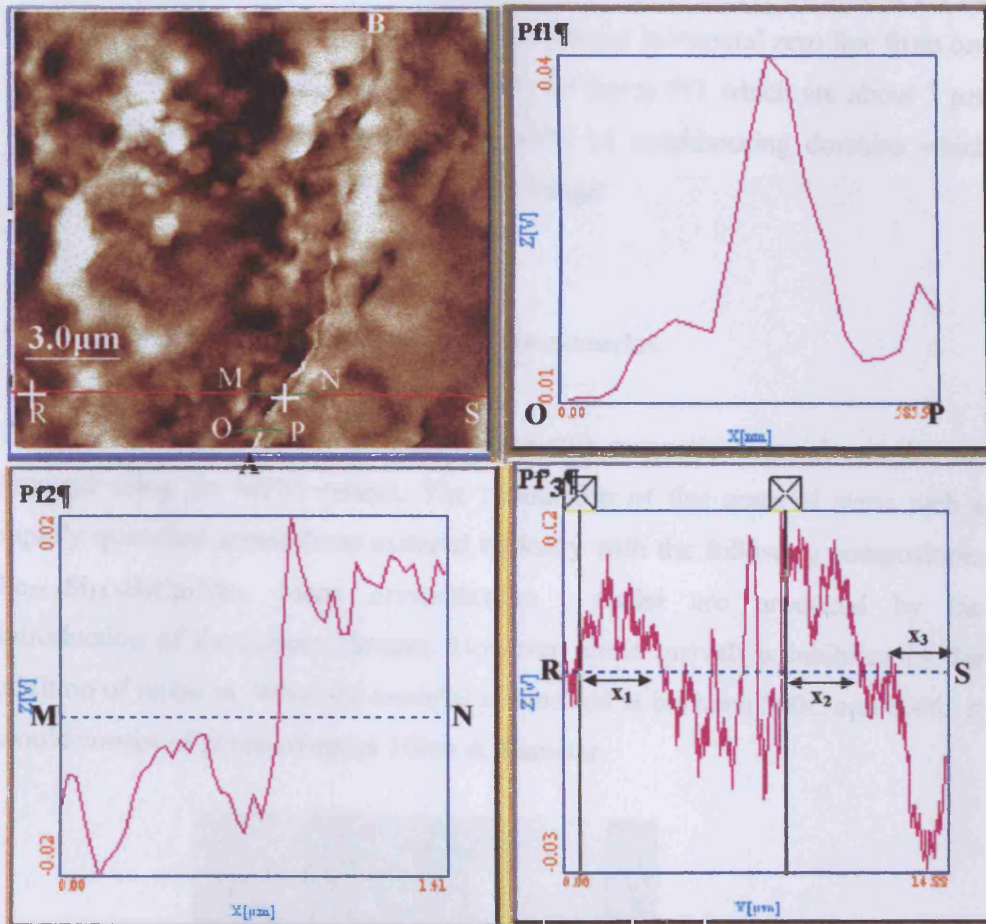


Fig. 6.18: A magnetic force gradient image of a g.o. Si-Fe material showing the field profiles at certain sections across a structure thought to be a grain boundary. (The zero lines on the profiles are the same as the labelled lines; e.g. MN)

From the investigation it could be argued that, the structure BA in the magnetic “phase” image could either represent a domain wall or a grain boundary. However, considering the material under investigation (3.25% g.o.silicon iron) whose domain walls generally have the characteristics of being straight, the curvature in BA is too much more than would be expected. Again, if it was a

Chapter Six: Observation of domain/grain boundaries using the MFM

domain wall detected, then over that area scanned ($15\ \mu\text{m} \times 15\ \mu\text{m}$), at least, another similar wall should have been encountered. For that matter, it could be concluded that the structure is not a domain wall but rather a grain boundary.

Also the signal Pf3 (figure 6.18) and the signal in figure 6.9(b) are similar for the fact that they both repeatedly cross over a common horizontal zero line from one end to the other. The widths; x_1 , x_2 and x_3 of signal Pf3 which are about $3\ \mu\text{m}$ each could then be considered to the width of neighbouring domains which unfortunately are shown clearly seen in the image.

6.4.5: Investigation into a nanocrystalline material.

A FeSiBnbCu (Iron-based) nanocrystalline soft magnetic material sample was scanned using the MFM system. The production of this material starts with a rapidly quenched amorphous material typically with the following composition: $\text{Fe}_{73.5}\text{Si}_{13.5}\text{B}_9\text{Cu}_1\text{Nb}_3$. Many crystallisation nuclei are produced by the introduction of the copper element. However, grain growth is inhibited by the addition of niobium. When the material is annealed at between 500C and 600C , it would consist of grains of about 10nm in diameter.

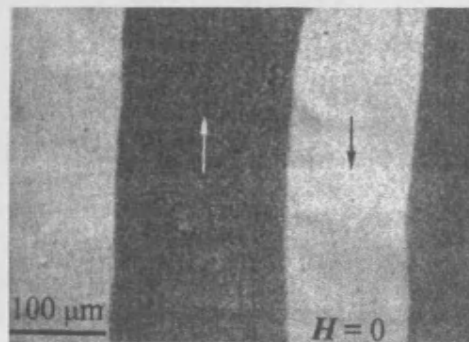


Fig. 6.19: Ordered domain structure on a nanocrystalline soft magnetic material [6.8].

Chapter Six: Observation of domain/grain boundaries using the MFM

Figure 6.19 is a diagram which illustrates an ordered domain structure of a nanocrystalline soft magnetic material. Figures 6.20 and 6.21 are MFM images obtained after scanning two samples of the same nanocrystalline material. In both cases, images (a1) and (b1) are surface topography obtained while (a2) and (b2) are the “phase” images.

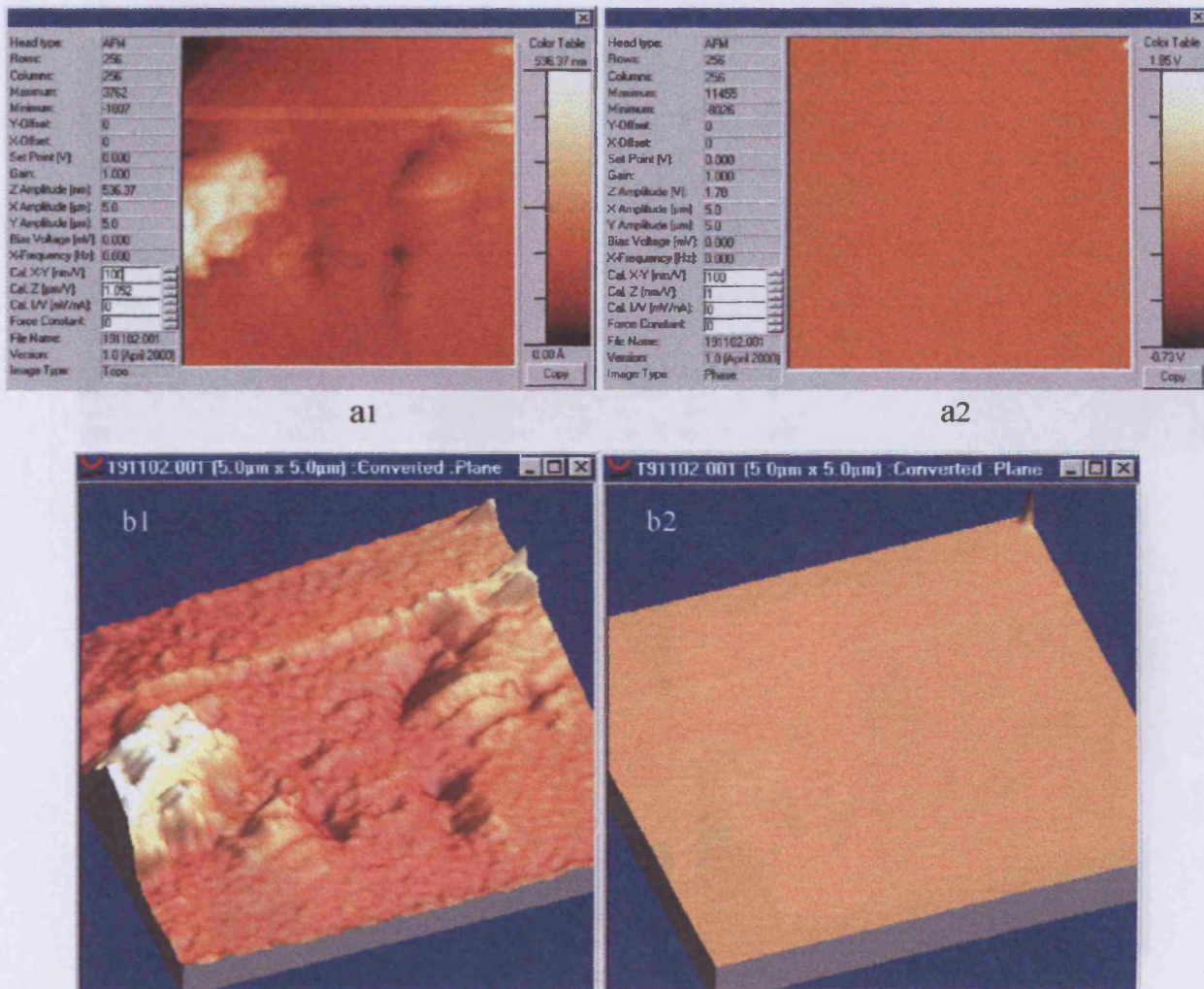
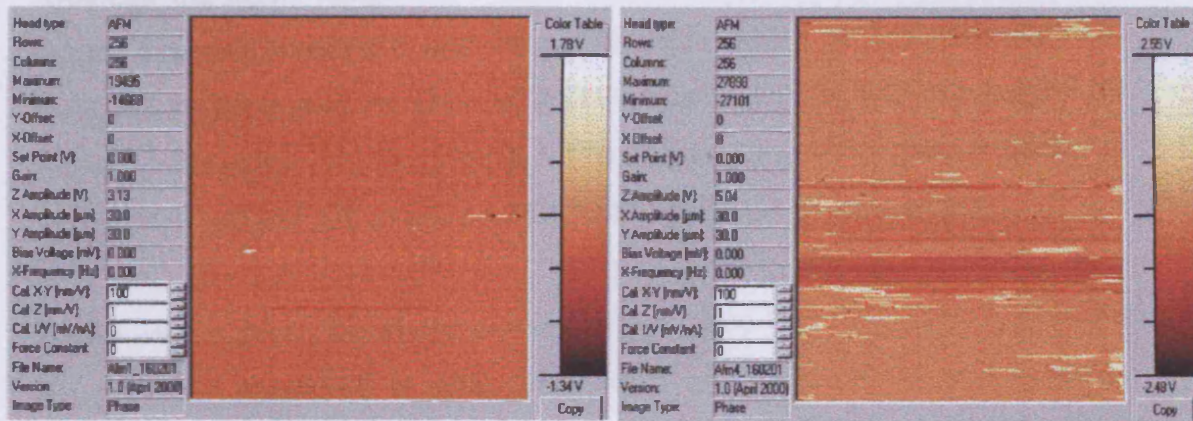


Fig. 6.20: MFM images of a nanocrystalline (5 μm x 5 μm)
a1, b1 are the topographical images
a2, b2 are the “phase” images

The images obtained in figures 6.19 and 6.20 are not as expected, They show characteristics of the nanocrystalline material. The areas scanned, as seen from the images, were $5\mu\text{m} \times 5\mu\text{m}$ and $30\mu\text{m} \times 30\mu\text{m}$. Scanning area in the range of nanometers may have revealed much more details from the surface of the material.



a1

a2

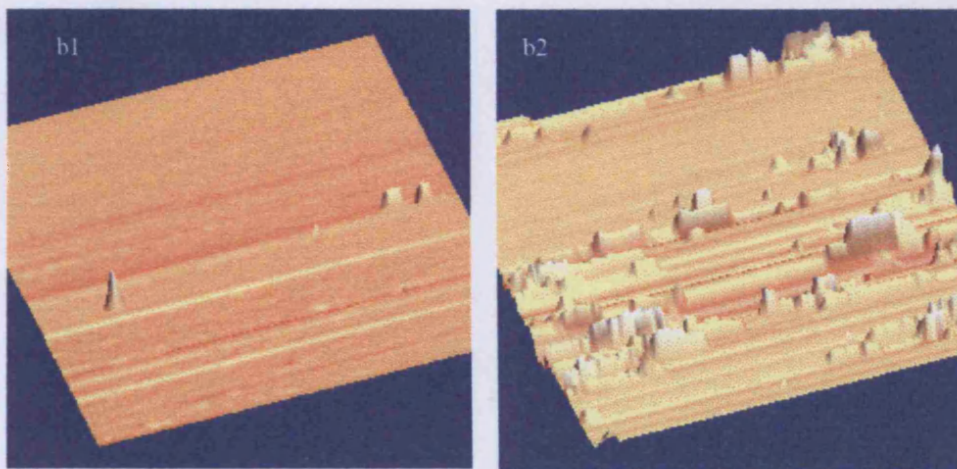


Fig. 6.21 MFM images of a nanocrystalline ($30\mu\text{m} \times 30\mu\text{m}$)

a1, b1 are the topographical images

a2, b2 are the “phase” images.

6.5 Conclusion

In conclusion, a Magnetic Force Microscopy system has been successfully used to study the internal structures of magnetic materials through the stray magnetic field at the surface of the samples.

Although the MFM images have been difficult to quantify because of the tip-sample magnetic interaction and the non-linearity of the ferromagnetic tip [6.5] [6.6], the application of the (WsxM) software package [6.7] has been helpful for further investigation into the original MFM images obtained. A grain boundary of average thickness of 120 nm of a 3.25% Si-Fe specimen was measured.

Future improvement, especially, on the software aspect of the system to overcome the problems mentioned is vital. That will, in addition to its high speed of evaluation, enhance the system's capability to fully analyse the magnitude of the detected surface magnetic field.

References

- [6.1] M. Mansuripur (1989), "Computation of fields and forces in magnetic force microscopy", IEEE Trans. Mag., 25, no. 5, pp. 3467-3469
- [6.2] I. Takekuma, M. Haseyama, K. Sueoka, K. Mukasa and M. Yasui (1999) "A study of magnetisation fluctuations in transition region using MFM image analysis", IEEE Trans Mag. 35, No. 5, pp. 2685-2687.
- [6.3] Wsmid / WsxM (2001), Scanning Probe Microscopy soft ware, Nanotec Electronics S. L., C/Padilla 1, 28006 Madrid (Spain).
- [6.4] MultiMode™ SPM instruction manual (1996-97), Digital Instruments, Inc. Version 4.31ce.
- [6.5] V. Strom and K. V. Rao (2000), "A novel method for magnetic imaging: determination of local in-plane susceptibility at a surface", J. Mag. Mag. Mat., 215-216, p723.
- [6.6] Y Shan, and Y. Wu (2004), "Response function study of a new kind of multiplayer-coated tip for magnetic force microscopy", IEEE Trans. Mag., 40, no.15, pp. 97-100
- [6.7] I. Ishii, K. Mukasa and Y. Kanai (1998), "A novel numerical approach to interpret images obtained by Magnetic Force Microscope", IEEE Trans Magnetism, MAG-34, No. 5, pp. 3455-3458.
- [6.8] A. Hubert and R. Schafer(1998), "Magnetic domains: the analysis of magnetic microstructures", Springer-Verlag ,1st edition, p 540.

CHAPTER SEVEN**DESIGN AND DEVELOPMENT OF POWER LOSS SYSTEM****7.1 Introduction (the overview of the system.)**

The block diagram of the 3-dimensional integrated Hall effect sensor/needle probes based measurement system developed and used for this work is shown in figure 7.1. The main components are the magnetizing system for applying fields to the sample, a precision (X-Y-Z) position control system with an on board microprocessor, a block of perspex specially designed to accommodate the integrated 3-dimensional Hall effect sensor (type: 3D-H-30), and the set (two pairs) of needle probes, the associated electronic signal conditioning, a data acquisition system (DAS) comprising on board microprocessor and analogue to digital converter (ADC), and a host personal computer (PC) for communicating with the computerized system element and displaying the result.

The perspex block housing the sensor package had one end attached to the X-Y-Z positioning system. The specimen to be scanned was placed on a separate stage which includes a manual vertical axis position. A yoke (C-core) with a 160 turns magnetizing coil was then placed on the specimen for magnetization while the scanning process took place around the centre of the sample in the uniform field region. Additionally, the vertical axis stage allows the computer to control precisely the sample-to-sensor spacing. For optimum results, the sensing element was set as close to the sample surface as possibly, but this also depends mostly on the distance

between the sensing element and the surface of the sensor.

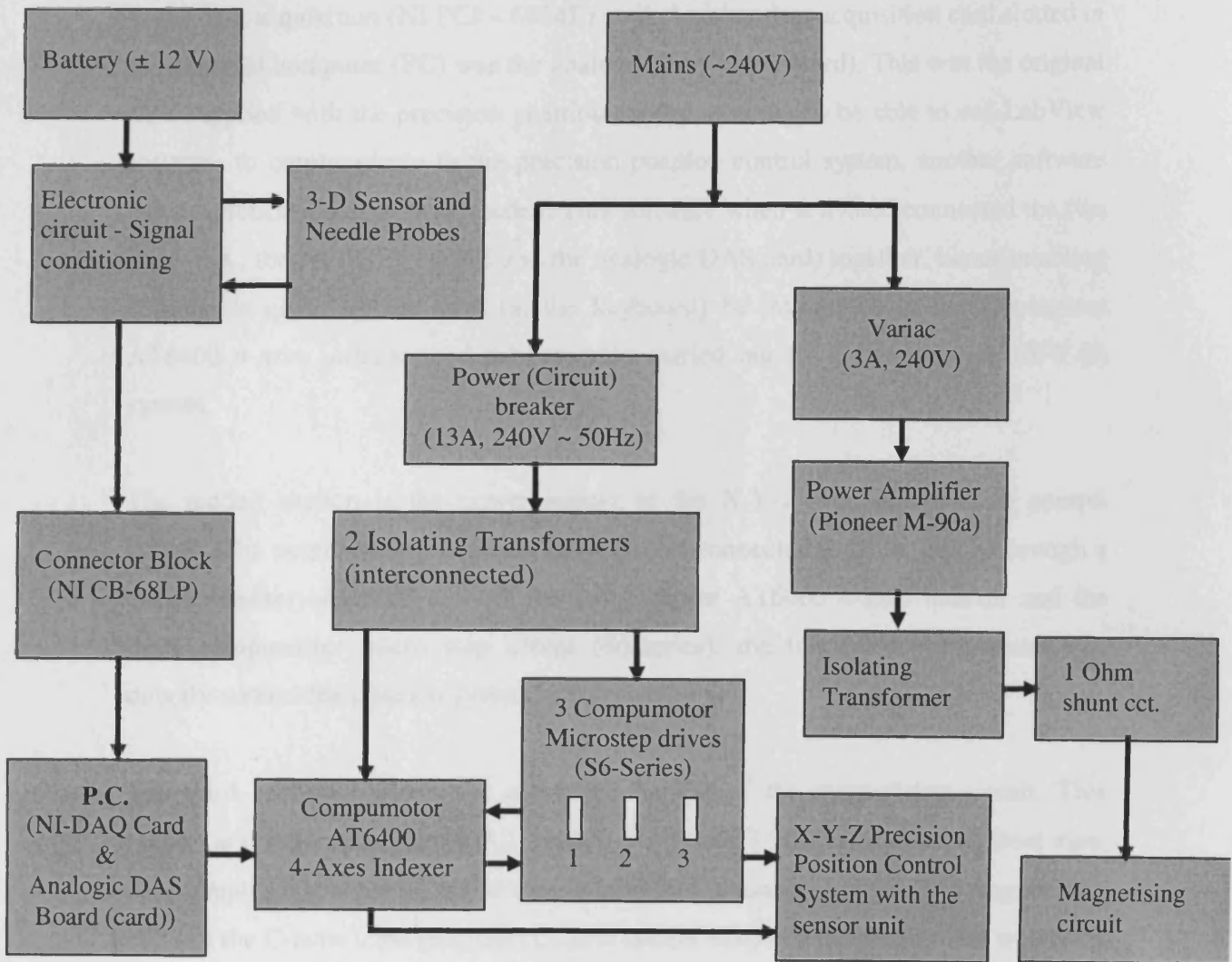
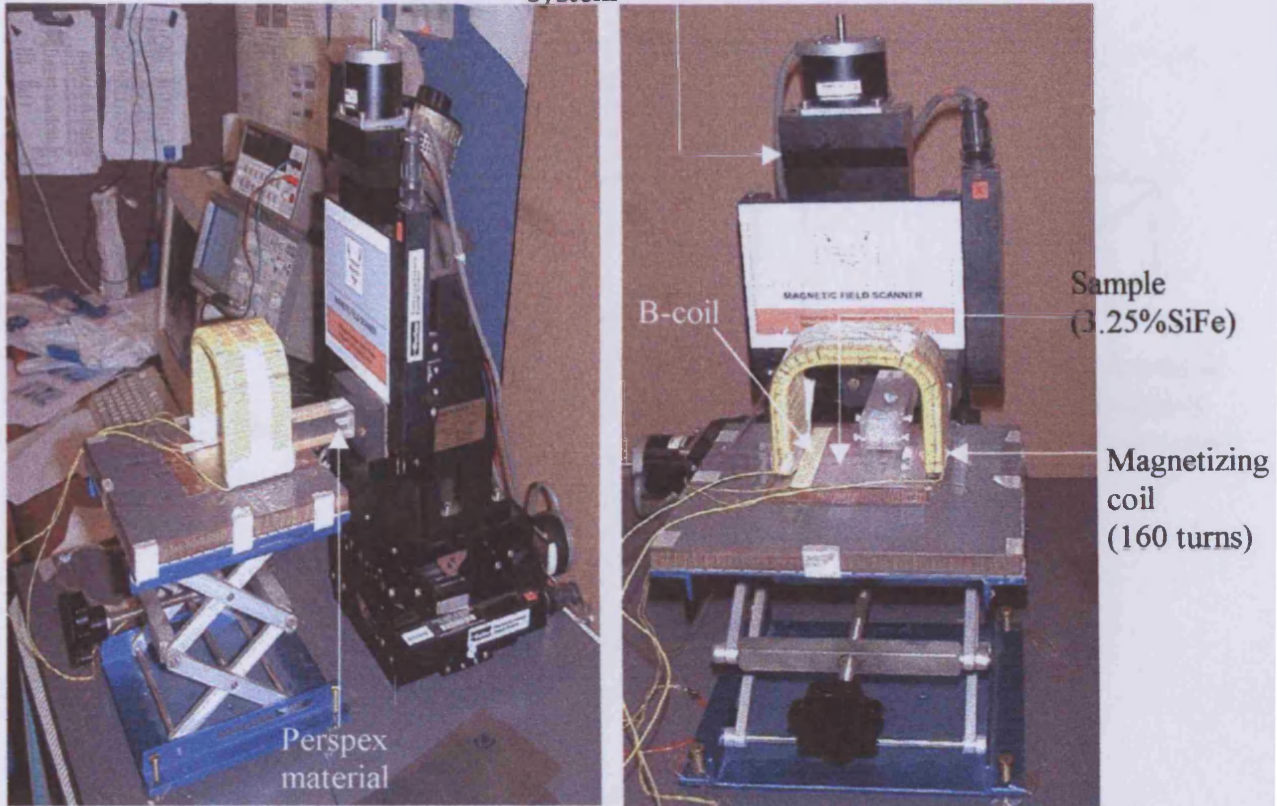


Fig. 7.1: A block diagram illustrating the measurement system

The measurement system (figure 7.1) has three main sections. The first comprises the signal conditioning circuit which is powered by a $\pm 12\text{V}$ d.c. supply. Power supplied to the 3-dimensional i.c. Hall effect sensor, and the output of both this 3-D sensor as well as the needle probes were all through the signal conditioning circuit. The output of the electronic circuit was fed via a connector block (NI CB-68LP) and a controller to the data acquisition (NI PCI – 6034E) card. Another data acquisition card slotted in the personal computer (PC) was the analogic DAS board (card). This was the original card supplied with the precision position control system. To be able to use LabView software to communicate to the precision position control system, another software named Motion Toolbox was needed. This software when activated connected the two cards (i.e., the NI PCI – 6034E and the analogic DAS card) together, hence enabling commands given by the user (at the keyboard) be interpreted to the Copumotor AT6400 4-axes indexer, and subsequently carried out by the positioning (X-Y-Z) system.

The second section is the power supply to the X-Y-Z-precision position control system. The output of two isolating transformers connected to 240V supply through a circuit breaker were fed to both the compumotor AT6400 4-axes indexer and the three compumotor micro step drives (S6-series), the two main components that directly control the position system.

The third section controls the excitation current of the magnetising circuit. This section is discussed in section 7.2. Figures 7.2(a) and 7.2(b) show side and front view photographs, respectively, of the magnetizing and scanning systems. The magnetizing coil (on the C-core), the specimen (3.25% silicon iron) and the platform on which the specimen was placed can be seen in both figures.

X_Y_Z Positioning
system

(a)

(b)

Fig. 7.2: Main components of the magnetizing and scanning systems: (a) side view and (b) front view.

The sensor package and the perspex block housing it can be identified in figure 7.2.

The magnetizing system and the sensor package are further shown in figure 7.3.

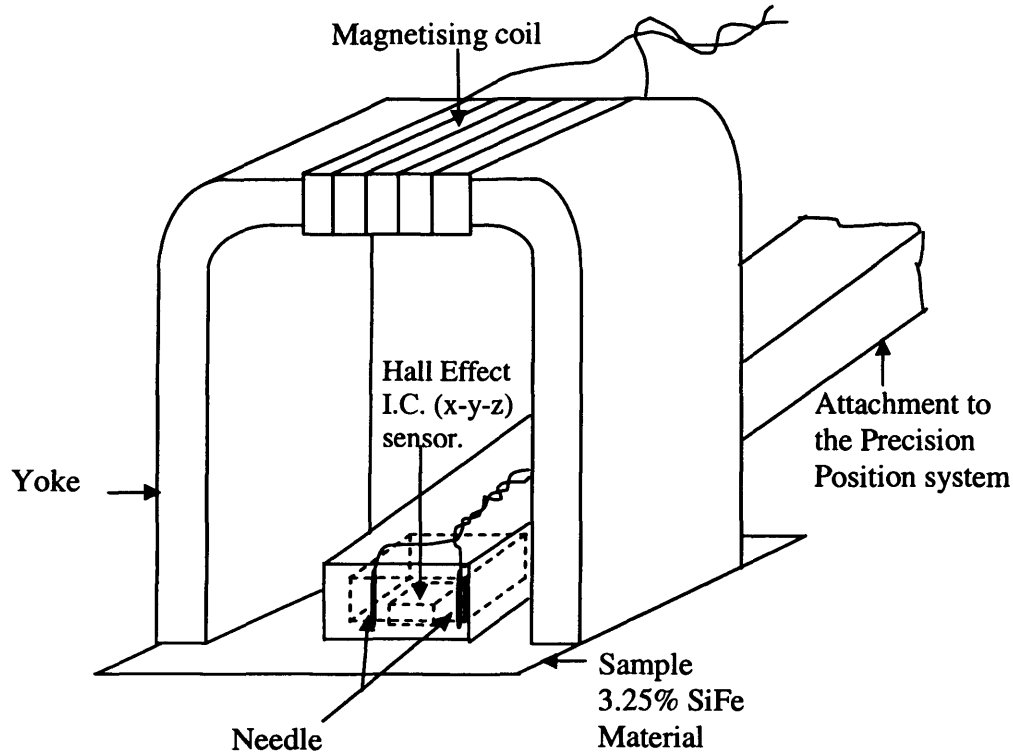


Fig. 7.3 The X-Y-Z-sensor and the needle probes (encapsulated) on the magnetised grain oriented electrical steel sample.

The LabView software package was used to run the system. The user can specify the step/sampling interval upwards (vertical) of 5mm (to make space for the spring loaded needles) and the scan area which is selectable with independent X and Y axis scan distances of up to 30mm.

Upon selection of the scanning command, movement instructions are sent to the positioning stage to raster scan the sensor combination (3-D integrated Hall effect sensor / Needle probes) over the sample surface.

7.2 The magnetizing system.

The magnetizing circuit is shown in both figures 7.2 and 7.3. The C-core is placed on the specimen to complete the magnetic circuit. Power supply to the circuit is as shown in figure 7.4. The variac, the isolating transformer and the amplifier are in the excitation current circuit. The mean length L (of the circuit) was 230 mm.. Many scans were performed but the average excitation current was maintained between 100 and 150 mA at 50Hz.

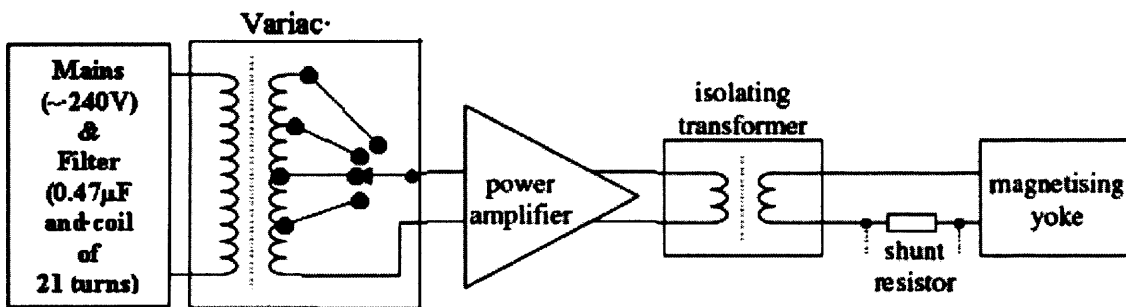


Fig. 7.4: Outline of the magnetizing circuit.

With the excitation current of 100mA, a magnetizing field of about 50A/m was generated in the magnetising circuit. A distorted output signal was observed whenever the current value reached about 200mA. It was quite safe to work at 150mA and below [7.1]

7.3 The static characteristics of the integrated Hall Effect sensor and the field detection.

The integrated 3-D Hall effect sensor used for this work was manufactured by the Sentron company [7.2]. Sentron Hall elements are characterized by a special feature of having their Hall elements sensitive to magnetic field components parallel to the chip surface and not as conventional Hall magnetic sensors perpendicular to the device surface [7.3]

The 3D-H-30 measures the 3-axis components of a magnetic field at the same position. The active zone ranges between 0.1mm and 0.3mm. It has a high magnetic field sensitivity and low current. It has a field range of about $\pm 477.48 \text{ Am}^{-1}$. The sensor has a sensitivity of 100 mVT^{-1} ($7.95 \times 10^7 \text{ mV/A/m}$) in the vertical (z) axis and 275 mVT^{-1} ($21.0 \times 10^7 \text{ mV/A/m}$) in both the (x) and (y) axes. The magnetic sensitive volume is $0.25 \times 0.25 \times 0.2 \text{ mm}^3$, and it is $35\mu\text{m}$ from the surface of the chip. It can therefore be used to measure the magnetic field with high spatial resolution [7.4]. All other parameters (i.e., absolute maximum ratings and other typical electrical characteristics) are shown in appendix 1.

The labView package was used to calibrate the characteristics of the 3-D (3D-H-30) sensor, employing the magnetizing circuit of the built system. Test was run at a frequency of 50 Hz, and applied current ranging from 0.2A to about 3.0 A. For better averaging, each test was run for 1000 of each result. The characteristics shown in figure 7.5 were obtained for the individual three axes of the sensor. The full data on the characterization is given in appendix 2.

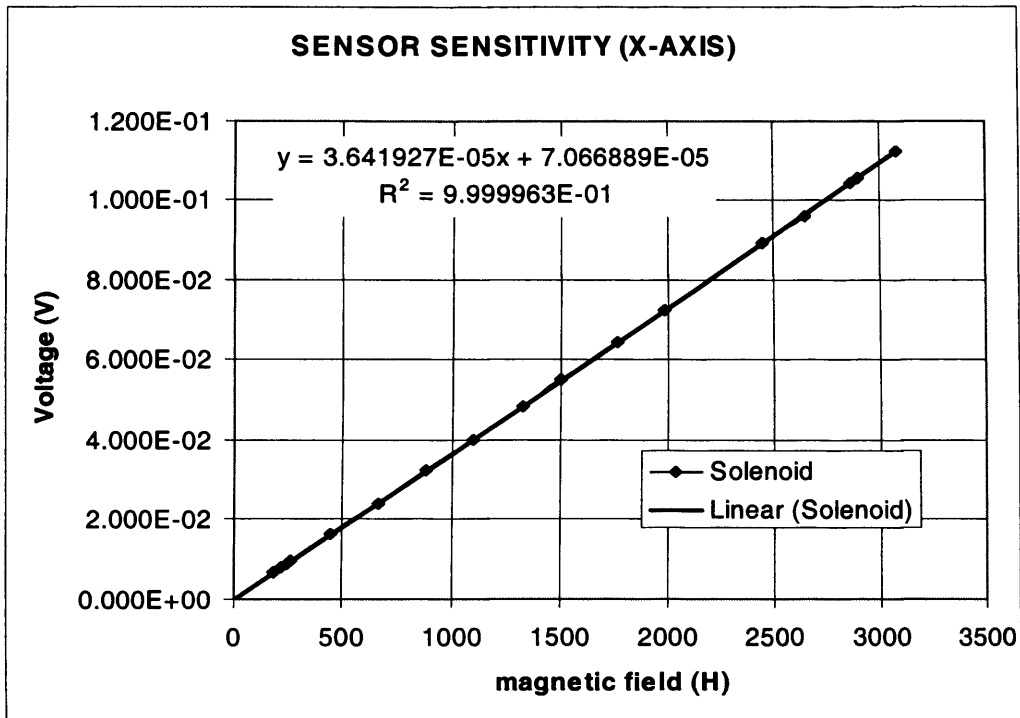


Fig. 7.5(a): Calibration of H_x component curve of 3-D Hall sensor at 50 Hz.. (H_x in A/m)

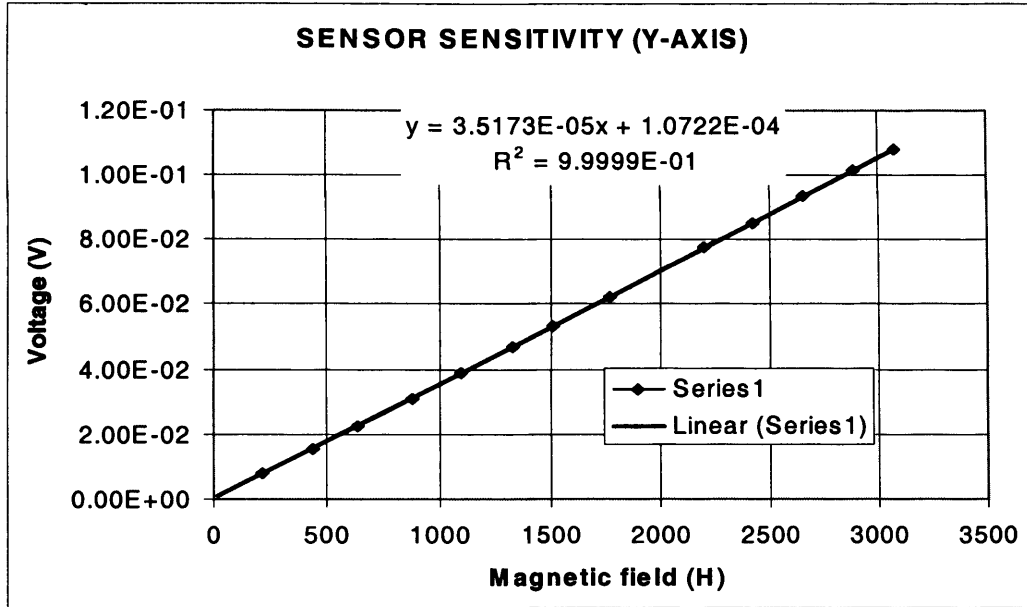


Fig. 7.5(b): Calibration of H_y component curve of 3-D Hall Sensor at 50Hz. (H_y in A/m)

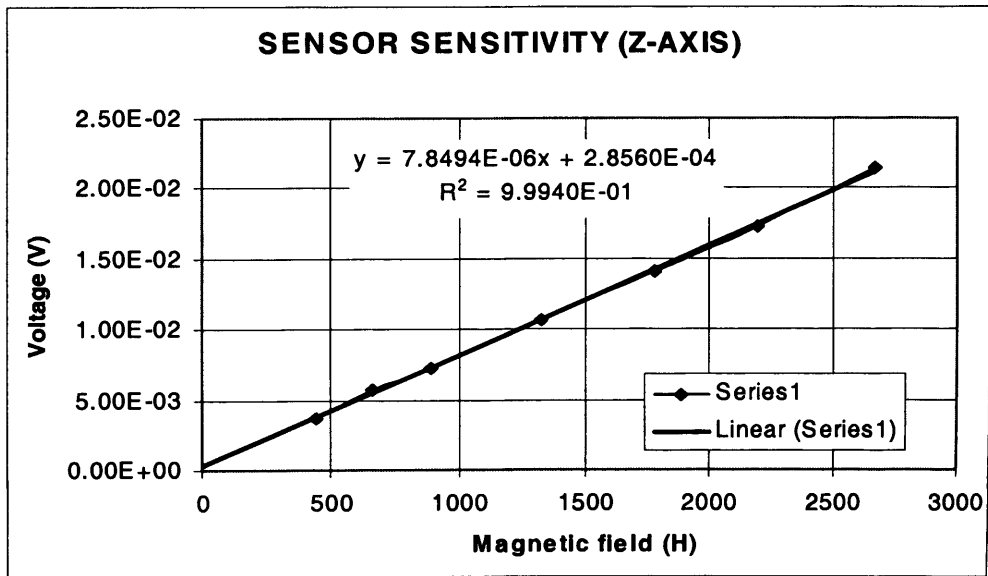


Fig. 7.5(c): Calibration of H_z component curve of 3-D Hall sensor at 50 Hz. (H in A/m)

7.4 The Needle Probes

A new technique for detecting localized flux density was reported [7.5]. However, the two most common techniques that have been used are the needle probes (NPT) and the B-coil techniques.

With the B-coil technique, holes are drilled in the sample, which has a harmful effect on its magnetic properties. The needle probes technique was first reported in a patent [7.6]. This technique is more widely used, because there is no need for holes.

The principle upon which the needle probe technique has been based is that, the potential difference generated or induced between two points at the surface of a

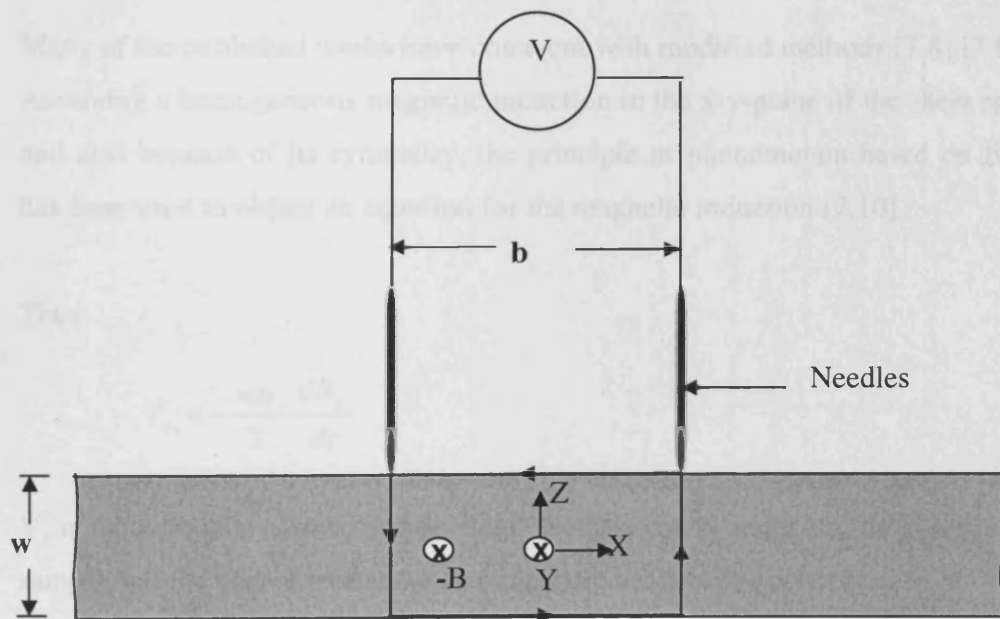


Fig. 7.6: Principle of the measurement of the magnetic induction (NPT).
(Patent [7.6])

magnetized piece of lamination is proportional to the voltage induced in the coil wrapped around the cross-sectional area of the lamination . The potential gradient at the conductive surface of the sample is caused by eddy currents which are also induced by variable flux density (as shown in figure 7.6).

Some basic problems that might lead to inaccuracies, as indicated through research into the needle probe system [7.7], include:

- (i) non-homogeneity of the flux distribution through the thickness of the lamination,
- (ii) wiring must be made very carefully to avoid picking up the stray flux
- (iii) some force must be applied to the needles in order to ensure electrical contact with the surface of the lamination, and
- (iv) positioning of the needles is usually prone to small errors

Many of the published works have come out with modified methods [7.8] [7.9]

Assuming a homogeneous magnetic induction in the x-y-plane of the sheet specimen, and also because of its symmetry, the principle or phenomenon based on figure 7.6 has been used to obtain an equation for the magnetic induction [7.10].

Thus:

$$V_y = -\frac{wb}{2} \cdot \frac{dB_y}{dt} \quad (7.1)$$

V_y is the voltage measured between the needles, and w and b are the thicknesss of the sample and the distance between two opposite needles respectively.

The output voltage across the other pair of needles placed in the y-axis is given by:

$$V_x = -\frac{wb}{2} \cdot \frac{dB_x}{dt} \tag{7.2}$$

Capsule with the sensors

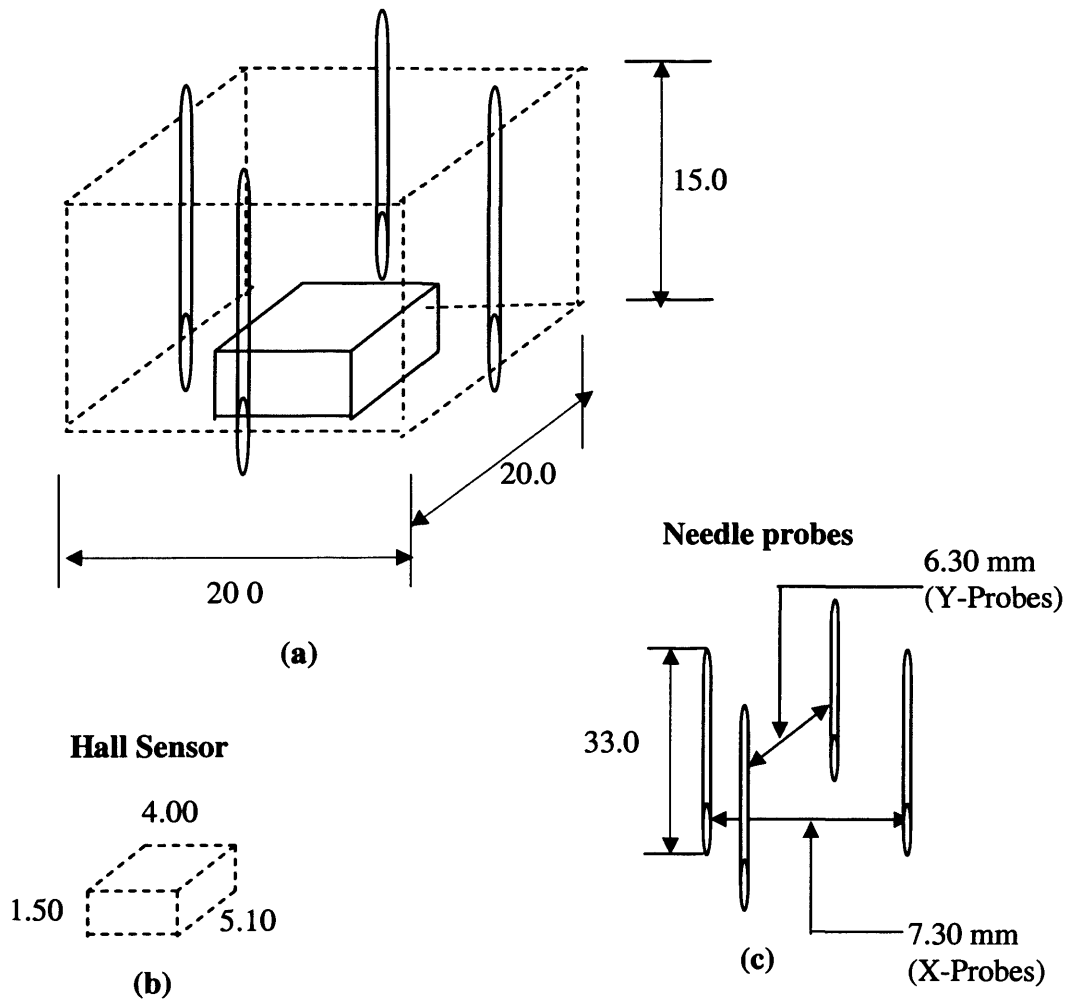


Fig.7.7 Component parts of the sensor system
(all dimensions are in mm)

Figure 7.7 shows the component parts of the sensor unit. The arrangement of the spring loaded needles (two pairs) in the perspex, together with the 3-D integrated Hall effect sensor, are arranged as shown in figure 7.7(a)

The two pairs of needles were placed orthogonally, and the distances between each pair was measured using a traveling microscope which has a resolution of one hundredth of a millimeter. The distances between the X-probes and the Y-probes are 7.30 mm and 6.30 mm respectively.

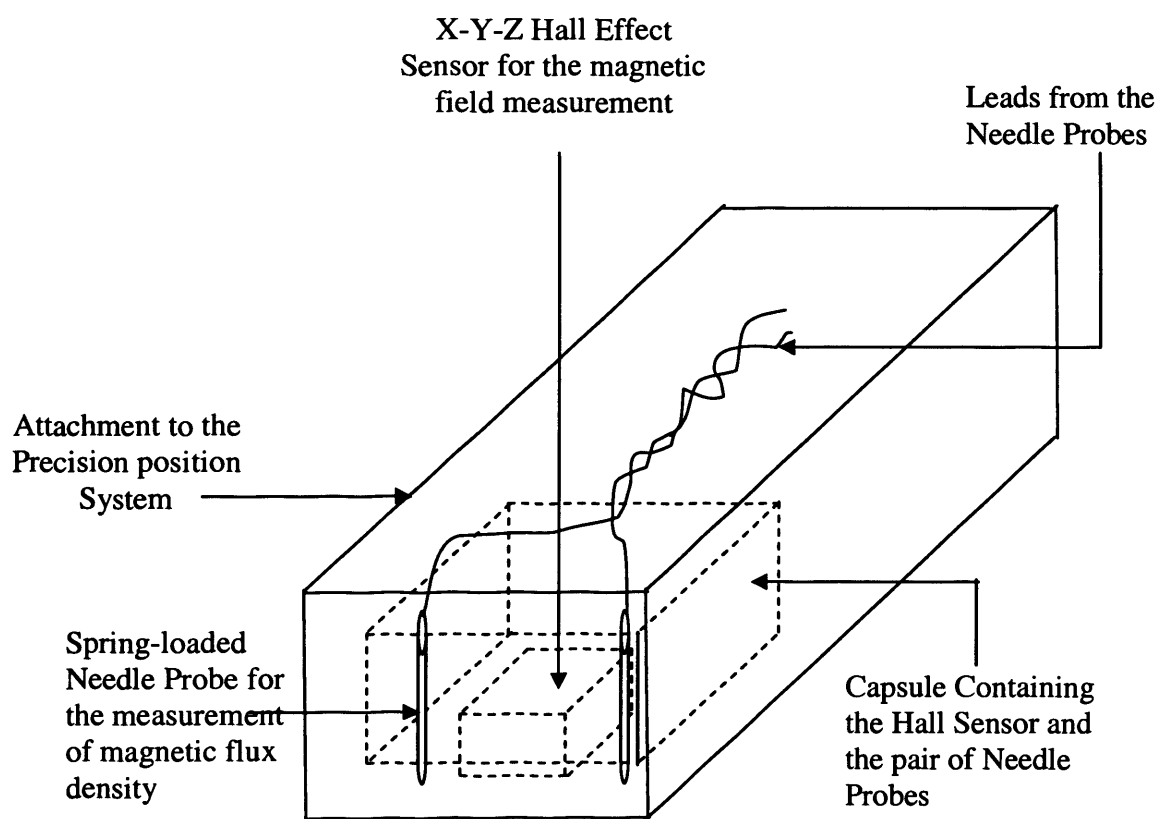


Fig. 7.8: Perspex block housing the 3D-H-30 and the 2 sets of needle probes.
(For clarity, only 1 pair of the needle probes is shown.)

Figure 7.8 also shows the perspex structure which accommodates the probes and the extension attached to the platform of the X-Y-Z precision position system. The output voltages of the two sets of needle probes are proportional to components of the rate of change of flux density in their respective directions (equations 7.1 and 7.2). These are essential parameters for the determination of the localized power loss.

7.5 The LabView programme.

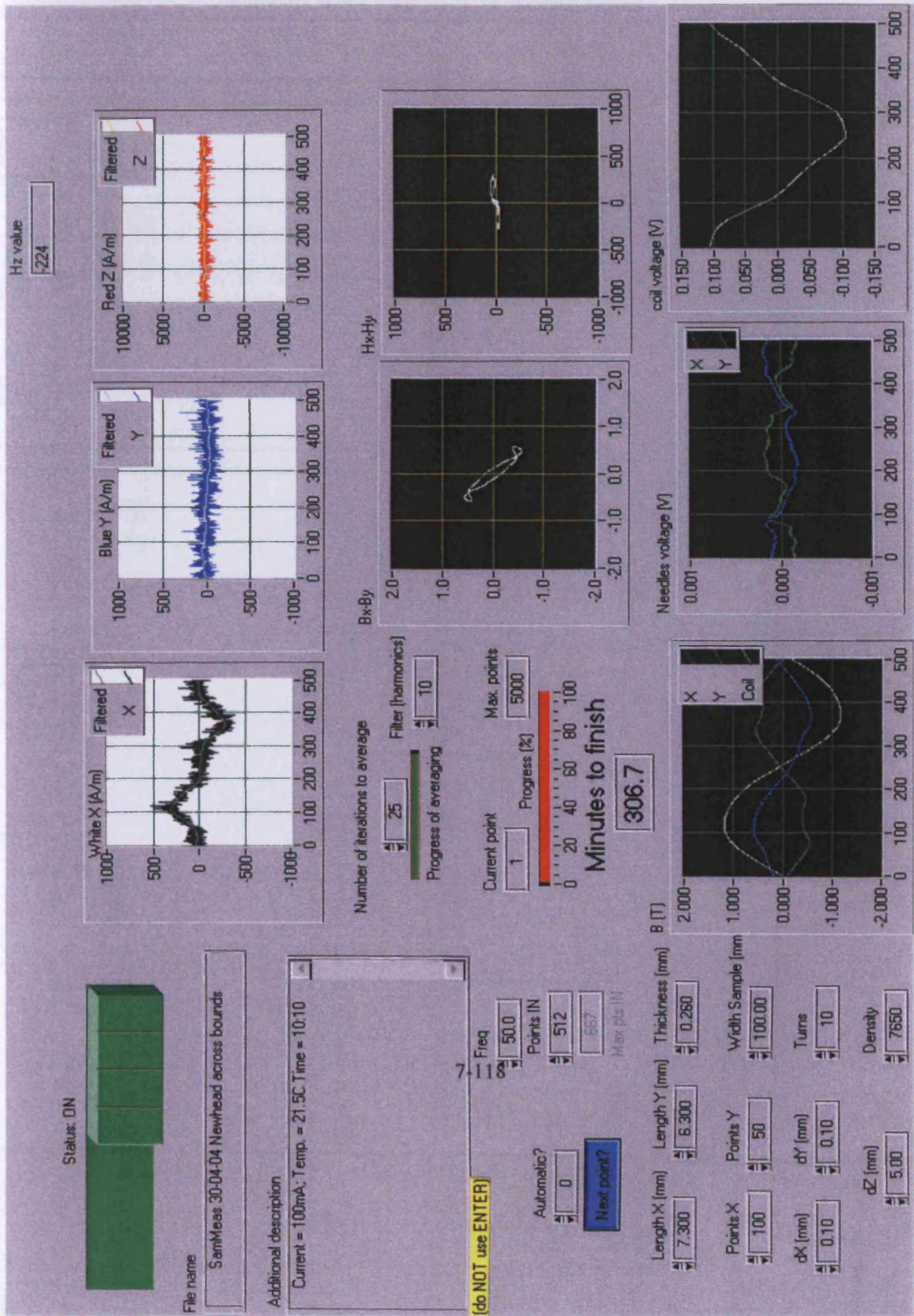
The LabView package was used for both data acquisition and processing, and also for motion control. These functions were performed simultaneously. The program for the whole system was built using LabView virtual instruments (VIs) [7.11]. Step by step, the component programs were developed into libraries (more complex forms). Initially, the data acquisition aspect of the programme was concentrated on. The X-Y-Z- precision position control system was manufactured by the Parker Hannifin Corporation. Although the version used, required the application of the LabView software package, the main software package for the system is called the Motion Toolbox. This package is a library of LabView virtual instruments (vi) for the Compumotor's 6000 series of motion controllers. For that reason it allows LabView programmers to develop programs for motion control systems for a wide range of applications. Motion Toolbox also supports both the Compumotor AT6400 4-axis (Drives) and the 6200 3-axis Indexers. A good working knowledge of LabView and the Labview Tutorial manual, was necessary to use Motion Toolbox effectively [7.12].

The most important components needed to get the precision position system working were the LabView package, the Motion Toolbox, NI DAQ (Data Acquisition) card, the AT64000 Compumotor Interface card and the Motion toolbox package.

Figure 7.9 shows the “Control (front) panel” of the main programme. The whole programme is controlled from the control panel. The block diagram, which represents the labview programme for the entire system is also shown in figure 7.10. Figure 7.11 shows another “control panel”. This is specifically used to preset X-Y-Z positioning system limits of travel or motion in all three directions before the automatic scanning process is commenced. The array diagram in figure 7.12 helps to set out the area of the specimen surface to perform a scan. By selecting a certain number of consecutive points on the X-axis and Y-axis, an area is automatically set out for the scan. Both figure 7.11 and figure 7.12 are linked to the main front panel whenever scanning is in progress, to control the automatic movements of the system.

All the system settings for a scan are made from the front or control panel,. In LabView, applications interact with the user through a graphical-based display featuring windows, menus, dialogue boxes and controls. The setting includes parameters such as, step resolution, sampling resolution, area of scan, number of iterations for averaging, etc. as shown on figure 7.9. Additionally, windows are available for monitoring the scanning process and progress, the nature of signals being obtained after every single scan.

Fig. 7.9: Control (front) panel of the scanning system



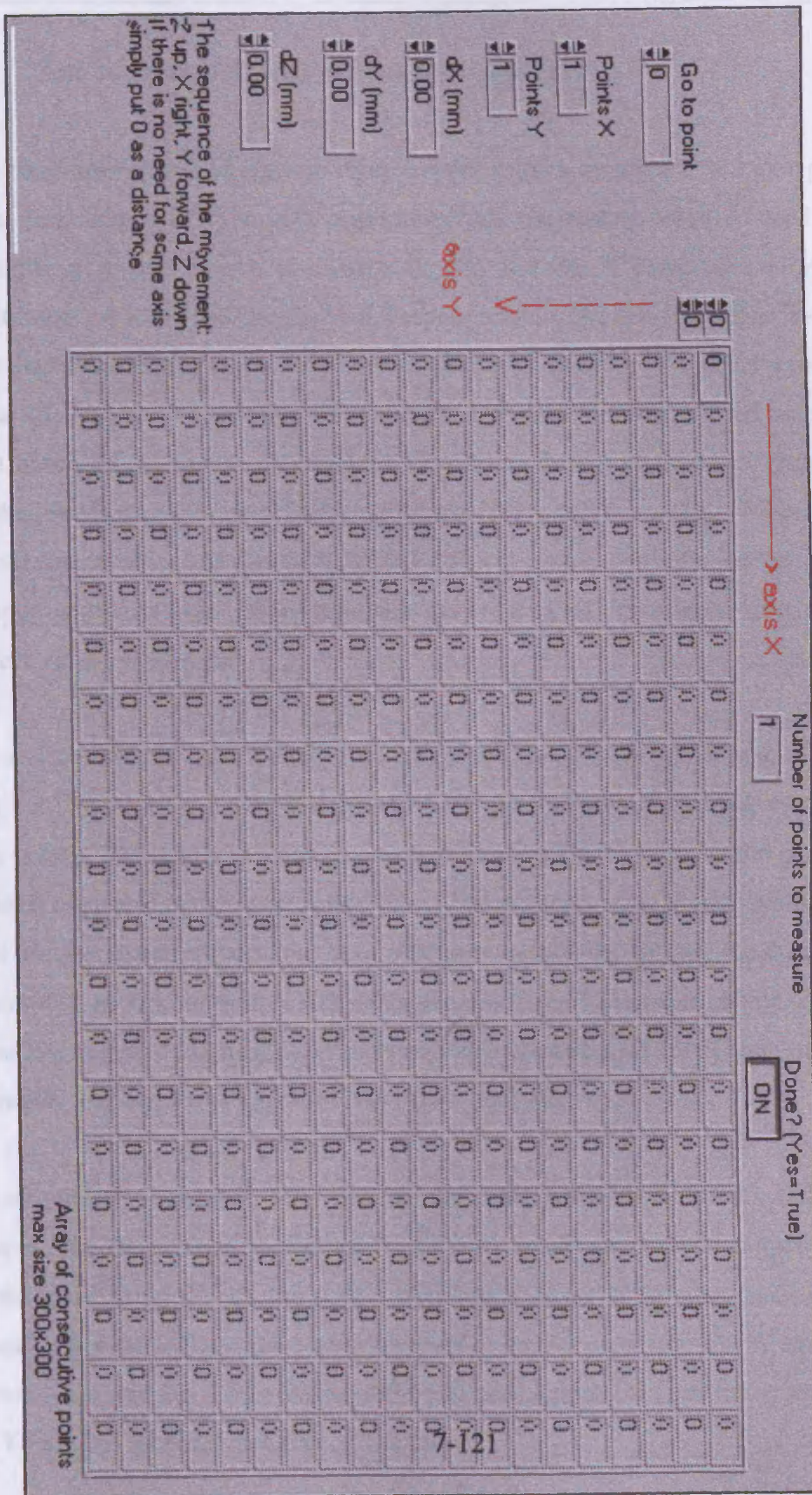


Fig.7.12: Array of points indicating the area on specimen to perform scanned.

7.6 The scanning / Precision Positioning system.

The positioning stage comprises three stepper motors arranged in a 3 axis positioning stage (See Fig 7.2). The X-Y component of the sliding stage is used for raster scanning a sensor over a stationary sample and the Z component allows precise positioning of the sensor height with respect to the sample surface. The X- Y- Z axes each have a sliding range of 60 mm respectively and are able to traverse a 30 mm linear distance in a minimum of 1 second. However, throughout the investigation a scan speed of 10 mm/sec was used. This speed was enough to let, especially, the needles settle properly or stabilise on the specimen before readings were taken. Also, the sensor combination (Integrated Hall effect sensor and needle probes), held in the perspex structure were simultaneously raster scanned on a prescribed area on the surface of the specimen.

The stepper motors have a maximum step resolution of 100 μm . A scan made over 20 mm x 20 mm area at a step resolution of 100 μm in both axes would result in 40,000 data points. The number of data points and hence total scan time could be reduced by making the step size larger, however, at the expense of a poorer quality magnetic field images. Alternatively, the scan area may be reduced to keep the number of data points to a minimum and to reduce total scan time. Scan areas in this investigation never exceeded a 20 mm x 20 mm region for reasons of total scan speed and to guarantee uniformity of applied field within the scan area.

For simplicity of control, the raster scan method was chosen for the field scanning system. The raster scan operation requires that the sensor be first scanned forwards a set distance along the X axis. Upon completion of the X axis forwards motion, the direction is reversed and the sensor returned to its start position. The Y axis motion is incremented and the X axis scan motion proceeds again. This process is repeated until the Y axis has incremented a set distance.

The speed of stage travel 10 mm/sec is considered acceptable for a laboratory based environment. For a 20 mm x 20 mm area, each X-axis forward motion takes another 2 seconds to complete. The following X-axis reverse motion takes another 2 seconds. The increment of the Y-axis motion for a 100 μ m step takes less than 0.5 seconds. Included in this time is the time taken for the host computer to communicate with the X- Y- Z stage as a result of communication handshaking. Therefore the total scan time for the sensor to traverse the whole 20 mm x 20 mm area (40,000 data points) is approximately 15 minutes. For 10mm x 10mm area (20,000 data points) the total scan time is approximately 4.5 minutes. An advantage of using the slower scan speed is that acceleration and deceleration steps are unnecessary to overcome initial inertia.

Additionally, operating the X- Y- Z table at a slower speed ensures more accurate and repeatable positioning as there is no whip lash caused by abrupt start / stopping motions. Also using 10 mm/sec scan speed operated well with the fixed range of sampling signal acquisition speeds that were available on the DAS card.

To enable parallel processing and a reduced work load on the host PC the X- Y- Z positioning stage includes a microprocessor based four axis indexer known as the compumotor AT6400 [7.13]. AT6400 inserts hardware registers for motor position, I/O, and system status. AT6400 is inserted into a single 16-bit Enhanced Industry Standard Architecture (EISA) expansion slot in the Host PC. The AT6400 provides multi-axis control of the positioner through the motion control language. A separate auxiliary board simplifies connection by interfacing the stepper motors to the AT6400.

7.7 Signal circuit and conditioning

The Integrated 3-dimensional Hall effect sensor (3D-H-30) used is a small outline integrated circuit (SOIC) with 8 pins. Its basic application circuit diagram is shown in figure 7.13

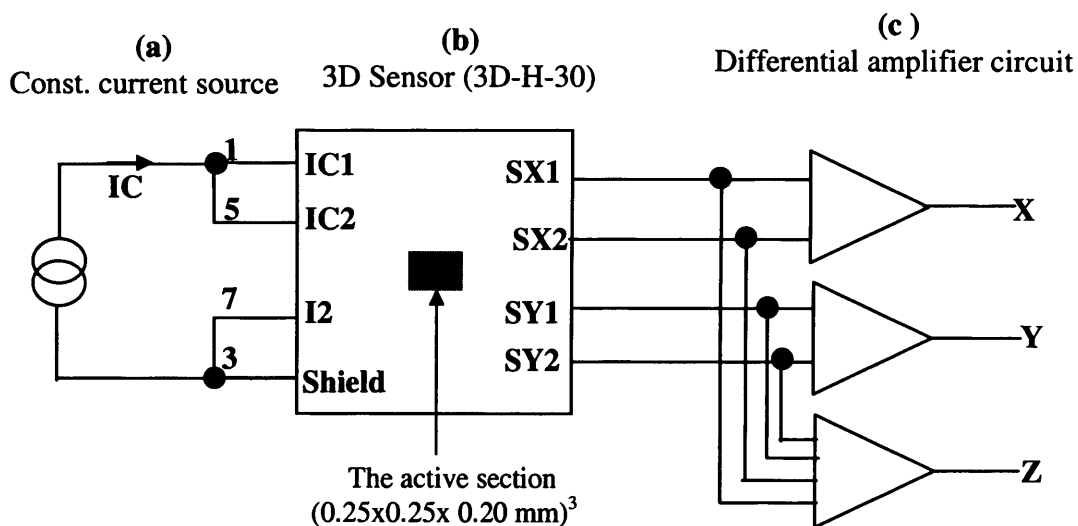


Fig.7.13: Typical 3D-H-30 sensor application with current source and amplifier.

$$\text{Output X} = \text{SX1} - \text{SX2}; \text{ Output Y} = \text{SY1} - \text{SY2}$$

$$\text{Output Z} = \text{SX1} - \text{SY2} + \text{SX2} - \text{SY1}$$

It can be seen from figure 7.10 that the 3D-H-30 application is basically divided into three sections: (a) the supply section, (b) the detection or sensing section and (c) the output section.

The electronic circuit diagram developed and built for the signal detection and conditioning is shown in figure 7.14. The Analog Devices precision current source

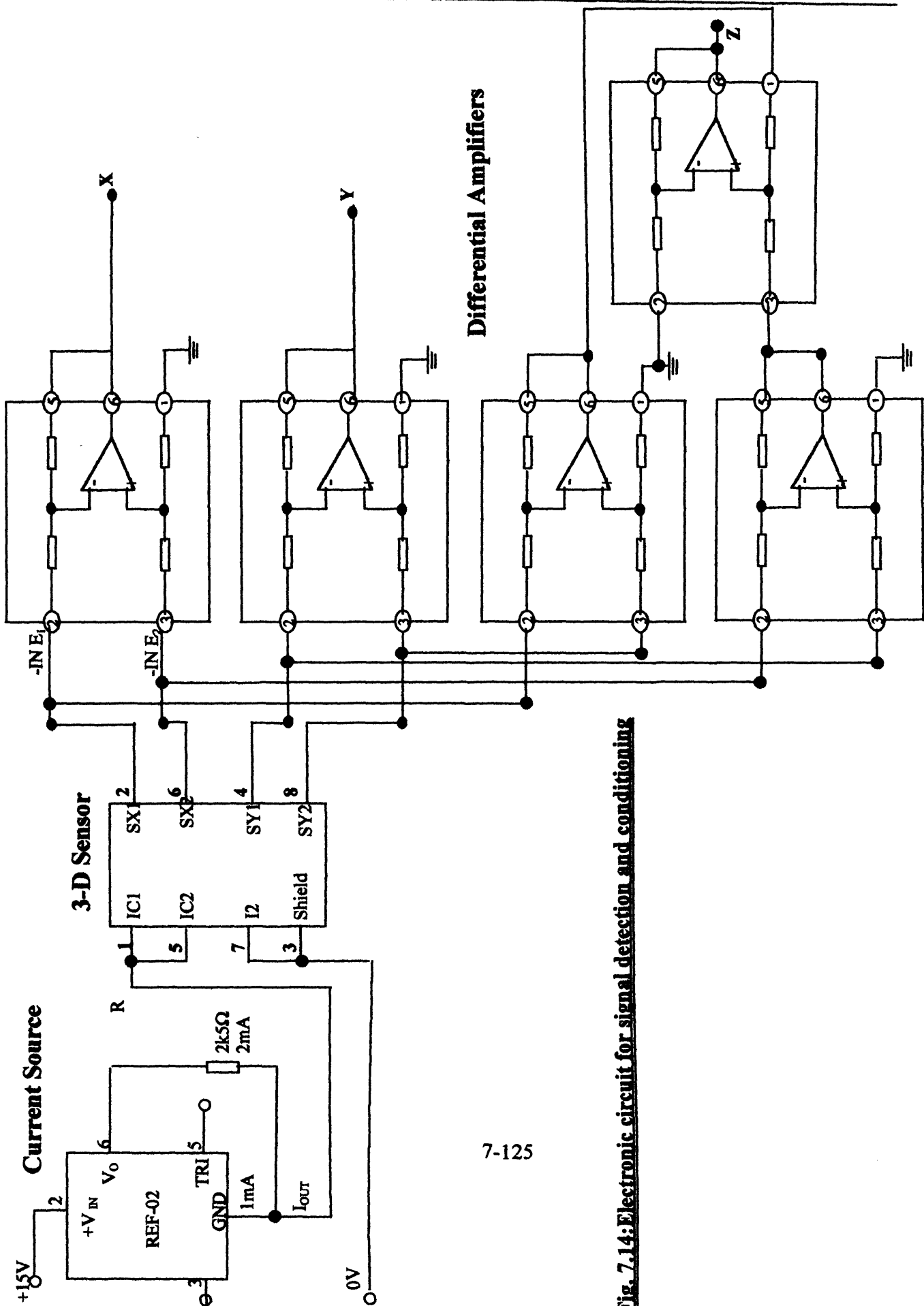


Fig. 7.14: Electronic circuit for signal detection and conditioning

(REF-02), was used (figure 7.15). The data sheet is shown in appendix 3.

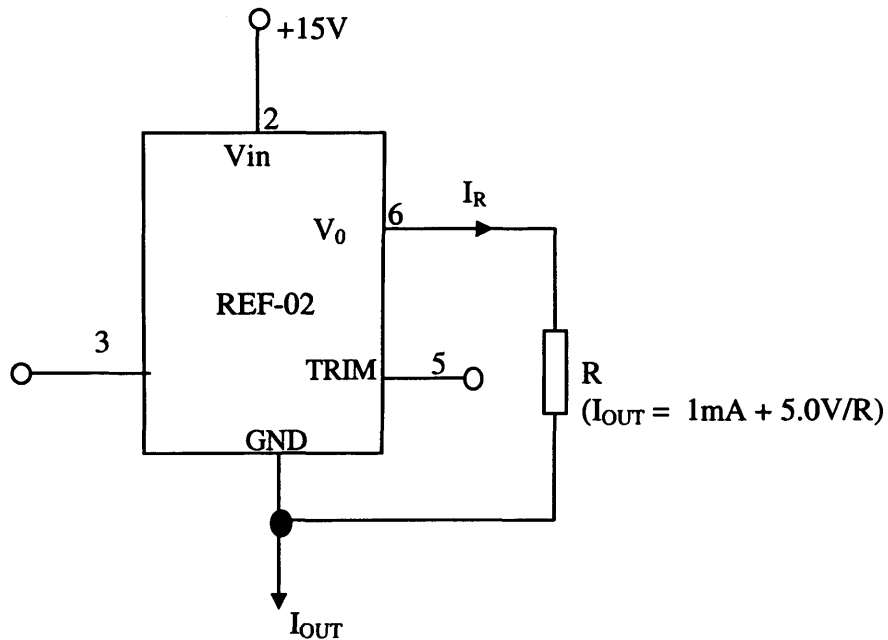


Fig. 7.15 Current Source
(Voltage compliance :-25V to +8V)

The sensor is in the middle section of figure 7.14. In the output section, five differential amplifiers, with commercial name AMP03, were arranged to produce the outputs of X, Y and Z axes. The detailed internal electrical circuit diagram of the AMP03, supplied by the manufacture, is shown in figure 7.16. (See Appendix 4 for the supplied data sheet).

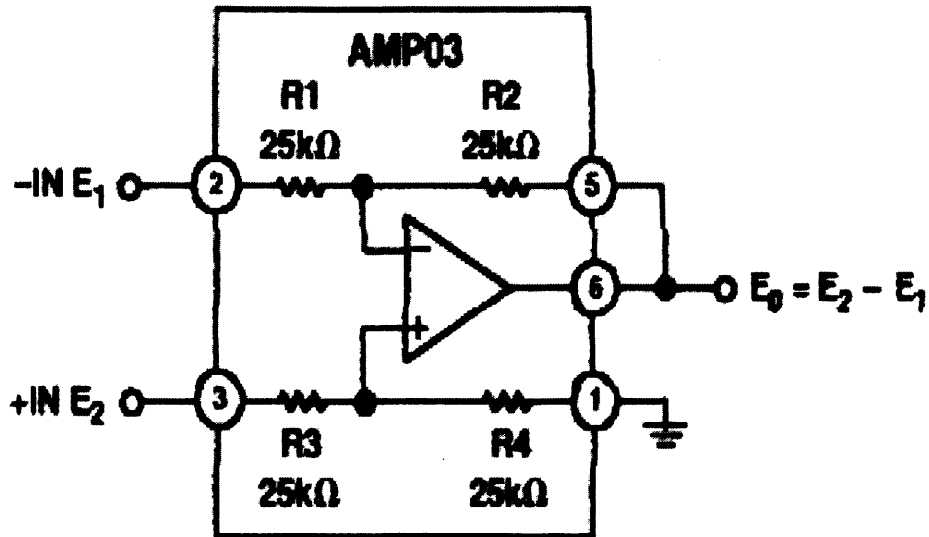


Fig 7.16: Instrumentation amplifier
(Amp03)

Finally the outputs of the 3D-H-30 sensor (i.e., X, Y and Z) as well as those of the needles were channeled through the black box containing the electronic signal conditioning circuit which, for stability, was powered by a 12V battery source. Then the output of the black box was connected to the connector block (see Fig. 7.1) then to a multifunction Data Acquisition card (NI PCI – 6034E) in the personal computer for processing.

7.8 Power loss representation

The total power loss in ferromagnetic sheet subjected to an alternating magnetic field is directly proportional to the area of the BH loop and can be calculated by means of a fieldmetric method from:

$$P = \frac{1}{T\rho} \int_0^T (H \frac{dB}{dt}) dt \quad [\text{W kg}^{-1}] \quad (7.3)$$

where: P – total power loss, [W/kg]; ρ – specific density of magnetised material, [kg/m³]; T - cycle of magnetisation, [s]; H – ~~power~~ magnetising field, [A/m]; instantaneous value of flux density, [T]; t – time, [s]

For two-dimensional magnetisation (different from alternating) the H and B vectors can be analysed into two components - for X and Y directions.

It should be stressed that equation (7.4) yields total power loss, which is correct even for non-circular magnetisation, e.g. elliptical or two-dimensional [7.14]. Similarly, the power loss in a lamination magnetized in one direction can be expressed as the product of the instantaneous values of surface magnetic field and the space average of the flux density. Therefore the equation (7.3) can be written as:

$$P = \frac{1}{T\rho} \int_0^T (H_x \frac{dB_x}{dt} + H_y \frac{dB_y}{dt}) dt \quad [\text{W kg}^{-1}] \quad (7.4)$$

where: the subscripts x and y denote components of the vectors in directions X and Y, respectively. The density term (ρ) converts the loss to per unit mass rather than unit volume in equation (7.4) [7.15].

Figure 7.17, is a schematic presentation of the magnetic field applied to a specimen of isotropic ferromagnetic material. The vector of flux density (B_r) lags the magnetic field (H_r) by some angle, ϕ .

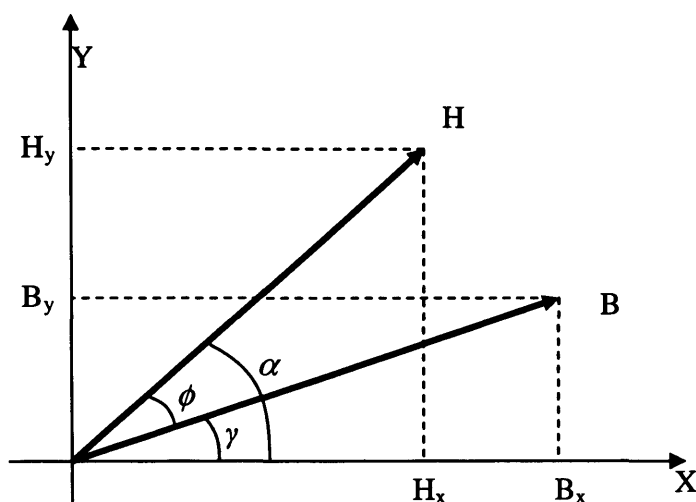


Fig. 7.17. Representation of magnetisation and orthogonal components of magnetic field and flux density.

After a scan, the X, Y and Z data outputs of the 3D-H-30 are used by the program to compute the parameters H_x , H_y and H_z respectively. The output of the needle probes (two pairs) placed orthogonally, also yield the parameters $\frac{dB_x}{dt}$ and $\frac{dB_y}{dt}$ respectively, as shown by equations (7.1) and (7.2). Applying equation (7.4) and at the frequency of 50 Hz, all the localised power loss is computed by the LabView program as in figure 7.10.

7.9. Uncertainty of the measurement

One important issue in measurements of any kind is the estimation of uncertainty. Many assumptions often have to be made in order to be able to assess the uncertainty [7.16]. However, the ability to make measurements to a known accuracy is vital so that products meet specification. It is also an essential element in the management of quality [7.17].

The estimation of the uncertainties of the measuring system has been carried out according to the recommendations given in [7.18]. Thus, the methodology and all the calculations were followed as to make it comparable to the uncertainties presented there. The uncertainties can be considered separately with regards to their random part and the systematic contribution, but both are combined and treated as if they are equivalent.

7.9.1 Random uncertainties

The random part of uncertainty, characterising the repeatability of the measurement is approximately given by the relative standard deviation, σ_r , which is calculated using n individual measurements, according to:

$$\sigma_r = \frac{1}{x} \sqrt{\frac{\sum_{i=1}^n (x_i - x)^2}{n-1}} \quad (7.5)$$

where: x_i – the measured value of the quantity,

x – the mean value of all the measurements

The random part of the uncertainty, μ_r is given by:

$$\mu_r = \lambda \cdot \tau \cdot \sigma_r \cdot \frac{1}{\sqrt{n}} \quad (7.6)$$

where: λ – the T-Student factor, τ – the probability factor

For number of measurements $n = 5$ the T-Student factor is $\lambda = 1.4$, and the probability factor $\tau = 2$ (for *Probability = 95%*) [7.18], we obtain the random part of the uncertainty, μ_r :

$$\mu_r = 1.2522 \cdot \sigma_r \quad (7.7)$$

7.9.2. Systematic uncertainties

A rectangular probability distribution of an individual uncertainty contribution may be an utmost limit to the real distribution, whereas the combination of several contributions with rectangular characteristics leads to a Gaussian distribution of the total systematic error, which corresponds to practical experience [7.18]. The measurement of magnetic field, H , is achieved by means of two orthogonal sensors. Practically, it can be assumed that both sensors have the same inaccuracy of the measurement. Therefore, we can write that:

$$\varepsilon_H = \varepsilon_{H_x} = \varepsilon_{H_y} = \sqrt{(\varepsilon_{H1})^2 + (\varepsilon_{H2})^2 + (\varepsilon_{H3})^2 + \dots} \quad (7.8)$$

where: ε_H , ε_{H_x} , ε_{H_y} – the uncertainty of the magnetic field measured with sensor in the direction X and Y , respectively; $\varepsilon_{H1,2,3}$ – the estimated maximum errors of the contributing component.

Assuming that the inaccuracy of both H sensors is practically the same, the uncertainty of magnetic field strength measurement becomes:

$$\mu_H = \frac{2}{\sqrt{3}} \cdot \sqrt{\varepsilon_{H_x}^2 + \varepsilon_{H_y}^2} = \frac{2 \cdot \sqrt{2}}{\sqrt{3}} \cdot \varepsilon_H \quad (7.9)$$

where: μ_H – total uncertainty of the magnetic field strength measurement.

Similarly, for the contribution of flux density errors, we obtain:

$$\varepsilon_B = \varepsilon_{B_x} = \varepsilon_{B_y} = \sqrt{(\varepsilon_{B1})^2 + (\varepsilon_{B2})^2 + (\varepsilon_{B3})^2 + \dots} \quad (7.10)$$

where: ε_B , ε_{B_x} , ε_{B_y} – the uncertainty of the flux density sensor measured with the needle probes in direction X and Y, respectively; $\varepsilon_{B1,2,3}$ – the estimated maximum errors of the contributing component.

Also:

$$\mu_B = \frac{2}{\sqrt{3}} \cdot \sqrt{\varepsilon_{B_x}^2 + \varepsilon_{B_y}^2} = \frac{2 \cdot \sqrt{2}}{\sqrt{3}} \cdot \varepsilon_B \quad (7.11)$$

The total systematic uncertainty is then

$$\mu_S = \sqrt{\mu_H^2 + \mu_B^2} \quad (7.12)$$

7.9.3. Total uncertainty

The total uncertainty, u_{tot} , is then obtained by means of the following equation:

$$\mu_{tot} = \sqrt{\mu_r^2 + \mu_s^2} \quad (7.13)$$

The components contributing to the uncertainty of the used H and B are presented in the Table 7.1

Table 7.1: Errors contributing to the systematic uncertainty

ORIGIN	ERROR CONTRIBUTION $\varepsilon(\%)$
For Sensors (H)	
Calibration of H-sensor	3
Voltage measurement	0.01
For Needle Probes (B)	
Thickness of the sample	1.0
Voltage measurement	0.01
Distance between Needles	0.07

Substituting the values from the Table 7.1 into equations (7.7)-(7.11), respectively, we obtain: $\mu_s = 5.0 \%$

The values in table 7.1 have been estimated in the following way:

It has been suggested in [7.19] that the final random uncertainty should be averaged over all measurements and all samples on the condition that random uncertainties should follow a normal distribution. Therefore the random uncertainty averaged over all measured points is $\mu_r = 1.04 \%$.

Thus, the total uncertainties calculated by means of equation (7.12) is 5.0% .

a) Calibration of the sensors (H)–The H -sensors have been calibrated as described in section 7.9.3. The maximum error did not exceed 3% of the errors contributing to the systematic uncertainty of the measurement (see figures 7.5 a, b and c; and for calibration results see Appendix C) thus this value was taken for the uncertainty calculations.

b) Voltage measurement – the manufacturer of the data acquisition card guarantees that total error of voltage measurement is below 0.01% .

c) Thickness of the sample – the thickness has been measured with an aid of electronic micrometer with a precision of 0.0025 mm . The thinnest sample was 0.26 mm thick, which gives an error of measurement 1.0% .

d) Distance between the needles – the minimum distance between the needles was 7.30 mm . Calculation of the error from these values yields 0.07% .

7.10 References

- [7.1] Unisil and Unisil – H, A.C. magnetization curve – Peak magnetic flux density vs peak magnetic field strength, European Electrical Steels Ltd.
- [7.2] Sentron Hall Elements (2004), Info@sentron.ch
- [7.3] R. Boll and K. J. Overshott (1989), Magnetic sensors”, VCHPublishers, NY, p. 36
- [7.4] D. Jiles (1991), “Introduction to magnetism and magnetic materials”, Chapman and Hall, 1st Edition, p. 55.
- [7.5] S. Zurek and T. Meydan (2004), “A novel capacitive flux density sensor, Proceedings of 5th Conference on European Magnetic Sensors and Actuators (EMSA), 4-7, Cardiff, United Kingdom.
- [7.6] Vorrichtung zum Messen des Wechselinduktionsflusses oder der Flussänderung inferromagnetischen Materialien aus der Induktionsspannung, “Apparatus for the measurement of the rate of change of magnetic induction or flux density inferromagnetic materials from induced voltage”, Austrian Patent Nr 180990
- [7.7] J. S. Oledzki (2003), “The needle method development for magnetic measurements”, SMM16, Germany.
- [7.8] G. Loisos and A.J. Moses (2001), “Critical evaluation and limitations of localised flux density measurements in electrical steels”, IEEE Trans. Magn., 37, No 4, , pp. 2755-2757

- [7.9] M. Enokizono, M. Morikawa and K. Kawamura (1996), "Distribution of two-dimensional magnetic properties in three-phase induction motor model core", IEEE Trans. Magn., 32, No. 5, pp. 4989-4991
- [7.10] K. Brix, K. A. Hempel and F. J. Schulte (1984), "Improved method for investigation of the rotational magnetization process in electrical steel sheets", IEEE Trans. Magn., MAG-20, No. 5, pp. 1708-1710.
- [7.11] National Instruments (2000), LabView tutorial manual.
- [7.12] Motion Toolbox™ User Guide (1997), "A library of LabView virtual instruments for motion control", Snider Consultants Inc.
- [7.13] Compumotor Division of Parker Hannifin Corporation (1992), 6000 Series software Reference Guide, Document No: 88-012966-01D, 5500 Business Park Drive, Rohnert Park, CA94928, USA.
- [7.14] Y Alinejad-Beromi, A.J. Moses and T. Meydan (1992), "New aspects of rotational field and flux measurement in electrical steel", Journal of Magnetism and Magnetic Materials, Vol. 112, pp. 135-138.
- [7.15] A.M. Gumaidh, W.L Mahadi, Y. Alinejad-Beromi, A.J. Moses and T. Meydan (1992), "Measurement and Analysis of Rotational Power Loss in Soft Magnetic Materials", 1st International Workshop on Magnetic Properties of Electrical Sheet steel under 2-Dimensional Excitation, Proceedings of the 93. PTB Seminar, pp 173 – 190.

Chapter Seven: Design and development of power loss system

- [7.16] A. T. J. Hayward (1977), Repeatability and accuracy, Mechanical Engineering Publications Ltd., London,
- [7.17] L. Henderson , M. Hall. J. Bartholomew, T. Drake and S. Harmon (2000)
“Magnetic Measurements for Instrument Calibrations: Are Yours Traceable?”
UKMAG, One day seminar, Warwick, U.K.
- [7.18] H. Sievert, M. Ahlers, B. Birkfeld, F. Conrnut, K. Fiorillo, A. Hempel,
T. Kochmann, A. Lebouc, T. Meydan, A.J. Moses, A.M. Rietto (1995),
“Intercomparison of measurements of magnetic losses in electrical sheet steel
under rotation flux conditions”, Commission of the European Communities,
Report EUR 16255 EN, EC Brussels, Luxembourg.

CHAPTER EIGHT

RESULTS AND DISCUSSION.

8.1 Introduction

The sensing unit comprising of an integrated 3-dimensional Hall effect sensor and four needles, as illustrated in figure 7.7(a), has been used to scan the field on the surface of a grain-oriented (g.o.) 3.25% silicon iron material. The sample was magnetised at 50 Hz along its rolling direction, and all the scans were performed at room temperature.

The needles were arranged orthogonally with the 3-D integrated Hall effect sensor whose sensitivity was $0.35\mu\text{V}/\text{A}/\text{m}$ at their centre. As a unit they were raster scanned (simultaneously) on the top surface of the sample at the steps of $50\ \mu\text{m}$.

Certain regions on the sample were marked out for scanning. Some of these scanned regions were within a single grain, while others covered areas across grains.

Images of the parameters of magnetic field (H), magnetic flux density (B), and power loss (P) were finally developed from the data obtained from the scans.

The power loss at each measuring point was determined from the components of B and H with the help of the computer program explained in section 7.8 based on the following equation:

$$P = \frac{1}{T\rho} \int_0^T (H_x \frac{dB_x}{dt} + H_y \frac{dB_y}{dt}) dt \quad (8.1)$$

which was introduced first as equation 7.4 in chapter 7.

This equation represents the sum of eddy current and hysteresis losses due to magnetisation in any direction in the plane of the sample, and can conveniently be used for power loss measurements [8.2][8.3]. The following sections show the results and analysis of the findings of the local field and power loss distribution in the grain oriented 3.25% silicon iron sample used.

8.2. Grain-Oriented electrical steel sheet

The high-permeability grain-oriented 3.25% silicon iron sample used for this project was obtained from Cogent Power Limited (Newport). It had the length and width of 100 mm and 90 mm respectively (the rolling direction along the width), and a thickness of 0.26 ± 0.02 mm. The grains structure of the material was visible from both surfaces. The average grain diameter was about 15 μ m.

The original coating on the sample had been removed to enable the grains to be visible from both surfaces. It was then coated with a thin layer of lacquer, and because of the transparency of the lacquer, the grains could still be seen. In this case, the benefit of the original surface coating of the sample is removed. Perhaps, as a result, there might be small increases in loss, and also the stress sensitivity may not so good. However, this is not important for the demonstration of the system's capability to detect localised power loss.



Fig. 8.1: Grain-oriented electrical steel showing regions A, B, C, D and E which were scanned on the top surface.

Regions A and C in figure 8.1 are two grains within which scans were performed. B, D and E are regions where scans were performed across two or more grains.

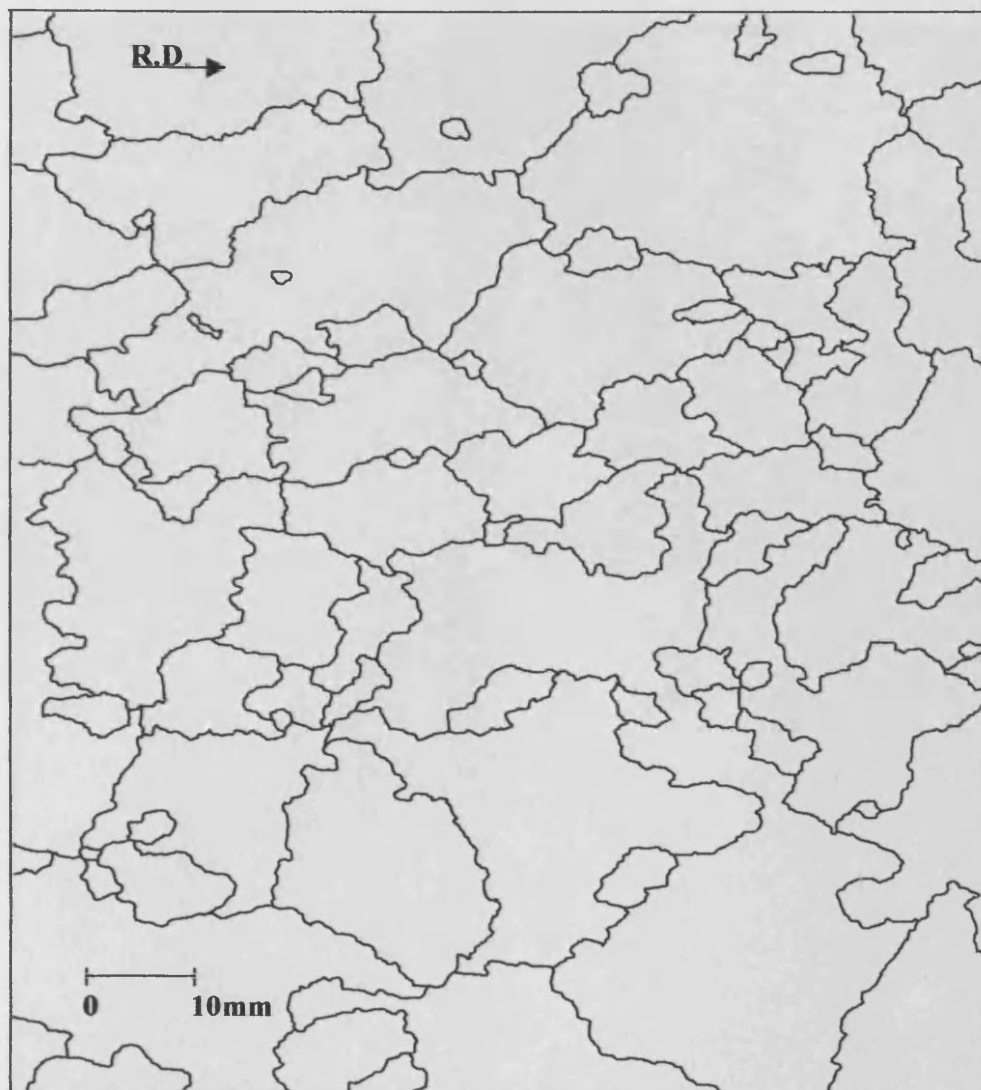


Fig. 8.2: Illustration of the outlines of the grains in the sample as captured by the scanner.

The image of the grain outlines illustrated in figure 8.2, was mapped out with the aid of a computer software.

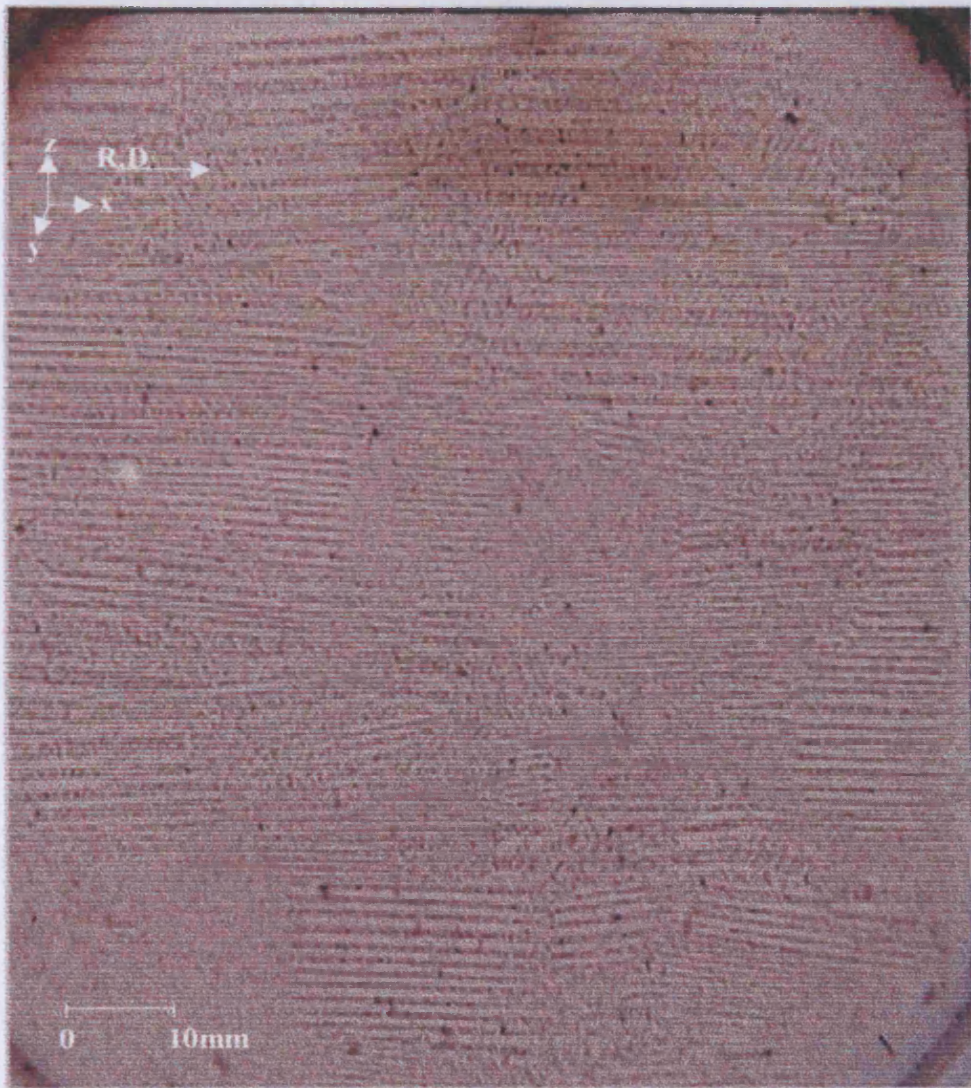


Fig.8.3 The general layout of the static domain structure of the sample (3.25% g.o. silicon iron material) as captured using a domain viewer.

To examine the grains more closely and to help ascertain the validity of the images of the grains produced by the scanner, a domain viewer was employed to capture the static domain structure of the sample. The result is shown in figure 8.3.

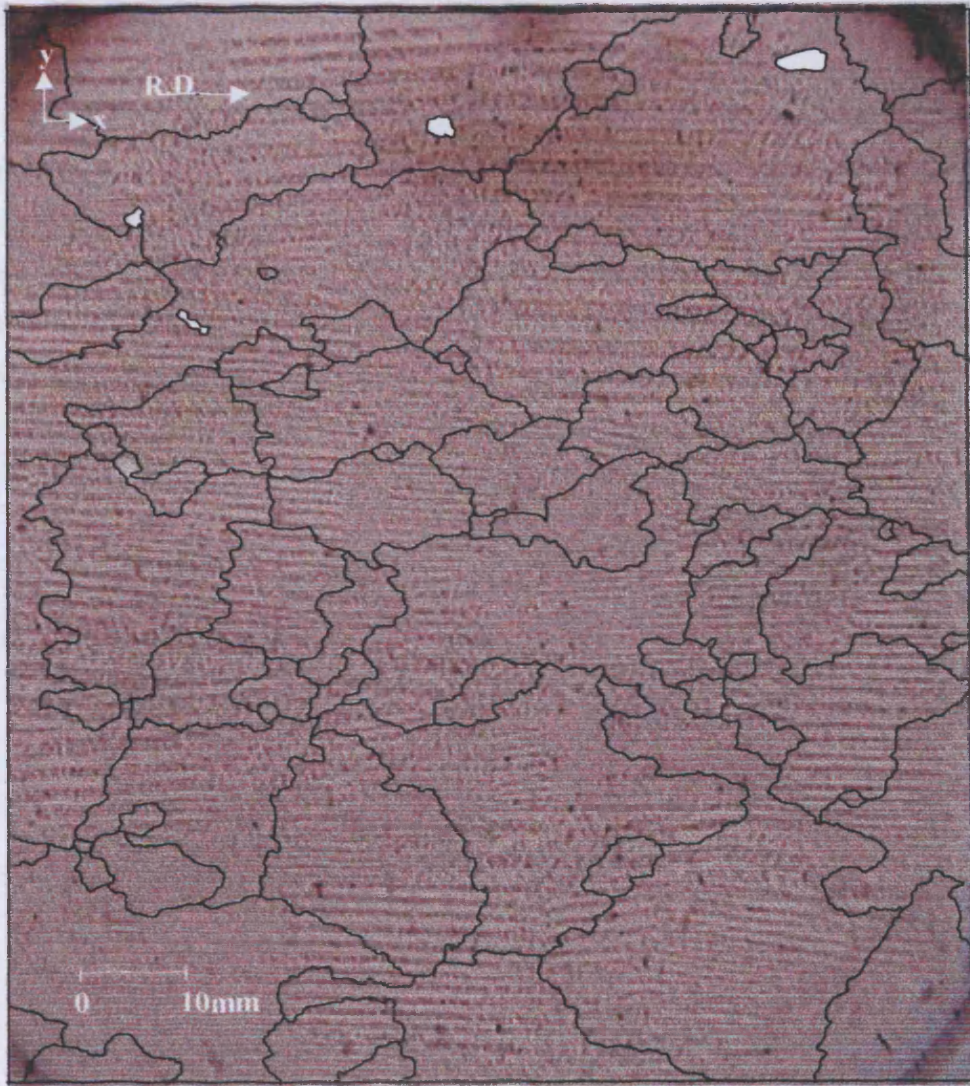


Fig. 8.4: The illustration of the grain outlines (fig. 8.2) superimposed on the static domains (figure 8.3).

The image of the grain outlines (figure 8.2.) was superimposed on the figure illustrating the static domain structure of the material (figure 8.3). The result is as shown in figure 8.4. This was done to match out the grain patterns against the domain patterns.

8.3 The sensor system

The “sensing area” of the Hall element is 0.25 mm x 0.25 mm and the orthogonal pairs of the needles were 7.3 mm and 6.3 mm apart as illustrated in figure 8.5. The sensors could only pick up average B and H data within the region under investigation. Also with the total surface area of the sensor compartment being 7.3 mm by 6.3 mm, was small enough to scan within individual grains such as A and C which are about 30 mm wide.

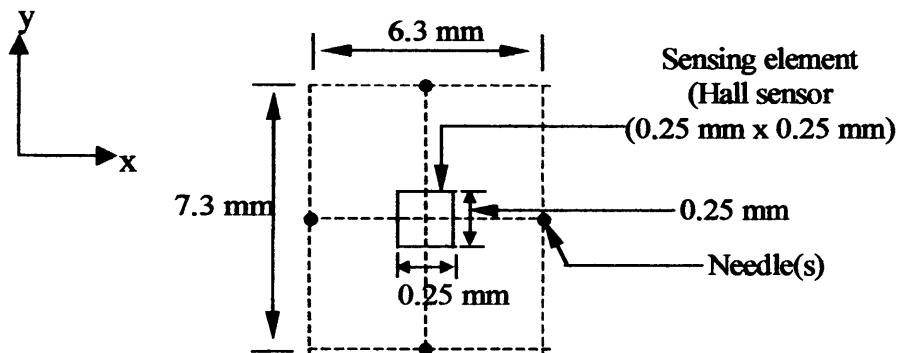


Fig. 8.5: Position of needle probes relative to the Hall sensor

Figure 8.6 illustrates how the data for the magnetic quantities B and H are obtained when the sensor is scanned. The arrows indicate the x and y directions in which components of H and B are detected.

The loss (P), at any instant, is averaged over the region with an area of 7.3 mm by 6.3 mm. The accurate measurement of loss depends on the flux density and field being uniform over the region, 7.3 mm length and 6.3 mm wide. It also depends on the area or region the sensitive part of the Hall effect sensor covers at a time. Ideally, the two regions should be the same. However, from the illustration in figure 8.6(a), it is observed that, the magnetic field (H_x) detected by the Hall effect sensor in the x-direction is averaged over an area of 0.25 mm by 0.25mm,

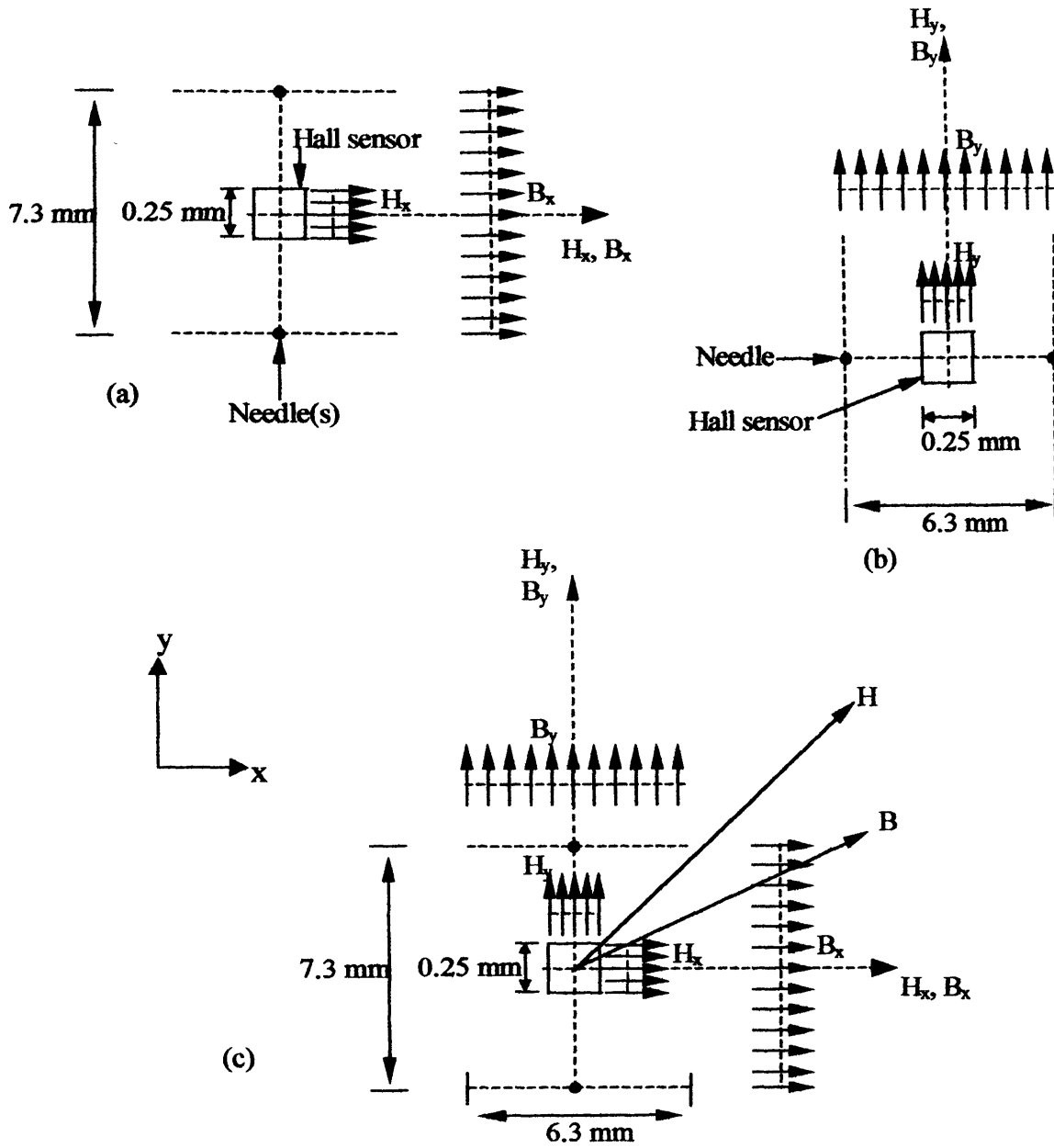


Fig. 8.6: Illustration of the components of detected B and H for averaged localised power loss. (a) H and B in the x-direction only, (b) H and B in the y-direction only, and (c) H and B in both directions. (The arrows indicate directions).

whereas the flux density (B_x) is averaged over 7.3mm by 6.3mm. Similarly, figure 8.6b shows that, the magnetic field (H_y) in the y-direction, is averaged over an area of 0.25 mm by 0.25 mm, while flux density (B_y) is averaged over 6.3 mm by 7.3 mm. This is unavoidable, primarily because of the dimensions of the Hall effect sensor (the position of the sensitive element) and also the design of the needle holder.

Figure 8.6(c) briefly illustrates how the power loss is determined by the integration of the products of the magnetic field (H) and flux density (B) components in x-axis and also in the y-axis.

8.4 Investigation into the images obtained.

As mentioned in chapter 7, the minimum steps in which the sensor unit was moved was 50 μm , and at each step peak values of magnetic field components H_z , H_x , and H_y were detected by the integrated Hall effect sensor, while flux density components; B_x and B_y were obtained from the needles.

At the commencement of the scanning process, the sensor unit moved from rest (zero point) and traveled from left to right (i.e. in the x-direction which was also the rolling direction). It moved in steps prescribed (either 50 μm , 100 μm or 200 μm). After traveling the whole length of a given path, the sensor unit moved straight back to the previous starting point. Then it advanced a step (a prescribed step e.g. 50 μm) in the y-direction, and then traveled along another path parallel to the first or previous one for the same distance. This procedure continued until a given area was covered.

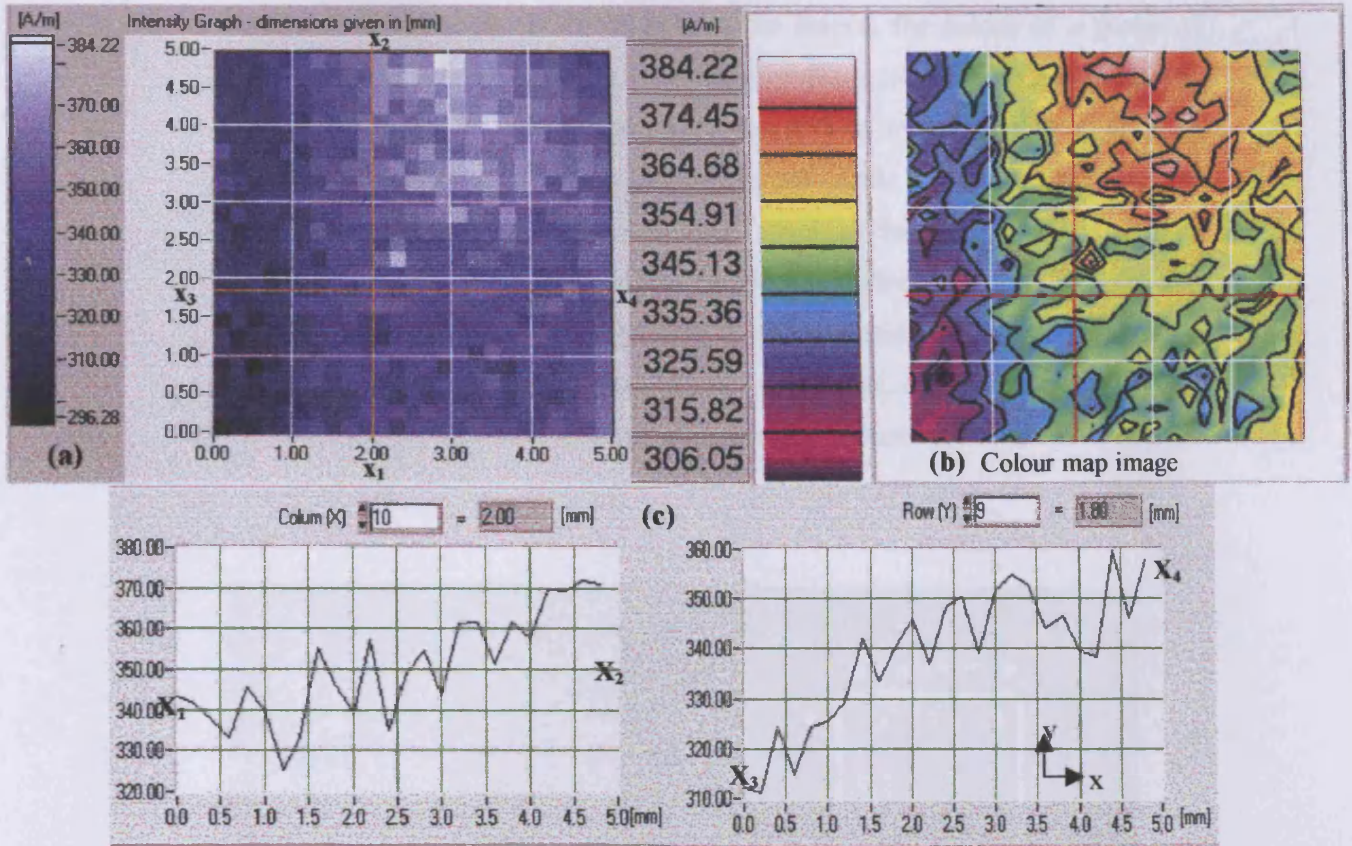


Fig. 8.7: Typical output result of the scanning system after a scanning process is completed. (a) the initial image produced (top left), (b) the colour map image showing the same results and (c) two signal profiles X_1X_2 and X_3X_4 obtained along paths x_1x_2 and x_3x_4 respectively.

The results of the scans are presented in the form of images (figure 8.7). All the parameters needed to determine the power loss in that region are presented in the form of images. The different shades of colour of the images represent the magnitude of the measured parameter at the various points within the considered region of the sample. This is illustrated by the legend which is to the left of each image.

As can be observed from figure 8.8, six hundred and twenty five (625) pixels (i.e. 25 x 25) fill the area of the initial output image. This applies to all the “initial images” (e.g., image (a) in figure 8.7) shown in this work unless otherwise stated. The “initial image” is so called because it is the first image obtained from the system after a scanning process is completed. Each pixel in the initial image indicates a point of contact between the sensor unit and the sample (i.e., the points

signals were detected). With the help of the legend, the colour of a group of pixels gives an indication of the magnitude of the considered parameter at that area. Furthermore, the area of the image was divided into a number of squares. Knowing the number of pixels in each square also made it easier to determine the average value of the magnitude of group of pixels of the same colour in an area. The profiles of signals taken over any area in a considered region also helped to determine the magnitude of the parameter under consideration in that area. The colour map image does not show any pixels, however, its distinct colour shades help to distinguish between different magnitudes more easily.

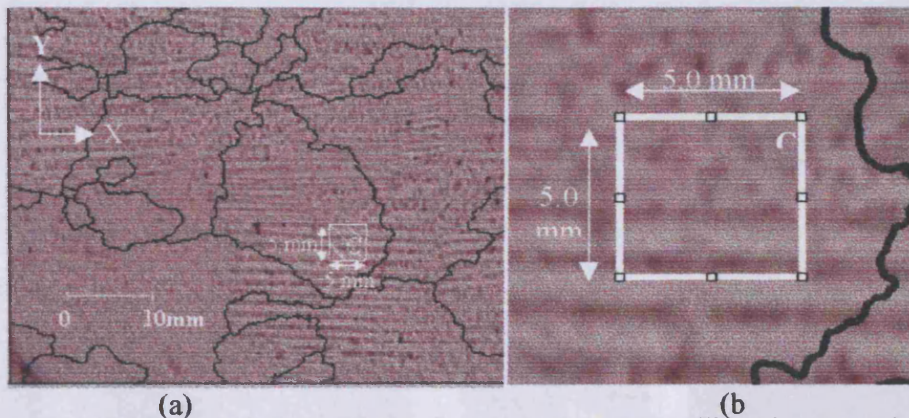


Fig. 8.8. Reproduction of the region C on the 3.25% silicon iron sample. (a) is a section of the sample including the region C (shaded), and (b) is region C magnified 5 times.

To investigate into the images obtained, two scans were carried out under the same conditions within the region C identified in figure 8.8, (reproduced from figure 8.1). The dimensions of the scanned region is given in millimeters (i.e. 5.0 mm x 5.0 mm) in the x-y plane.

The results of the two scan are presented from figure 8.9 to figure 8.13. The first scan is referred to as scan I, and the second, scan II. In each figure, the output of both scans (scan I and scan II are compared on the basis of one of the following

parameters: peak values of the magnetic field components H_z , H_x , and H_y ; the flux density components; B_x and B_y , and finally the power loss.

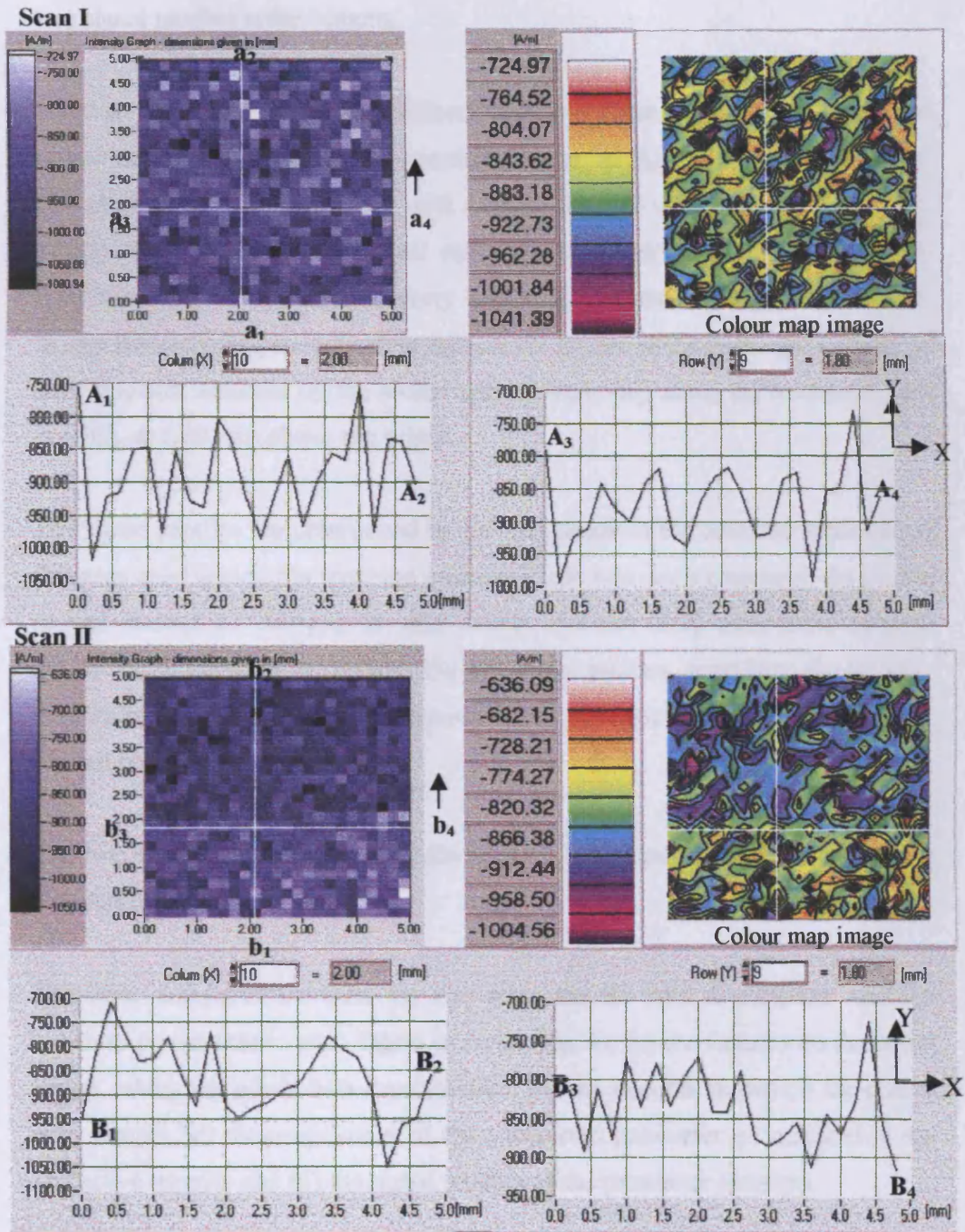


Fig. 8.9: Images of the vertical component of the stray magnetic field (H_z peak). Scan I: Signal A_1A_2 was obtained along the path a_1a_2 shown on both the initial image and the colour map, while A_3A_4 was obtained along path a_3a_4 . Scan II: Signal B_1B_2 was obtained along the path b_1b_2 shown on both the initial image and the colour map, while B_3B_4 was obtained along path b_3b_4 .

In each figure, like figure 8.7, four different output results are put together: the initial output image of the parameter scanned is shown at the top left, the same output but presented as a colour map image is also presented at the top right, and two signal profiles at the bottom.

The two signal profiles were obtained from two chosen paths along which the sensor unit traveled during the scanning process. In figure 8.9, for instance, the two profiles are labeled as A_1A_2 and A_3A_4 in the first scan (scan I). A_1A_2 is the profile of the detected peak signal values of parameter Hz in the y-direction at 2.00 mm from the left edge of every horizontal path traveled by the sensor unit during the scanning process, while A_3A_4 is the profile of the peak signal values of the parameter detected by the sensor unit at every step along the horizontal path (x-axis), at 1.80 mm above the origin.

The signal profiles are determined by the magnitude of the detected parameter at the steps used during the scanning process. In the two scans compared the system moved in steps of 200 μm . In other words, 200 μm (0.20 mm) is the distance moved from one pixel to another. The use of the profiles, apart from the legends, enables how to determine the magnitude of the parameter being considered at any desired point of the region.

The two chosen paths traveled by the sensor unit are indicated on all the colour map images (not labeled)

The items compared between the two scans are the field distribution and the localised power loss in each figure by observing the (a) the features on the initial image, taking the pixels into consideration, (b) the features shown on the colour map images, (c) the magnitudes of the considered parameter as indicated in the respective legends and (d) the signal profiles of the parameter obtained.

In figure 8.9, the initial output image of scan I (top left image) is compared with the one in scan II. The colour map image of scan I also corresponds to the one in scan II. Also the path a_1a_2 of scan I corresponds to the path b_1b_2 of scan II.

Therefore the signal profile A_1A_2 obtained along path a_1a_2 is compared with profile B_1B_2 obtained along b_1b_2 . Similarly, the profiles A_3A_4 is compared with D_3D_4 . Ideally, the compared features should look the same.

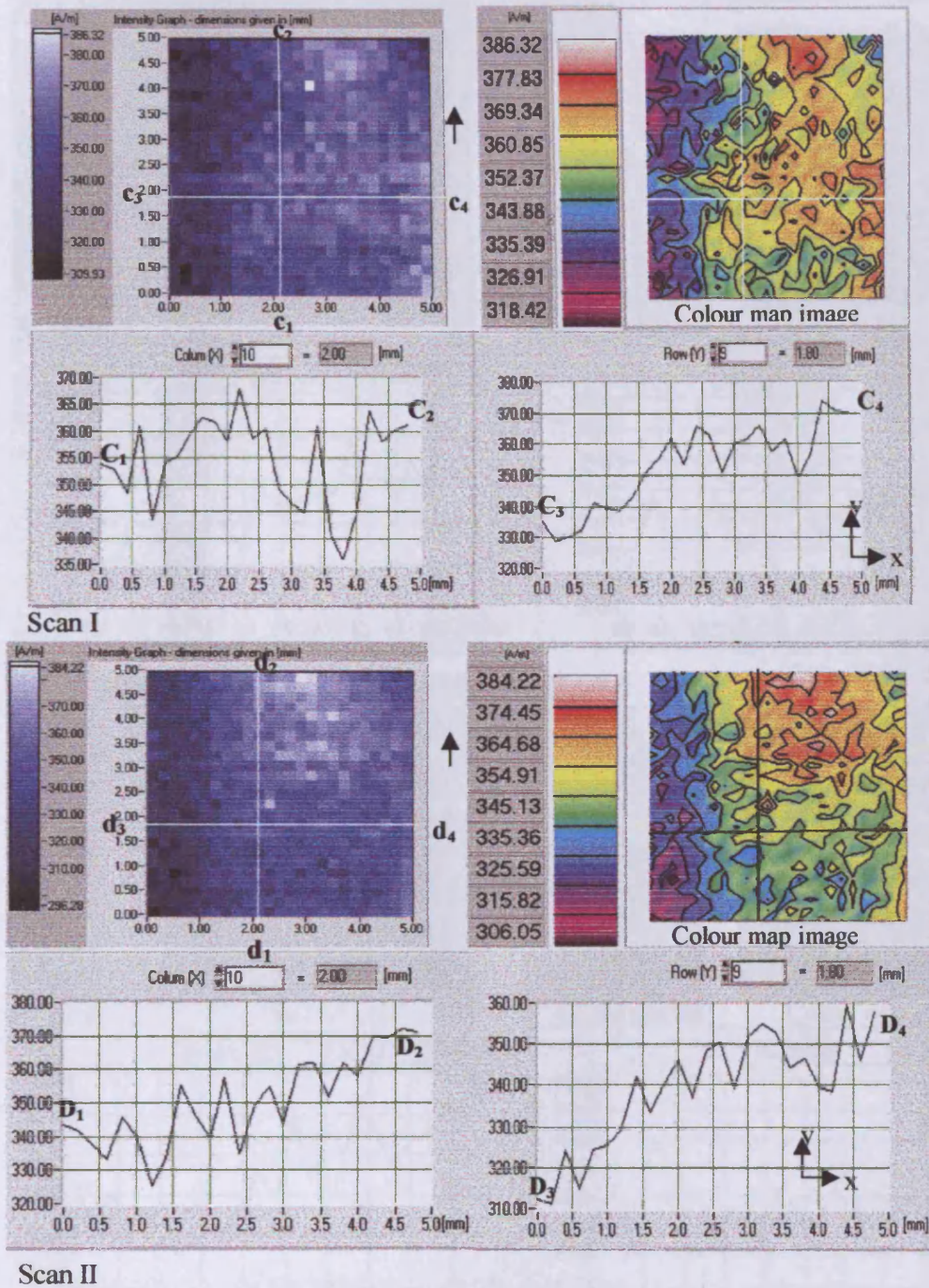
The parameter under consideration in figure 8.9 is the vertical component (H_z) of the stray magnetic field. Both positive and negative values can be observed in the legend. The upward vertical field detected by the integrated Hall sensor is considered positive, while the field into the sample (i.e., away from the sensor) is considered by the sensor as negative.

In figure 8.9 which compares the H_z in both scans, there is not much similarities in the images (both the initial and the colour maps). The profiles are not similar with the exception of profiles A_3A_4 and B_3B_4 . Their shapes are quite similar and their average detected field both within the region of 900 A/m.

In figure 8.10, images of the x component of the stray magnetic field in the two scans are compared. The chosen paths along which the signal profiles were obtained, though are the same as those in figure 8.9, are labeled c_1c_2 and c_3c_4 for scan I and d_1d_2 and d_3d_4 for scan II. Their corresponding profiles are C_1C_2 and C_3C_4 and then D_1D_2 and D_3D_4 respectively.

The features of the initial images are not the same but quite similar especially when the colour maps are compared. The figures shown on the legends are also the same or vary slightly. The signal profiles of C_3C_4 (scan I) and D_3D_4 (scan II) look similar.

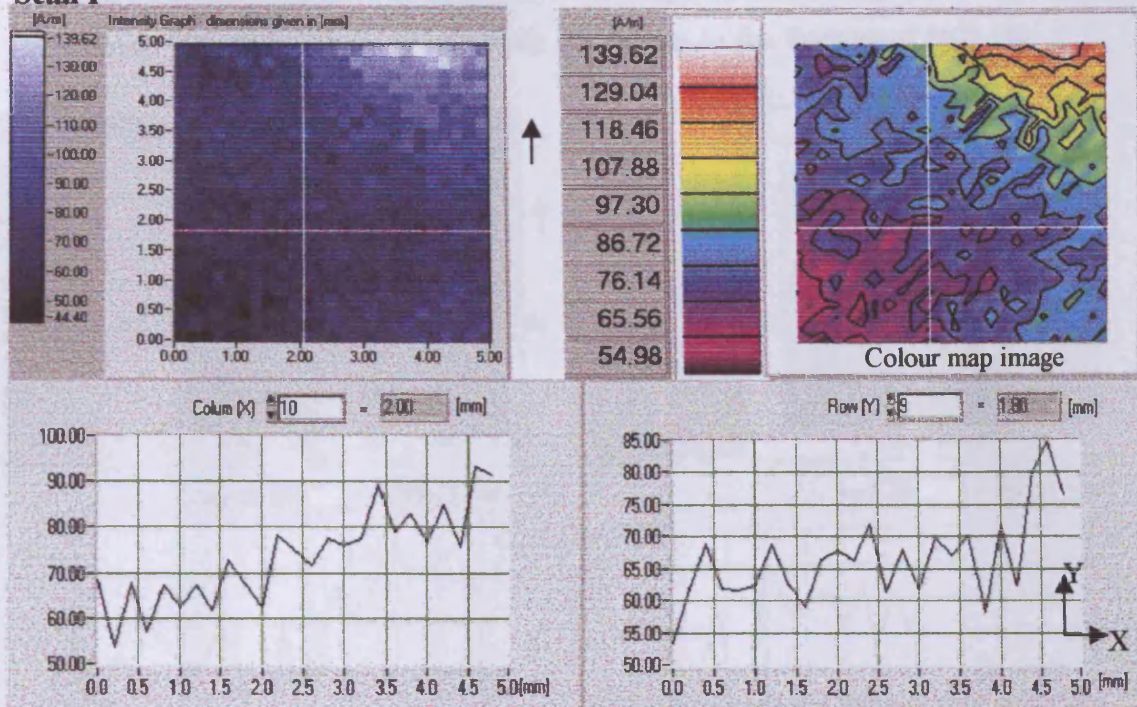
Figure 8.11 compares the out images of the y components of the stray magnetic field (H_y). Almost all the respective images look almost identical. The signal profiles also look alike, and the average field was about 70.0 A/m.



Scan II

Fig. 8.10: Image of the x component of the stray magnetic field (H_x peak). Scan I: Signal C_1C_2 was obtained along the path c_1c_2 shown on both the initial image and the colour map, while C_3C_4 was obtained along path c_3c_4 . Scan II: Signal D_1D_2 was obtained along the path d_1d_2 shown on both the initial image and the colour map, while D_3D_4 was obtained along path d_3d_4 .

Scan I



Scan II

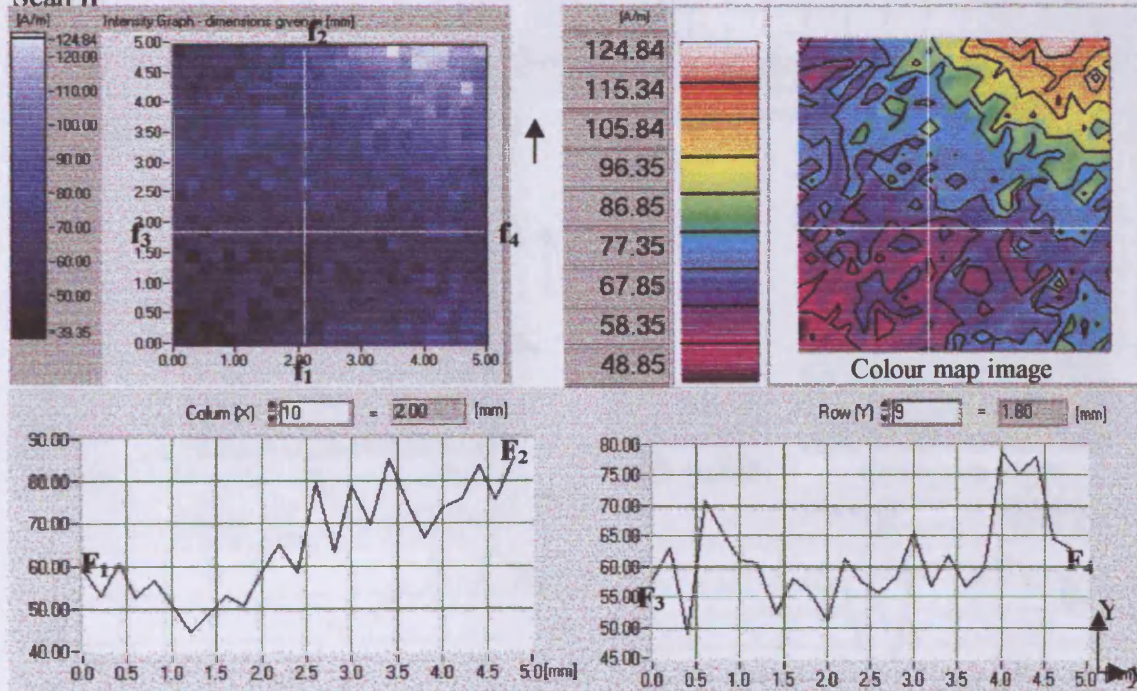


Fig. 8.11: Image of the y component of the stray magnetic field (H_y peak).

Scan I: Signal E_1E_2 was obtained along the path e_1e_2 shown on both the initial image and the colour map, while E_3E_4 was obtained along path e_3e_4 .

Scan II: Signal F_1F_2 was obtained along the path f_1f_2 shown on both the initial image and the colour map, while F_3F_4 was obtained along path f_3f_4 .

Figure 8.12 compares the x components of the magnetic flux density (B_x) of the two scans. Generally, There is not much similarities in the features of both the

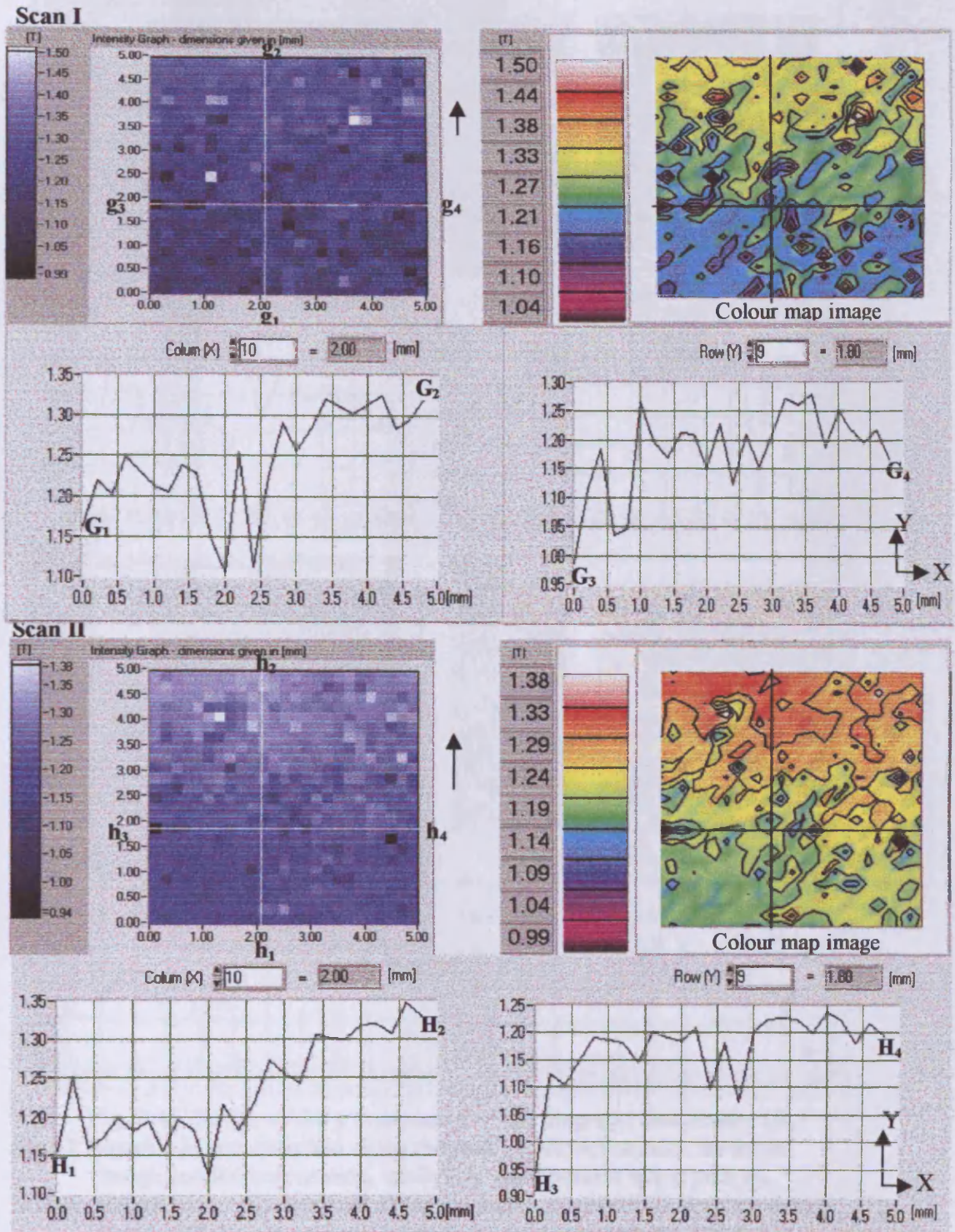


Fig. 8.12: Image of the x component of the magnetic flux density (B_x).

Scan I: Signal G_1G_2 was obtained along the path g_1g_2 shown on both the initial image and the colour map, while G_3G_4 was obtained along path g_3g_4 .

Scan II: Signal H_1H_2 was obtained along the path h_1h_2 shown on both the initial image and the colour map, while H_3H_4 was obtained along path h_3h_4 .

initial and colour map images. The legends also show differences in the values

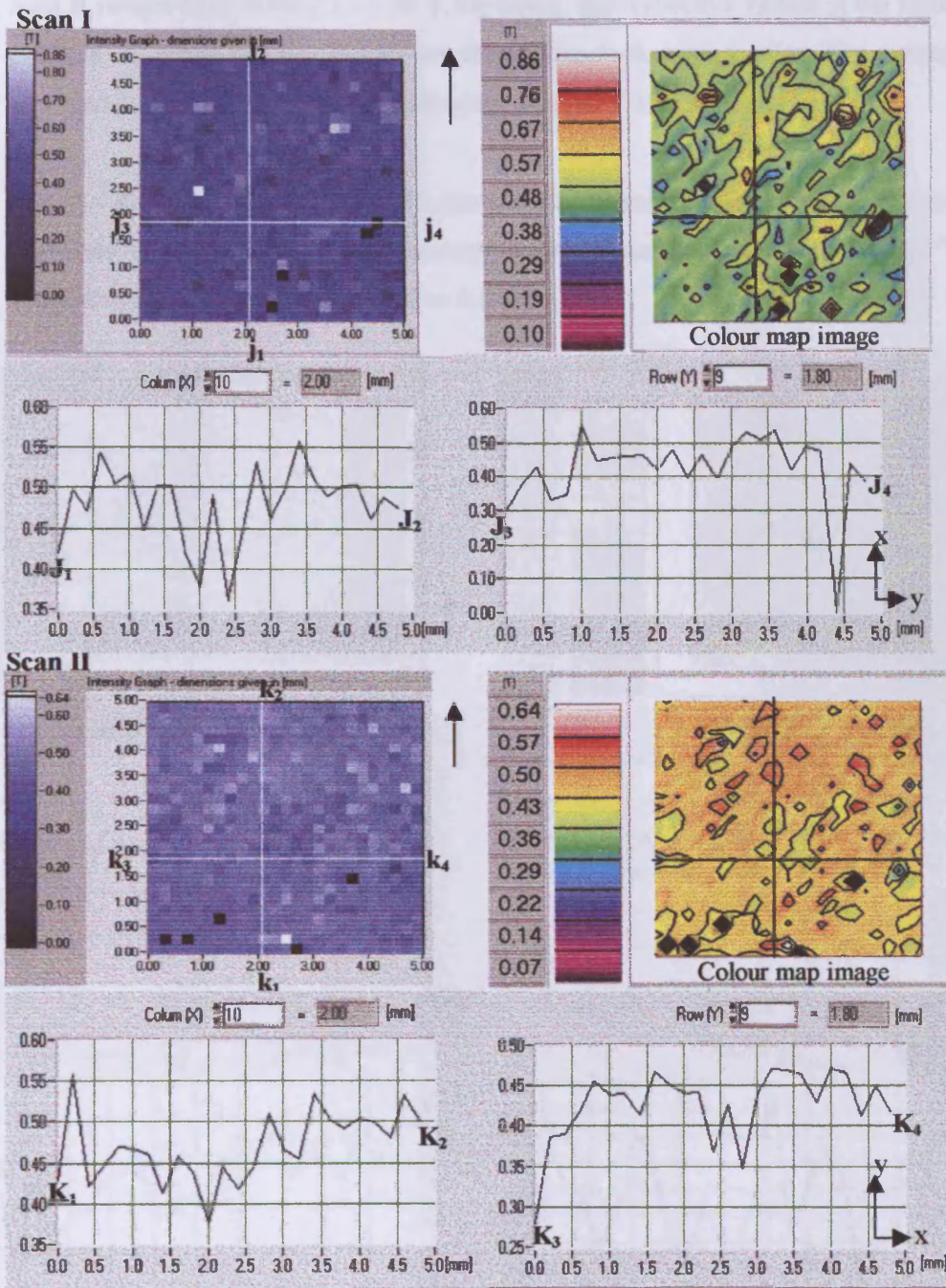


Fig. 8.13: Image of the y component of the magnetic flux density (B_y)
 Scan I: Signal J_1J_2 was obtained along the path j_1j_2 shown on both the initial image and the colour map, while J_3J_4 was obtained along path j_3j_4 .
 Scan II: Signal K_1K_2 was obtained along the path k_1k_2 shown on both the initial image and the colour map, while K_3K_4 was obtained along path k_3k_4 .

obtained, e.g. the values of scan I ranging from 1.04 T to 1.50 T while that of scan II ranges from 0.99 T to 1.38 T. However, the respective values of the signal profiles are equal and the signals are themselves look quite similar. The average flux density in both scans were determined as 1.30 T for both scans.

The results obtained in figure 8.13 show a considerable difference in the values indicated by the legends. While the output of scan I ranges from 0.10 T to 0.80 T, That of scan II ranges from 0.07 T to 0.64 T.

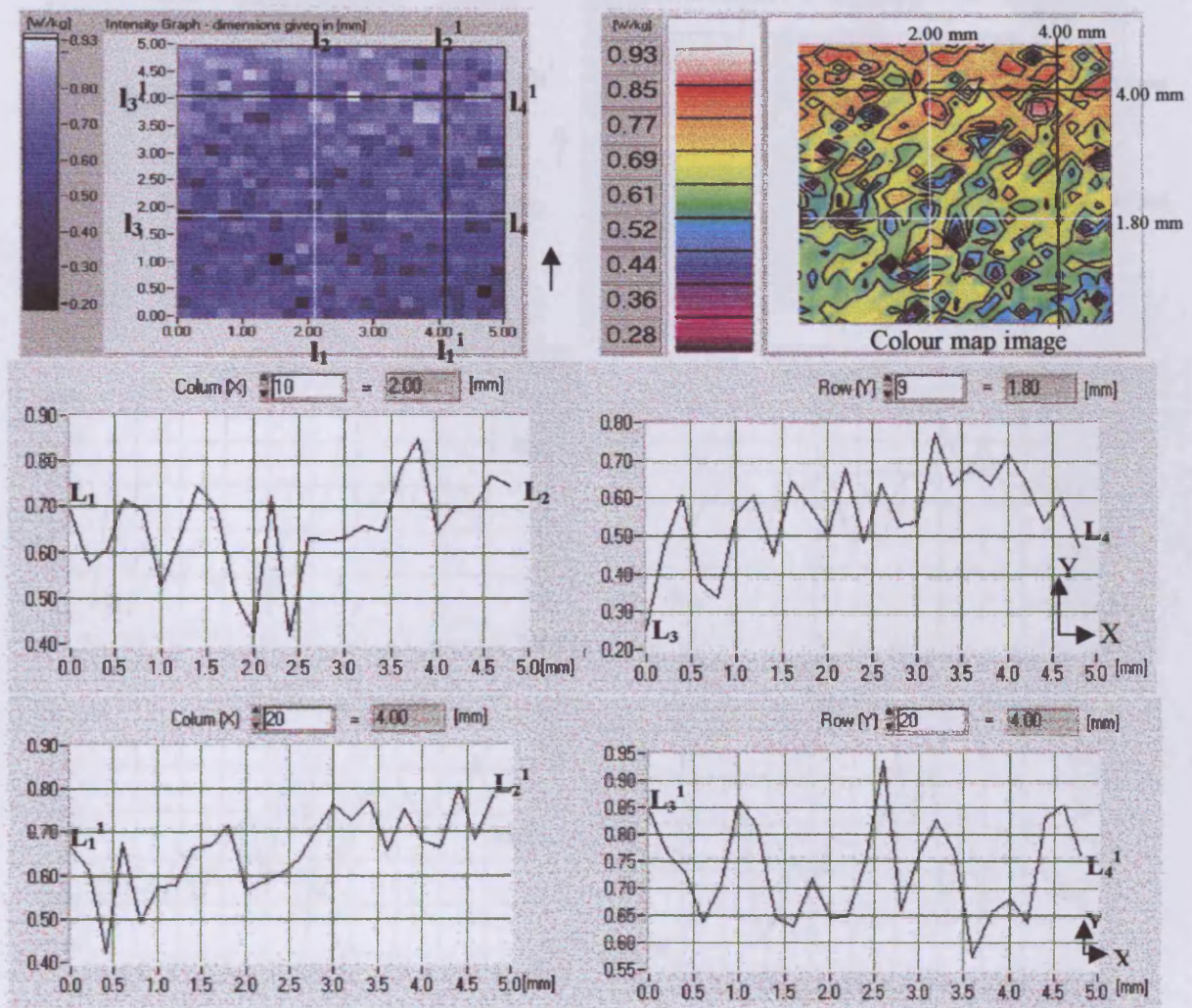


Fig. 8.14: Image of the Power loss (P) from scan I

L_1L_2 was obtained along the path l_1l_2 shown on both the initial image and the colour map, while L_3L_4 was obtained along path l_3l_4 .

Signal $L_1^1L_2^1$ was obtained along the path $l_1^1l_2^1$ shown on both the initial image and the colour map, while $L_3^1L_4^1$ was obtained along path $l_3^1l_4^1$.

Figure 8.14 shows the output images of the localised power loss of only scan I. The reason for this is that, two chosen sensor traveling paths indicated here as l_1l_2 and l_3l_4 and $l_1^1l_2^1$ and $l_3^1l_4^1$. The corresponding signal profiles for scan I are L_1L_2 and L_3L_4 and $L_1^1L_2^1$ and $L_3^1L_4^1$.

These are compared with results of figure 8.15 where the traveled paths and their respective signals are as follows: m_1m_2 and m_3m_4 and then $M_1^1M_2^1$ and $M_3^1M_4^1$.

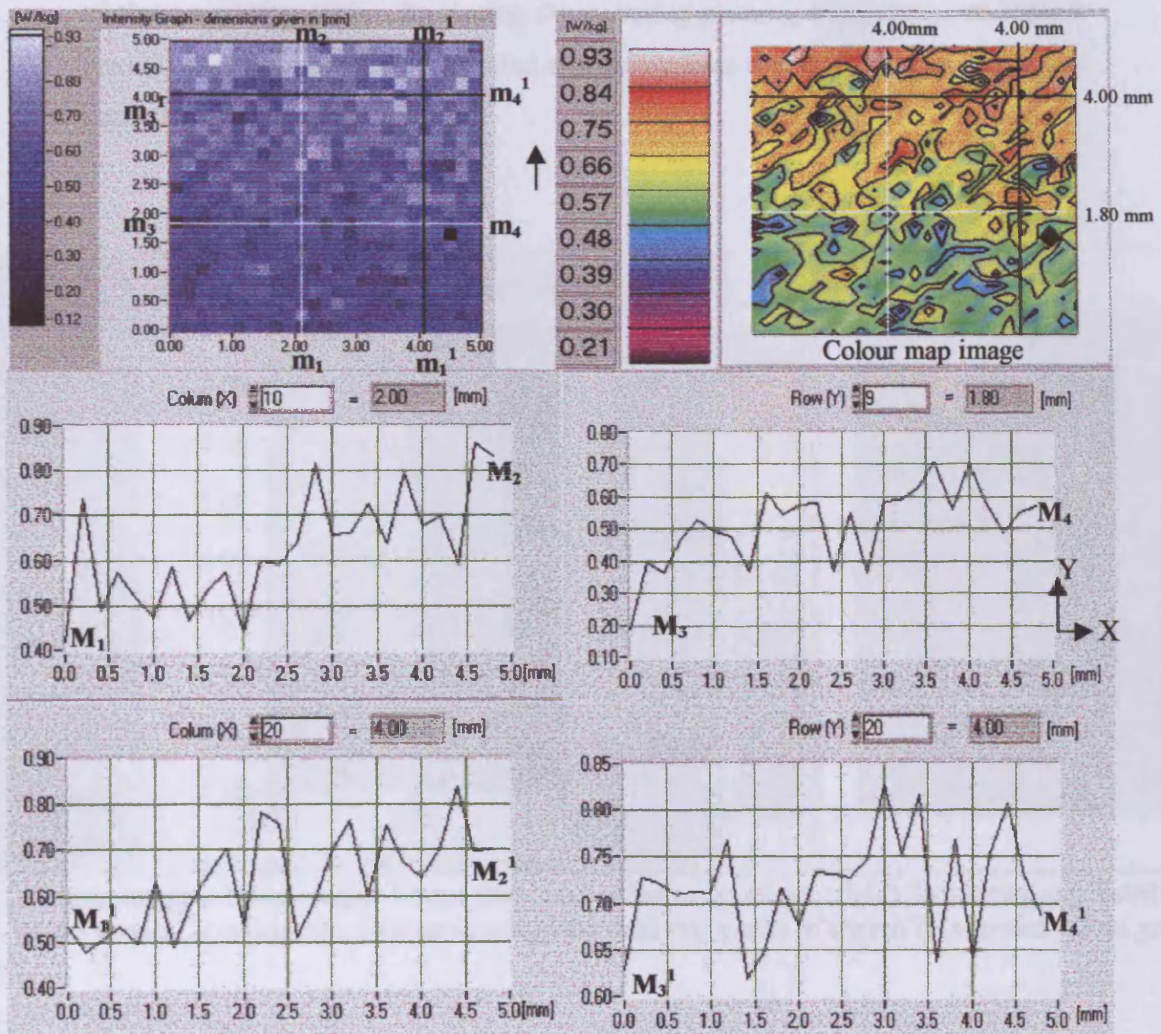


Fig. 8.15: Image of the Power loss (P) from scan II

M_1M_2 was obtained along the path m_1m_2 shown on both the initial image and the colour map, while M_3M_4 was obtained along path m_3m_4 .

Signal $M_1^1M_2^1$ was obtained along the path $m_1^1m_2^1$ shown on both the initial image and the colour map, while $M_3^1M_4^1$ was obtained along path $m_3^1m_4^1$.

Striking similarities are observed as the images of the two figures are compared. The initial output images are very close in appearance. The output figures indicated by the respective legends are almost the same. The signal profiles are almost similar.

8.5 Investigation of region E (across grain boundaries).

Region E in figure 8.1, the region in which this scan was performed, covers parts of three separate grains. So during the scanning process, the sensor unit moved across grain boundaries as illustrated with white lines in the initial output image in figure 9.1

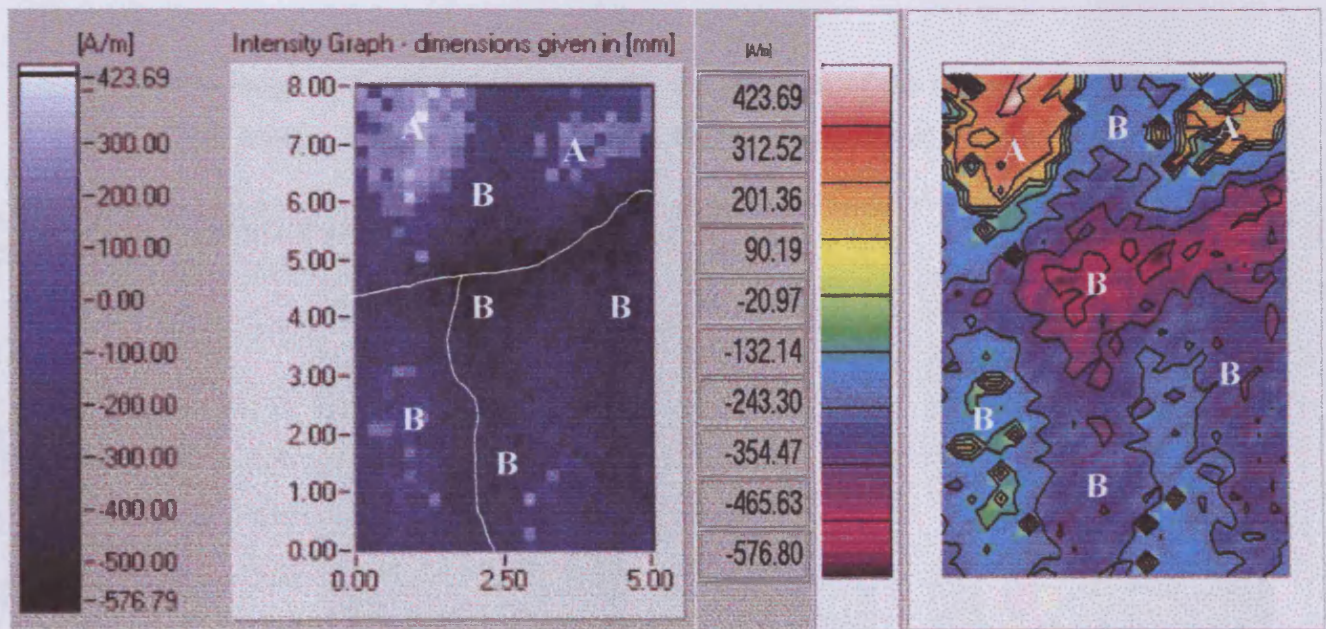


Fig. 9.1: Output images: Initial output image (left) and colour map image (right) illustrating the distribution of the vertical component of the stray magnetic field (H_z peak) of region E (scanned across grains).

The images shown from figure 9.1 to figure 9.6 were obtained from the scan over the region E (5.0 mm by 8.0 mm). In any of the figures (from figure 9.1 to 9.6), the initial output image is placed to the left while the colour map image is on the right. Using the pixels as mentioned in section 8.4, and putting the two images together, certain values were obtained.

Figure 9.1 illustrates the image of the stray vertical component of the magnetic field (H_z) obtained from the scan. With the help of the legend provided, the highest magnitude of the magnetic field (about 300 A/m) measured within the region of is in the upper section. It can be observed from figure 8.1 that, this section is within one grain. It can also be observed that, in average, the weakest stray magnetic field is about 20 A/m.

The colour map also indicate similar results. The images appear to confirm the presence of the boundaries. A close observation of the colour map reveals the field (H_z) in the area labeled (A) are in the upward direction, towards the Hall effect sensor, while those in the areas marked (B) are in the downward direction, moving into the sample, and the two fields are almost of the same magnitude.

The image in figure 9.2 illustrates the x component of the magnetic field (H_x). Both images seem to indicate that the highest magnitude of the field emanates

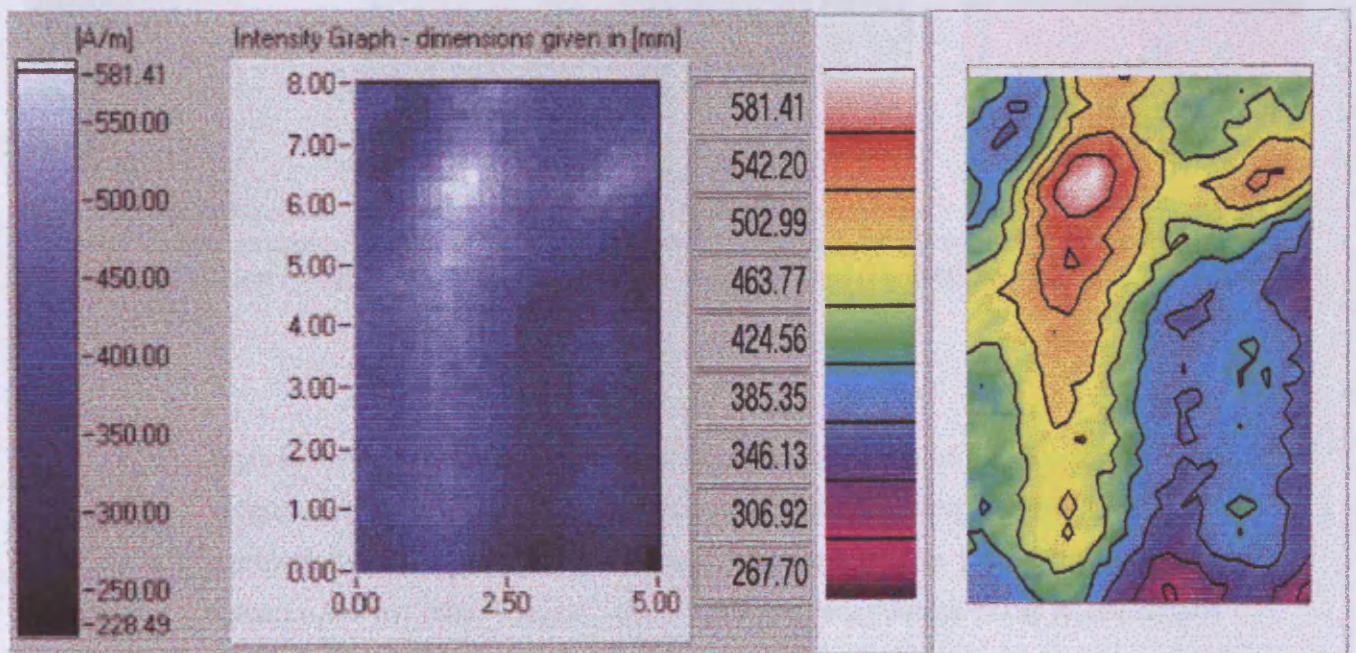


Fig. 9.2: :Output images: Initial output image (left) and colour map image (right) illustrating the distribution of the x component of the stray magnetic field (H_x peak) of region E. (scanned across grains).

from the area where all the three boundaries meet.

Figure 9.3 shows the images of the y component of the magnetic field (H_y). These images also show a higher magnitude of the field of about 450 A/m in the upper section of the image and lower values (about 82 A/m) at the lower section. The suspected position of the grain boundary is still observed. This is the section labeled XX.

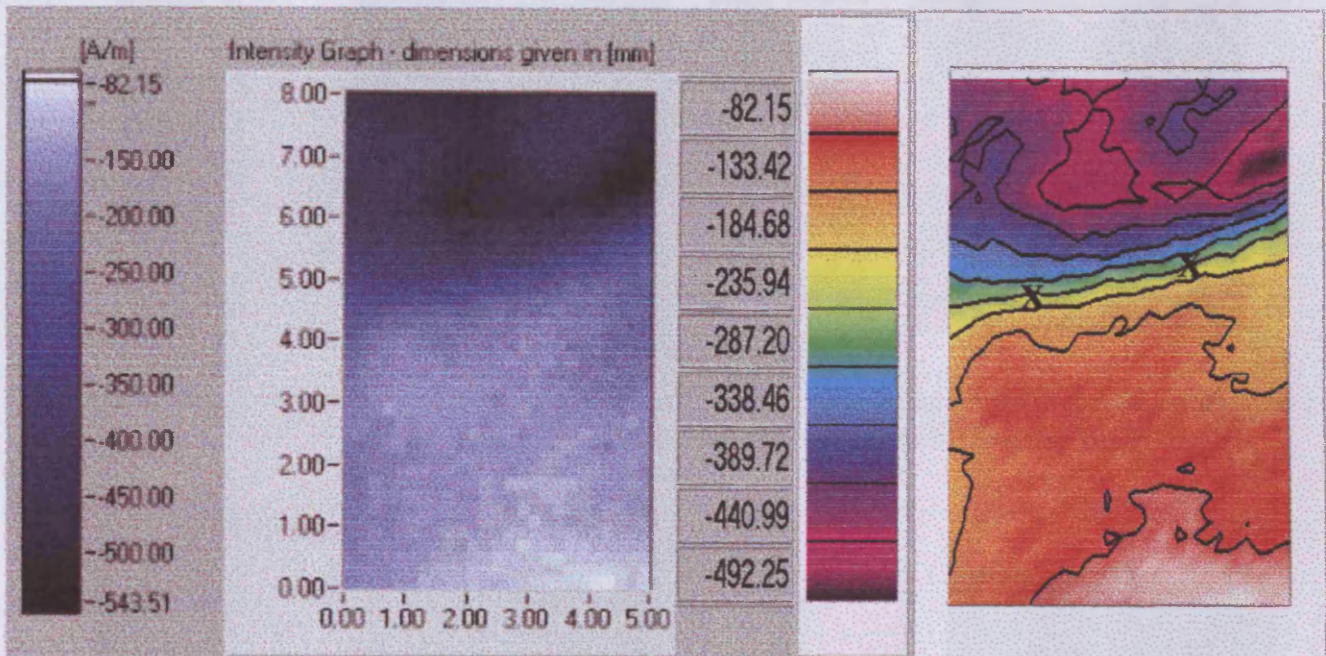


Fig. 9.3: Output images: Initial output image (left) and colour map image (right) illustrating the distribution of the y component of the stray magnetic field (H_y peak) of region E. (scanned across grains).

Figure 9.4 shows the output images of the x component of the flux density. The colour of the pixels and that of the colour map show the region divided into two horizontally around the middle area of the region. The image shares similar features like the other images, where the higher magnitudes of the parameter are at the upper section and the lower magnitudes at the bottom.

In figure 9.5 which illustrates the y component of flux density (B_y), the colour map image is not clear, however, it can be observed that the region is divided into

two just like the other images, and it can be noticed from the legend that the lower section has the lower field of the average of about 20 A/m.

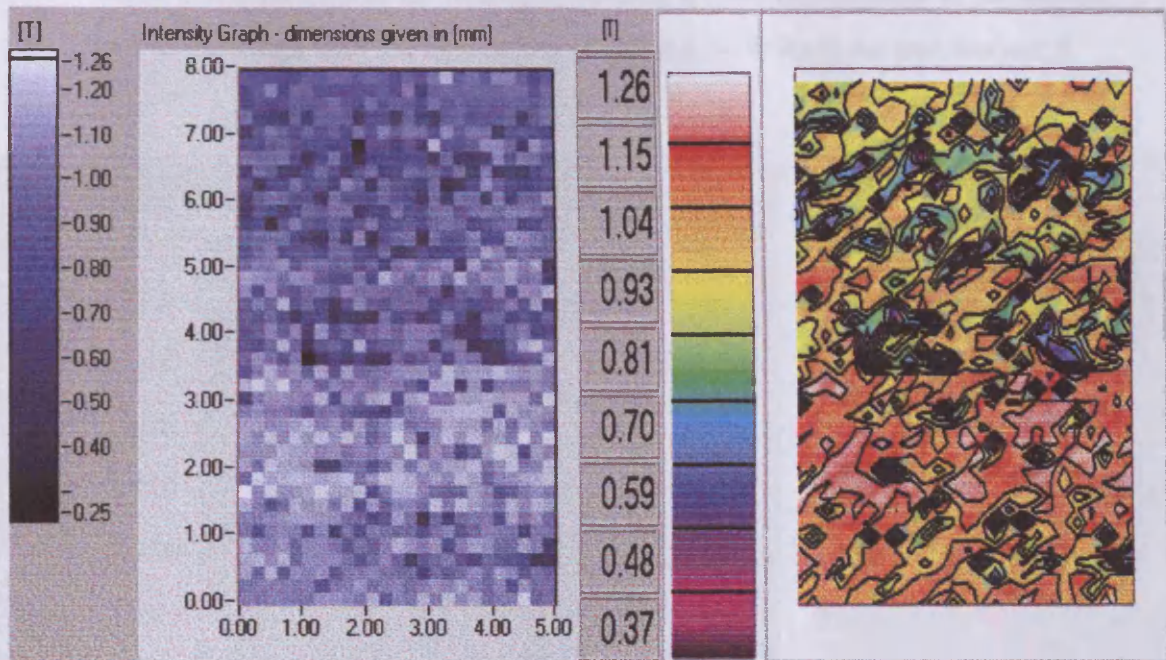


Fig. 9.4: Output images: Initial output image (left) and colour map image (right) illustrating the X component of the magnetic flux density (B_x) of region E. (scanned across grains).

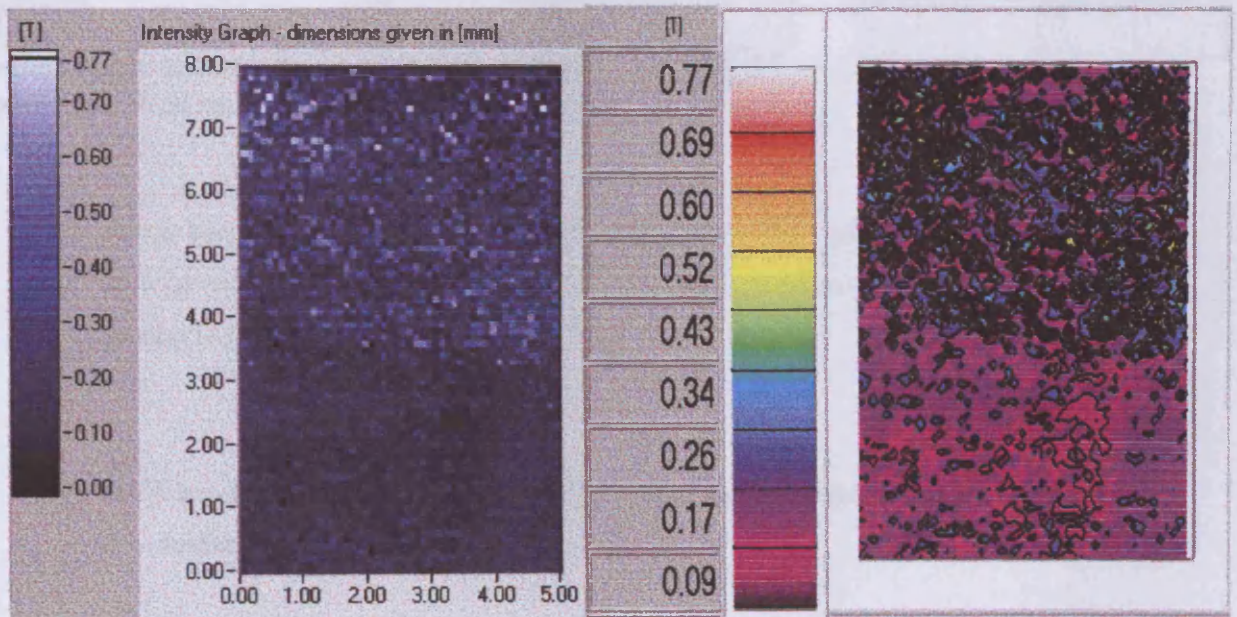


Fig. 9.5: Output images: Initial output image (left) and colour map image (right) illustrating the y component of the magnetic flux density (B_y) of region E. (scanned across grains).

The power loss images, especially the colour map in figure 9.6, show the loss which is non uniform in the region, however, it is more concentrated in the bottom part of the image with the highest loss of about 2.70 W/kg at the area marked X.

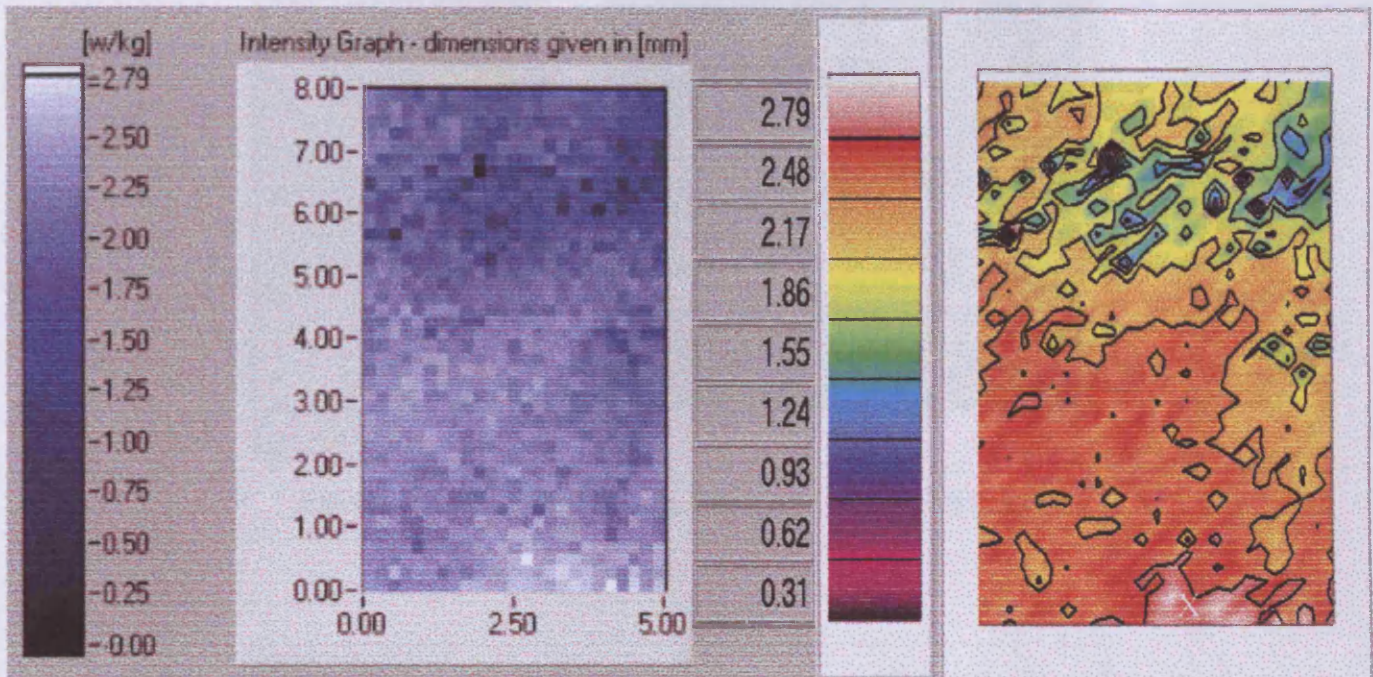


Fig. 9.6: Output images: Initial output image (left) and colour map image (right) illustrating the Localised power loss in of region E. (scanned across grains).

It can be observed from the colour map image that about 50% of the region has a loss of over 2.50 W/kg. That is much more than one would expect for a 3.25% silicon iron material.

8.6 Variation of power loss within individual regions and the use of a “Soken tester”.

Figure 10 shows an image (colour map) of the power loss in region D of figure 8.1, which is across grains. The colour map makes it possible to locate the

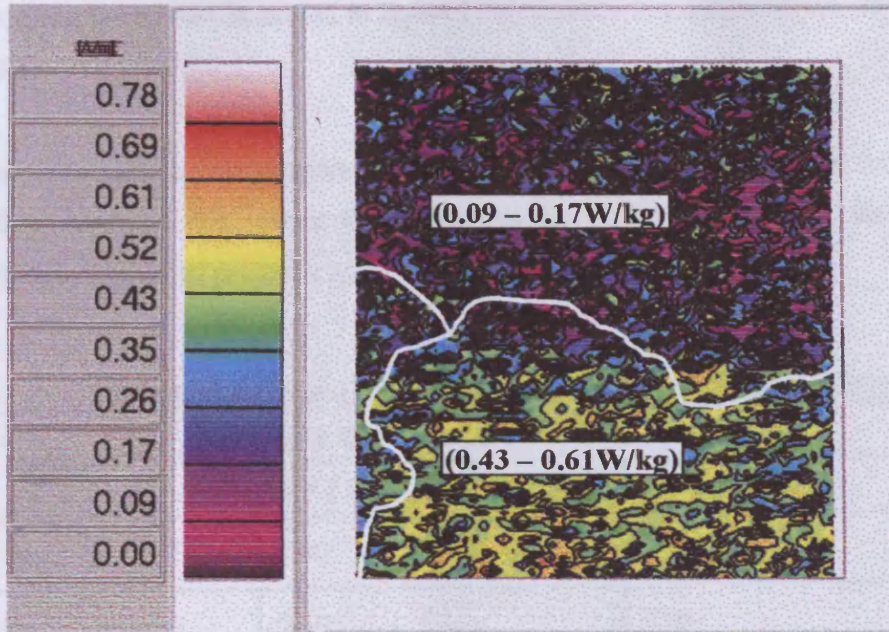


Fig.10: Power loss colour map (image) of region D (Fig.8.1)

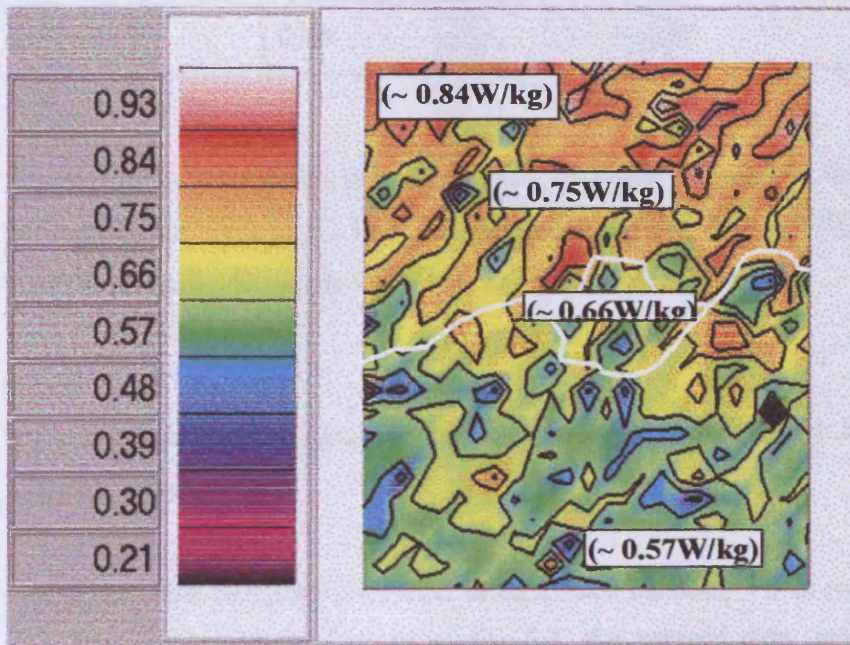


Fig.11: Power loss colour map (image) of region B. (Fig. 8.1)

average power loss in different regions within that particular scanned area. Similar regions have been identified in figure 11 too, which is a region labeled B in figure 8.1.

Even though the range of the values of the power loss given in figure 9.6 is more than expected (i.e., about 0.9 W/kg instead of 2.79W/kg given), the over all images appear to project a good view of what is expected.

Table 8.1: Results of a soken tester measurements on specified regions

Region	Iron loss (W/kg)	
	B = 1.0 T	B = 1.5 T
A	0.80	1.32
B	0.60	1.30
C	0.85	1.80
D	0.70	1.30
E	0.80	1.30

A soken (iron loss) tester, type DAC-TR-1 was used to measure the iron loss in the regions across A, B, C, D and E (figure 8.1) at flux densities (B) of 1.0T and 1.5T. The results, shown in Table 8.1, are quite close.

8.7 Variation of alternating power loss with induction in 3.25% grain oriented silicon iron.

Based upon the fieldmetric method as expressed equation 7.3 in section 7.8 and also the graphical illustration in section 8.3, the scanned data was used to plot graphs showing the relationship between the flux density and the total power loss, and also the losses in the x and y directions for regions A, B, and D (figure 8.1).

The individual regions were magnetised from about 0.8 T to about 1.7 T (the highest).

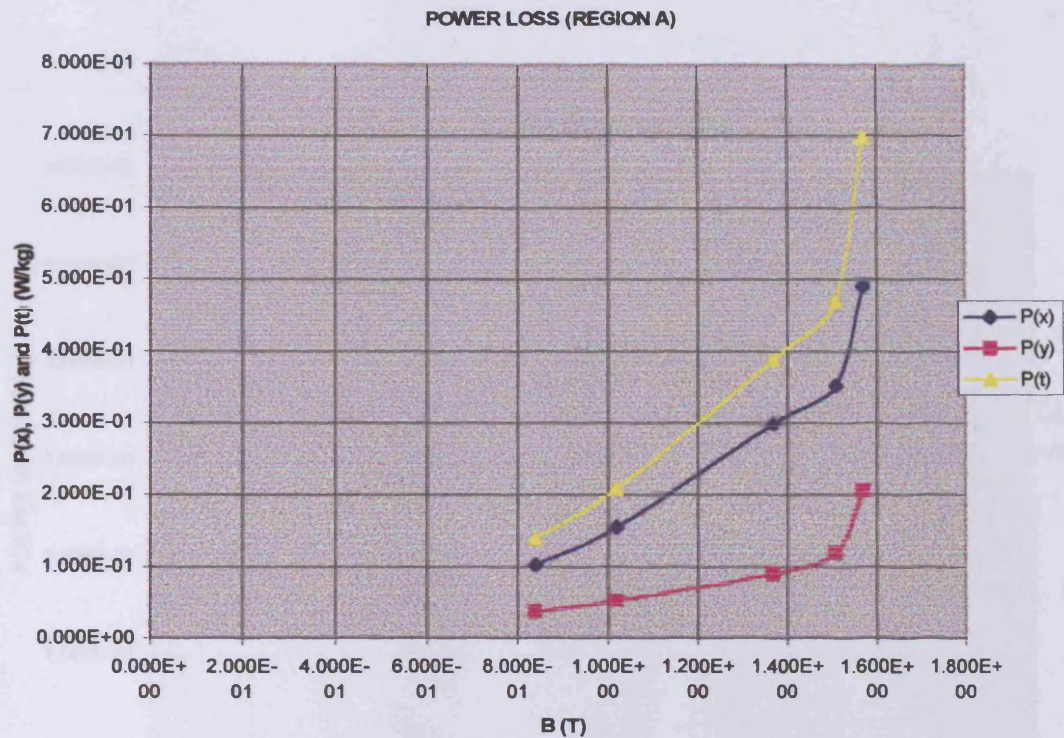


Fig. 12: Variation of power loss with flux density (T) in region A (within a grain) $P(\text{tot})$ is the total power loss, $P(x)$: x component of the power loss and $P(y)$: the y component of power loss.

In all the cases, at certain points, the magnitude of the flux density would not increase any more irrespective of what level the current was raised to.

It was observed from the graphs obtained that the levels of the y – components of the power loss were minimal compared to the x – components, and the total localised power loss, $P(t)$ was the sum of $P(x)$ and $P(y)$.

Figure 12 shows the localised power loss of region A within a grain. Figure 14, however, shows the localised losses in the region D at grain boundaries. It can be observed from figure 8.1 that region D, which has the highest localised power loss as shown from the graph, also has the highest concentration of grain boundaries [8.7].

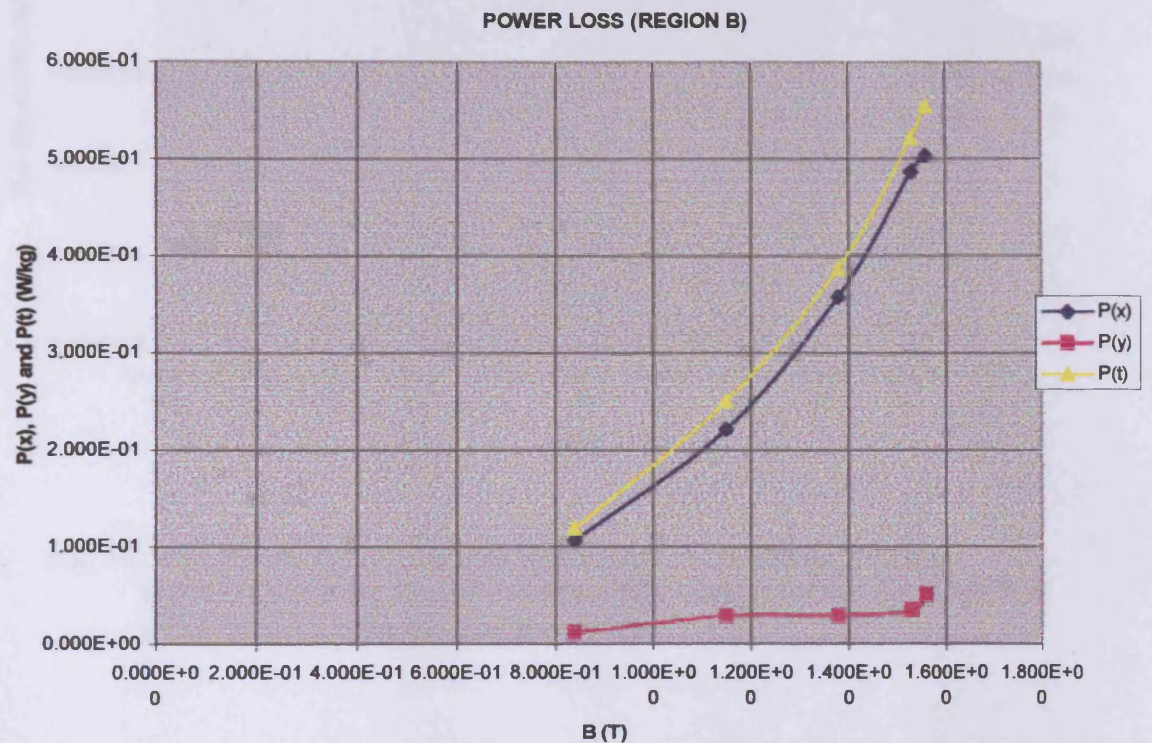


Fig. 13: Variation of power loss with flux density (T) in region B (across grains): P(t) is the total power loss, P(x): x component of the power loss and P(y): the y component of power loss.

It can be observed also that the higher the magnitude of P(y), the greater the difference between the P(x) and P(t).

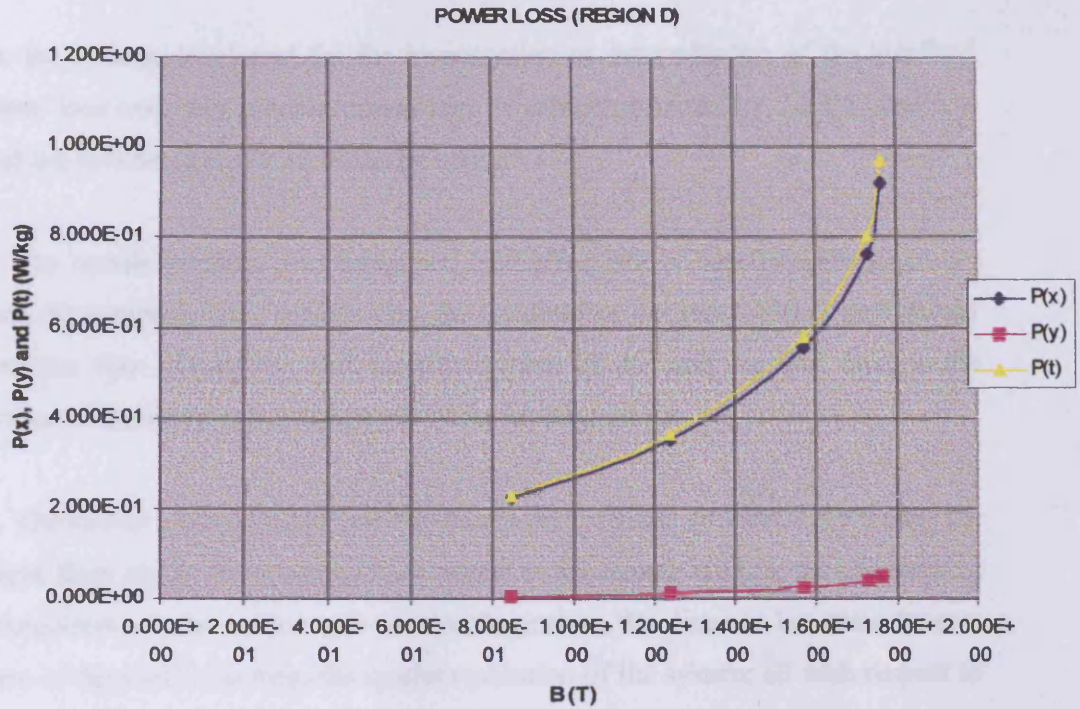


Fig. 14: Variation of power loss with flux density (T) in region D (across grains):P(tot) is the total power loss, P(x): x component of the power loss and P(y): the y component of power loss.

The nature of the graphs obtained indicate that the system measures alternating losses instead of rotational losses. Also all the three graphs show the evidence of the power loss in the y – direction. In every magnetic measurements of power loss in ferromagnetic sheets subjected to alternating magnetic field, the manufacturer measures P(x) as the total power loss, which is represented by equation 7.3. However, P(y), though may be small in magnitude it still contributes to the heating effect.

8.8 Conclusion.

For the system developed for the investigation or determination of the localised power loss over any predetermined area of a high permeability 3.25% electrical steel the following conclusion can be made:

- 1). The needle probes / 3-D integrated Hall effect sensor based system produces three dimensional maps representing the localized power loss which is determined from the flux density in, and the distribution of the stray vertical field at the surface of the electrical steel sample under investigation.
- 2). The clarity of the images was dependent on a number of factors, including the height from the 3- D integrated Hall sensor to the sample surface, the geometrical arrangement of the sensor and the needle probes, the distance between the two pairs of the needle probes, the spatial resolution of the system: all with respect to the rolling direction of the sample.
- 3). The overall mapped results showed a good correlation with predictions made from observed static domains. The correlation not only showed that loss varies from grain to grain, but it is non-uniform in the individual grains.
- 4). In the magnetic measurements of power loss in ferromagnetic sheets subjected to alternating magnetic field, the component, $P(y)$, should be considered since it contributes to the heating effect.
- 5). The system has good industrial potential and could be employed on the steel production line, especially where contour and colour images of power loss and other parameters of steel could be monitored on line. This will enable the detection of any deficiency arising during the manufacturing process.
- 6). With the advent of smaller and more sensitive sensors, the system has room for future improvement for more accurate loss measurements.

8.9 Reference

- [8.1] C. Bengtsson and H. Pfutzner (1984), "Stray fields at grain boundaries in magnetized stress coated Hi-B sheets, IEEE Transactions on Magnetics, vol. Mag-20, No. 5, pp.1478-1480.

- [8.2] H. Pfutzner, "Fundamental aspects of measuring field quantities and losses in anisotropic soft magnetic materials" JSAEM Studies in Applied Electromagnetics 1, Two – Dimensional Magnetic Measurements and its properties, 1993, pp 57 – 69.

- [8.3] A.J Moses,, and T. Meydan, (1993)"Results of Thermal and H-coil Sensor Measurements of Rotational Loss in Soft Magnetic Materials", JSAEM Studies in Applied Electromagnetics 1, Two – Dimensional Magnetic Measurements and its properties, pp71-82.

- [8.4]. H. Pfutzner, G. Schwarz. and J Fidler, (1983) "Computer-Controlled Domain Detector" Japanese Journal of Applied Physics, Vol. 22, No. 2, pp. 361-364.

- [8.5] K. Mohri and T. Fujimoto (1977), "New grain-detecting method for grain-oriented Si-Fe sheets with coating", Memoirs of the Kyushu Institute of Technology, Engineering No. 7, pp.33-37.

- [8.6] S. Tumaski. And M. Strbrowski (1998), "Electrical Steel sheet testing with the magetovision Method", Meas. Sci. Tech. 9, pp. 488-495.

- [8.7] C. R. Boon and J. E. Thompson(1965), "Alternating and rotational power loss at 50 c/s in 3% silicon iron sheets", Proc. IEE, vol.112, no. 11, pp. 2147 – 2151.

CHAPTER NINE**CONCLUSION AND FUTURE WORK**

For the system developed for the investigation or determination of the localised power loss over any predetermined area of a high permeability 3.25% electrical steel the following conclusion can be made:

(1). The magnitude of the surface field varies a great deal and does not appear to be directly related to individual grains. The very high field region extends over a region with grains of different size and orientation.

(2). If surface field measurements are used to predict local losses or domain structures then care is needed in the interpretations of the results obtained from one side of a sheet only because small changes in tangential field will also occur on either side. Normally it is assumed that any specific bar domain will be identical at either surface but this is expected not to be the case in practice because of the grain boundary profiles. Future studies are necessary to quantify the effect of this phenomenon in the interpretation of surface or bulk properties of electrical steels using surface field sensors.

(3). The combination of needle probes and 3-D Integrated Hall Effect Sensor based field scanning system produces three dimensional maps or plots representing the localised power loss which is determined from the flux density in, and the distribution of the stray vertical field at the surface of the electrical steel sample under investigation.

(4). The clarity of the images was dependent on a number of factors, including the height from the 3- D Integrated Hall Sensor to the sample surface, the geometrical arrangement of the sensor and the needle probes, the distance between the two pairs

of the needle probes, the special resolution of the system: all with respect to the rolling direction of the sample. The narrower the distance between the needles the better, to enable scan within a single grain. However, the geometrical dimensions of the “integrated probe system” depended on the dimensions of the hall sensor.

(5). In the magnetic measurements of power loss in ferromagnetic sheets subjected to alternating magnetic field, the power loss component, $P(y)$, should be considered since it contributes to the heating effect.

(6). The overall Mapped results showed a good correlation with predictions made from observed static domains. The correlation not only showed that loss varies from grain to grain, but it is non-uniform in the individual grains.

(7). The system has good industrial potential and could be employed on the steel production line, especially where contour and colour images of power loss and other parameters of steel could be monitored on line. This will enable the detection of any deficiency which arises during the manufacturing process.

(8). With the advent of a smaller and more sensitive sensors, the system has room for future improvement. It could be improved for more accurate loss measurement if the real magnitude of the over the sample surface and the fix in the material is detected, thus all errors reduced to the barest minimum.

Future work

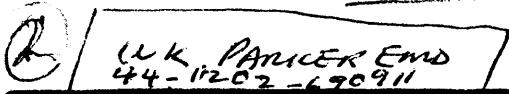
The advancement in technology has made it possible for 3-dimensional sensors which have smaller dimensions to be available in the market. More handy precision positions systems are also easily obtainable. A more accurate system can therefore be built more easily for further future work on the determination of power loss in grain oriented materials with smaller grains.

APPENDIX A

CHARACTERISTICS

OF

INTEGRATED 3-D HALL EFFECT SENSOR



SENTRON

Sentron AG, Baarerstr. 73, CH-6300 Zug, Switzerland
 Tel.: +41 41 711 21 70 Fax: +41 41 711 21 88
 E-Mail: info@sentron.ch

Products Support New Downloads How to find us Contact Home

Hall Elements

Switzerland.

SENTRON Hall elements are sensitive to magnetic field components parallel to the chip surface and not as conventional Hall magnetic sensors perpendicular to the device surface. This allows to manufacture unique Hall elements with unmatched performances:

The **CYH22** single-axis Hall element demonstrates world-record sensitivity by taking advantage from magnetic flux concentrators directly integrated on the chip. The element is particularly useful for applications where fields are weak or where the distance between a magnet and the sensor is high.

The **2D-VH-11** measures two magnetic field components simultaneously and in the same spot with an angular error of less than 0.1°. The sensitivity of the two axes matches to about 99.9% without adjustment. This element is particularly useful for high accuracy non-contact angular position/speed sensing over a wide temperature range.

The **3D-H-30** is our worldwide patented, true 3-axis single-chip Hall element.

Moreover, all of the above mentioned SENTRON Hall elements feature:

- a very high long term stability (the magnetic sensitivity does not vary more than 0.01 % over a year if the element is mounted on a ceramic substrate)
- high sensitivity at low bias current. A biasing current of 1mA per axis is sufficient to obtain a sensitivity between 100 and 400 mV/T with the 2D-VH-11 and the 3D-H-30 and up to 2500mV/T with the CYH22.

Hall Element	Features	Applications
High-sensitivity: <u>CYH22</u>	<ul style="list-style-type: none"> • sensitive parallel to the chip surface • integrated flux concentrators • very high sensitivity • low noise 	<ul style="list-style-type: none"> • long distance signal detection • current measurement • translation displacement • rotary displacement
Two-axis single-chip: <u>2D-VH-10 and 2D-VH-11</u> see demo: <u>angular position sensor</u>	<ul style="list-style-type: none"> • Measures the 2-axis of a magnetic field at the same spot. • Max. error from -10..60°C < 1° angle • High Magnetic Field Sensitivity • Low control current • Available in 8 Pin-SOIC and in chip form 	<ul style="list-style-type: none"> • Mapping of a magnetic field • 2-D position sensing • Contactless potentiometer • Angular position sensor for micromotors • Miniaturise contactless encoder

Three-axis single-chip:
3D-H-30 (0.3mm active zone)
3D-H-10 (0.1mm active zone)

- Measures the 3-axis of a magnetic field at the same spot.
- High Magnetic Field Sensitivity
- Low control current
- Available in 8 Pin-SOIC and in chip form

- Mapping of a magnetic field
- 3-D position sensing
- Contactless potentiometer
- Angular position sensor for micromotors
- Joystick

Integrated 3-Axis Hall Element**3D-H-30****Features**

- Measures the 3-axis of a magnetic field at the same spot.
- High Magnetic Field Sensitivity
- Low control current
- Available in 8 Pin-SOIC and in chip form

Application

- Mapping of a magnetic field
- 3-D position sensing
- Contactless potentiometer
- Angular position sensor for micromotors
- Joy-stick

Absolute Maximum Ratings

Item	Symbol	Condition	Limit	Unit
Max. Input Current	Ic	T = 300 K	5	mA
Max. Input Voltage	Vc	T = 300 K	15	V
Shield voltage	Vs	With respect to any other terminal	0 to -10	V
Operating Temp. Range	Topr.	at the nominal current	-40 to 110	°C
Storage Temp. Range	Tstg.		-40 to 125	°C

Typical Electrical Characteristics

Item	Symbol	Conditions	min.	max.	Typ.	Unit
Shield leakage current	Ileak	Vs = -10 V		1		nA
Nominal control current	Ic	See Ic in Fig.3			3	mA
Input resistance	Rin	B = 0mT, Ic = 3mA			1,8	kΩ
Output resistance	Rout	B = 0mT, Ic = 3mA			10	kΩ
Output voltage Sx1-Sx2 Sy1-Sy2	Vhx Vhy	Const. Current Drive B = 1T, Ic = 3mA			275	mV
Offset voltage	Voff	B = 0mT, Ic = 3mA	-3	+3	0	mV
Field equivalent output noise (peak-peak) X, Y	Bnoise	Within 10 min Ic = 3mA		±10		μT
Z	Bnoise			±30		μT
Sensitivity X, Y	Sx, Sy	Ic = 3mA	250	300	275	mV/T
Sensitivity Z	Sz	Ic = 3mA			100	mV/T
Temp. coef. of sensitivity	αS	B = 10mT, Ic = 3mA			0.1	%/°C
Temp. coef. of Vin	αVin	B = 0mT, Ic = 3mA			1	%/°C
Temp. coef. of Voff	αVoff	B = 0mT, Ic = 3mA			1	%/°C
Longterm instability of sensitivity				100		ppm/ year
Magnetic sensitive volume			0.25x0.25x0.2			mm ³
Bandwidth	Bw	-3 dB			30	kHz

Note: The shield S must not be biased positively with respect to any other terminal ! One way to ensure this is to connect S to the neg. input terminal I2 (see Fig.3)

Field range ?

Pin Configuration

Dice Information:		
Die Size	1.40 x 1.40	mm
Die Thickness	0,38 or 0,5	mm
Pad Size	0.15 x 0.15	mm

*Magnetic sensitive Vel 0.25 x 0.25 x 0.2 mm³
 250um x 250um x 2um
 abt 35um from surface.*

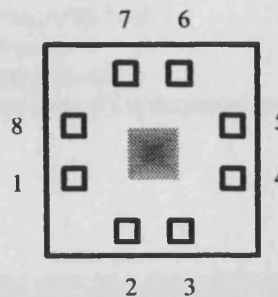


Fig.1: Die top view

Pin Configuration:

Pad	Function
1	IC1
2	SX1
3	Shield S
4	SY1
5	IC2
6	SX2
7	I2
8	SY2

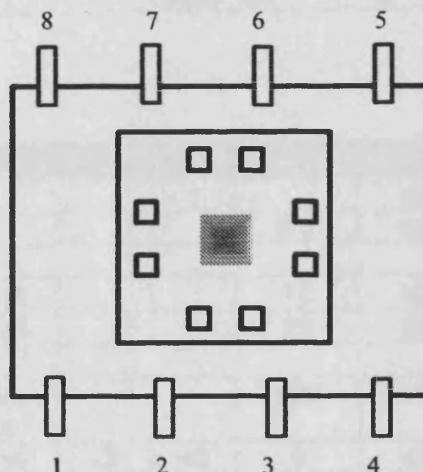
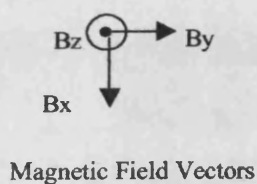


Fig.2: SOIC-8 top view

Interface Circuit:

*Out X = SX1- SX2 ; Out Y = SY1- SY2;
 Out Z = SX1- SY2 + SX2 - SY1*

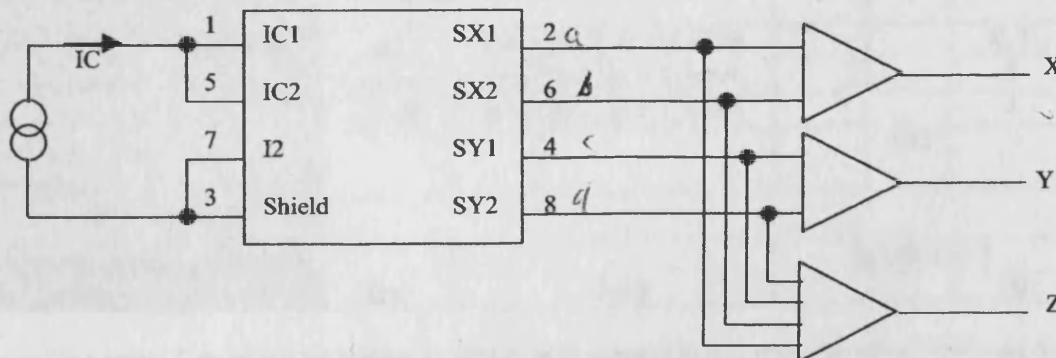


Fig.3: Typical application with current source and amplifier

Integrated 3-Axis Hall Generator**3D-H-10****Features**

- Measures the 3-axis of a magnetic field at the same spot.
- High Magnetic Field Sensitivity
- Low control current
- Available in 8 Pin-SOIC and in chip form

Application

- Mapping of a magnetic field
- 3-D position sensing
- Contactless potentiometer
- Angular position sensor for micromotors
- Joy-stick

Absolute Maximum Ratings

Item	Symbol	Condition	Limit	Unit
Max. Input Current	Ic	T = 300 K	1	mA
Max. Input Voltage	Vc	T = 300 K	15	V
Shield voltage	Vs	With respect to any other terminal	0 to -10	V
Operating Temp. Range	Topr.	at the nominal current	-40 to 110	°C
Storage Temp. Range	Tstg.		-40 to 125	°C

Typical Electrical Characteristics

Item	Symbol	Conditions	min.	max.	Typ.	Unit
Shield leakage current	Ileak	Vs = -10 V		1		nA
Nominal control current	Ic	See Ic in Fig.3			0.5	mA
Input resistance	Rin	B = 0mT, Ic = 0.5 mA			12	kΩ
Output resistance	Rout	B = 0mT, Ic = 0.5 mA			30	kΩ
Output voltage Sx1-Sx2	Vhx	Const. Current Drive			220	mV
Sy1-Sy2	Vhy	B = 1T, Ic = 0.5mA				
Offset voltage	Voff	B = 0mT, Ic = 0.5mA	-3	+3	0	mV
Field equivalent output noise (peak-peak) X, Y	Bnoise	Within 10 min Ic = 0.5mA		±30		μT
Z	Bnoise			±40		μT
Sensitivity X, Y	Sx, Sy	@ 0.5mA	200	240	220	mV/T
Sensitivity Z	Sz	@ 0.5mA			160	mV/T
Temp. coef. of sensitivity	αS	B = 10mT, Ic = 0.5mA			0.1	%/°C
Temp. coef. of Vin	αVin	B = 0mT, Ic = 0.5mA			1	%/°C
Temp. coef. of Voff	αVoff	B = 0mT, Ic = 0.5mA			1	%/°C
Longterm instability of sensitivity				100		ppm/year
Magnetic sensitive volume				0.1x0.1x0.1		mm ³
Bandwidth	Bw	-3 dB			10	kHz

Note: The shield S must not be biased positively with respect to any other terminal ! One way to ensure this is to connect S to the neg. input terminal I2 (see Fig.3)

Pin Configuration

Dice Information:		
Die Size	1.40 x 1.40	mm
Die Thickness	0,38 or 0,5	mm
Pad Size	0.15 x 0.15	mm

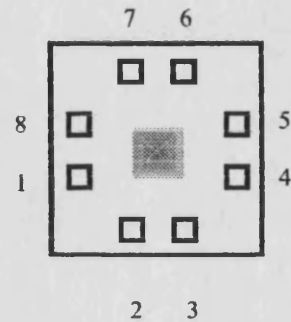


Fig.1: Die top view

Pin Configuration:

Pad	Function
1	IC1
2	SX1
3	Shield
4	SY1
5	IC2
6	SX2
7	I2
8	SY2

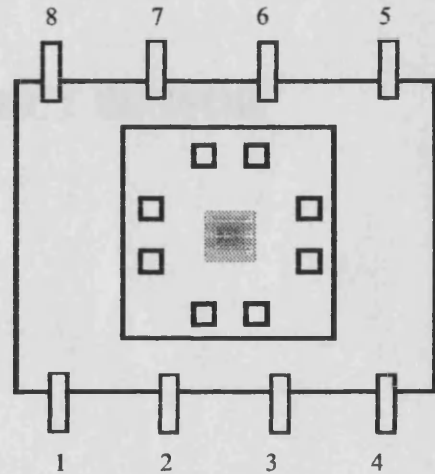
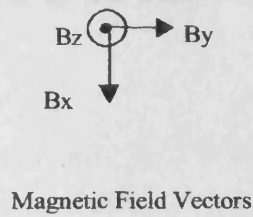


Fig.2: SOIC-8 top view

Interface Circuit:

$$\text{Out X} = \text{SX1} - \text{SX2}; \text{ Out Y} = \text{SY1} - \text{SY2};$$

$$\text{Out Z} = \text{SX1} - \text{SY2} + \text{SX2} - \text{SY1}$$

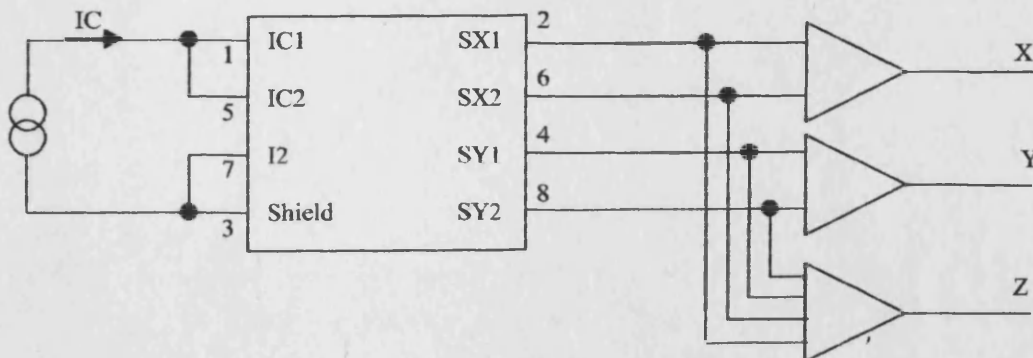


Fig.3: Typical application with current source and amplifier

APPENDIX B

CALIBRATION

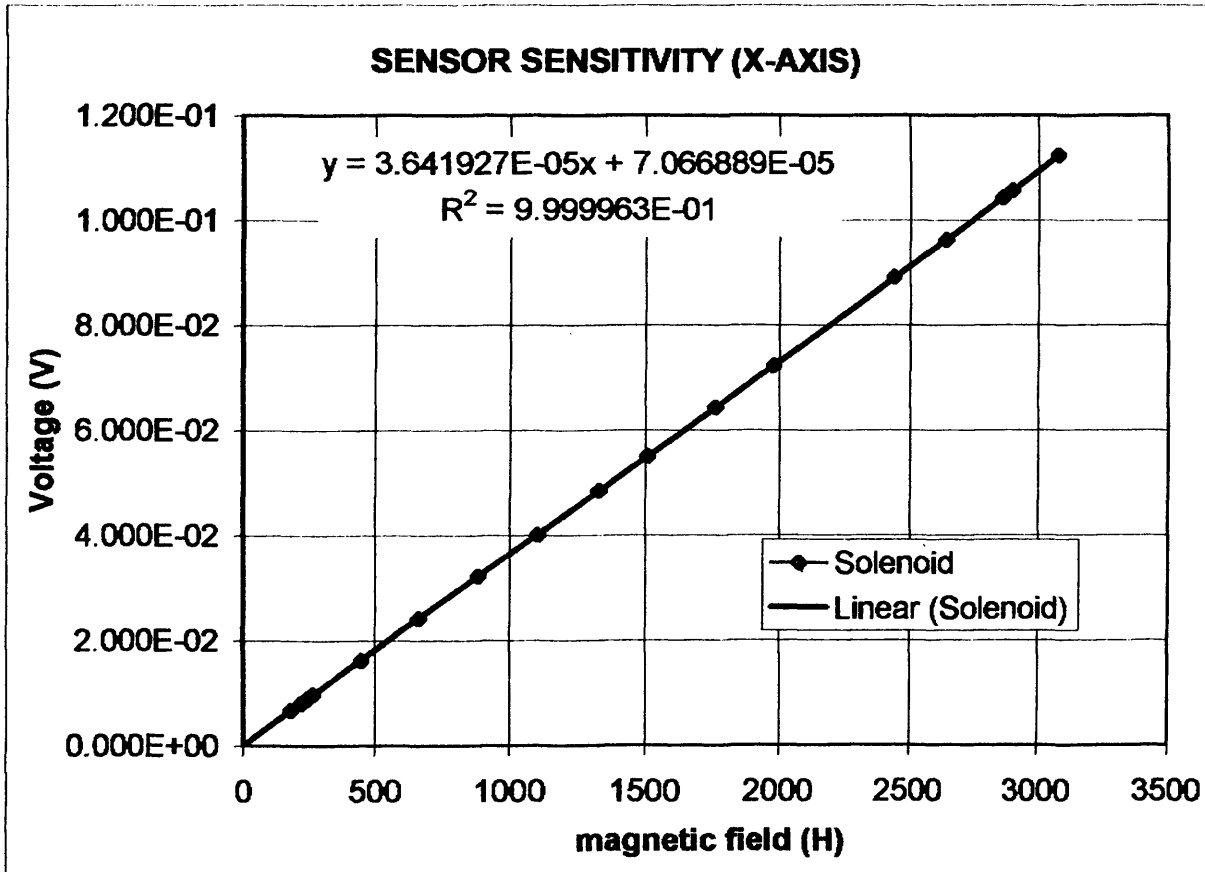
OF

INTEGRATED 3-D HALL EFFECT SENSOR

READINGS FOR -DIRECTION OF 3D SENSOR (17/9/03)

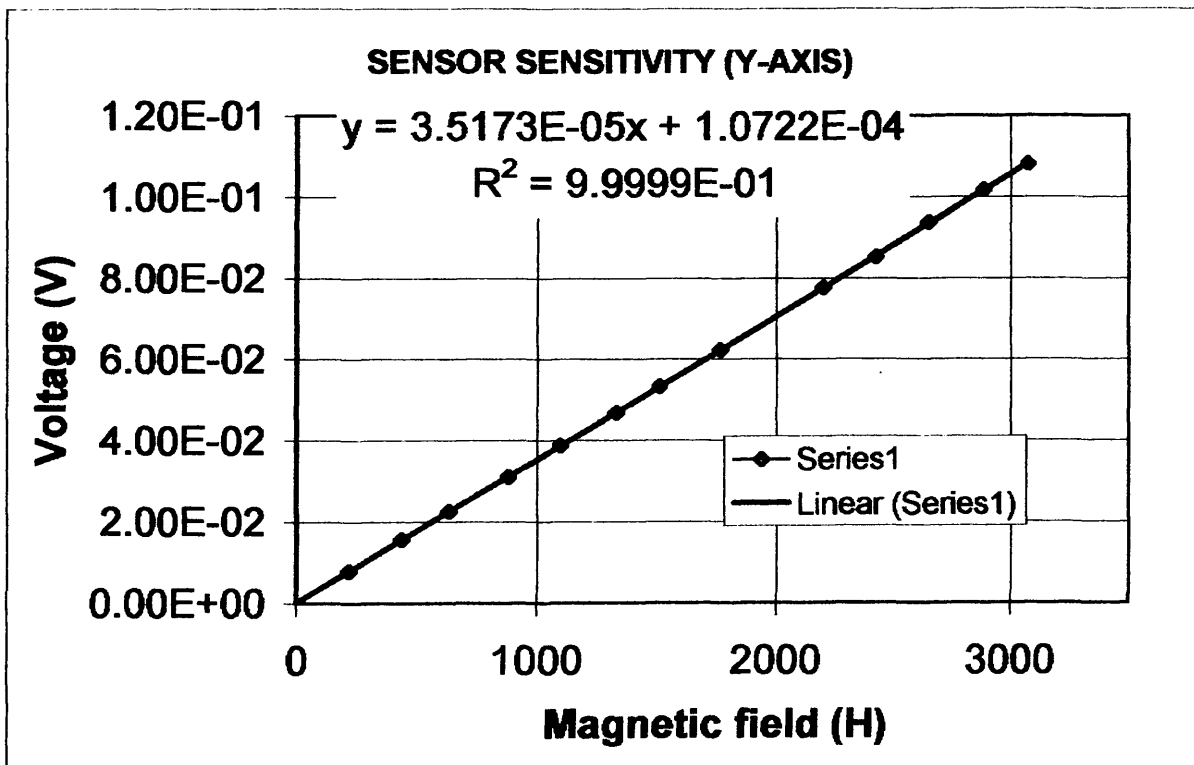
Current (A)	LabView number	Magnetising Field (He)	LabVIEW field
0.205	6.731E-03	180.391	1.829E+02
0.25	8.066E-03	219.989	2.195E+02
0.276	8.904E-03	242.868	2.425E+02
0.301	9.740E-03	264.866	2.655E+02
0.508	1.626E-02	447.017	4.446E+02
0.753	2.410E-02	662.606	6.597E+02
1.004	3.225E-02	883.475	8.835E+02
1.252	4.02E-02	1101.704	1.101E+03
1.507	4.84E-02	1326.092	1.326E+03
1.711	5.50E-02	1505.603	1.508E+03
2.002	6.43E-02	1761.670	1.764E+03
2.251	7.22E-02	1980.779	1.982E+03
2.774	8.91E-02	2440.995	2.445E+03
3.002	9.62E-02	2641.625	2.639E+03
3.253	1.04E-01	2862.494	2.861E+03
3.5	1.12E-01	3079.843	3.081E+03
3.295	1.06E-01	2899.452	2.897E+03

For X-axis, $x=(y-B)/A = 5.14026E-05$



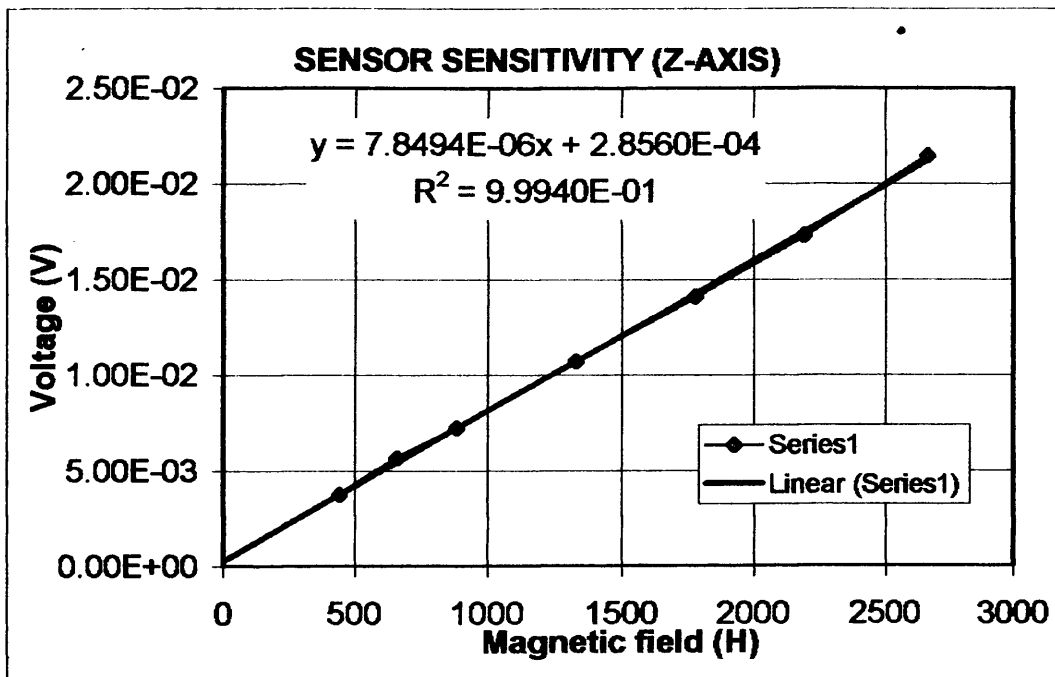
For Y-axis, $x=(y-B)/A = 4.96531E-05$

current	Labview	Magnetising Field (He)	LabVIEW field
0.249	7.89E-03	219.109	2.212E+02
0.501	1.56E-02	440.858	4.414E+02
0.726	2.25E-02	638.847	6.374E+02
1.002	3.11E-02	881.715	8.814E+02
1.248	3.87E-02	1098.184	1.098E+03
1.512	4.68E-02	1330.492	1.327E+03
1.716	5.33E-02	1510.003	1.511E+03
2.006	6.23E-02	1765.190	1.767E+03
2.501	7.75E-02	2200.768	2.201E+03
2.756	8.52E-02	2425.156	2.418E+03
3.013	9.36E-02	2651.305	2.659E+03
3.282	1.02E-01	2888.013	2.889E+03
3.495	1.08E-01	3075.443	3.072E+03



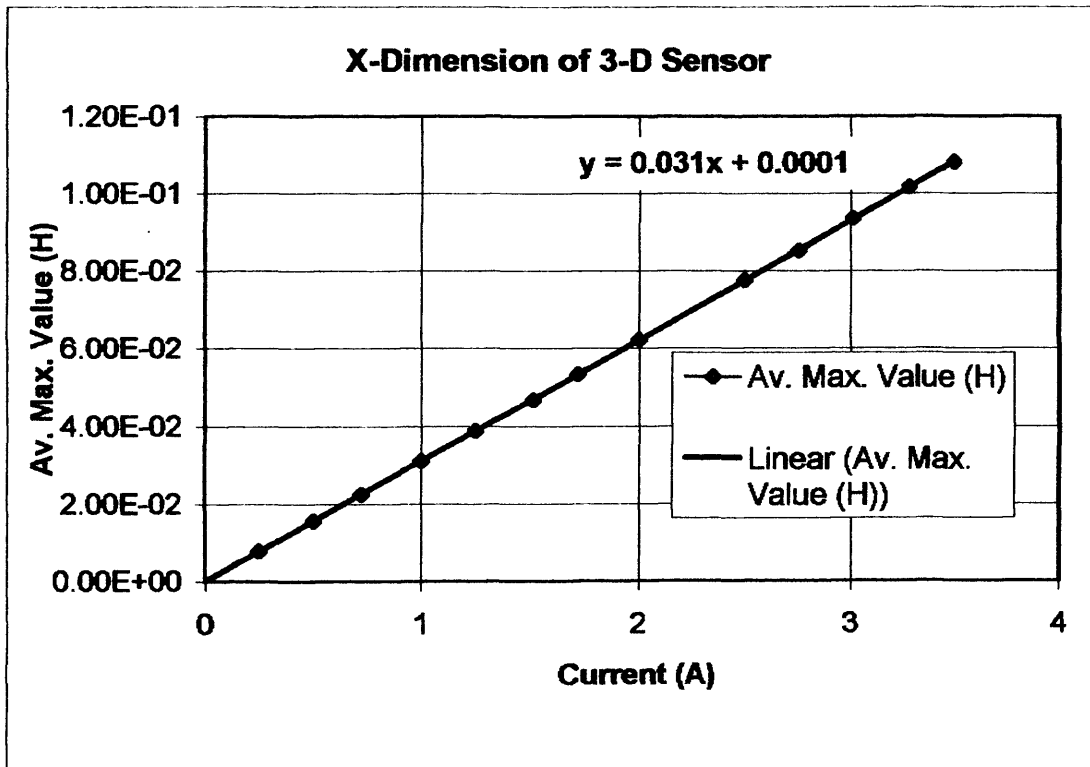
For Z-axis, $x=(y-B)/A = 1.13E-05$

current	labview	field	LabVIEW field
0.505	3.74E-03	444.377	4.394E+02
0.752	5.66E-03	661.726	6.842E+02
1.008	7.24E-03	886.995	8.855E+02
1.51	1.07E-02	1328.732	1.327E+03
2.02	1.41E-02	1777.509	1.758E+03
2.49	1.73E-02	2191.088	2.166E+03
3.03	2.15E-02	2666.264	2.696E+03



READINGS FOR X-DIRECTION OF 3D SENSOR (17/9/03)

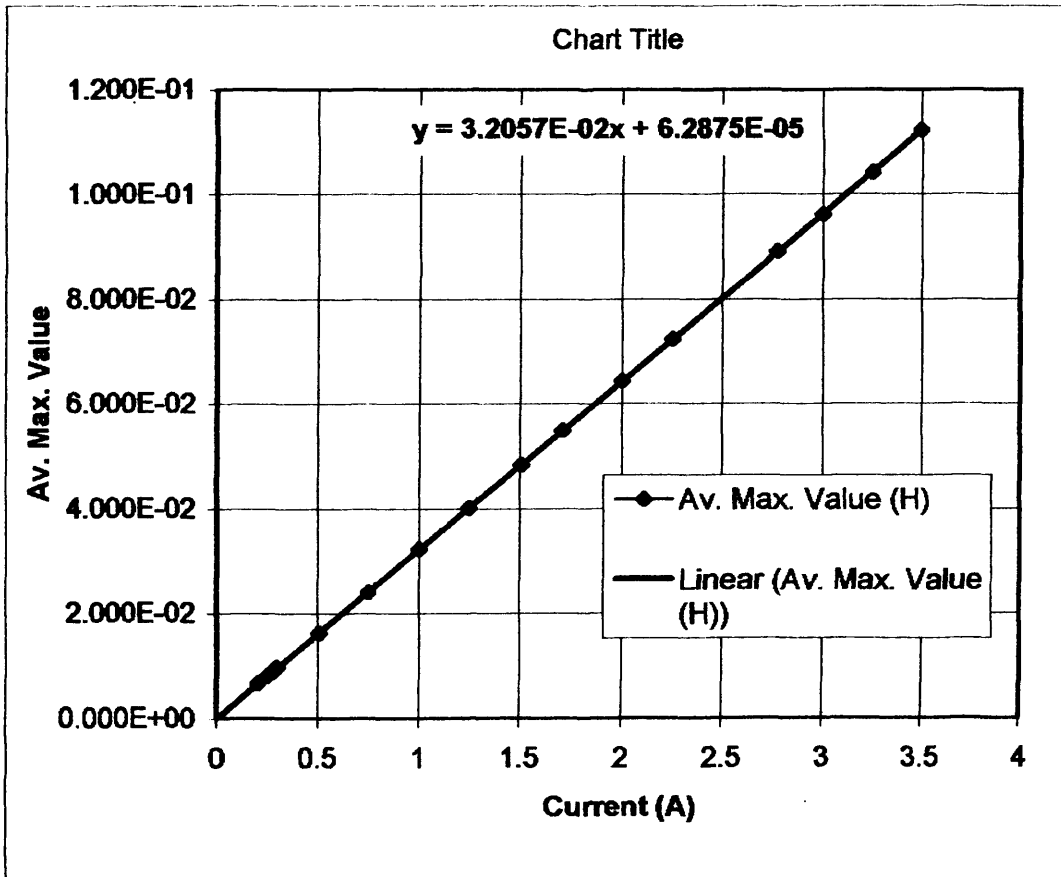
Current (A)	Av. Max. Value (H)	Standard Deviation (H)
0.249	7.89E-03	
0.501	1.56E-02	
0.726	2.25E-02	
1.002	3.11E-02	
1.248	3.87E-02	
1.512	4.68E-02	
1.716	5.33E-02	
2.006	6.23E-02	
2.501	7.75E-02	
2.756	8.52E-02	
3.013	9.36E-02	
3.282	1.02E-01	
3.495	1.08E-01	



READINGS FOR Y-DIRECTION OF 3D SENSOR (17/9/03)

Current (A)	Av. Max. Value (H)	Standard Deviation (H)
0.205	6.731E-03	
0.25	8.066E-03	
0.276	8.904E-03	
0.301	9.740E-03	
0.508	1.626E-02	
0.753	2.410E-02	
1.004	3.225E-02	
1.252	4.02E-02	
1.507	4.84E-02	
1.711	5.50E-02	
2.002	6.43E-02	0.024494897
2.251	7.22E-02	
2.774	8.91E-02	
3.002	9.62E-02	
3.253	1.04E-01	
3.5	1.12E-01	
3.295	1.06E-01	3.2037E-02 31.21417948

gradient constant current error
 3.21E-02 31.19443491 1.048449 0.769231

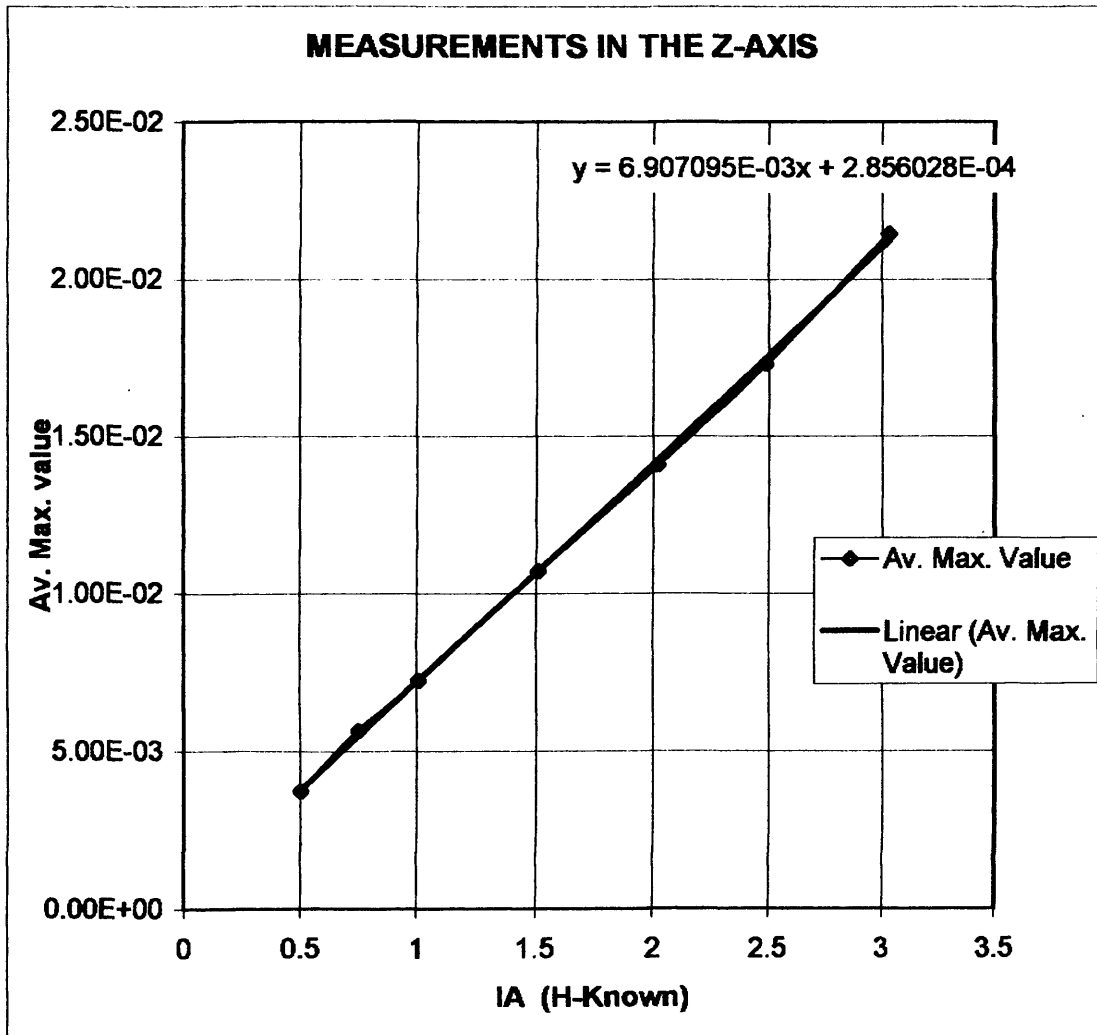


EXPERIMENTAL READINGS - 17/9/2003

(1000 iterations)

I(A)	Av. Max. Value	Standard Deviation
0.505	3.74E-03	1.20E-03
0.752	5.66E-03	8.61E-04
1.008	7.24E-03	6.76E-04
1.51	1.07E-02	7.73E-04
2.02	1.41E-02	6.25E-04
2.49	1.73E-02	5.75E-04
3.03	2.15E-02	1.57E-02

gradient constant current error
 6.91E-03 144.778666 3.851315206 0.819371728



APPENDIX C

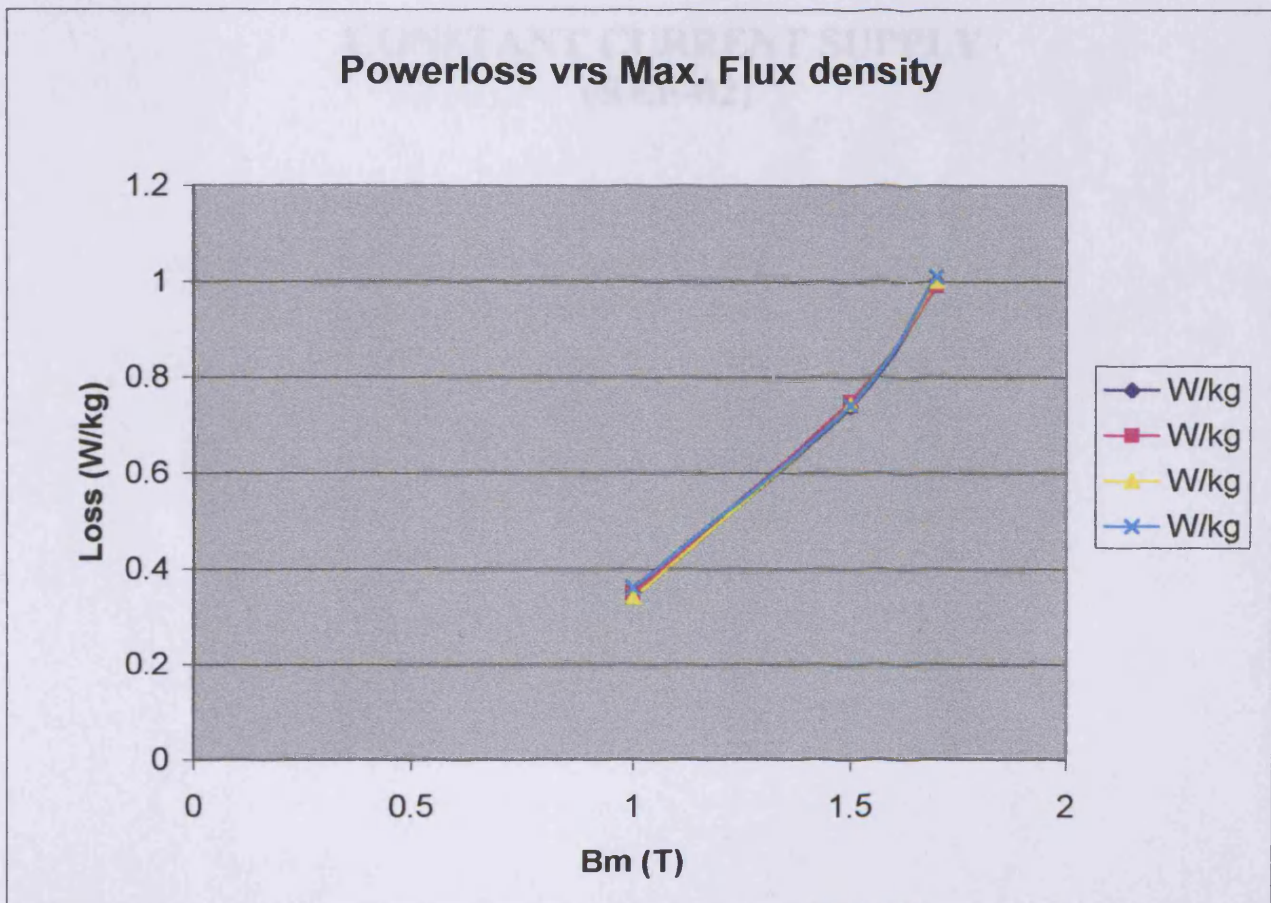
ERROR / UNCERTAINTY

DETERMINATION

Bm	W/kg	W/kg	W/kg	W/kg	W/kg	W/kg	st.dev	stdev %
1	0.35	0.35	0.34	0.36	0.365	0.365	0.009746794	0.974679434
1.5	0.74	0.75	0.745	0.743	0.743	0.743	0.003701351	0.37013511
1.7	1	0.99	1	1.01	0.98	0.98	0.011401754	1.140175425
								0.82832999
							total random	1.037234813

Uh 4.90%
 Ub 1.7
 Total Us 5.18
 total Error 5.28

APPENDIX D
 DATA SHEET



APPENDIX D

DATA SHEET

OF

CONSTANT CURRENT SUPPLY
(REF-02)

4



+5V Precision Voltage Reference/Temperature Transducer

REF-02

FEATURES

- 5 Volt Output $\pm 0.3\%$ Max
- Temperature Voltage Output $2.1\text{mV}/^\circ\text{C}$
- Adjustment Range $\pm 3\%$ Min
- Excellent Temperature Stability $8.5\text{ppm}/^\circ\text{C}$ Max
- Low Noise $15\mu\text{V}_{\text{p-p}}$ Max
- Low Supply Current 1.4mA Max
- Wide Input Voltage Range 7V to 40V
- High Load-Driving Capability 20mA
- No External Components
- Short-Circuit Proof
- MIL-STD-883 Screening Available
- Available in Die Form

GENERAL DESCRIPTION

The REF-02 precision voltage reference provides a stable +5V output which can be adjusted over a $\pm 6\%$ range with minimal effect on temperature stability. Single-supply operation over an input voltage range of 7V to 40V, low current drain of 1mA, and excellent temperature stability are achieved with an improved bandgap design. Low cost, low noise, and low power make the REF-02 an excellent choice whenever a stable voltage reference is required. Applications include D/A and A/D converters, portable instrumentation, and digital voltmeters. The versatility of the REF-02 is enhanced by its use as a monolithic temperature transducer. For +10V references, see the REF-01 and REF-10 data sheets.

ORDERING INFORMATION †

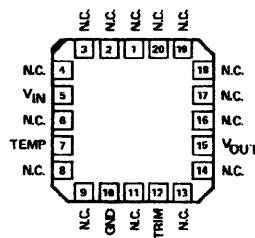
$T_A = 25^\circ\text{C}$ V_{OS} MAX (mV)	PACKAGE				OPERATING TEMPERATURE RANGE
	TO-99	CERDIP 8-PIN	PLASTIC 8-PIN	LCC 20-CONTACT	
± 15	REF02AJ*	REF02AZ*	-	-	MIL
± 15	REF02EJ	REF02EZ	-	-	COM
± 25	REF02J*	REF02Z*	-	REF02RC/883	MIL
± 25	REF02HJ	REF02HZ	REF02HP	-	COM
± 50	REF02CJ	REF02CZ	-	-	COM
± 50	-	-	REF02CP	-	XIND
± 50	-	-	REF02CS††	-	XIND
± 100	REF02DJ	REF02DZ	REF02DP	-	COM

* For devices processed in total compliance to MIL-STD-883, add /883 after part number. Consult factory for 883 data sheet.

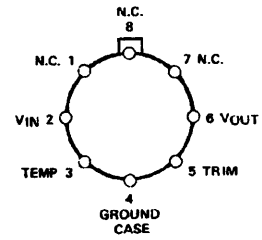
† Burn-in is available on commercial and industrial temperature range parts in CerDIP, plastic DIP, and TO-can packages.

†† For availability and burn-in information on SO and PLCC packages, contact your local sales office.

PIN CONNECTIONS

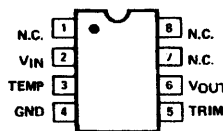


REF-02RC/883
LCC (RC-Suffix)

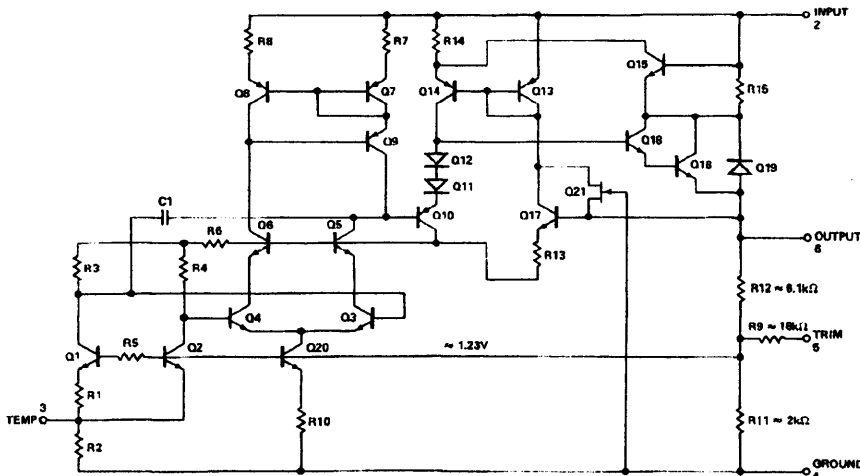


TO-99 (J-Suffix)

- 8-PIN HERMETIC DIP (Z-Suffix)
- EPOXY MINI-DIP (P-Suffix)
- 8-PIN SO (S-Suffix)



SIMPLIFIED SCHEMATIC



REV. B

Information furnished by Analog Devices is believed to be accurate and reliable. However, no responsibility is assumed by Analog Devices for its use, nor for any infringements of patents or other rights of third parties which may result from its use. No license is granted by implication or otherwise under any patent or patent rights of Analog Devices.

One Technology Way, P.O. Box 9106, Norwood, MA 02062-9106, U.S.A.
 Tel: 617/329-4700 Fax: 617/326-8703 Twx: 710/394-6577
 Telex: 924491 Cable: ANALOG NORWOODMASS

REF-02

ABSOLUTE MAXIMUM RATINGS (Note 1)

Input Voltage	
REF-02A, E, H, RC, All DICE	40V
REF-02C, D	30V
Output Short-Circuit Duration (to Ground or V_{IN})	Indefinite
Storage Temperature Range	
J, RC, and Z Packages	-65°C to +150°C
P Packages	-65°C to +125°C
Operating Temperature Range	
REF-02A, REF-02, REF-02RC	-55°C to +125°C
REF-02E, REF-02H	0°C to +70°C
REF-02CJ, CZ, REF-02D	0°C to +70°C
REF-02CP, CS	-40°C to +85°C
Lead Temperature (Soldering, 60 sec)	300°C

Junction Temperature (T_J) -65°C to +150°C

PACKAGE TYPE	θ_{JA} (NOTE 2)	θ_{JC}	UNITS
TO-99 (J)	170	24	°C/W
8-Pin Hermetic DIP (Z)	162	26	°C/W
8-Pin Plastic DIP (P)	110	50	°C/W
20-Contact LCC (RC, TC)	120	40	°C/W
8-Pin SO (S)	160	44	°C/W
20-Contact PLCC (PC)	80	39	°C/W

NOTES:

1. Absolute maximum ratings apply to both DICE and packaged parts, unless otherwise noted.
2. θ_{JA} is specified for worst case mounting conditions, i.e., θ_{JA} is specified for device in socket for TO, CarDIP, P-DIP, and LCC packages; θ_{JA} is specified for device soldered to printed circuit board for SO and PLCC packages.

ELECTRICAL CHARACTERISTICS at $V_{IN} = +15V$, $T_A = +25^\circ C$, unless otherwise noted.

PARAMETER	SYMBOL	CONDITIONS	REF-02A/E			REF-02/H			UNITS
			MIN	TYP	MAX	MIN	TYP	MAX	
Output Voltage	V_O	$I_L = 0$	4.985	5.000	5.015	4.975	5.000	5.025	V
Output Adjustment Range	ΔV_{trim}	$R_p = 10k\Omega$	± 3	± 6	—	± 3	± 6	—	%
Output Voltage Noise	e_{np-p}	0.1Hz to 10Hz (Note 7)	—	10	15	—	10	15	μV_{p-p}
Line Regulation (Note 2)		$V_{IN} = 8V$ to 33V	—	0.006	0.010	—	0.006	0.010	%/V
Load Regulation (Note 2)		$I_L = 0$ to 10mA	—	0.005	0.010	—	0.006	0.010	%/mA
Turn-on Settling Time	t_{ON}	To $\pm 0.1\%$ of final value	—	5	—	—	5	—	μs
Quiescent Supply Current	I_{SQ}	No Load	—	1.0	1.4	—	1.0	1.4	mA
Load Current	I_L		10	21	—	10	21	—	mA
Sink Current	I_S	(Note 8)	-0.3	-0.5	—	-0.3	-0.5	—	mA
Short-Circuit Current	I_{SC}	$V_O = 0$	—	30	—	—	30	—	mA
Temperature Voltage Output	V_T	(Note 3)	—	630	—	—	630	—	mV

ELECTRICAL CHARACTERISTICS at $V_{IN} = +15V$, $-55^\circ C \leq T_A \leq +125^\circ C$ for REF-02A and REF-02, $0^\circ C \leq T_A \leq +70^\circ C$ for REF-02E and REF-02H, $I_L = 0mA$, unless otherwise noted.

PARAMETER	SYMBOL	CONDITIONS	REF-02A/E			REF-02/H			UNITS
			MIN	TYP	MAX	MIN	TYP	MAX	
Output Voltage Change with Temperature (Notes 4, 5)	ΔV_{OT}	$0^\circ C \leq T_A \leq +70^\circ C$ $-55^\circ C \leq T_A \leq +125^\circ C$	—	0.02	0.06	—	0.07	0.17	%
Output Voltage Temperature Coefficient	TCV_O	(Note 6)	—	3	8.5	—	10	25	ppm/°C
Change in V_O Temperature Coefficient with Output Adjustment		$R_p = 10k\Omega$	—	0.7	—	—	0.7	—	ppm/%
Line Regulation ($V_{IN} = 8$ to 33V) (Note 2)		$0^\circ C \leq T_A \leq +70^\circ C$ $-55^\circ C \leq T_A \leq +125^\circ C$	—	0.007	0.012	—	0.007	0.012	%/V
Load Regulation ($I_L = 0$ to 8mA) (Note 2)		$0^\circ C \leq T_A \leq +70^\circ C$ $-55^\circ C \leq T_A \leq +125^\circ C$	—	0.006	0.010	—	0.007	0.012	%/mA
Temperature Voltage Output Temperature Coefficient	TCV_T	(Note 3)	—	2.1	—	—	2.1	—	mV/°C

NOTES:

1. Guaranteed by design.
2. Line and Load Regulation specifications include the effect of self heating.
3. Limit current in or out of pin 3 to 50nA and capacitance on pin 3 to 30pF.
4. ΔV_{OT} is defined as the absolute difference between the maximum output voltage and the minimum output voltage over the specified temperature range expressed as a percentage of 5V.

$$\Delta V_{OT} = \left| \frac{V_{MAX} - V_{MIN}}{5V} \right| \times 100$$

5. ΔV_{OT} specification applies trimmed to +5.000V or untrimmed.
6. TCV_O is defined as ΔV_{OT} divided by the temperature range, i.e.,

$$TCV_O = \frac{\Delta V_{OT}}{70^\circ C}$$

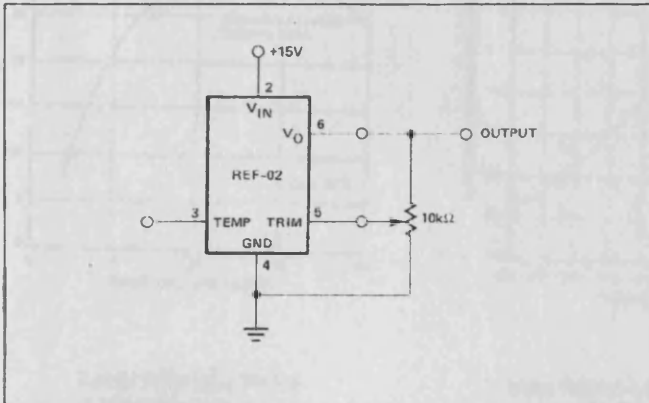
7. Sample Tested.
8. During sink current test the driver meets the output voltage specified.

OUTPUT ADJUSTMENT

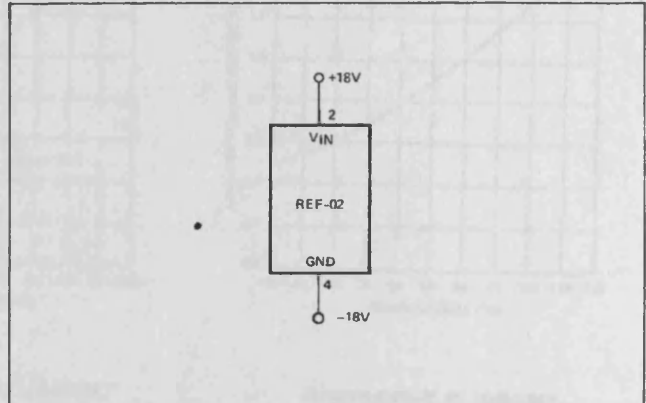
The REF-02 trim terminal can be used to adjust the output voltage over a $5V \pm 300mV$ range. This feature allows the system designer to trim system errors by setting the reference to a voltage other than 5V. Of course, the output can also be set to exactly 5.000V or to 5.12V for binary applications.

Adjustment of the output does not significantly affect the temperature performance of the device. Typically, the temperature coefficient change is $0.7ppm/^{\circ}C$ for 100mV of output adjustment.

OUTPUT ADJUSTMENT CIRCUIT

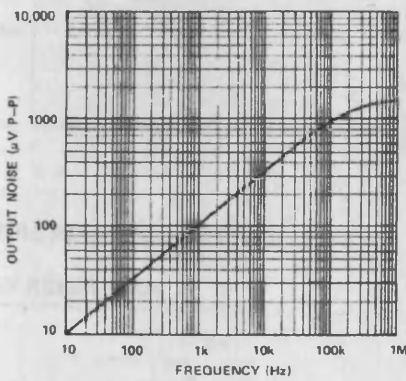


BURN-IN CIRCUIT

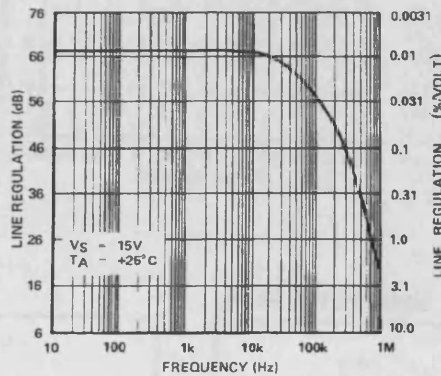


TYPICAL PERFORMANCE CHARACTERISTICS

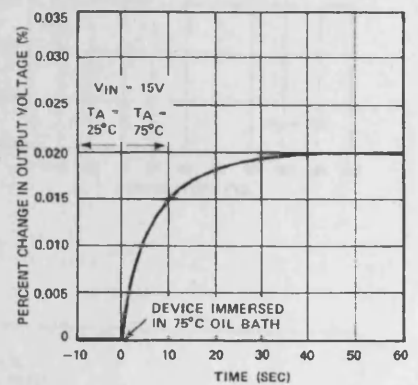
OUTPUT WIDEBAND NOISE vs BANDWIDTH (0.1Hz TO FREQUENCY INDICATED)



LINE REGULATION vs FREQUENCY



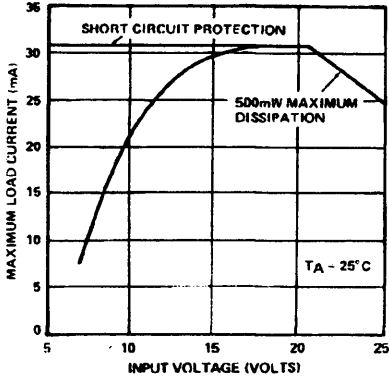
OUTPUT CHANGE DUE TO THERMAL SHOCK



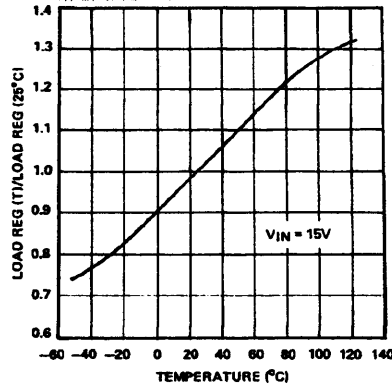
REF-02

TYPICAL PERFORMANCE CHARACTERISTICS

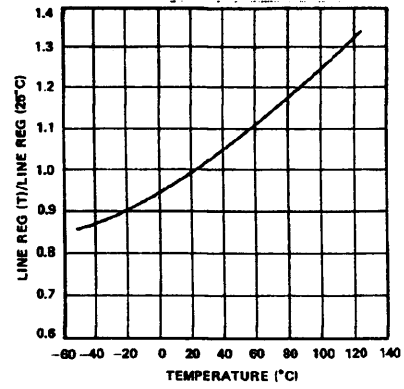
MAXIMUM LOAD CURRENT vs INPUT VOLTAGE



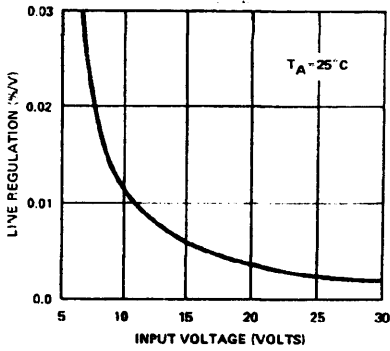
NORMALIZED LOAD REGULATION ($\Delta I_L = 10\text{mA}$) vs TEMPERATURE



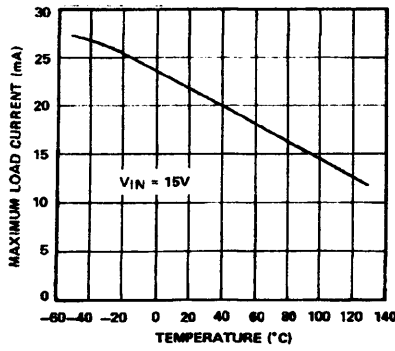
NORMALIZED LINE REGULATION vs TEMPERATURE



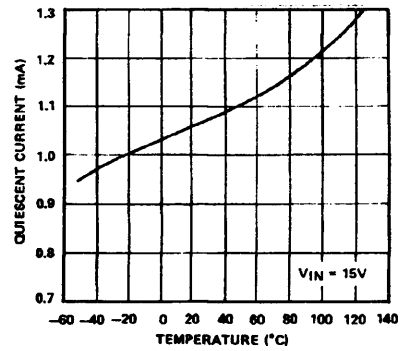
LINE REGULATION vs SUPPLY VOLTAGE



MAXIMUM LOAD CURRENT vs TEMPERATURE

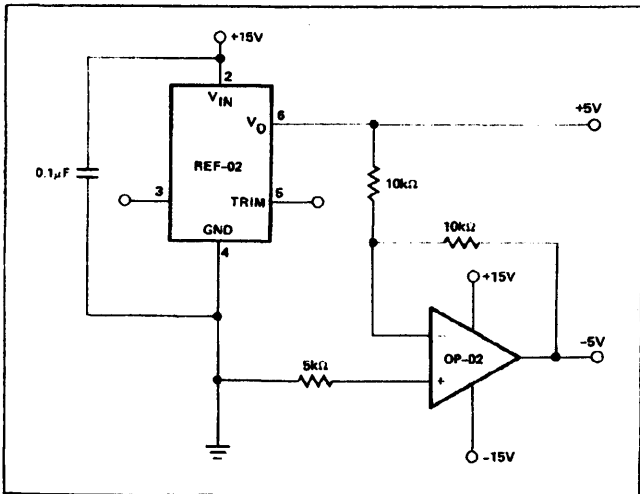


QUIESCENT CURRENT vs TEMPERATURE

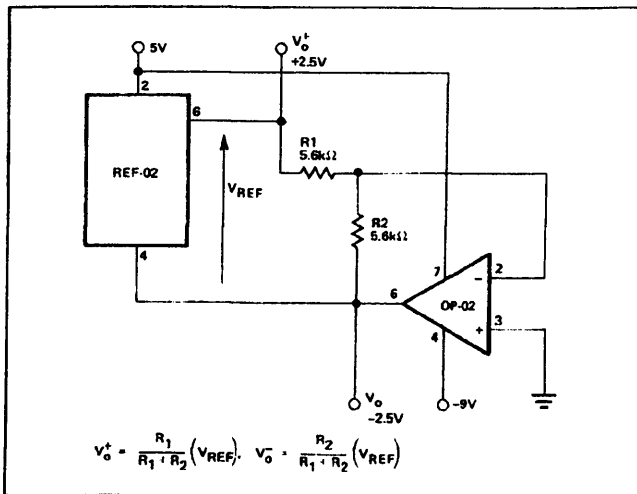


TYPICAL APPLICATIONS

±5V REFERENCE



±2.5V REFERENCE



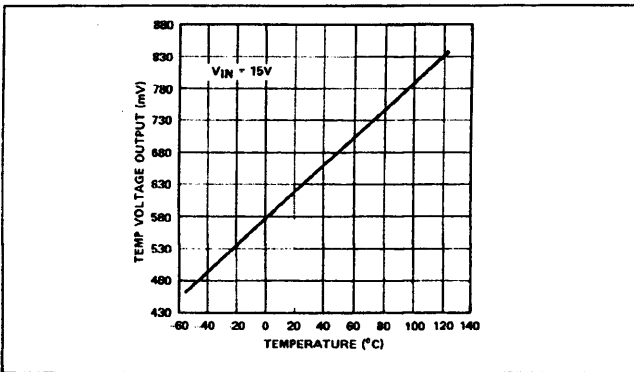
REF-02

PRECISION TEMPERATURE TRANSDUCER WITH REMOTE SENSOR

RESISTOR VALUES			
TCV _{OUT} SLOPE (S)	10mV/°C	100mV/°C	10mV/°F
TEMPERATURE RANGE	-55°C to +125°C	-55°C to +125°C	-67°F to +257°C
OUTPUT VOLTAGE RANGE	-0.55V to +1.25V	-5.5V to +12.5V*	-0.67V to +2.57V
ZERO-SCALE	0V @ 0°C	0V @ 0°C	0V @ 0°F
R _b (± 1% resistor)	9.09kΩ	15kΩ	7.5kΩ
R _{b1} (± 1% resistor)	1.5kΩ	1.82kΩ	1.21kΩ
R _{bp} (Potentiometer)	200Ω	500Ω	200Ω
R _c (± 1% resistor)	5.11kΩ	84.5kΩ	8.25kΩ

*For 125°C operation, the op^amp output must be able to swing to +12.5V, increase V_{IN} to +18V from +15V if this is a problem.

TYPICAL TEMPERATURE VOLTAGE OUTPUT vs TEMPERATURE (REF-02A)



REFERENCE STACK WITH EXCELLENT LINE REGULATION

Two REF-01's and one REF-02 can be stacked to yield 5.000V, 15.000V and 25.000V outputs. An additional advantage of this circuit is near-perfect line regulation of the 5.0V and 15.0V outputs. A 27V to 55V input change produces an output change which is less than the noise voltage of the devices. A load bypass resistor (R_B) provides a path for the supply current (I_{SY}) of the 15.000V regulator.

In general, any number of REF-01's and REF-02's can be stacked this way. For example, ten devices will yield ten outputs in 5V or 10V steps. The line voltage can range from 100V to 130V. However, care must be taken to ensure that the total load currents do not exceed the maximum usable current (typically 21mA).

TEMPERATURE CONTROLLER

NOTES:

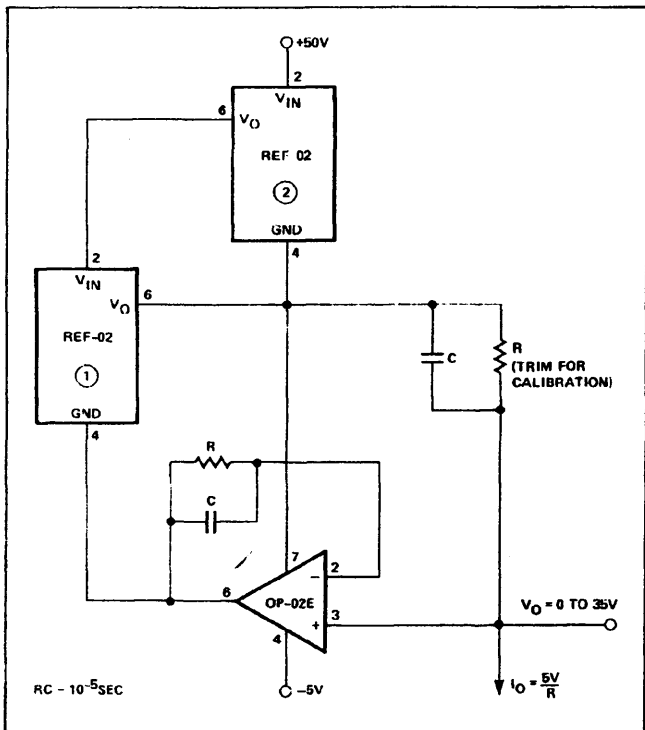
- REF-02 SHOULD BE THERMALLY CONNECTED TO SUBSTANCE BEING HEATED.
- NUMBERS IN PARENTHESES ARE FOR A SETPOINT TEMPERATURE OF 60°C.
- R₃ = R₁/R₂ × R₆

REF-02

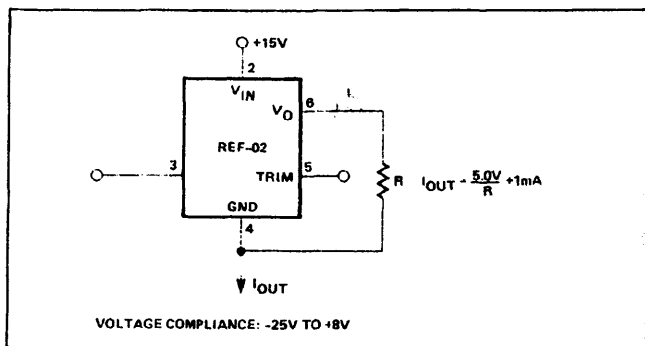
PRECISION CURRENT SOURCE

A current source with 35V output compliance and excellent output impedance can be obtained using this circuit. REF-02 (2) keeps the line voltage and power dissipation constant in device (1); the only important error consideration at room temperature is the negative supply rejection of the op amp. The typical $3\mu\text{V/V}$ PSRR of the OP-02E will create a 20ppm change ($3\mu\text{V/V} \times 35\text{V}/5\text{V}$) in output current over a 35V range. For example, a 5mA current source can be built ($R = 1\text{k}\Omega$) with $350\text{M}\Omega$ output impedance.

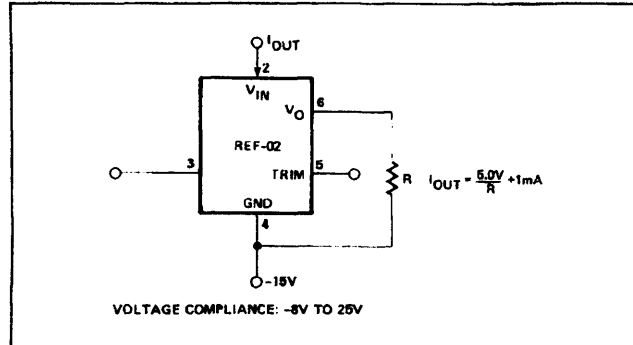
$$R_0 = \frac{35\text{V}}{20 \times 10^{-6} \times 5\text{mA}}$$



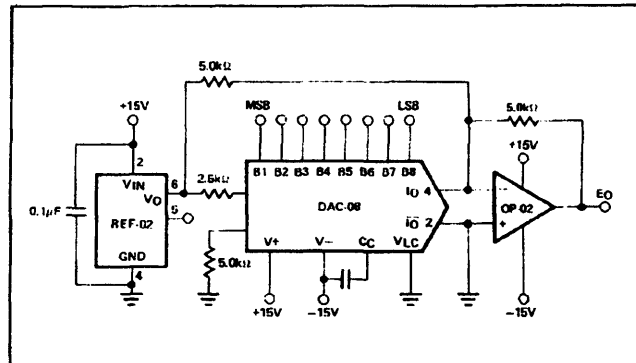
CURRENT SOURCE



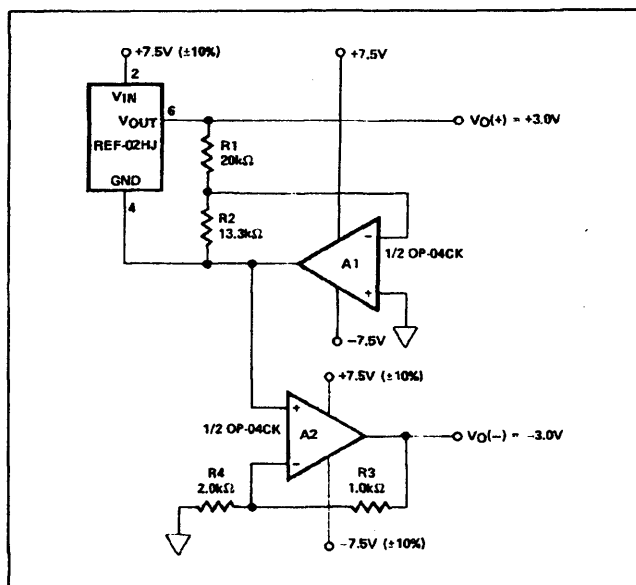
CURRENT SINK



D/A CONVERTER REFERENCE



$\pm 3\text{V}$ REFERENCE



SUPPLY BYPASSING

For best results, it is recommended that the power supply pin is bypassed with a $0.1\mu\text{F}$ disc ceramic capacitor.